BAKU STATE UNIVERSITY

9th INTERNATIONAL CONFERENCE "MTP-2025"

MODERN TRENDS IN PHYSICS

BOOK OF ABSTRACTS

NOVEMBER 27-28, 2025

BAKU STATE UNIVERSITY
BAKU, AZERBAIJAN

BAKU STATE UNIVERSITY

9th INTERNATIONAL CONFERENCE MTP-2025: MODERN TRENDS IN PHYSICS

BOOK OF ABSTRACTS

November 27 – 28, 2025

Baku State University
Baku, Azerbaijan

Book of Abstracts. 9th International Conference MTP-2025: Modern Trends in Physics. November 27–28, 2025. Baku State University, Baku, Azerbaijan. Baku: BSU Publishing House, 2025. – 264 p.

ISBN: 978-9952-588-43-9

ORGANIZING COMMITTEE

Chairman:

Elchin Babayev – Rector of Baku State University (BSU), Azerbaijan

Deputy chairman:

Huseyn Mammadov – Vice Rector for Science and Innovations, BSU, Azerbaijan

Members:

Farid Nagiev – Director of the Centre for Organization of Scientific Activity and Innovations, BSU, Azerbaijan

Mais Suleymanov – Director of Institute for Physical Problems, BSU, Azerbaijan

Mahir Pirguliyev – Head of the Rector's Secretariat, BSU, Azerbaijan

Bakhtiyar Pashayev – Dean of Physics faculty, BSU, Azerbaijan

Mustafa Muradov – Deputy Director for Education, Programs and Cooperation of Excellence Center for Research, Development and Innovations, BSU, Azerbaijan

Mirnamik Bashirov – Head of the Department of Doctorate, BSU, Azerbaijan

Muhammad Iftikhar Khan – Head of Department of Physics, The University of Lahore, Islamic Republic of Pakistan

Vusal Mammadov – Deputy Dean for Academic Affairs of the Physics Faculty, BSU, Azerbaijan

Shahla Hajiyeva – Deputy Dean for Scientific Affairs of the Physics
– Faculty, BSU, Azerbaijan

Tahmasib Aliyev – Professor, Middle East Technical University, Türkiye

Stefano Bellucci – Professor, NIMP, Bucharest, Romania

Majid Gojayev – Associate Professor, Theoretical Physics Department, BSU, Azerbaijan

Lala Gahramanli – Leading researcher, EC Nano Research Lab, BSU, Azerbaijan

Sara Rahimzade – Specialist of Physics faculty, BSU, Azerbaijan

Shahriyar Jafarzade – Arizona State University, United States of America

PROGRAM COMMITTEE

Chairman:

Aydin Kazimzade – Rector's advisor for Science and Education, BSU, Azerbaijan

Members:

Raheel Qamar – Dean of faculty of Sciences, COMSATS University, Islamic Republic of Pakistan

Oktay Gasimov – Director of Institute of Biophysics, Ministry of Science and Education, Azerbaijan

Sakin Jabarov – Associate Professor, Deputy Chairman of the Supreme Attestation Commission, Azerbaijan

Farhad Rustamov – Head of Condensed Matter department, Institute for Physical Problems, BSU, Azerbaijan

Namig Ahmedov – Head of Biophysics department, Institute for Physical Problems, BSU, Azerbaijan

Najeeb-ur-Rehman – Dean of the Faculty of Physics, COMSATS University, Islamic Republic of Islamic Republic of Pakistan

Ahmad Abdinov – Head of the Department of Physical Electronics, BSU, Azerbaijan

Vagif Salmanov – Head of the Department of Semiconductor Physics, BSU, Azerbaijan

Rena Gasimova – Head of the Department of Optics and Molecular Physics, BSU, Azerbaijan

Maarif Jafarov – Head of the Department of Chemical Physics of Nanomaterials, BSU, Azerbaijan

Sajida Abdulvahabova – Head of the Department of Matter Structure, BSU, Azerbaijan

Mammad Rajabov – Head of the Department of Theoretical Physics, BSU, Azerbaijan

Mehdi Mahmudov – Head of the Department of Solid State Physics, BSU, Azerbaijan

Kamala Alisheva – Head of the Department of Astrophysics, BSU, Azerbaijan

MATERIAL SCIENCE

FLEXIBLE AND DURABLE POROUS POLYSILOXANE/MWCNT NANOCOMPOSITES FOR NEXT-GENERATION TRIBOELECTRIC NANOGENERATORS

[1,2*]Gulahmadov O.G., [1]Muradov M.B., [1]Gahramanli L.R., [1]Jiseok Kim, [3]Nadia Todorova, [3]Christos Trapalis

[1]Baku State University, Azerbaijan
[2]Karabakh University, Azerbaijan
[3]Institute of Nanoscience and Nanotechnology, National Center for Scientific Research "Demokritos", Agia Paraskevi, Athens, Greece
ogulahmadov@bsu.edu.az

AIn this study, porous polysiloxane (PS)/multi-walled carbon nanotube (MWCNT) nanocomposite films were developed as high-performance triboelectric layers for flexible triboelectric nanogenerators (TENGs). TENGs, which convert irregular and low-frequency mechanical motion into electricity through contact electrification and electrostatic induction, are emerging as a promising approach for self-powered electronic systems. The nanocomposites were fabricated via a doctor blading method, with porosity introduced through a simple and scalable salt-leaching process. Controlled pore morphology was achieved using sieved salt particles of different sizes, resulting in films with fine, medium, and large pores. Raman spectroscopy confirmed the uniform dispersion of MWCNTs and strong interfacial interaction within the PS matrix, while SEM analysis verified the presence of well-defined porous structures.

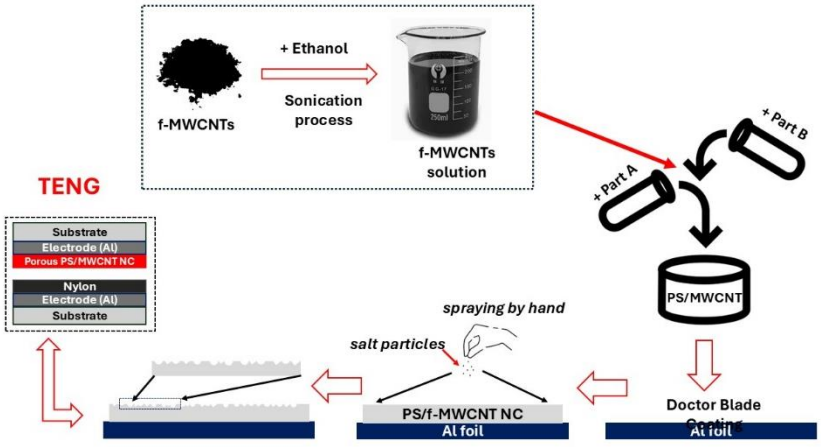

Dielectric measurements showed a reduction in permittivity with increasing pore size, due to the incorporation of air, which directly affects charge storage and transfer. Triboelectric output improved significantly with porosity, with the medium-porosity sample showing the best performance: an open-circuit voltage of 65 V, a short-circuit current of 6.9 μA, a maximum power density of 280.6 mW m^{-2}, and a surface charge density of 245 μC m^{-2}. This performance enhancement is attributed to the synergistic effect of MWCNT-induced interfacial polarization and optimized porous microstructure, which together increase surface roughness, contact area, and charge trapping capability. These results demonstrate that porous PS/MWCNT nanocomposites offer a scalable, flexible, and cost-effective platform for next-generation TENGs with great potential in wearable electronics, self-powered sensors, and sustainable energy-harvesting applications.

ENHANCED DIELECTRIC AND OPTICAL PERFORMANCE IN $BaTiO_3$/Graphene/PVA NANOCOMPOSITES VIA SOLUTİON CASTING: STRUCTURAL, MORPHOLOGICAL, AND INTERFACİAL INSIGHTS

Gahramanli L.R., *Alakbarova Sh.S.
Baku State University, Azerbaijan
alakbarova.safiqa.safar@bsu.edu.az

Solution casting was used to produce the $BaTiO_3$/Graphene/PVA nanocomposites, which were then thoroughly examined using structural, morphological, optical, and dielectric methods. The microstructure was found to be heterogeneous by scanning electron microscopy, with rod-like extensions (5–9 μm), localized agglomerates, and plate-like grains (23–50 μm thick, 42–50 μm wide) that provided favorable pathways for interfacial polarization and domain alignment. With complete UV blocking below 350 nm and approximately 50% transparency throughout the visible–near-infrared region (350–1000 nm), optical transmission spectra verified $BaTiO_3$'s wide-band-gap nature. Effective band-gap energies in line with perovskite oxides were revealed by tauc analysis. The coexistence of polymer, graphene, and ceramic vibrational features was confirmed by FTIR and Raman spectroscopy, which also preserved the $BaTiO_3$ lattice modes and confirmed strong filler–matrix interactions. Strong frequency and temperature dependence was found in dielectric studies: dielectric loss and AC conductivity exhibited thermally activated Jonscher-type behavior, while permittivity was high at low frequencies due to Maxwell–Wagner–Sillars interfacial polarization, decreased with frequency, and increased with temperature.

Through the synergistic interaction of dense microstructure, interfacial polarization, and conductive pathways, these results show that $BaTiO_3$/Graphene / PVA composites exhibit improved dielectric and optical performance, highlighting their potential for advanced dielectric, optoelectronic, and flexible energy-storage applications.

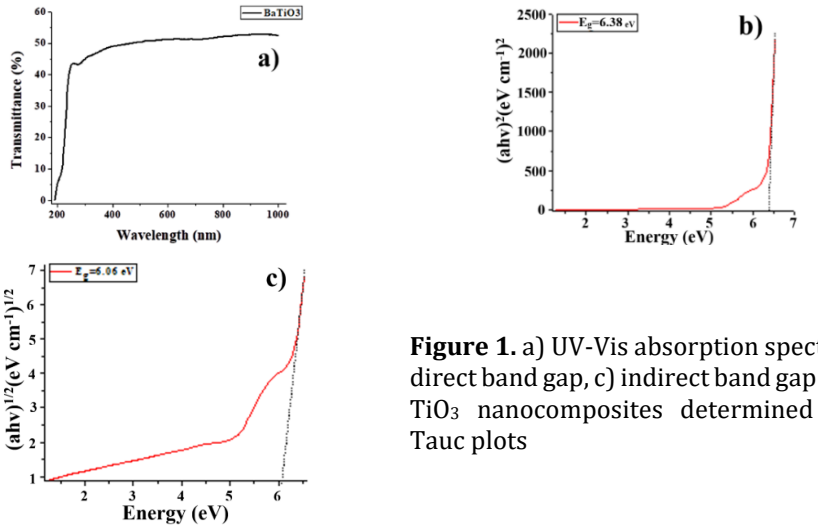

Figure 1. a) UV-Vis absorption spectra; b) direct band gap, c) indirect band gap of $BaTiO_3$ nanocomposites determined from Tauc plots

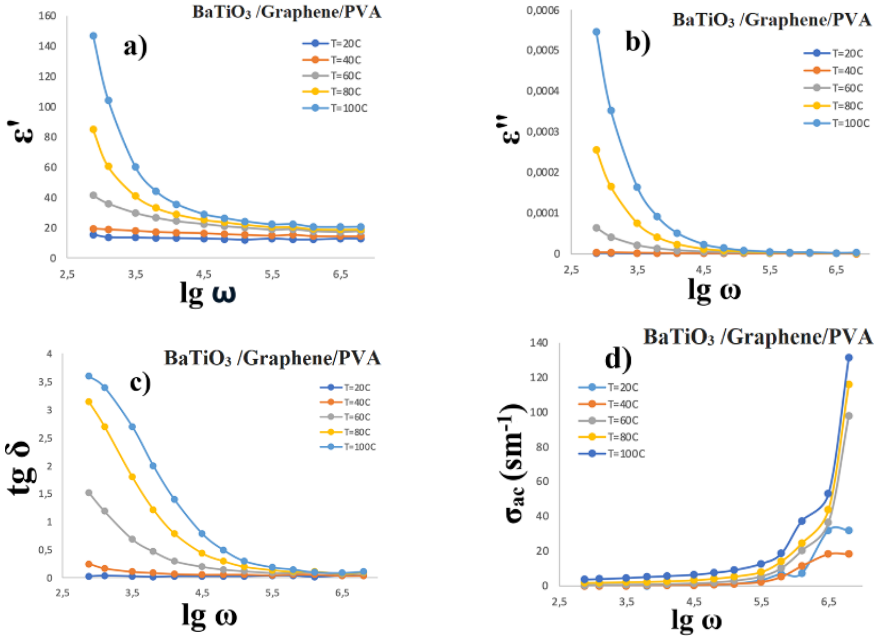

Figure 2. a) Real permittivity ε′, b) imaginary permittivity ε”, c) dielectric loss tangent, d) AC conductivity of $BaTiO_3$/Graphene/PVA at different temperatures

MATRIX-DEPENDENT STRUCTURE-PROPERTY RELATIONSHIPS IN SiC/POLYMER NANOCOMPOSITES: COMPARATIVE STUDY OF POLYPROPYLENE AND POLYSTYRENE SYSTEMS

Gahramanli L.R., *Alakbarova Sh.S.
Baku State University, Azerbaijan
alakbarova.safiqa.safar@bsu.edu.az

Silicon carbide (SiC) nanostructures were incorporated into polypropylene (PP) and polystyrene (PS) matrices to directly compare how polymer type governs structure-property relationships in SiC-based nanocomposites. Composites containing 1-10 wt% SiC were prepared by solvent-assisted dispersion, ultrasonication, and hot-pressing at 160 °C, and systematically examined by XRD, SEM, UV-Vis, FTIR, Raman spectroscopy, and dielectric analysis.

XRD confirmed cubic β-SiC in both systems, with additional α-monoclinic PP peaks and an amorphous halo in PS. In PP, crystallite size varied nonlinearly with filler loading, from 2.01 nm (1 wt%) to 51.32 nm (2 wt%) and 24.24 nm (10 wt%), reflecting confinement and agglomeration. In PS, crystallites remained stable (13.84 nm, Williamson-Hall; 44.22 nm, Debye-Scherrer), with SEM revealing ~10 μm faceted grains compared to SiC nanowires in PP.

Optical behavior diverged: SiC/PP exhibited wide band gaps (5.82-5.98 eV) with maxima at 1 wt% and 7 wt%, driven by strong quantum confinement, while SiC/PS showed a monotonic band gap widening from 3.91 eV (1 wt%) to 4.22 eV (5 wt%) with pronounced UV attenuation at higher loadings. FTIR and Raman confirmed stronger filler-matrix interactions in PP, whereas PS preserved polymer vibrational integrity while adding SiC-specific modes.

Dielectric studies revealed thermally tunable permittivity in PP ($\varepsilon' = 7.48$ at 20 °C, $\lg \omega = 3.1$ to 8.34 at 100 °C, $\lg \omega = 6.7$), whereas PS composites displayed systematic enhancement, from $\varepsilon' = 2.6$ (pure) to 4.1 (10 wt%), with tan δ rising from 0.02 to 0.15 and σac increasing several orders at 7–10 wt%.

These results demonstrate that SiC/PP is best suited for band gap engineering and thermally stable optoelectronics (optimum 3 wt%), while SiC/PS offers continuous dielectric enhancement and UV shielding (optimum 7 wt%). This is the first direct comparison of SiC in semi-crystalline versus amorphous polymer matrices, highlighting matrix choice as a key design parameter for multifunctional nanocomposites.

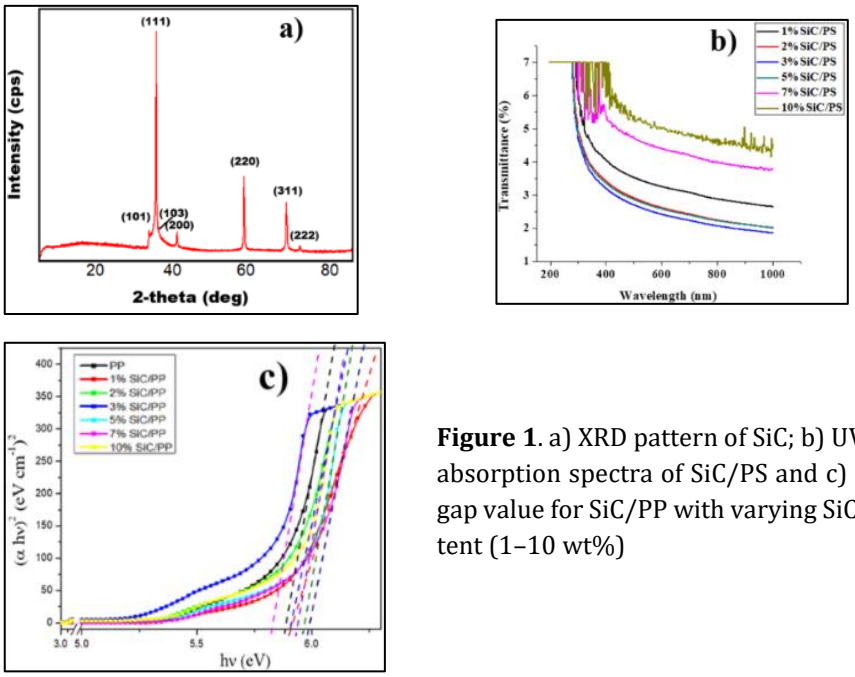

Figure 1. a) XRD pattern of SiC; b) UV–Vis absorption spectra of SiC/PS and c) band gap value for SiC/PP with varying SiC content (1–10 wt%)

SYNTHESIS, STUDIES, STRUCTURE, AND PROPERTIES OF HALOGEN SUBSTITUTED PYRIMIDINE-THIONE-THIONE-THIONE DERIVATIVES

[1]*Nazarov N.M., [1,2]Mahmudov I.H, [1]Babayev S.S., [1]Rzayeva I.A., [1]Ahmadova C.C., [1]Qrigoriyeva N.M.

[1]Institute of Chemistry of Additives, Ministry of Science and Education, Azerbaijan
[2]Baku Engineering University, Azerbaijan

The desired organic compound was synthesized using a one–step three–component condensation reaction using 4-chlorobenzaldehyde, thiourea, and diethylmalonate. The reaction scheme is as follows.

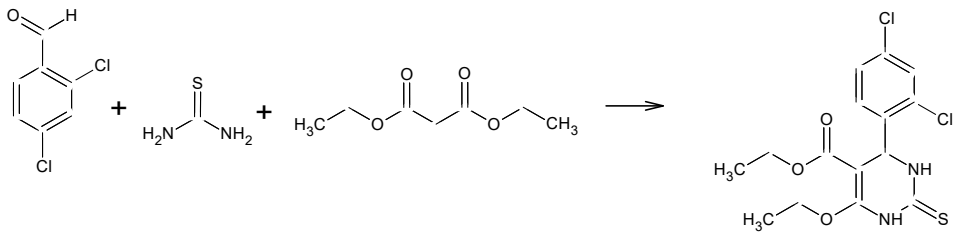

Using FT-IR infrared spectral analysis structure of the synthesized compound was confirmed.

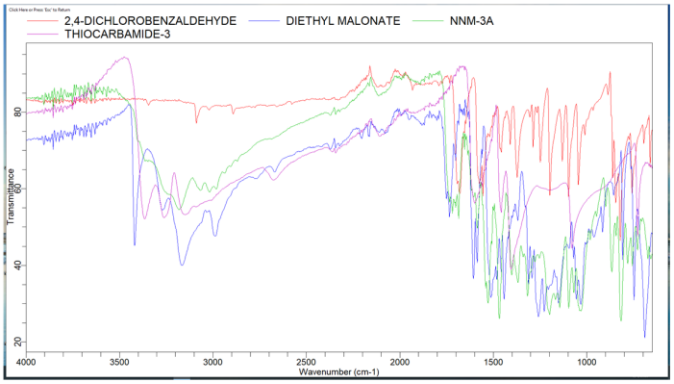

According to the compound observed variety of wavenumbers. Like 3300-3400 cm^{-1} refers to the group NH, 850 cm^{-1} bond between carbon and chlorine, 1100 cm^{-1} wavenumber refers to carbon and nitrogen bond, wavenumber 1560 cm^{-1} double bond between carbon atoms in a cyclic system, and wavenumber 1380 cm^{-1} refers bond between carbon and hydrogen in an aldehyde. The elemental analysis of the synthesized compound was studied using a LECO device, and the diagrams below reflect the obtained results.

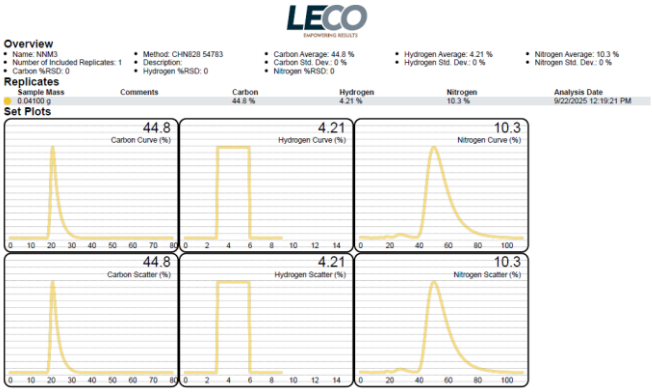

The antioxidant properties of this compound were studied and, according to the results obtained, it has high efficiency as an inhibitor. The parameters reflecting the inhibitory properties of this compound are shown in the table.

Sample	f	K7 (mmole*c)	r, minute
NNM-3	4,2	3,7	2,75

*NNM-3A –code of synthesized compound

EFFECT OF THE ANODIZING ELECTROLYTE COMPOSITION ON THE STRUCTURE AND MORPHOLOGY OF TIO2 NANOTUBE ARRAYS

***Jalilova Kh.D., Eminov Sh.O., Abdullaeva S.H., Mammadova G.H.**
Institute of Physics, Ministry of Science and Education, Azerbaijan
jalilova1951@gmail.com

In this article, the effect of the anodizing electrolyte composition on the structure and morphology of titanium dioxide (TiO_2) arrays with nanotube structures synthesized through the anodic oxidation of titanium thin films has been studied. Based on the analysis of SEM images of the obtained structures, significant differences in the morphology of TiO_2 layers were identified in three different electrolytes (ethylene glycol, glycerol, and formamide), each containing 0.75% wt.%NH_4F, 2wt% H_2O, and morphology of nanotube arrays at different concentrations of NH_4F. It is noted that in formamide, which has a high dielectric permittivity, a non-porous and dense TiO_2 layer is formed. In the case of a glycerol-based electrolyte, the surface of the anodized sample exhibits a mesomorphic disordered structure. It has been demonstrated that the highly ordered structure composed of TiO_2 nanotubes is only achieved when anodization is conducted in an ethylene glycol-based solution.

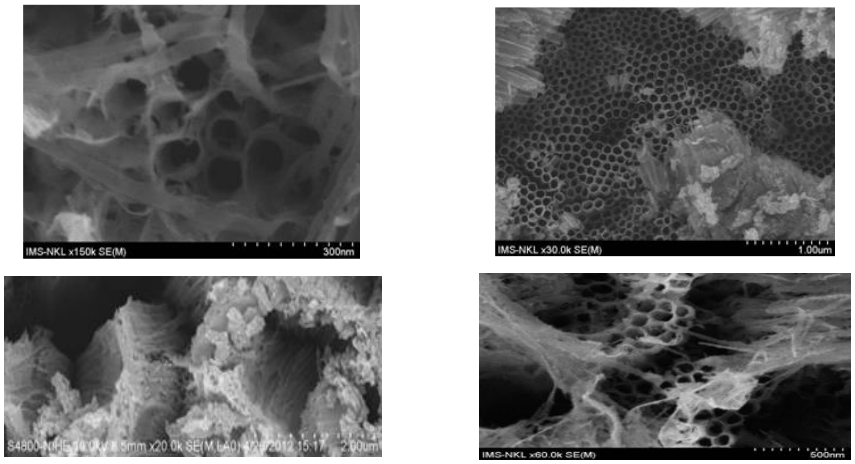

Fig. 1. SEM images of TiO_2 nanotube arrays synthesized in ethylene glycol electrolyte with 2% H_2O and different quantities of NH4F added at an anodization voltage of 45V : (a) 0.25%,(b) 0.4%, (c) 0.5%, (d) 0.6%

Using SEM images of the obtained structures, differences in the morphological and geometric properties of the TiO_2 layers received in different electrolytes were shown. It was noted that thin films with a smooth outer surface and

self-organized TiO_2 nanotubes were obtained only in solution based on ethylene glycol. These tubes have a network of pores with an outer diameter of 250 nm and an inner diameter of about 10 nm.

Thus, we have noted that when titanium is anodized in a formamide-based solution with a high dielectric permittivity, a non-porous dense TiO_2 layer is formed. An irregular structure of TiO_2 pores with a thick wall surface is observed when anodized in glycerol. This indicates that as the viscosity of the medium increases, the rate of formation of the nanotube structure decreases due to the weakening of ion diffusion. Therefore, a highly ordered structure composed of TiO_2 nanotubes is formed only when anodizing is carried out in an ethylene glycol-based solution.

SYNTHESIS AND CHARACTERIZATION OF NI-GO NANORODS WITH ENHANCED OXIDATION REDUCTION REACTION FOR ALKALINE MEMBRANE FUEL CELL

***Nadeem ur Rehman, Abid Hussain, Ahtasham Ahmad**

Department of Mechanical Engineering, University of Engineering and Technology, Peshawar, Pakistan
Nadeem.rehman@uetpeshawar.edu.pk

The Nickel graphene oxide (NI-GO) Nano composites were prepared from hydrothermally synthesized Nickel Nano rods and graphene oxide. Electrocatalytic performance for the oxygen reduction reactions (ORR) of the fabricated NI-GO Nano composites was evaluated using the rotating disk electrode (RDE) method. It is found that NI-GO Nano composites deliver significantly enhanced performance compared to standalone NI and GO, with current density and onset potential values of 5.1 mA/cm2 and 0.93 V versus reversible hydrogen electrode (RHE), respectively. The alkaline membrane fuel cell (AMFC) characteristics were also studied. In particular, the single-cell alkaline fuel cell stack with NI-GO Nano composite as cathode loading produced a peak power density value of 82 mW/cm2. Our findings revealed great potential for NI-GO Nano composites for their electrocatalytic performance and utilization in AMFC as the cathode. Namely, NI-GO achieved fuel cell functionalities that were comparable to the widely used commercial Pt/C. The enhanced electrochemical performance of NI-GO is attributed to the synergistic interaction between highly conductive GO sheets and active sites of NI Nano rods. The commendable performance of NI-GO suggests that it can be used as electro catalysts in alkaline fuel cell applications.

PARAMETRIC INSTABILITY OF PLASMA WITH EXCITATION OF LOW-FREQUENCY ION AND HIGH-FREQUENCY ELECTRON OSCILLATIONS

***Mammadov F.E., Akberov E.M., Gurbanov I.I., Aliev A.A., Aliev S.A., Eminov Sh.O., Khalilov A.J.**

Institute of Physics, Ministry of Science and Education, Azerbaijan
mammadov.f.e@gmail.com

The interaction of electromagnetic fields with plasma leads to the emergence of parametric instabilities. The study of such processes is important for the development of plasma heating methods, as well as devices in which plasma is used to generate and convert various waves, etc. The effect of a high-frequency (HF) electric field on a magnetized plasma in the pump frequency range $\omega_{pi} \ll \omega_0 \ll \omega_{pe}$ ($\omega_{pi,e}$ – are the ion and electron frequencies, ω_0 - is the frequency of the external field) is accompanied by the excitation of longitudinal hydrodynamic oscillations in the plasma.

Our experiments have shown that applying a high-frequency field to plasma leads to parametric instability of lower-hybrid electron and low-frequency ion oscillations. A low-pressure arc discharge was ignited in a cooled brass chamber between the cathode and anode. The plasma column was maintained in a uniform longitudinal magnetic field with an intensity of up to 200 oE. A high-frequency electric field $\vec{E}$ perpendicular to the magnetic field $\vec{H}$ was created using a plasma capacitor. The capacitor was supplied with high-frequency voltage from an external generator with a tunable frequency [$\omega_0/2\pi \approx (7 \div 40)$ MHz], which made it possible to obtain an alternating voltage Ũ of up to ~300 V on the capacitor. The plasma parameters and high-frequency oscillations were recorded using cylindrical probes.

The imposition of an HF field on the plasma leads to instability of the decay type with the excitation of a low-frequency branch of plasma oscillations, characteristic of systems with effective Cherenkov damping of electrons. The experiments established the excitation threshold of oscillations based on the magnitude of the pump field strength, which indicates the parametric nature of the instability.

Experiments have shown that applying an HF field to a plasma leads to parametric instability. In the studied pump frequency range $\omega_{pi} \ll \omega_0 \ll \omega_{pe}$, the parametric instability of lower-hybrid electron and low-frequency ion oscillations is considered using a theory of the. In the case of $\gamma \gg \omega_0$, the line width of

the high-frequency oscillations is large, and the corresponding low-frequency spectrum differs significantly from the ion-sound spectrum. In this case, the spectrum of oscillations in the low-frequency region has a set of satellite frequencies of both lower and higher values than the pumping frequency. In our experiments, the case $\gamma \gg \omega_0$ is realized. In this case, the threshold of parametric instability is expressed by the following formula (γ-decrement of attenuation of ion-acoustic waves)

$$E_{thres}^2/4\pi n_e T_e = 16\omega_0\gamma/\omega_{pe}^2$$

where E_{thres} – threshold value of the excitation intensity of parametric instability.

Thus, in the described experiments, when an HF field is applied to the plasma, a parametric instability of the decay type is realized with the excitation of a low-frequency branch of oscillations and oscillations in the region of the pump frequency.

EXPERIMENTAL INVESTIGATION OF BUBBLE DYNAMICS IN VERTICAL WATER CHANNELS/VESSELS

*Nadeem ur Rehman, Abid Hussain., Ahtasham Ahmad

Department of Mechanical Engineering, University of Engineering and Technology, Peshawar, Pakistan

Nadeem.rehman@uetpeshawar.edu.pk

The research investigates the rising movement of individual air bubbles in vertical water channels through experimental observation. The research group examines how size changes in the channels affect bubble movement patterns, which are generated by an injection needle below the fluid level. Two high-speed digital cameras recorded bubble motion through two separate views that showed the front direction (x–y) and the side view from (y–z). Post-processing of recorded videos required MATLAB software to obtain bubble trajectory information, followed by MS Excel software development of visual representations. During lower air flow conditions, the bubble generates a spiral trajectory while normally following straight lines. The measurements confirming that vertical water channel dimensions did not influence how the single bubble ascended proved inconclusive. The study provides essential insights about restricted vertical bubble motions that improve knowledge in fluid mechanics and multiphase flow applications.

SYNTHESIS AND STRUCTURAL INVESTIGATION OF $BaTiO_3$@Fe_3O_4 CORE–SATELLITE HYBRID STRUCTURES

***Shirinova H.A., Karimova A.H., Nuriyeva S.G., Gahramanli L.R., Humbatov Sh.A.**

Baku State University, Azerbaijan
habiba.shirinova@bsu.edu.az

The synthesis and application of $BaTiO_3$-based polymer nanocomposites represent one of the current frontiers in modern materials science. The rapid advancement of technology has highlighted the demand for innovative materials with multifunctional properties. In this context, the combination of $BaTiO_3$, known for its high dielectric constant, with Fe_3O_4, distinguished by its magnetic properties, holds significant scientific and technological importance.

In this study, particular attention was focused on coating the surface of $BaTiO_3$ nanoparticles with Fe_3O_4 nanoparticles. The co-precipitation method was employed to deposit Fe_3O_4 nanoparticles onto the $BaTiO_3$ surface. This approach effectively minimized agglomeration among the particles and optimized the functional characteristics of the resulting nanocomposite.

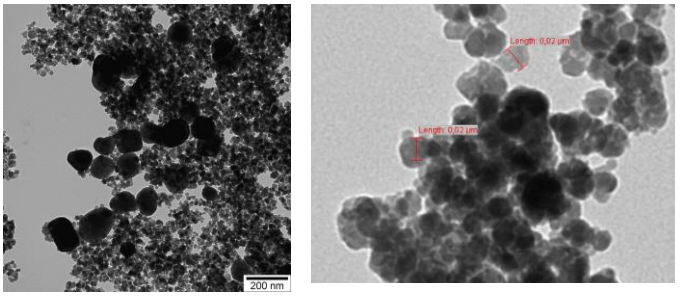

Figure 1. TEM image of $BaTiO_3$@Fe_3O_4 hybrid nanostructures

The synthesis of $BaTiO_3$@Fe_3O_4 core–shell structures was carried out as follows: 0.002 g of polyvinylpyrrolidone (PVP) was dissolved in 50 mL of distilled water. Then, 1 g of $BaTiO_3$ was added, and the mixture was stirred at 70 °C for 1 hour. In the next step, 0.008 mol of $FeCl_3 \cdot 6H_2O$ and 0.015 mol of $FeSO_4 \cdot 7H_2O$ iron salts were added to the solution. Ammonium hydroxide ($NH_3 \cdot H_2O$) was then introduced to adjust the pH to the range of 11–12. The mixture was cooled to room temperature and washed six times with ethanol. Finally, the obtained $BaTiO_3$@Fe_3O_4 particles were dried under vacuum at 45 °C.

The morphology of the obtained nanohybrid system was investigated using the TEM method, and it was found that Fe_3O_4 nanoparticles, upon deposition on the surface of $BaTiO_3$ particles with an average size of about 80 nm, formed new core-satellite-type nanostructures.

DEFECT STRUCTURE INVESTIGATION OF PVDF-BASED β-Ga_2O_3–CNT NANOCOMPOSITES BY POSITRON ANNIHILATION LIFETIME SPECTROSCOPY

***Ahmadova S.A., Ibragimov G.B.**

[1]Institue of Physics, Ministry of Science and Education, Azerbaijan
sedefahmadova@gmail.com

The precise characterization of defects in modern nanocomposite materials is of particular importance for understanding their functional properties, and in this context, positron annihilation lifetime spectroscopy (PALS), with its high sensitivity, serves as a powerful research tool. In this study, the defect structure of PVDF-based nanocomposites synthesized with β-Ga_2O_3 and carbon nanotubes (CNTs) was investigated using the PALS method. Measurements revealed that in pure β-Ga_2O_3 samples, medium-sized vacancy clusters ($\tau_2 \approx 369$ ps) are dominant, while in CNT structures, large-volume voids and o-Ps formation ($\tau_3 \approx 2.8$ ns) were observed. In the nanocomposites, depending on the CNT/β-Ga_2O_3 ratio, the variation of the τ_2 component in the range of 652–853 ps indicated the formation of interfacial porosity and large-volume defects. Analyses based on the two-state trapping model showed that changes in the τb, kd, and τ_2–τ_b parameters confirmed variations in both the density and size of the defects. The results demonstrate that in PVDF-based β-Ga_2O_3–CNT nanocomposites, defect engineering and interfacial interactions can be optimized by controlling the composition. These features highlight the potential of such materials for applications in sensor technologies, optoelectronic devices, and radiation-resistant systems.

THE INFLUENCE OF TRANSITION METALS ON THE CATALYTIC PROPERTIES OF HZSM-5 ZEOLITE IN THE CONVERSION OF BIOETHANOL TO THE BTX FRACTION

[1]Mammadova Kh., [1]Kerimli F., [2]*Mammadov E.

[1]Baku State University, Azerbaijan
[2]The Baku Branch of Lomonosov Moscow State University, Azerbaijan
memmedovaxanimbaci549@gmail.com

Currently, due to the growing demand for hydrocarbon fuels, the depletion of oil reserves, and the tightening of environmental requirements, active research is being conducted on replacing traditional hydrocarbon raw materials

with alternative non-hydrocarbon feedstocks. Bioethanol is one type of renewable feedstock obtained through the fermentation of plant biomass. Bioethanol can be used as a base raw material for producing motor fuel components and petrochemical industry products.

For obtaining valuable organic substances and petrochemical products from bioethanol, it is necessary to develop catalysts with high activity, selectivity, and stable performance. In the presence of ZSM-5 zeolites, which have nano-sized straight (0.53 × 0.55 nm) and sinusoidal (0.51 × 0.53 nm) channels, the conversion of bioethanol yields aliphatic and aromatic hydrocarbons of various structures. ZSM-5-based catalysts are considered more promising for the conversion of bioethanol into C2–C3 olefins and aromatic hydrocarbons. Considering this, the present work studies the influence of transition metals (Ga, Zn, Fe, Cr, Ni) on the catalytic properties of HZSM-5 zeolite in the process of converting bioethanol into the BTX fraction.

In the presence of unmodified HZSM-5 zeolite, bioethanol mainly undergoes decomposition and aromatization. In its presence, the yield of the gasoline (BTX) fraction is 46.2%. When HZSM-5 zeolite is modified with Zn, its cracking and aromatization properties significantly decrease. In the presence of the Zn-HZSM-5 catalyst, the yield of the gasoline fraction decreases to 41.7%. However, an increase in the yield of C4–C14 isoparaffin hydrocarbons (17.3%) is observed with the Zn-HZSM-5 catalyst.

HZSM-5 zeolite modified with nickel exhibits higher isomerization activity. In its presence, the yield of iso-C_4–C_{14} hydrocarbons reaches 19.5%. Unlike other modifying metals (Zn, Cr, Fe, Ga), the Ni-HZSM-5 catalyst shows considerably lower aromatization activity, with a gasoline fraction yield of 31.8%. Modification with Cr, Fe, and Ga enhances the aromatization activity of HZSM-5 zeolite, with Ga-HZSM-5 exhibiting the highest aromatization performance. The highest yield of the gasoline fraction (63.2%) is obtained in the presence of the Ga-HZSM-5 catalyst.

Thus, the catalytic properties of HZSM-5-based catalysts strongly depend on the nature of the metal incorporated into their structure: catalysts modified with Zn and Ni direct bioethanol conversion mainly toward isomerization products, whereas the Ga-modified catalyst promotes the aromatization pathway.

LATTICE PARAMETER EXPANSION AND MICROSTRAIN BEHAVIOR OF WNi ALLOYS EXPOSED TO HIGH-DOSE γ-RADIATION

[1]Samadov S.F., [1]Abiyev A.S, [1*]Samedov O.A., [2]Ahmadova A.B.

[1]Institute of Radiation Problems, Ministry of Science and Education, Azerbaijan
[2]Baku State University, Azerbaijan
oktaysamedov9@gmail.com

High-resolution X-ray diffraction (XRD) analysis was carried out to investigate the structural evolution of WNi alloys subjected to different doses of γ-irradiation. The results showed that although the irradiation process preserved the primary bcc-W phase (Im-3m, No. 229) of the alloy, it led to significant changes in the lattice parameters and microstructural characteristics. The diffraction peaks were indexed to the (111), (200), and (211) crystallographic planes. The initially observed WNi_4 phase (I4/m space group) gradually lost its long-range ordering with increasing irradiation dose, and at the highest dose (3566 kGy), its diffraction peak intensity drastically decreased, approaching an almost amorphous state. Rietveld refinement revealed that both the lattice parameters and the unit cell volume increased progressively with dose; the sharp expansion observed at the first irradiation step is attributed to local swelling or void formation induced by irradiation-generated defects. At higher doses, this expansion weakened, indicating that the system approached a saturation regime, which may be related to defect recombination, reduction in defect size, or their migration toward grain boundaries.

To achieve a more precise assessment of the microstructural changes, the Williamson-Hall method was applied, allowing the investigation of texture and microstrain dynamics under irradiation. The calculations showed that at the initial dose, microstrain decreased, which can be explained by the transformation of large-scale lattice distortions into smaller ones and by defect annihilation. At higher doses, however, microstrain began to increase again, which is attributed to the formation of new defects and their clustering. The obtained results demonstrate that the processes of defect formation, migration, and recombination in γ-irradiated WNi alloys are highly interconnected and have a significant impact on the structural stability of the material. Such studies are of particular importance for nuclear technology and the development of radiation-resistant structural materials.

MICROSTRUCTURAL AND SURFACE MORPHOLOGY EVOLUTION OF ZrC NANOCRYSTALS UNDER HIGH-DOSE GAMMA IRRADIATION

[1]Samadov S.F., [1*]Samedov O.A., [1]Mirzayev M.N., [2]Hajiyeva Sh.N.

[1]Institute of Radiation Problems, Ministry of Science and Education, Azerbaijan
[2]Baku State University, Azerbaijan
oktaysamedov9@gmail.com

The radiation resistance of materials used in modern nuclear technologies and high-temperature applications is crucial for ensuring their safety and long-term performance. In this context, the effect of high-dose gamma irradiation on the microstructure and surface morphology of ZrC nanocrystals was investigated. FTIR spectra revealed that gamma exposure leads to transformations of functional groups on the surface of ZrC crystals, with the emergence of new peaks at 1337 and 1436 cm^{-1} and splitting of the 1436 cm^{-1} band. These changes are attributed to the formation of oxidation centers and carbonyl groups on the crystal surface. SEM results indicate that increasing irradiation dose promotes nanoparticle mobilization and partial amorphization, leading to particle growth.

HRTEM investigations confirmed a progressive thickening of the amorphous oxide layer on the surface of ZrC nanocrystals after irradiation. The oxide layer thickness increased from 0.312 nm in the pristine state to 0.330 nm at 1500 kGy and 0.347 nm at 3000 kGy. Additionally, the average crystallite size exhibited a measurable growth, increasing from 20.16 nm to 23.46 nm as a result of radiation-induced grain coalescence. These structural changes are attributed to point defect generation, lattice distortions, and the clustering of radiation-induced vacancies, which act as nucleation sites for oxide layer growth. The combined FTIR, SEM, and TEM results provide a consistent picture of radiation-driven microstructural evolution, highlighting the balance between defect accumulation and grain growth processes under intense gamma fields. The findings confirm that ZrC preserves its overall crystalline integrity while exhibiting contro-lled surface modification, making it a promising candidate for use as a structural and fuel coating material in next-generation nuclear systems, where both thermal and radiation stability are required.

ELECTROPHYSICAL PROPERTIES OF OPTIMALLY MODIFIED POLYPROPYLENE WITH A PHTHALIMIDE ADDITIVE

[1,2*]Mehrabova M.A., [1]Safarova S.I., [1]Kerimov F. Sh., [3]Hasanov N.H., [1]Jafarova G.S., [1]Rehimov R.S.

[1]Azerbaijan Technical University, Azerbaijan
[2]Institute of Radiation Problems, Ministry of Science and Education, Azerbaijan
[3]Baku State University, Azerbaijan
metanet.mehrabova@aztu.edu.az

For the first time, the composition and amount of the low-molecular-weight organic additive phthalimide for modifying the electrophysical properties of polypropylene grade (01030) have been determined. The developed polypropylene composition is distinguished by a significantly small amount of the additive used and its technological compatibility. The content of the additive in the polypropylene composition was varied within the range of 0.01-0.1 wt%. Experimental results showed that a phthalimide content of 0.05 wt% is optimal, as it provides the greatest stability of electrical properties compared to both the original polypropylene and compositions with other additive concentrations. The optimally modified polypropylene shows a noticeable increase in electric strength and volume resistivity, and a decrease in the dielectric loss tangent.

The dependencies of the tangent of the dielectric loss angle (tgδ), specific volume, electrical resistivity (ρ_v), and dielectric permittivity (ε) on temperature have been studied, as well as the kinetics of physico-electrical changes in these parameters under the influence of electrical discharges in air and UV radiation.

It has been found that the addition of 0.05 wt% of the organic compound phthalimide significantly increases its resistance to the effects of electrical discharges and UV radiation.

The rate of decrease in the dielectric strength of polypropylene film during aging, when a small amount of the organic additive phthalimide is introduced, also indicates the formation of densely packed structures due to a spherulitic organization, which hinders oxygen diffusion and the development of ionization processes during electro-destruction.

OPTICAL PROPERTIES OF TiO_2 NANOTUBULAR FILMS OBTAINED BY ANODIC OXIDATION OF GLASS / ITO /Ti STRUCTURES

***Eminov Sh.O., Jalilova Kh.D., Abdullayeva S.H., Aliyev A.A., Aliyev S.A., Rajabli A.A.**

Institute of Physics, Ministry of Science and Education, Azerbaijan
shikhamirem@gmail.com

This work presents the results of structural and spectroscopic ellipsometry diagnostics of nanostructured titanium dioxide (TNT) synthesized via anodic oxidation of a thin titanium film deposited by magnetron sputtering onto a glass substrate with a transparent conductive indium–tin oxide (ITO) layer. X-ray diffraction and Raman spectroscopy confirmed the formation of the anatase phase with an ordered nanotubular morphology, which was additionally visualized by scanning electron microscopy (SEM), clearly revealing vertically aligned TiO_2 nanotube arrays (*Fig.a&b*). Ellipsometric measurements were performed at room temperature using a rotating-analyzer spectroscopic ellipsometer (J.A. Woollam Co.) at an incident angle of 75° in the photon energy range of 1–5 eV. The experimental $\psi(E)$ and $\Delta(E)$ spectra were fitted using a parametric dispersion model based on Cauchy, Genssen–Oscare, and Lorentz functions. From the fitted model, the complex dielectric functions $\varepsilon_1(E)$ and $\varepsilon_2(E)$ were reconstructed, along with the corresponding dispersion of the refractive index n(E), extinction coefficient k(E), and absorption coefficient $\alpha(E)$. The raw ψ/Δ curves alongside the fitted model, as well as comparative literature data for anatase TiO_2, will be presented for validation. The sharp increase in ε_2 near 4.2 eV is a signature of strong interband optical absorption in TiO_2, specifically due to electrons moving from the oxygen *2p* orbitals in the valence band to the titanium 3d orbitals in the conduction band, while ε_2 approached zero below the band gap (~3.2 eV), indicating high optical transparency in the visible range. A reduction in the refractive index down to $n \approx 2.2–2.3$ compared to dense TiO_2 was attributed to the porosity and anisotropic ordering of the nanotubular structure. The computed $\alpha(E)$ is reasonably consistent with typical literature for anatase TiO_2. The values are in the correct order of magnitude, the absorption edge is in the right place, and the shape (rising rapidly after the bandgap, peaking in UV) is sensible.

The integrated analysis – combining SEM visualizations (Fig. a & b), optical modeling (Fig. c), ψ/Δ curves, and ellipsometric reconstructions of $\varepsilon(E)$, n(E), k(E), and $\alpha(E)$ (Fig. d–h) – supported by literature comparisons, demonstrates the robustness of the proposed approach for characterizing nanoporous oxide systems and highlights the promising potential of anodic TiO_2/ITO films in optoelectronic, photoelectrochemical, and photocatalytic applications.

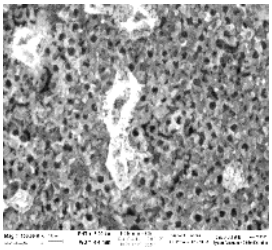

a)

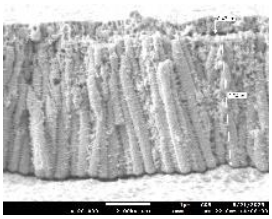

b)

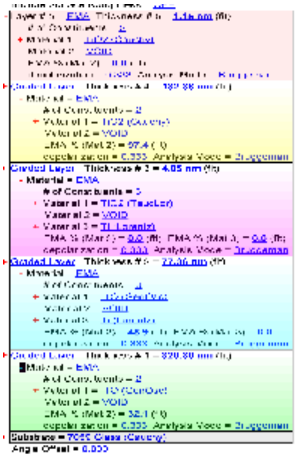

c)

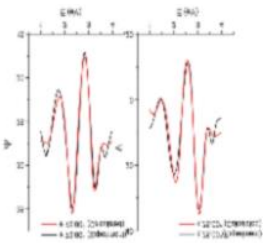

d)

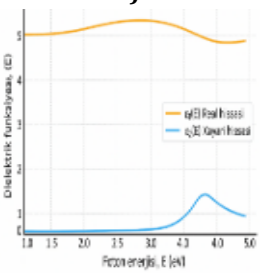

e)

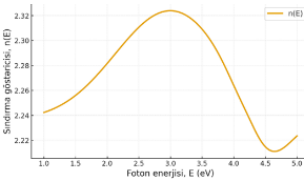

f)

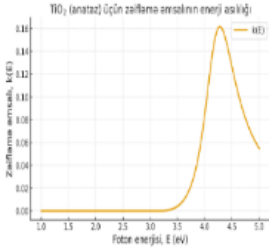

g)

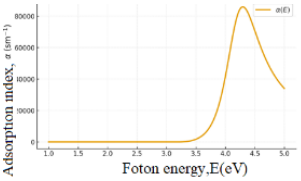

h)

PHOTOLUMINESCENCE MECHANISMS IN AAO–Cu NANOCOMPOSITES CONTAINING ELECTROCHEMICALLY GROWN COPPER NANOWIRES

***Eminov Sh.O., Ismailov N.J., Karimova A.Kh., Mamedova G.H., Rajabli A.A.**

Institute of Physics, Ministry of Science and Education, Azerbaijan
shikhamirem@gmail.com

The integration of copper nanowires into nanoporous anodic aluminium oxide (Al_2O_3, AAO) templates *(Figure1, SEM images of AAO template)* enables precise control over wire orientation, morphology, and optical response, making these hybrid systems promising for photonic, sensing, and optoelectronic applications. Here, we investigate the photoluminescence (PL) behaviour of

AAO–Cu nanocomposites with Cu nanowires electrochemically deposited inside vertically aligned AAO pores. The PL spectrum shows an intense, broad emission band centred at ~575 nm (*Figure 2, PL spectra of Cu-AA)*. Luminescence arises from several mechanisms: defect-related recombination in Cu nanowires (Cu vacancies, oxide-induced defects), quantum confinement effects due to nanoscale wire diameters, and radiative transitions in surface copper oxides (Cu_2O and CuO) formed during post-deposition oxidation in air environment. The 530–600 nm region is characteristic of Cu_2O band-to-band and defect-assisted emission. The PL maximum (~575 nm) originates from Cu_2O (Eg ≈ 2.1 eV) rather than metallic copper. During air exposure, thin Cu_2O (n-type) and CuO (p-type) shells form spontaneously on nanowire surfaces. Cu_2O direct transitions give orange-red emission (~590–620 nm), while CuO (Eg ≈ 1.4–1.7 eV) (Fig.3 PL of Cu_2O və CuO) contributes to red/near-infrared luminescence via defect-mediated recombination.

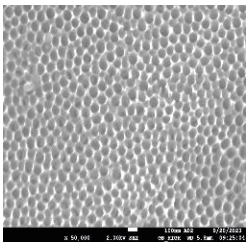

Figure 1

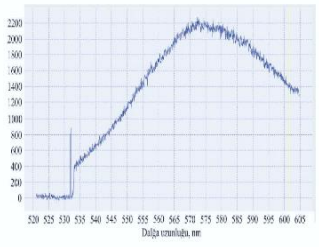

Figure 2

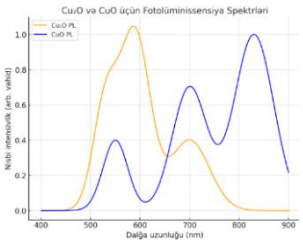

Figure 3

Oxygen vacancies (V_0) and interstitial Cu^+/Cu^{2+} ions act as luminescence centres, producing broadband emission from green to red. The AAO matrix, transparent in the visible range, serves as a dielectric scaffold; its confined geometry may also influence charge carrier dynamics through spatial restriction and local field enhancement. Red/near-infrared CuO emission is not observed in the spectrum due to measurement limits. PL was measured using a Confocal Nanofinder 30 Raman spectrometer (Tokyo Instruments, Japan) with a 532 nm laser at 10 mW and 60 mW.

Overall, PL in AAO–Cu nanocomposites originates predominantly from copper oxide surface phases rather than bulk copper, with structural confinement, defect chemistry, and interfacial oxidation defining the emission behaviour. Understanding these mechanisms is essential for designing AAO-based nanocomposites for light-emitting, sensing, and energy-harvesting applications.

COMPENSATION FOR CHARGE SHARING IN PIXELATED SEMICONDUCTOR RADIATION DETECTORS

Guliyev E.G.
Redlen Technologies Inc (Canon Corporation), Victoria BC, Canada
elmaddin.guliyev@redlen.com / e.g.guliyev@gmail.com

In typical photon-counting X-ray applications currently in use, the charge cloud resulting from an X-ray photon impinging on a sensor is converted to an amplified voltage by a charge-sensitive amplifier (CSA). The voltage output of the CSA is compared against a number of user-settable thresholds. Each threshold level is associated with a counter that increments when the voltage output falls between the minimum and maximum thresholds associated with the counter. Thus, each counter records the number of photons detected within the energy range between two adjacent thresholds, which is referred to as an energy bin. The lowest threshold is set to slightly above the noise level, and a voltage above this threshold indicates that an X-ray photon has been detected. After the CSA output voltage has stabilized, the counter corresponding to the highest energy bin threshold crossed is incremented, thus recording one detection event in that energy bin. As the count is registered in an energy bin, the CSA is reset, enabling the detector pixel to record another X-ray detection event. If the X-ray photon is absorbed near the center of a pixel detector, this process yields an accurate count of photon energies. However, if the X-ray photon is absorbed near the boundary of a pixel detector or within the gap between two or more pixel detectors, the charge cloud produced by the photon absorption may be shared between two or more pixel detectors, resulting in an inaccurate count of photon energies due to charge sharing.

We present methods to compensate for charge-sharing in pixelated photon-counting X-ray detectors by learning a correspondence factor that maps measured per-bin counts to estimated incident energy-bin counts. The factor is derived by estimating the incident spectrum, convolving it with the detector's energy resolution, generating a charge-sharing model parameterized by the detector's charge-sharing fraction, and fitting the model to measure energy-bin counts. The resulting mapping reduces spectral distortion and improves quantitative imaging metrics without hardware changes.

Operationally, the method uses an energy-resolution operator to blur a prior incident spectrum, applies a charge-sharing matrix derived from a sharing percentage, and compares predicted and measured energy-bin counts to derive a correspondence operator that transforms measurements to incident counts. The approach supports regularization for stability and can be calibrated with standard targets (e.g., K-edge lines). In imaging, compensation improves material-decomposition accuracy, reduces beam-hardening artifacts, and enhances CNR/SNR under typical exposure conditions.

PRODUCTION AND DIELECTRIC CHARACTERIZATION OF MWCNT–Si-BASED NANOCOMPOSITES

[1*]Masimova A.I., [1]Shirinova H.A., [2]Suleymanova N.Y.

[1]Baku State University, Azerbaijan

[2]Institute of Physics, Ministry of Science and Education, Azerbaijan

aiselmasimova@gmail.com

Carbon nanotube (CNT)-based nanocomposites have attracted significant attention due to their exceptional electrical, thermal and mechanical properties. Adding silicon (Si) nanoparticles to multi-walled carbon nanotube (MWCNT) matrices has synergistic effects that improve dielectric performance and structural stability. These MWCNT–Si nanocomposites combine the high aspect ratio and conductivity of MWCNTs with the dielectric properties and chemical stability of Si, making them promising for electronic and energy storage applications. This study focuses on the production, structural characterization and dielectric evaluation of MWCNT–Si-based nanocomposites, aiming to optimize their performance for next-generation electronic devices. The synthesis of MWCNT–Si-based polymer nanocomposite was carried out by combination of the salution mixing and hot pressing methods.

The primary challenge in creating such hybrid nanocomposites is ensuring homogeneous dispersion of both the CNTs and Si nanoparticles within the polymer matrix, which is crucial for maximizing interfacial area and, thus, the dielectric enhancement.

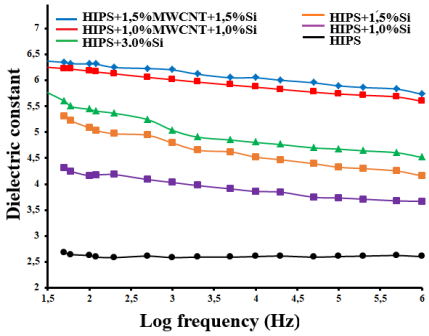

Figure 1. Dielectric constant-frequency dependence of MWCNT–Si- based polymer nanocomposite

The Figure 1 shows the variation of the dielectric constant with frequency for HIPS-based nanocomposites containing different ratios of MWCNT and Si. As seen, the dielectric constant decreases slightly with increasing frequency and the samples with both MWCNT and Si exhibit higher dielectric values compared to pure HIPS, indicating improved interfacial polarization.

VIBRATIONAL AND STRUCTURAL ANALYSIS OF GeS SINGLE CRYSTALS VIA RAMAN SPECTROSCOPY

***Guliyeva S.S., Balayeva L.A., Huseynov A.H.**
Baku State University, Azerbaijan
qsevinc52@gmail.com

GeS is a layered orthorhombic semiconductor with promising optical characteristics, making it a strong candidate for next-generation thin-film and 2D photovoltaic devices. Each layer consists of strongly covalently bonded Ge and S atoms, while adjacent layers are linked by weak vdW forces, enabling easy exfoliation into ultrathin structures. The Ge - S bond exhibits partial ionic character, producing an asymmetric charge distribution that distorts the sp^3 hybridization within the tetrahedral coordination. This structural asymmetry induces pronounced anisotropy in the optical and vibrational behavior of GeS, influencing charge transport, phonon dynamics, and light-matter interactions.

In the present study, single crystals of GeS were synthesized using the Bridgman method under a controlled temperature gradient. Structural characterization was performed through Raman spectroscopy to investigate the phonon modes and confirm the crystal symmetry. The Raman spectrum exhibits prominent peaks at ~ 214.9, 245.2 and 266.9 cm^{-1}, which correspond to the A_1g, B_1g, and A_2g vibrational modes, respectively. Additional modes were observed near 212.7, 221.4, 234.4, and 290.7 cm^{-1}. The peaks at 212.7 cm^{-1} and 221.4 cm^{-1} are attributed to interlayer shear and breathing modes, originating from the relative vibrations between adjacent GeS layers. The mode near 234.4 cm^{-1} is likely associated with a defect- or strain-induced phonon, activated by local lattice distortions. The higher-frequency feature around 290.7 cm^{-1} is interpreted as an overtone or combination mode, arising from the interaction between two phonons. The corresponding phonon energies for these vibrational modes, arranged in ascending order, were determined as 26.38, 26.64, 27.45, 29.07, 30.43, 33.09, and 36.05 meV. The phonon lifetime at the most intense Raman peak was calculated to be approximately 51.9 fs. The dominant A_2g mode is attributed to the symmetric stretching of Ge-S bonds. The narrow linewidths of the observed Raman peaks indicate high crystalline quality and a low density of structural defects.

SYNTHESIS AND CHARACTERIZATION OF A NEW $SnBi_4Te_4$ VAN DER WAALS TOPOLOGICAL MATERIAL

[1*]Mehtiyeva Kh.Z., [1,2]Amiraslanov I.R., [3,4]Casciaro Martina, [3,4]Papagno Marco, [1,2]Aliev Z.S.

[1]Baku State University, Azerbaijan
[2]Institute of Physics, Ministry of Science and Education, Azerbaijan
[3]Università della Calabria, Rende (Cs), Italy
[4]STAR IR, Via Tito Flavio, Università della Calabria, Rende (CS), Italy
xatira.mehtiyeva@bsu.edu.az

The ternary topological insulator $SnBi_2Te_4$ consists of seven-layer (SL) Te–Bi–Te–Sn–Te–Bi–Te blocks separated by van der Waals gaps (vdW). Adding Bi bilayers (BLs) on top of SL blocks forms a new stable phase, $SnBi_4Te_4$, with a trigonal *P-3m1* structure. This compound is predicted to exhibit topological semimetal or semiconductor behavior, promising for spintronic and thermoelectric applications.

The present work reports the study of the crystal structure, chemical composition, and morphology of $SnBi_4Te_4$ by using X-Ray Diffraction (XRD), X-Ray Photoelectron Spectroscopy (XPS), and Scanning Tunneling Microscopy (STM). All measurements were performed along the (001) plane. XRD confirmed phase purity and orientation, while XPS and STM characterized the chemical composition and atomic-scale surface morphology.

The XPS spectrum of $SnBi_4Te_4$ shows sharp peaks without oxygen or carbon contamination, confirming a clean surface. High-resolution core-level spectra reveal Te and Sn 3d, and Bi 4f states, allowing direct comparison with the parent phases. STM imaging of freshly cleaved surfaces displays a layered BL–SL–BL–SL... stacking connected by vdW interactions. Atomically resolved images show a hexagonal lattice for both surface terminations.

Furthermore, preliminary angle-resolved photoemission spectroscopy measurements compared with density functional theory calculations on SnB_4Te_4 suggest a topological semimetal character.

Our results suggest that $SnBi_4Te_4$ could serve as an ideal platform for the development of new thermoelectric topological materials.

ASSESSMENT OF THE THERMAL STABILITY OF ANILINE AMIDE OF NATURAL PETROLEUM ACIDS BY TG/DTG/DTA METHOD

[1*]Dadashova N., [1]Abbasov V., [1,2]Aghamaliyeva D., [1]Aliyeva N., [1]Ahmedova S.

[1]Institute of Petrochemical Processes, Ministry of Science and Education, Azerbaijan
[2]Azerbaijan State Oil and Industry University, Azerbaijan
nasrindadashova@gmail.com

This study investigates the thermal behavior and stability of aniline amide of natural petroleum acids (TNTAA) using thermogravimetric analysis (TG), derivative thermogravimetry (DTG), and differential thermal analysis (DTA) under a nitrogen atmosphere. The thermal decomposition of the compound exhibits a two-step process with a total weight loss of 87.58% over the temperature range of 30–420 °C. The first stage involves a gradual mass loss of 23.64%, attributed to the removal of adsorbed moisture, volatile components, and partial degradation of weak intermolecular interactions. The main decomposition stage starts at 311.0 °C and reaches a maximum at 374.9 °C with a peak decomposition rate of –20.07%/min, accompanied by a pronounced endothermic effect observed in the DTA curve, corresponding to the cleavage of amide bonds and the degradation of hydrocarbon chains.

The results indicate high thermal stability of TNTAA up to 200 °C, confirming its potential as a thermally resistant corrosion inhibitor and as a functional additive in formulations operating under elevated temperatures. TG/DTG/DTA analysis provides insights into the decomposition mechanism and identifies the temperature range suitable for practical applications.

Overall, the synthesized amide demonstrates significant promise for use in protective systems, including oil, gas, and chemical industry applications, while also highlighting the potential of natural petroleum acids as environmentally friendly and effective corrosion inhibitors. The findings enhance understanding of the thermal characteristics and structural stability of amide derivatives of natural acids, providing a foundation for further optimization and industrial implementation.

CHARACTERISTICS OF MICROCRYSTALLINE CELLULOSE OBTAINED FROM VARIOUS DOMESTIC NON-WOODY INDUSTRIAL CROPS

[1*]Tkachenko T.V., [1]O.O. Haidai, [1,2]Kamenskyh D.S., [3]Jafarov M.A., [1]Korinenko B.V., [2,4]Starik S.P., [5]Bratishko V.V., [1]Povazhny V.A., [6]Ruban S.V., [1]Yevdokymenko V.O.

[1]V.P. Kukhar Institute of Bioorganic Chemistry and Petrochemistry of the NAS of Ukraine, Ukraine

[2]V. Bakul Institute for Superhard Materials of the NAS of Ukraine, Ukraine

[3]Baku State University, Azerbaijan

[4]Frantsevich Institute for Problems of Materials Science of the NAS of Ukraine, Kyiv, Ukraine

[5]National University of Life and Environmental Sciences of Ukraine, Kyiv, Ukraine

[6]LLC RPE «RD PRODUCTION GROUP», Kyiv, Ukraine

ttv13ttv@gmail.com

Many studies focus on methods for obtaining microcrystalline cellulose (MCC) from non-woody industrial crops; however, systematic investigations are lacking. We aimed to investigate the characteristics of MCC from various domestic non-woody industrial crops.

Air-dry Giant miscanthus (M), hemp fiber (H) Hlesia varieties and flax (F), the technical crops of the 2023 harvest, from Kyiv and Chernigiv's region of Ukraine were used. All chemicals used were analytical grade reagents. MCC was obtained by the “green” one-step method of organ-solvent cooking. The obtained MCC were analysed for morphology and composition using different methods: low-temperature nitrogen sorption-desorption, XRD, XRF, FTIR-ATR, AFM, SEM, TGA, and DSC. The yield of cellulosic product was estimated by weighing.

It was established that by the organo-solvent cooking method, it is possible to obtain MCC with a yield of 95.9 (M), 90.0 (H), and 96.3 (F) %. The highest purity is characterized by MCC (H): ash content – 0.2%, lignin – 0.8%. The XRD method showed that the obtained samples have a typical structure for MCC. Based on the XRD data, the crystallinity index was calculated: 0.73 (M), 0.84 (H), and 0.86 (F). The polymerization degree of the obtained samples was determined to be 240 (M), 160 (H), and 277 (F). The FTIR-ATR showed that the obtained MCCs have similar functional groups to the commercial ones. Low-temperature nitrogen sorption-desorption established that all the obtained MCC samples had a non-porous structure. AFM analysis demonstrated that the particles were nanoscale in size.

Thus, it was found that the best raw materials for obtaining MCC from industrial non-wood crops are hemp and flax fibers.

AVALANCHE FIELD-EFFECT TRANSISTOR (AFET) BIOSENSOR FOR ULTRA-SENSITIVE EARLY CANCER DETECTION: MODELING AND SIMULATION STUDY

***Heyderli N.R., Saydgov A.Z., Ahmadov G.S.**
Nuclear Research Department, IDDA, Azerbaijan
nabaheyderlit5@gmail.com

Early cancer detection continues to be one of the grand challenges in modern biomedicine, as early-stage biomarkers are often present in extremely low concentrations that conventional detection methods fail to identify. Traditional Field-Effect Transistor (FET)-based biosensors, while offering real-time and label-free detection, are limited by intrinsic electronic noise, charge trapping at the dielectric–semiconductor interface, and insufficient signal-to-noise ratio (SNR) at ultra-low analyte concentrations. To address these fundamental constraints, this study proposes a novel Avalanche Field-Effect Transistor (AFET) biosensor architecture designed to achieve internal electrical amplification through impact ionization. The AFET introduces a localized high-field region within the semiconductor channel, enabling carrier multiplication and significantly amplifying the weak bioelectrical signals produced during molecular recognition events.

Comprehensive modeling and simulation of the AFET biosensor were carried out using Synopsys Sentaurus TCAD and COMSOL Multiphysics software tools. The simulated electric-field distribution revealed strong localization near the hemispherical drain tips, where the field intensity reached approximately 6.5×10^5 V/cm, surpassing the silicon ionization threshold and confirming the feasibility of controlled avalanche multiplication. The simulated current–voltage (I–V) characteristics indicated a clear avalanche onset at $V_{DS} \approx 7.5$ V, resulting in an internal gain factor of $M \approx 20$. Quantitative noise modeling further showed that this internal gain improves the SNR by more than 13 times compared to a standard FET biosensor operating under identical bias conditions.

The AFET biosensor demonstrates a detection limit (LOD) as low as 10^{-15} M, representing a million-fold improvement over conventional FET biosensors (10^{-9} M). Additionally, the response time is reduced from 1 second to 0.25 seconds, allowing faster and more accurate detection. The tunable avalanche gain (M = 5–20) offers flexibility in adjusting sensitivity and dynamic range, enabling reliable detection across a wide range of biomarker concentrations.

Overall, this modeling and simulation study confirms that AFET biosensors provide an advanced and CMOS-compatible platform for ultra-sensitive, label-

free, and real-time cancer biomarker detection. The proposed structure's inherent amplification capability eliminates the need for external circuitry, paving the way for portable, low-power, and cost-effective diagnostic devices suitable for point-of-care applications and continuous health monitoring.

EFFECT OF γ-IRRADIATION ON DIELECTRIC PROPERTIES OF POLYMER NANOCOMPOSITES

*Aysel N.M.N., Musafir Q.M., İsmayilova R.S.
Institute of Radiation Problems, Ministry of Science and Education, Azerbaijan
aysel.nabiyeva21@gmail.com

Different polymers exhibit distinct responses to radiation, which are intrinsically linked to their chemical structures- causing either degradation or cross-linking - and while high doses damage all materials, controlled low-dose radiation can enhance valuable commercial properties. Moreover, radiation effects on dielectric properties are scientifically important and widely used in modern engineering.

Accordingly, the present study investigates the influence of gamma radiation on the dielectric permittivity of HDPE and nanocomposites based on it. Dielectric constant (ε′) measurement was performed over a frequency range from (25 Hz) to (1 MHz) at room temperature for unirradiated and irradiated (at D=500kGy) pure HDPE and HDPE/x%α-Al_2O_3 (x=0;1;3) nanocomposite films. ε′=f(ν) dependences in HDPE/α–Al_2O_3 are similar, in the studied frequency range, the value ε' hardly depends on frequency. While the presence of nano filler leads to an increase in permittivity only for samples with 3% filler content than for unfilled PE. On the one hand, this increase is due to the dipoles introduced by the nanostructuration, and on the other hand, especially at low frequencies, to the interfacial polarization induced by electrical charge at the nanofiller-polymer interface, which contact area increases as filler concentration enhances. ε′ values in HDPE +1% α–Al_2O_3 are smaller than in neat HDPE. In the case of HDPE, the dielectric strength Δ ε' parameter is the difference between the dielectric values at low and high frequencies, is given by $\Delta\varepsilon'=\varepsilon_s'-\varepsilon_\infty'$, is 0.11.

The 500kGy irradiation dose leads to an increase in the value of ε'. The increase in ε' induced by gamma irradiation is attributed to the generation of free charge carriers and ionized groups in the material. While pure HDPE displays frequency-independent behavior, the 1% and 3% samples show identical curve

characteristics. Specifically, ε' decreases slightly from 25 Hz to 2 kHz, decreases considerably from 2 kHz to 50 kHz, remains constant between 50 kHz and -200 kHz, and then increases until the end of the scale. The increase of ε′ values with a decrease of frequency at the low frequency region can be attributed to the interfacial polarization, which exists due to the difference in the permittivity and conductivity values of the α–Al_2O_3 nanopowder and the HDPE matrix. The dominant contribution of interfacial polarization in the enhancement of low-frequency dielectric permittivity is a common characteristic of the polymer nanocomposite materials. It is well established that the charge state of composites is determined by electron–ion interactions occurring within their volume. Consequently, our ongoing research focuses on elucidating the mechanisms underlying these phenomena in the investigated composite materials.

EFFECT OF GAMMA IRRADIATION ON THE THERMOPHYSICAL PROPERTIES OF PVA AND PVA/CdS NANOCOMPOSITES

***Gasimova A.I., Nuriyev M.A.**

Institute of Radiation Problems, Ministry of Science and Education, Azerbaijan
a.a7787@mail.ru

The synthesis and investigation of the properties of polymer-based nanocomposites with potential applications in various industrial fields is one of the main challenges in science and technology. The properties of such composite materials can be controlled either by changing the concentration of nanoparticles in the polymer matrix or by exposing them to ionizing radiation.

From this perspective, the present study, dedicated to the investigation of the structural and thermophysical properties of polyvinyl alcohol (PVA)-based PVA/CdS nanocomposites treated with gamma radiation at doses of 200, 300, and 500 kGy, can be considered highly relevant. The thermophysical properties of the samples were studied using differential thermal analysis (DTA) and thermogravimetry (TGA) methods. The values of some parameters calculated from the TGA and DTA thermograms of PVA and PVA/CdS nanocomposites are presented in the table below.

As seen from the comparative analysis of the obtained values, a higher residual mass is observed not for the PVA/10cyc. CdS composite, which contains a greater amount of nanoparticles, but rather for the PVA/5cyc.CdS composite. The relatively high value of this parameter (~32%) for PVA/ 5cyc. CdS is

attributed to a more homogeneous distribution of the formed nanoparticles within the polymer matrix. In this case, the polymer-filler interaction becomes stronger due to the larger effective surface area of the filler and the higher concentration of radiation-induced cross-links, resulting in a higher residual mass observed in the TG spectra. On the other hand, comparison of the mass loss rate values calculated from the TGA thermograms indicates that the nanocomposites decompose at a slower rate. All these findings suggest that the nanocomposites exhibit greater thermal stability compared to the pure polymer.

The values of certain parameters calculated from the TGA and DTA spectra of PVA and PVA/CdS nanocomposites

Samples	D, kGy	Residual mass parameters, T = 620 °C				
		Mass loss rate, %/min	First mass, M, mg	Residue		Residue/M, mg,
				%	mg	
PVA	0	11,25	6,7	6,96	0,47	0,07
	200kGy		1,82	18,85	0,34	0,19
	300kGy		2,16	13,21	0,28	0,13
	500kGy		1,49	22,3	0,33	0,22
PVA/3cyc.CdS	0	4,47	2,59	14,87	0,38	0,15
	200kGy		1,54	21,27	0,33	0,21
	300kGy		2,03	20,23	0,41	0,20
PVA/5cyc.CdS	0	4,84	1,33	32,79	0,43	0,32
	200kGy		1,48	31,2	0,46	0,31
PVA/10cyc.CdS	0	4,68	3,82	24,27	0,93	0,24
	200kGy		7,32	17,93	1,32	0,18

PHYSICO-MECHANICAL IMPROVEMENT OF HNBR COMPOSITES VIA EPSU-BASED CROSSLINKING

***Azizova A.S., Khankishiyeva R.F., Akhundzada H.N., Mammadov A.Kh., Salehov A.Kh., Valiyeva S.A., Khudaverdiev V.**

Institute of Radiation Problems, Ministry of Science and Education, Azerbaijan
aidaazizova889@gmail.com

This study explores the modification of hydrogenated nitrile butadiene rubber (HNBR) using ethylphenylsilylurea (EPSU), a novel organosilicon crosslinking agent synthesized via the reaction of ethylphenyldichlorosilane with

urea. The resulting multifunctional additive effectively reinforces the rubber matrix. Mechanical tests showed that EPSU-modified composites have higher tensile strength, tear resistance, and Shore A hardness, with optimum performance at 1.5 phr EPSU. Resistance to aggressive media such as oil, toluene, hydrochloric acid, and nitric acid increased by 30–50%, attributed to the formation of a dense, chemically stable siloxane–urea crosslinked network.

The incorporation of EPSU significantly improved the physico-mechanical characteristics of HNBR vulcanizates (tab. 1). Even at low concentrations, EPSU enhanced strength, elasticity, and structural stability. Tensile strength increased by about 5%, and hardness rose from 55 to 61 Shore A units, indicating a more compact network. Tear strength also increased from 63 to 70 kN/m, demonstrating improved resistance to crack propagation. Although a slight reduction in elasticity occurred with higher EPSU levels, the properties remained within acceptable limits. The most balanced combination of strength, hardness, and elasticity was achieved at 1.5 phr EPSU (HNBR-X2), representing the optimal formulation.

Table 1. Physical properties of the samples of rubbers based on HNBR with different contents of EPSU

Formulation	EPSU (phr)	Equilibrium swelling (%)	Soluble fraction (%)	Mc ($g \cdot mol^{-1}$)	Crosslink density ($mol \cdot cm^{-3}$)	Hardness (Shore A)
HNBR-X0	0	339	6.04	60,000	1.6×10^{-5}	55
HNBR-X1	0.5	312	4.88	45,000	2.1×10^{-5}	57
HNBR-X2	1.5	263	4.39	30,000	3.1×10^{-5}	61
HNBR-X3	2.0	283	4.60	24,000	4.0×10^{-5}	63

Thermal aging tests (393 K, 36 h) revealed that EPSU-modified samples retained mostof their mechanical properties and exhibited superior thermal-oxidative stability. Adhesion to metal substrates increased to 10 MPa, expanding potential use in rubber–metal bonded components, gaskets, and seals.

In summary, EPSU serves as an effective organosilicon crosslinking modifier for HNBR elastomers, enhancing crosslink density, hardness, and thermal stability while maintaining adequate elasticity. These features make EPSU-modified HNBR materials promising for oil, gas, automotive, and industrial applications.

DOPING-INDUCED OPTIMIZATION OF THERMOELECTRIC PERFORMANCE IN $Au_3In_5Se_9$–$Ag_3In_5Te_9$ SYSTEMS FOR INFRARED APPLICATIONS

Ragimov R.Sh., *Sarmasov S.N.

Baku State University, Azerbaijan
suleymansarmasov@bsu.edu.az

This paper presents an in-depth investigation of the thermoelectric and thermomagnetic properties of the semiconductor compounds $Au_3In_5Se_9$ and $Ag_3In_5Te_9$. The study aims to determine the correlation between the temperature-dependent Seebeck coefficient, electrical conductivity, and thermal conductivity, considering the effects of controlled doping and annealing. The samples were synthesized by sealed-ampoule sintering followed by gradual cooling and post-annealing, ensuring homogeneous, structurally stable crystals.

Indium incorporation into the $Ag_3In_5Te_9$ lattice resulted in a pronounced enhancement of the thermoelectric figure of merit (ZT) and output voltage near 510 K, primarily due to an increase in carrier density and interface conductivity. The $Au_3In_5Se_9$ compound exhibited low thermal conductivity and remarkable signal reproducibility at ambient temperature, which confirms its suitability for low-gradient thermal systems.

The observed inversion of the Seebeck and Hall coefficients indicates a transition from n-type to p-type conduction, associated with changes in the band curvature and scattering rate of charge carriers. This behavior supports the theoretical predictions of phonon scattering and carrier localization in narrow-gap semiconductors. Furthermore, both compounds demonstrate excellent thermal cycling stability, maintaining their properties over extended operation periods.

In addition to their intrinsic thermoelectric efficiency, the materials also reveal strong potential for use in infrared detectors, thermoelectric amplifiers, and self-powered sensors. The tunability of their electrical and thermal parameters through doping provides a valuable design tool for engineering advanced, miniaturized energy-harvesting devices. Future work will focus on optimizing defect structures and exploring nanostructured morphologies to further enhance their ZT values and thermal reliability.

PHOTOLUMINESCENCE INVESTIGATION OF ZnO/ZnS Core–Shell NANOSTRUCTURES

***Feyzullayeva L.S., Nuriyeva S.G.**
*Baku State University, Azerbaijan
sevincnuriyeva@bsu.edu.az

ZnO–ZnS core–shell nanostructures have attracted significant attention due to their superior optical and structural characteristics compared to pure ZnO. The ZnS shell effectively passivates surface defects of the ZnO core, increasing emission efficiency, optical quality, and chemical stability. These heterostructures are promising for optoelectronic and photonic applications owing to their tunable emission spectra and stability under operating conditions.

This research is important because there is a growing interest in controlling electron transitions in ZnO–ZnS structures to improve their luminescent properties. Enhancing photoluminescence intensity and minimizing surface-related defects remain essential challenges for the fabrication of high-efficiency nanomaterials. Therefore, establishing simple, low-temperature synthesis methods for such nanostructures holds both scientific and practical importance.

In this study, ZnO nanoparticles were produced using the co-precipitation technique. In the following step, a ZnS coating was deposited on the ZnO nanoparticles through a simple chemical method. As a result, ZnO–ZnS core–shell nanostructures were successfully fabricated, and their optical properties were analyzed using photoluminescence spectroscopy.

The main emission peak observed around 384–386 nm is 86 nm is due to near-band-edge recombination in ZnO. The ZnO/ZnS structure exhibits significantly higher PL intensity, which can be explained by the ZnS shell reducing surface defects such as oxygen vacancies and zinc interstitials, boosting radiative recombination.

Weak emission peaks within 400–500 nm (418, 461, and 486 nm) are caused by surface or deep-level defects, whereas faint signals near 600 nm correspond to yellow–red defect-related emissions.

Overall, the ZnS coating effectively passivates the ZnO surface, enhances luminescence intensity, and decreases surface defect density, leading to improved optical quality and higher quantum efficiency.

GREEN SORBENTS BASED ON SAPONITES FOR THE REMOVAL OF CATIONIC DYES

[1*]Bohatyrenko V. A., [2]Kamenskyh D. S., [2]Tkachenko T. V., [2]Yevdokymenko V.O.

[1]Dragomanov Ukrainian state university, Kyiv, Ukraine;
[2]V.P. Kukhar Institute of Bioorganic Chemistry and Petrochemistry (IBOPC) of the National Academy of Sciences of Ukraine, Kyiv, Ukraine
vitabog@gmail.com

In order to limit the increasing technogenic and anthropogenic load on the natural environment, increasing attention is being paid to adsorption purification methods with an emphasis on the use of green technologies for producing sorbents, in particular those based on natural clays. Adsorbents based on dioctahedral smectites (2:1) attract attention and are widely used due to their environmental friendliness and low cost. However, their surface characteristics, including those with respect to the sorption of cationic dyes, are generally inferior to modern biosorbents and require strengthening, which is achieved by additional modification of clay-layered aluminosilicates. In this context, the ability of sorbents obtained by acid modification of purified natural trioctahedral saponites enriched with Fe, the ability to effectively remove cationic dyes such as methylene blue (MB), fuchsine, and methyl violet, was studied.

The morphology, porosity, and structural characteristics of elemental and phase composition of the obtained sorbents were determined using instrumental methods such as SEM, EDX, FTIR spectroscopy, ED XRF, XRD, as well as the N_2 adsorption-desorption method. The distribution of active centers of saponite surface particles was assessed by determining the integral acidity of the pH_S suspensions, establishing the point of zero proton charge P_{ZNPC} and studying the adsorption of acid-base organic dyes using the Hammett method.

It was found, as a result of concentrated nitric and orthophosphate acids impact, some disintegration of the microcrystalline lamellar aggregates (predominantly 2-5 μm in diameter) of purified natural saponite due to the partial removal of exchangeable cations and the minor formation of amorphous silica occurs. HNO_3 has a somewhat stronger impact. As a result, the acid-base nature of the particle surface transforms, resulting in the formation of exclusively acidic surface centers, as confirmed by determining the point of zero proton charge (P_{ZNPC} 3÷4,5). This modification significantly increases the effectiveness of the sorbents relatively to cationic dyes, as evidenced by a more than twofold

increase in the sorption capacity of the sorbents compared to the sorption activity of natural saponite (the sorption capacity was determined according to GOST 21283-93). The maximum adsorption capacity for the best adsorbent at 293 K was found to be 605 мг $г^{-1}$. The Langmuir and the Freundlich models were used to quantitatively evaluate the adsorption process of cationic dyes.

ELECTRICAL CHARACTERIZATION OF DEEP-LEVEL DEFECTS IN TE-DOPED N-TYPE GASB GROWN BY THE CZOCHRALSKI METHOD

[1*]Bushra Bushra, [2]Aneeqa Sabah

[1*]Eye Interaction Ltd, United Kingdom

[2]Lahore college for Women University, Pakistan

bushrasalim400@gmail.com

This Thesis intends to observe the electrical properties of unintentional deep levels in Te-doped n-type GaSb grown by the Czochralski technique. The major techniques used in this look at have been I-V. C-V, Deep Level Transient Spectroscopy and Hall Effect. This characterization approach has been determined to be very versatile in imparting information about the entice parameters like activation power, seize cross phase, density of states, and nature of traps. I-V and C-V measurements display that the maximum of the fabricated diodes was properly fine. C-V measurements confirmed that the pattern of the samples had a donor level doping of 8.3*1016cm-^{3}. One electron lure classified A turned into located to dominate the DLTS spectrum at zero.29 eV underneath the conduction band. The obvious electron seize move sections of this level are discovered to be five.1x10^{-15} cm^{2}.

INVESTIGATION OF THE POSSIBILITY OF A NEW DETECTOR BASED ON SiPM IN NUCLEAR FORENSICS

[*]Piraliyeva F.K., Sadigov A.Z., Naghiyev J.A.

*Nuclear Research Department, IDDA, Azerbaijan

fatimepireliyeva86@gmail.com

The continuous advancement of nuclear technologies and the growing use of radioisotopes, radiopharmaceuticals, and other radioactive materials have substantially increased the demand for efficient and reliable radiation detection

systems. Ensuring nuclear safety and enabling precise identification of nuclear materials require detectors that are not only highly sensitive but also compact, cost-effective, and easy to operate. Conventional high-purity germanium (HPGe) detectors, while offering excellent spectrometric resolution, are expensive, require cryogenic cooling with liquid nitrogen, and must be operated by trained personnel. Therefore, the development of compact and efficient alternatives represents a crucial goal in modern nuclear instrumentation, radiation monitoring, and forensic analysis.

This study investigates the performance of a silicon photomultiplier-based detector (MAPD-3NM-II) coupled with a $LaBr_3$(Ce) scintillator. The experimental setup employed a 16-element MAPD array integrated with the Spectrig MAPD readout interface, optimized for high-resolution acquisition of scintillation signals. Gamma-ray spectra were recorded from several standard radioactive sources, including ^{241}Am, ^{137}Cs, natural uranium, and depleted uranium, covering an energy range of 13–1001 keV. The $LaBr_3$(Ce) scintillator demonstrated excellent optical performance, while the detector achieved an energy resolution of 3.3% at 662 keV and maintained high linearity across the tested energy range.

Spectrometric analysis of uranium samples revealed distinct differences between natural and depleted uranium, based on the characteristic gamma lines at 185.7 keV (^{235}U) and 1001 keV (^{238}U). The ratio of these photopeaks – 15.19 ± 1.51 for natural uranium and 6.63 ± 1.38 for depleted uranium – was in strong agreement with results obtained using a reference HPGe detector. These findings confirm that the MAPD-3NM-II + $LaBr_3$(Ce) detection system can reliably differentiate uranium isotopic compositions without relying on cooling or complex analytical software.

The results demonstrate that the proposed MAPD and $LaBr_3$(Ce)-based spectrometer offers a portable, cost-effective, and highly sensitive alternative to conventional germanium detectors. Due to its compact design, low power consumption, and robust performance, it can be effectively employed as a mobile spectrometric device for in-field nuclear forensics, enabling rapid identification of radio nuclides and isotopic compositions directly at inspection sites. This makes the system highly suitable for nuclear security monitoring, border control, emergency response, environmental surveys, and on-site forensic investigations.

ON THE PROPERTIES OF AN ACOUSTIC FILTER IN METAMATERIALS BASED ON THE PROBLEMS OF WAVE PROPAGATION THROUGH ELASTIC SOLIDS WITH PERIODIC ARRAYS OF DEFECTS

***Remizov M.Yu.**
Western Caspian University, Azerbaijan
remizovmyu72@gmail.com

The problem is devoted to the derivation of analytical expressions for reflection and transmission coefficients R, T, when a plane longitudinal wave falls on a system of a finite number of consecutive identical plane lattices, where each one consists of an infinite periodic array of collinear cracks in an elastic isotropic medium in antiplane and plane formulation. In one-mode frequency range, the applied method leads to a system of hypersingular integral equations, the solution of which gives the reflection and transmission coefficients, as well as the representation of the wave field inside the medium for the case of 1,2,3 and $M(\geq 2)$ arrays. It is assumed that with normal wave incidence $\exp(ik_1x)$ there is a propagation of one mode at $ak_2 < \pi$, where $k_1, k_2 -$ the wave numbers of the longitudinal and transverse waves, $2a -$ the period of the system, $2b -$ the length of each crack (Fig. 1). The distance between the systems d is such, that $d/a \gg 1$ is fulfilled.

The problems suggested are related to the theory and practice of «acoustic metamaterials», having the property of acoustic filter – cutoff of propagating waves at certain frequency intervals. The determination of regularities of wave propagation through a system with periodic defects in elastic media allows solving practical problems about the transmission of waves through different natural and synthesized heterogeneous metamaterials as objects for high responsibility. The technique allows for conducting experimental studies for the investigation of physical and mechanical properties of natural and synthesized metamaterials.

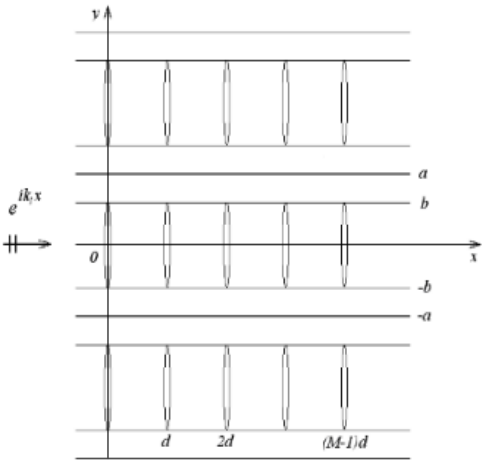

Fig. 1. Periodic system of defects

TUNING STRUCTURAL AND OPTICAL PROPERTIES OF CdS via Cd:S RATIO CONTROL USING SILAR TECHNIQUE

***Hamidova S.N., Gahramanli L.R., Mammadov V.U.**
Baku State University, Azerbaijan
hamidova.sevinc.natiq@bsu.edu.az

This work investigates the structural, morphological, and optical properties of CdS nanocomposites synthesized by the successive ionic layer absorption and reaction (SILAR) technique in a PVA polymer matrix at different Cd:S ratios (1:0.1, 1:0.25, 1:0.5, 1:0.75, and 1:1). X-ray diffraction (XRD) results reveal a structural transition from a pure hexagonal phase (1:0.1) to mixed cubic–hexagonal phases (1:0.25, 1:0.5), reverting to a dominant hexagonal phase (1:0.75), and finally to an amorphous phase at a 1:1 ratio. AFM analysis confirms size variations between 5–70 nm, showing a correlation between Cd:S ratio and particle aggregation. UV–Vis spectroscopy demonstrates a systematic reduction of the band gap from 3.32 eV to 2.41 eV with increasing sulfur content, followed by a slight increase (2.52 eV) for the amorphous phase, attributed to the quantum confinement effect. FTIR spectra indicate red shifts in O–H and CH_2 stretching bands due to strong CdS–PVA interactions. Raman analysis shows the emergence of 1LO (~298 cm^{-1}) and 2LO (~600 cm^{-1}) phonon modes at a 1:0.5 ratio, reaching maximum intensity at 1:0.75, indicating high crystallinity. PL spectra display emission peaks at 450, 486, 564, and 669 nm, with the highest exciton recombination efficiency at 1:0.75, confirming the optimal structural ordering. The results demonstrate that fine-tuning the Cd:S ratio effectively controls crystallinity, particle size, and optical behavior, offering a viable approach for designing CdS-based materials in optoelectronic, sensing, and energy conversion applications.

ELECTRIC CURRENT GENERATION IN SCHOTTKY DIODES UNDER THE EFFECT OF AN ADDITIONAL ELECTRIC FIELD

Mamedov R.K., *Aslanova A.R.
Baku State University, Azerbaijan
rasimmammadov@bsu.edu.az

Some electrical properties of real Schottky diodes (SDs), created using various contacting metals and semiconductors, are difficult to fit within the Schottky model. In particular, the dependence of the potential barrier height on

the applied forward voltage of real SDs is stronger than predicted by the Schottky model. The phenomenon of the emergence of an additional electric field (AEF) in real SDs demonstrates that the complex electronic processes occurring within them can be described by a two-dimensional energy structure.

This report presents the features of the two-dimensional energy structure of the DS developed by us with the corresponding electrophysical parameters, schematically shown in Fig. 1.

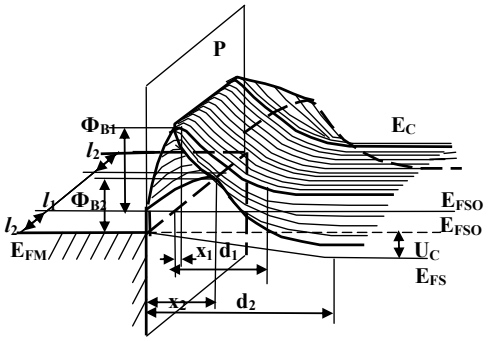

Fig. 1. Schematic two-dimensional energy structure of real SD

AEF in the SD, which arises due to the potential difference between the interface surface and the adjacent free surfaces of the semiconductor and metal, exists in almost all real MSCs. The AEF tension is directed from the edge part of the contact surface of the metal to the free surfaces of the contacting materials. The general contact surface of the SD consists of an inner part with a high potential barrier height $\Phi_{B1,}$ and an edge part with a low potential barrier height Φ_{B2}, where $\Phi_{B1} > \Phi_{B2}$. The potential barrier has a maximum value of Φ_{B1} at a distance x_1 from the interface in the inner part of the contact and decreases along the direction to the periphery in the edge part of the contact to a minimum value of Φ_{B2} at a distance x_2 from the interface. Under the influence of the AEF, a redistribution of charge carriers occurs in the peripheral contact area, and a voltage drop ($-U_C$) occurs.

PHOTOLUMINESCENCE IN STAIN-ETCHED POROUS SILICON AFTER IMMERSION PLATING DEPOSITION OF Cu

***Rustamov F.A., Darvishov N.H., Mamedov M.Z., Bobrova Y.E., Askerova H.O.**

Baku State University, Azerbaijan
farhad.rustamov@bsu.edu.az

The effect of immersion deposition of Cu on the luminescent properties of stain-etched porous silicon (PS) has been investigated. The PS layers were obtained by stain etching on p-type monocrystalline silicon wafers at room tem-

perature and under natural light in a solution of HF: HNO_3: CH_3COOH in a volume ratio of 1200:1:800. Then Cu was deposited from aqueous solutions of $CuCl_2$ and $CuSO_4$ (10^{-3} M) by electroless immersion plating for 1 min. After deposition, the samples were washed in bidistilled water and isopropyl alcohol and dried by N_2 jet.

It was shown that Cu deposition leads to complete quenching of photoluminescence. To clarify the role of the deposited metal in PL quenching, some samples were etched in HNO_3 for 1÷60 min after deposition. Such treatment in acid should lead to the removal of the deposited metal from the PS surface. Despite the etching of the deposited metal, this did not result in the restoration of the PL. To clarify the role of various bonds on the PS surface, FTIR spectra of the samples were studied before and after Cu deposition.

The main changes in FTIR spectra are observed in 1000 ÷ 1300 cm^{-1} and 2000 ÷ 2300 cm^{-1} region and are associated with oxygen and hydrogen bonds. Peak identification was performed after baseline correction of those FTIR spectra by Origin-Pro.

When cooper is deposited, a fairly intense and broad new absorption peak at 1221 cm-1 appears on the spectrum (Fig. 1 porSi: Cu), which is not typical for PS. It is noteworthy that this peak is also observed after etching the metal with acid. The proximity of this peak to the peak at 1172 cm^{-1} (stretching mode Si-O-Si) indicates its connection with oxygen vibrations. However, the absence of PL indicates that the oxide produced by the metal

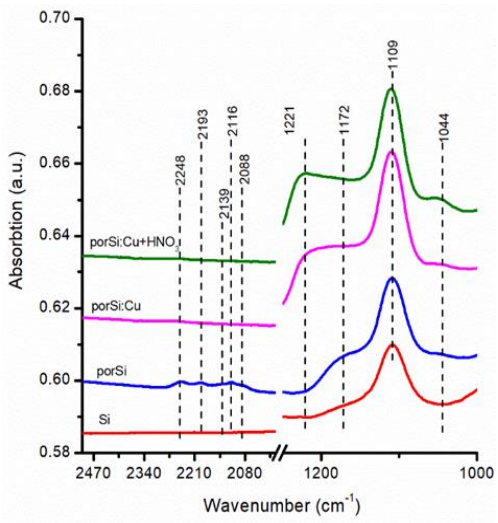

Fig. 1. FTIR spectra of silicon wafer (Si), stain etched PS (porSi), PS after immersion plating of Cu (porSi:Cu) and PS after removing of Cu by HNO_3.

is of poor quality. These deformed oxygen bonds lead to the emergence of non-radiative recombination centers in the PS gap, which suppresses PL.

INTRACAVITY LASER FREQUENCY MIXING UNDER QUASI-PHASE-MATCHING CONDITIONS

Kerimli N.V.
Azerbaijan Medical University, Azerbaijan
nkerimli@amu.edu.az

Miniature laser sources that produce intense coherent radiation over a broad wavelength range are a vast class of nonlinear optical devices. An intracavity structure is widely utilized to increase the effective interaction length in nonlinear crystals as well as the fundamental wave intensity. This technique offers several advantages over the single-pass approach, including a smaller form factor, lower cost, and high conversion efficiency and output power18-29. MgO: PPLN is a promising material for the low-cost, small-watt-level lasers that our research group has developed for laser displays and biomedical applications1,3. MgO: PPLN manufacturing results in lengthy crystals with huge aperture sizes (0.5-1 mm) compared to the laser cavity's beam widths (usually <100 microns). The extensive body of research available for MgO: PPLN, as evidenced by the previously stated studies, emphasizes the need to build empirical relations to guide the design and optimization of MgO: PPLN-based lasers.

Intracavity frequency conversion is a single, integrated process that generates basic radiation and converts nonlinear frequencies. As a result, phase variations between interacting waves in the same cavity have a direct impact on conversion efficiency. In this setting, phase effects are critical, necessitating research into how these phase connections influence the sum-frequency wave's generation efficiency and determining optimal conditions for effective frequency conversion. Thus, it is advisable to carry out a theoretical investigation of intracavity conversion using the constant-intensity approximation, which incorporates the phase variations of all interacting waves.

The current study describes frequency conversion processes in a polydomain consisting of two phases of "grating" modulation of nonlinear susceptibility (i.e., from four consecutively organized domains). As a result, the complex amplitudes of interaction waves at the outlet of each main serve as the entry values for the equivalent complex amplitudes in the subsequent domain. The factors that limit the effectiveness of frequency conversion have been investigated. In addition, the scenario of n domains has been considered. Furthermore, in this approximation, coherent length is found to be dependent on task characteristics such as basic radiation intensity and medium losses, as well as interaction wave mismatch. Constant-intensity approximation allows for a more

rigorous analysis of the nonlinear interaction of waves in a regular domain structure (RDS) compared to the constant-field approximation, which does not consider the given change. It has been found that selecting suitable pump intensity and phase ratio settings can greatly improve conversion efficiency when compared to the noncavity arrangement. The examination of η3(lj) indicates that as the main number increases, the steepness of dependence reduces. In other words, the process of frequency conversion has reached saturation. Using two domains increases conversion efficiency by 3.69, three domains by 1.97, four domains by 1.46, five domains by 1.22, and six domains by 1.02. As a result, the transit through the layer domains from the right to the left efficiently transfers laser radiation energy to the energy of the sum-frequency wave [η3(l6), practically, achieves 100%].

Under realistic experimental conditions, numerical estimates Under realistic experimental conditions, numerical estimates closely match predicted efficiencies. The suggested theoretical method can be used to investigate parametric intracavity frequency conversion.

RAMAN SPECTROSCOPIC INVESTIGATION OF BORON-DOPED GaSe CRYSTALS

*__Balayeva L.A., Huseynov A.H.__
Baku State University, Azerbaijan
blamiye99@gmail.com

GaSe is a layered semiconductor of the A_3B_6 group, well known for its remarkable optical and nonlinear properties. Owing to its high photosensitivity and anisotropic structure, GaSe is widely utilized in photodetectors and optoelectronic applications. Modifying its lattice through atomic substitution provides an efficient strategy to tailor its physical properties. In this study, gallium atoms in GaSe were partially substituted with boron (x = 1%) to investigate the influence of boron incorporation on the vibrational, structural, and optical behavior of the crystal.

The Raman spectrum of $Ga_{0.99}B_{0.01}Se$ revealed several distinct peaks. When compared with pure GaSe, where the main phonon modes appear near 130 cm^{-1} ($A_1(1)$), 210–250 cm^{-1} (E(2)), and 308 cm^{-1} ($A_1(2)$), the doped crystal retains the primary modes but exhibits slight red-shifts and variations in intensity. The $A_1(1)$ mode at 132.3 cm^{-1} remains nearly unchanged, suggesting that the long-range

crystal symmetry is preserved. Meanwhile, the E(2) and $A_1(2)$ modes shift to lower frequencies (197.9 and 303.1 cm^{-1}), attributed to lattice strain and altered interatomic force constants due to the substitution of lighter B atoms for heavier Ga atoms. Additionally, new Raman-active modes were detected at 153.7, 413.0, 639.3, and 749.4 cm^{-1}, absent in pristine GaSe. The 153.7 cm^{-1} band likely corresponds to local vibrational modes (LVMs) of B–Se or B–Ga bonds, confirming substitutional incorporation of boron into the GaSe lattice. The higher-frequency peaks above 400 cm^{-1} are associated with multiphonon and overtone processes activated by local symmetry breaking. The broad bands at 639 and 749 cm^{-1} indicate B–Se stretching vibrations, confirming strong chemical bonding between boron and selenium. An enhancement of the $A_1(1)$ mode intensity suggests strengthened electron–phonon coupling in the boron-doped structure. Overall, the Raman spectral changes indicate that boron doping introduces local lattice distortions while preserving the layered GaSe framework. These findings agree with structural and optical observations in similar GaSe-based solid solutions, showing that boron incorporation primarily affects the short-range order while maintaining long-range periodicity.

In conclusion, Raman spectroscopy confirms successful boron incurporation into the GaSe lattice. The observed spectral shifts, emergence of new vibrational modes, and intensity enhancement demonstrate that boron doping effectively modifies the lattice dynamics and slightly perturbs the symmetry of GaSe. These structural and vibrational alterations are expected to influence charge carrier scattering and optical transitions, offering potential improvements in the optoelectronic performance of $Ga_{1-x}B_xSe$ – based photodetectors.

EFFECT OF GAMMA IRRADIATION ON THE OPTICAL PROPERTIES OF $FeGaInS_4$/ PVA COMPOSITES

*Addayeva Z.R., Muradov M.B.
Baku State University, Azerbaijan
zeynab.addayeva@bsu.edu.az

The properties of polymer-based materials depend on factors such as crystallinity, molecular arrangement, and morphology. Besides filler composition and geometry, processing and modification techniques critically influence their functionality. Among these, gamma irradiation effectively tailors polymer properties by modifying conductivity, dielectric behavior, and resistivity. Interaction

of gamma photons with the polymer matrix induces chain scission, oxidation, and crosslinking, whose extent depends on radiation dose, polymer type, and environmental conditions.

In this work, a layered crystal ($FeGaInS_4$) and a semicrystalline polymer (PVA) were used. $FeGaInS_4$/PVA nanocomposites were fabricated using a solution casting technique. Initially, $FeGaInS_4$ crystals were synthesized separately before being incorporated into a 5 wt.% aqueous solution of polyvinyl alcohol (PVA).

Figure 1(a) shows the absorbance and Figure 1(b) the transmittance spectra of samples N_0–N_3: N_0 (non-irradiated), N_1 (500 kGy), N_2 (1500 kGy), and N_3 (2500 kGy).

As shown in Fig.1a, the composites' light absorbance decreases with increasing gamma dose, with minimal change at low doses. At 500 kGy, enhanced crosslinking increases crystallinity, leading to reduced defects and photon trapping, which lowers absorbance and raises transmittance. At higher doses, chain scission and oxidation further decrease absorbance by eliminating absorption centers. Consequently, the transmittance spectra show a clear increase, especially at 2500 kGy, indicating greater transparency due to irradiation-induced structural reorganization. Based on UV-Vis spectroscopy results, a decrease in absorption and an increase in trans-mittance were observed at 500 kGy, attributed to enhanced crystallinity.

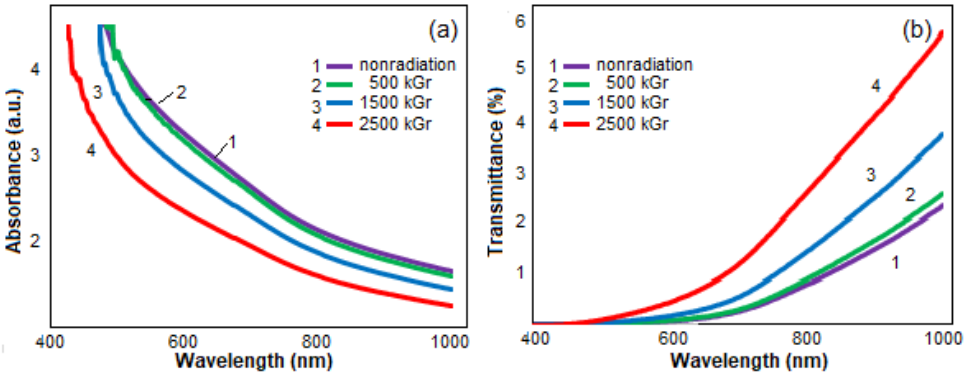

Fig. 1. UV–Vis spectra of $FeGaInS_4$/PVA nanocomposites at different γ-irradiation doses: (a) Absorbance and (b) Transmittance spectra for (1) N0 –(non-irradiated), (2) N1 – (500 kGy), (3) N2– (1500 kGy), (4) N3 – (2500 kGy).

STRUCTURAL CHANGES OF NITROGEN-DOPED GRAPHENE NANOPLATES

Gahramanli L.R., *Huseynzade R.R.
Baku State University, Azerbaijan
reshidehuseynzade03@gmail.com

Graphene can be doped with N as well as with other heteroatoms (B, P, S, etc.). Doping of graphene with different atoms disturbs the ideal sp^2 hybridization of carbon atoms and transforms it into an sp^3 hybridization state, resulting in significant changes in its electronic properties as well as its reactivity. During nitrogen doping of graphene, due to the high reactivity at the edges of the graphene sheets, three main C–N bonding configurations are typically formed: pyridinic N, pyrrolic N, and graphitic N.

In the presented work, nitrogen doping of graphene was carried out in the following sequence: first, graphene was dispersed in distilled water at a concentration of 5 mg/mL. As the N source, 62.5 mL of dopamine (4%, 40 mg/mL) was used. The graphene dispersion was mixed with the N source and sonicated for 1 h. Then, the solid product was heated in a microwave oven, and the obtained material was dried at 150°C for 3 h. The Raman spectra of the obtained sample were compared with those of pristine graphene.

In pristine graphene, the D peak observed at 1351.77 cm^{-1} was associated with the presence of disorder in the aromatic structure or the edge effect of graphene, while the G band observed at 1584.32 cm^{-1} corresponds to the in-plane C=C bond stretching in graphene. The peak observed at 2728.08 cm^{-1}, known as the 2D band, is related to the thickness of the graphene layers .

In the Raman spectrum of N-doped graphene, two sharp peaks were observed at 1342 and 1570.9 cm^{-1}, which correspond to the D and G bands, respectively. The lower I_D/I_G ratio (0.94) indicates that the N-doped graphene contains fewer defects. The peak observed at 2703.57 cm^{-1} corresponds to the 2D band. Studies have shown that the intensity of the 2D peak is sensitive to lattice defects and doping in graphene. The low I_{2D}/I_G ratio (0.45) and the broad 2D peak in the Raman spectrum indicate the multilayer structure of the graphene. The red shift of the G band (from 1584.32 cm^{-1} to 1570.9 cm^{-1}) and the weakening of the 2D band (from 2728.08 cm^{-1} to 2703.57 cm^{-1}) in N-doped graphene compared with pristine graphene confirm the incorporation of N atoms into the graphene lattice. Different percentages of N-doped graphene will be prepared.

NONSTATIONARY CONVERSION OF ULTRASHORT RADIATION PULSE FREQUENCIES

[1,2,3*]Amirov Sh.Sh., [2]Kasumova R.J., [2]Safarova G.A.

[1]Azerbaijan Medical University, Azerbaijan
[2]Baku State University, Azerbaijan
[3]Khazar University, Azerbaijan
phys_med@mail.ru

Amplification of weak signals and broadening the frequency range of laser radiation require the development of optical parametric amplifiers. An interest in the nonstationary interaction of ultra pulses is related to the creation of sources of pulses for which the durations are measured in femtoseconds. First theoretical studies of such parametric amplifiers showed that the character of interaction between modulated ultrashort pulses depends mainly on the dispersive properties of the medium. This dependence seems more obvious with a decrease in the pulse duration.

Metamaterials with a negative refractive index are attractive due to specific features of interaction with electromagnetic waves. The frequency conversion in those materials was mainly investigated by us in the constant intensity approximation. In metamaterials, unlike group velocities, the phase velocities are in the same direction. However, in dispersive media, the difference in the rates of change of the frequency components of the pulse causes non-stationary distortion of the pulse. Such distortion is especially pronounced for ultrashort pulses and is of great importance for pulses with durations in the femtosecond range. Therefore, when studying the nonlinear parametric interaction of ultrashort pulses in metamaterials, both phase velocity dispersion and group velocity dispersion must be taken into account simultaneously.

In this work, the nonstationary frequency conversions are analyzed by the set of truncated equations presented in the nonstationary form using the constant field approximation, where the amplitude of the fundamental pulse is considered to be constant. Those equations include both the first and second order partial derivatives with respect to time. Analytical expressions for the pulse spectral density were obtained by taking into account the effects of group velocity difference as well as the group velocity dispersion via Fourier transformations.

Analysis showed that with an increase in the ratio $l_{n/l}\,/l_{\nu}$, the width of the maxima of spectral densities decreases, and the maxima shift toward lower values of $\omega\tau$. It was obtained that the maxima of spectral density decrease with the increase of the ratio z $/l_{n/l}$. Such a decrease is also observed when the phase

modulation parameter increases. Under phase-matching conditions, dependencies of spectral density are symmetric, with relatively positive and negative values of the frequency modulation parameter $\omega\tau$.

CRYSTALLIZATION KINETICS OF AMORPHOUS $TlIn_{1-x}Sn_xTe_2$ FILMS

[1*]Alekperov E.Sh., [2]Ibragimov G.B., [2]Nazarov A.M.

[1]Baku State University, Azerbaijan

[2]Institute of Physics, Ministry of Science and Education, Azerbaijan

alekperoveldar@mail.ru

Experimental data on the interactions of atoms in solids and on valence electrons in atoms can be obtained using electron diffraction methods, of which electron diffraction is the most suitable for this research. Using this method, data on the kinetic parameters of crystallization of amorphous $TlInTe_2$ films doped with tin impurity are presented. Studying the temperature-time dependence of film crystallization helps elucidate their growth mechanism.

The studied amorphous films, ~36 nm thick, were obtained in a vacuum of $2x10^{-5}$ Pa using the thermal method by simultaneously depositing $TlInTe_2$ and Sn from two tungsten furnaces onto substrates of freshly cleaved NaCl and KCl, maintained at a temperature of 213–238 K and pre-coated with a carbon film. To prevent evaporation of the volatile component and oxidation processes resulting from subsequent heat treatment, a carbon film was applied to the resulting films. After dissolving the substrate, the studied film was transferred to a tungsten furnace substrate, where it was heat-treated. The crystallization temperature of amorphous $TlIn_{1-x}Sn_xTe_2$ films, obtained with a deposition rate of 3–6 nm/s, varied between 425÷485 K. A polycrystalline phase with a tetragonal syngony formed. Kinematic electron diffraction patterns reveal a phase transformation, i.e., changes in the number and intensity of lines of the growing crystalline phase are observed. During isothermal heat treatment of amorphous $TlIn_{1-x}Sn_xTe_2$ films crystallizing with a tetragonal unit cell, kinematic electron diffraction patterns of varying durations were recorded in the indicated temperature range. Measurements of the diffraction lines in the electron diffraction pattern showed that the crystallization process of the amorphous film occurs systematically, i.e., $I_{hkl} \sim V$. As is known, the intensity of the I_{hkl} lines is related to the irradiated volume of the crystalline substance by the ratio

$$I_{hkl} = I_0\lambda\left|\frac{\Phi_{hkl}}{\Omega}\right|^2 V\frac{d_{hkl}^2\Delta}{4\pi L\lambda}P.$$

Here, I_o – is the primary radiation beam intensity, λ – is the electron wavelength, Φ – is the structural amplitude of the diffraction reflection, which is calculated in the kinematic approximation from the atomic scattering factors, Ω – is the unit cell volume, and V – is the irradiated volume of the polycrystalline sample. The parameters d_{hkl} and Δ indicate the interplanar spacing and the Debye ring's small section, P – is the diffraction reflection enhancement repeatability factor, and Lλ – is the instrument constant, which is determined depending on the applied electron accelerating voltage.

Interpretation of the kinematic electron diffraction patterns confirms the Avrami-Kolmogorov crystallization process for amorphous films, i.e.,

$$V_t = V_o[1 - \exp(-kt^m)].$$

In this study, we found that three-dimensional crystal growth occurs during the phase transition in the temperature range studied. In crystalline films obtained after the phase transition, the lattice parameters of the unit cells increase by 5÷6% in accordance with the impurity concentration.

STRUCTURAL CHANGES OF NITROGEN-DOPED REDUCED GRAPHENE OXIDE

Gahramanli L.R., *Huseynzade R.R.
Baku State University, Azerbaijan
reshidehuseynzade03@gmail.com

The biggest challenge in the synthesis of graphene-based materials is to obtain a material with high conductivity and large surface area, which has been overcome by nitrogen-doped reduced graphene oxide (NrGO). Experiments conducted on nitrogen-doped and non-doped materials have shown that the addition of nitrogen increases the energy storage capacity and electrical conductivity of the material, the optical energy gap becomes controllable, and the ion mobility and electrical charge transfer are improved. Nitrogen doping of rGO is of great interest in the field of electronics and energy storage devices. Thus, doped nitrogen atoms (especially pyridinic and graphitic N) can provide more active centers for the oxygen reduction reaction (ORR). Therefore, NrGO shows very high electrocatalytic activity for ORR. At the same time, N-rGO has been widely applied in sensors because it exhibits higher sensitivity compared to pure rGO.

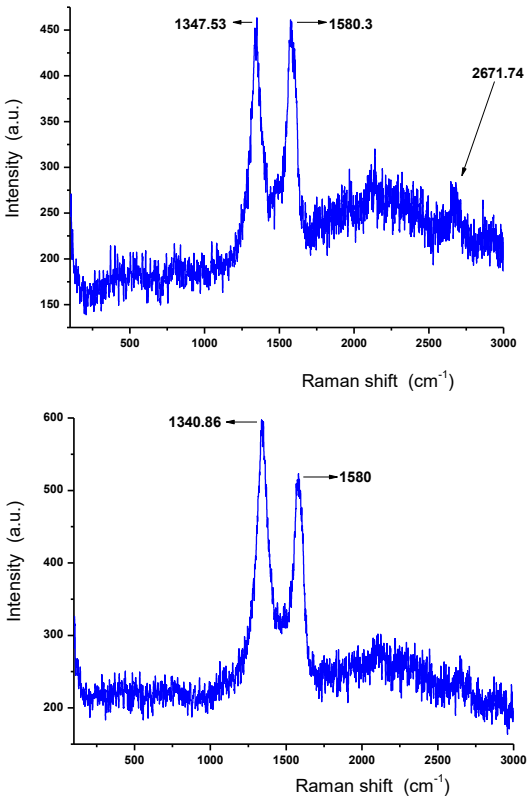

Fig. 1. Raman spectrum of N-doped rGO

In the presented work, nitrogen doping of rGO was carried out in the following sequence: 25 ml of GO solution (6 mg/ml) was prepared, and the pH value was adjusted to 10 by adding $NH_3 \cdot H_2O$ (ammonia water). Then, 20 ml of $N_2H_4 \cdot H_2O$ (hydrazine hydrate) was added to the pH-adjusted solution and stirred for 30 min with a magnetic stirrer. The mixture was transferred to a reaction vessel and kept at 130°C for 5 h. The obtained product was washed several times with distilled water and ethanol by centrifugation. Finally, the product was dried in a vacuum at 60 °C and N-RGO was obtained. The Raman spectra of the obtained sample (Figure 1) were compared with the spectra of pure rGO.

Two characteristic peaks were observed in both pure rGO and N-doped rGO at 1348 and 1580 cm^{-1}, corresponding to the D and G bands. The ID/IG ratio increased to 1.01 in rGO and 1.14 in NrGO. Thus, more defects were formed in the sample after doping. In addition, a weak 2D peak (2671.74 cm^{-1}), which is characteristic of graphene materials, was also observed in the Raman spectra. Graphene samples doped with nitrogen at different percentages will be prepared.

MOLECULAR ANALYSIS OF DRUG-POLIGLUSAM INTERACTIONS ON Fe_3O_4 nanoparticles

***Orujova F.R., Karimova A.H.**
Baku State University, Azerbaijan
orucova.fidan30@gmail.com

The coating of magnetite (Fe_3O_4) nanoparticles with poliglusam $(C_6H_{11}NO_4)_n$ enhanced their stability, biocompatibility, and drug binding. Ferrous sulfate heptahydrate ($FeSO_4 \cdot 7H_2O$) and ferric chloride hexahydrate ($FeCl_3 \cdot 6H_2O$) were used as precursors of iron ions in chemical co-precipitation to produce Fe_3O_4 nanoparticles. The aqueous solution of ammonia (NH_4OH) was added in drops until the pH value was around 10 and resulting in the appearance of the black Fe_3O_4 precipitates.

This simple procedure results in magnetite nanoparticles that can be used in biomedicine. Before the conjugation process, the surface of Fe_3O_4 nanoparticles was coated with poliglusam to improve their stability and provide active functional groups for further modification. After coating, 5,7-DHF ($C_{15}H_{10}O_4$) was loaded onto the surface of the poliglusam-coated Fe_3O_4 nanoparticles. 5,7-DHF is a flavonoid that exerts powerful antioxidant and neuroprotective effects and has been applied in multiple research experiments for its anti-inflammatory and cytoprotective influences. The drug was conjugated to the coated Fe_3O_4 nanoparticles using both covalent and non-covalent approaches for the investigation of drug-polymer-nanoparticle interactions. During the non-covalent procedure, the drug was bound to the nanoparticle's surface through electrostatic interaction and hydrogen bonding. These samples were referred to as Sample A**.** In the covalent procedure, the drug was chemically attached to the coated nanoparticle surface, ensuring a stable linkage. The samples obtained by this method are named sample B. The molecular structure of the samples was analyzed using FTIR spectroscopy. In the spectrum of both samples, a broad band around 3445 cm^{-1} corresponds to O-H stretching vibrations, which indicates the presence of hydroxyl groups from poliglusam as well as phenolic -OH groups of 5,7-DHF. In Sample B, the broad band at 3445 cm^{-1} comes from the O-H adjacent to hydrogen bonding and has a strong interaction or partially covalent bond. In Sample A, although the O-H band at 3445 cm^{-1} is still broad, it is less intense than the B sample and has a faint weak signal at 3728 cm^{-1} corresponding to free -OH groups. The aliphatic C-H stretching bands observed in both spectra 2920-2860 cm^{-1} range similarly. However, the peaks have been slightly shifted from 2924 and 2868 cm^{-1} in the B to 2923 and 2861 cm^{-1} in the Sample A. These small red shifts indicate that Sample A exhibits

somewhat weaker van der Waals interactions than the covalent composite. The latter shows stronger chemically-linked interactions between the 5,7-DHF and coated Fe_3O_4 surface that alter the local electronic environment around the C-H bonds, and lead to the subtle change in the electron density of the bonds. Two development peaks assigned to characteristic aromatic C=O and C=C are shown at approximately 1644 cm^{-1} in both spectra, but have different intensities. In the covalent conjugate, the vibrations are sharper, which indicates that the carbonyl group is partially involved in either Sample B bonding or coordination with the iron ions. In Sample A, the same peaks are not as pronounced, suggesting that the aromatic ring and carbonyl groups are functioning primarily as physical adsorbents rather than as chemical bonders. Both spectra demonstrate strong Fe-O vibrations between 509-639 cm^{-1}, confirming the magnetite phase and indicating that Sample B has slightly stronger Fe_3O_4-surface interactions compared to Sample A. Overall, both samples achieved effective drug loading and preserved the magnetite core, but Sample B showed stronger stability and Fe_3O_4 surface interactions.

ISOTOPE RESOLVED (n,p) ACTIVATION IN ZnO NANOPARTICLES CROSS SECTIONS AND INVENTORY MODELING

Izzatova I.V.

Institute of Radiation Problems, Ministry of Science and Education, Azerbaijan
ilahaizzatova@gmail.com

Neutron irradiation offers a scalable method to engineer the physical behavior of nanoparticles by inducing controlled defect populations and phase-stable compositional changes. ZnO nanoparticles are widely used in electronics, optics, and catalysis, where neutron exposures (reactor testing, mixed-field environments) can generate short- to medium-lived copper radionuclides via zinc (n,p) channels. Among these, ^{67}Cu from ^{67}Zn is especially valuable for post-irradiation diagnostics and potential tracer use, but reliable inventory forecasts require isotope-resolved cross-section benchmarks over the fast-neutron range. Using computer simulation outputs with harmonized axes of Incident Energy (MeV) versus Cross Section (barns), we compile the excitation functions for $^{64}Zn(n,p)^{64}Cu$, $^{66}Zn(n,p)^{66}Cu$, $^{67}Zn(n,p)^{67}Cu$, and $^{68}Zn(n,p)^{68}Cu$ relevant to ZnO nanomaterials. All plots are labeled “Incident Energy (MeV)” and “Cross Section (barns),” enabling direct, like-for-like comparison across isotopes.

The curves display threshold-dominated behavior characteristic of (n,p) reactions, with negligible probabilities at thermal–epithermal energies and

rising yields in the fast domain. For ^{64}Zn, the linear-scaled panel spans 0–20 MeV with cross sections reaching the 10^{-1}–$10^{-0.2}$ b envelope (tick marks up to ~$10^{-0.2}$ b), indicating comparatively strong response under fast spectra. ^{68}Zn exhibits a similar 0–20 MeV abscissa but lower peak magnitudes, with ticks up to ~3×10^{-2} b (0.03 b). ^{66}Zn is presented on a logarithmic ordinate from 10^{-6} to 10^{-2} b, reflecting a weaker channel over the same energy window. The focal ^{67}Zn plot employs a broad log scale (10^{-10}–1 b), underscoring generally small (n,p) probabilities that nevertheless rise across the fast region, consistent with an energy threshold and competition with other open channels. In the nanoparticle regime, reduced self-shielding means intra-particle reaction rates closely follow the external spectrum, improving spectrum-to-yield fidelity for ^{67}Cu buildup. Oxygen does not contribute to Cu via (n,p), so copper inventories track zinc isotopes and flux. Proton emission and recoil ranges are comparable to nanoparticle dimensions, implying distinct defect distributions and possible partial loss or redistribution of reaction products – effects that should be included in post-irradiation transport and mass-balance models for ZnO powders and coatings. Across Zn isotopes in ZnO nanoparticles, ^{64}Zn and ^{68}Zn provide higher immediate (on-beam/early cooldown) (n,p) activation, while ^{67}Zn – though lower in cross section – remains strategically important because its product ^{67}Cu sustains a medium-lived post-irradiation source term.

OPTIMAL GRAVITY AND FIELD ORIENTATION CONDITIONS FOR BONE TISSUE HEALING USING MAGNETIC NANOPARTICLES AND SCAFFOLDS

[1*]Yusif-zada K., [2]Gasanova S., [3]Allahyarov E.

[1]Leyla Medical Center, Azerbaijan
[2]Baku State University, Azerbaijan
[3]Case Western Reserve University, Cleveland, Ohio, USA; Recognition Science Institute, Austin, Texas, USA; Institut für Theoretische Physik II: Weiche Materie, HH-Universität Düsseldorf, Germany
yusifzadekr@yahoo.com

Bone fracture healing in microgravity poses critical challenges for extended space missions, where traditional mechanical loading mechanisms are absent. This study proposes an innovative therapeutic approach combining magnetic nanoparticles embedded in porous scaffolds (MNP-PS) with magnetoactive ferrogels (MFG) to accelerate bone regeneration under varying gravity conditions. Such a novel method increases bone regeneration by 2–3 fold over that of the control. The results of such treatment depend not only on the gravity

condition, but also on the direction of the applied magnetic field relative to the gravity and the scaffold alignment in the wound. Thus, the directionality of several factors plays a significant role in enhancing the efficacy of bone tissue engineering (BTE). This may also affect blood circulation and the delivery of nutrients to the healing bone tissue. The current study proposes the use of a set of bone healing protocols under different gravity and applied field conditions, aiming to achieve fast and effective bone healing both in space and on the ground.

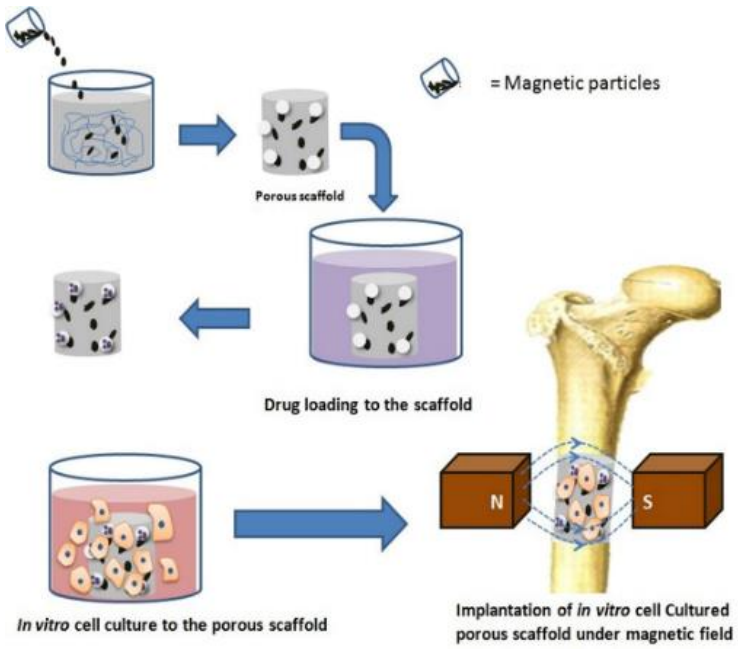

Fig. 1. Schematic illustration of the MNP-PS methodology showing magnetic nanoparticles distributed within a porous scaffold structure under external magnetic field stimulation.

The proposed project specifically elaborates on how the mechanical properties of the regenerated bone and its retention capacity of biological fluids depend on the final composition of Magnetic Nanoparticles in Porous Scaffolds meta-materials, as well as on the mutual orientation of the applied field, gravity, and scaffold alignment.

IMPROVING THE ADHESION OF THERMALLY SPRAYED COATINGS BY OPTIMIZING SPRAYING PARAMETERS

[1]Rakhadilov B.K,[2*]Abizhanovaa I.K., [2]Abdulina S.A., [2]Kengesbekov A.B., [2]Magazov N.M., [2]Kussainov A.E.

[1]PlasmaScience LLP Ust-Kamenogorsk, Kazakhstan

[2]D. Serikbayev East Kazakhstan State Technical University Ust-Kamenogorsk, Kazakhstan

iabizhanova@gmail.com

Thermal barrier coatings (TBCs) are an effective means of providing thermal insulation and protecting components in the hot section of gas turbine engines. Their quality and performance largely depend on the microstructural features and the bonding strength between the bond coat and the substrate. This study aimed to determine the optimal spraying regime that ensures the formation of coatings with superior microstructural integrity and adhesion strength.

The object of the study was gas-thermally sprayed NiCrAlY bond coats deposited onto the nickel-based superalloy Inconel 718, widely used in aerospace gas turbine engines. The substrate surface was sequentially polished (grit size 100–2500) and sandblasted with electrocorundum to enhance coating adhesion. NiCrAlY powder (45–100 μm) was deposited using an SX-80 thermal spray system. The microstructure and phase composition were analyzed using SEM/EDS (Tescan VEGA 4) and X-ray diffraction (X'Pert Pro), while porosity, surface roughness, microhardness, and adhesion strength were evaluated using an Olympus BX53M optical microscope, SSR300+ profilometer, Fischerscope HM2000, and tensile testing in accordance with ASTM C633.

The parameters of atmospheric plasma spraying, such as powder feed rate and arc power, were found to exert a significant influence on the microstructure, phase composition, bond strength, hardness, and porosity of NiCrAlY coatings deposited on Inconel 718 substrates. The optimal condition corresponded to a low powder feed rate and high spraying power, resulting in uniform particle melting and deposition, and consequently, a dense lamellar structure with minimal internal stresses and microcracks. Under milder spraying conditions, oxidation was minimized, with oxygen localized mainly along splat boundaries, preventing the formation of excessive Cr_2O_3 that could deteriorate adhesion.

According to microstructural analysis, the coating produced at 8.4 kW exhibited a low porosity of 0.5 % and virtually no interlamellar defects, outperforming coatings obtained at higher powers. This regime provided the

maximum adhesion strength of 9.67 kN, significantly exceeding that of other samples (1.07 kN). The improvement is attributed to complete particle melting, enhanced inter-splat bonding, uniform particle deposition, and strong interfacial contact with the substrate. The results demonstrate that precise optimization of spraying parameters in accordance with the equipment configuration and powder feed characteristics can yield coatings with superior properties, even when using nonstandard power settings.

THE RAMAN ANALYSIS OF GRAPHENE AND PHOSPHORUS-DOPED GRAPHENE-BASED MATERIALS

Gahramanli L.R., *Isayeva L.R.
Baku State University, Azerbaijan
laleisayeva526@gmail.com

Due to graphene oxide (GO) having a wide range of reactive oxygen functional groups, GO-based materials are considered potential materials for the nano-engineering field. Some properties of GO can be changed by atomic and molecular doping, and recently, doping with heteroatoms has been investigated. The electronegativity of P atoms (2.16) is lower than that of C atoms (2.55). P-doped carbon materials are used for supercapacitors, batteries, field-effect transistors, and catalysts for oxygen reduction reaction.

In the present study, GO materials have been synthesized by the Hummers method. The aim is to determine the structural changes of GO after doping with P. As a P source, KH_2PO_4 is used. 0.1 g GO dissolved in 10 ml DW and 0.1 g KH_2PO_4 in 10 ml DW, then sonicated for 30 minutes separately. After mixing, the final solutions were sonicated for 30 minutes. Then it was influenced by microwave for 4 minutes, cooled to room temperature, and then centrifuged with DW. The final sample was heated with a vacuum oven at 250°C for 5 hours.

In the literature, pure rGO has been observed with D band 1353.2, G band 1586.56, and 2D band 2706.2 cm^{-1} peaks. In our pure rGO sample, the peaks corresponding to D, G, and 2D bands were observed at 1351.17 cm^{-1}, 1576.92 cm^{-1}, and 2695.65 cm^{-1}. The ID/IG ratio for GO was 0.9 and 0.97 for rGO. In the literature, P-rGO has 2 distinct peaks were observed near about 1350 cm^{-1} and 1580 cm^{-1}, which correspond to D and G bands, respectively. In the Raman spectrum of P-doped GO, 2 peaks are observed at wavenumbers of 1351 cm^{-1} (D) and 1574 cm^{-1} (G). The ID/IG ratio is equal to 0.94. As can be seen from the results, the value of the D band remained the same, while the G band slightly

decreased and shifted towards smaller wavenumbers. This is consistent with the trend shown in the literature. When graphene was doped with a small amount of P, the difference did not manifest itself in the D band, but in the G band; it was very small. At the same time, when GO was used as the starting material, the results obtained were consistent with the obtained RGO, as the amount of oxygen in its composition decreased during heating of the samples and transferred to RGO, as a result of which the ID/IG ratio for RGO after reduction increased due to the restoration of sp^2 carbon and the decrease in the average size of sp^2 domains during reduction.

EFFECT OF THERMAL ANNEALING ON THE OPTICAL PROPERTIES OF GO/$FeGaInS_4$/PVA COMPOSITES

***Mamedova C.H., Muradov M.B., Addayeva Z.R.**
Baku State University, Azerbaijan
cinaremamedova71@gmail.com

The role of external influences on polymer composites and their properties lies in the fact that factors such as temperature, chemical environment, and electric and magnetic fields affect the interaction between the polymer matrix and the filler, thereby altering the material's structural stability, electrical and thermal conductivity, mechanical strength, chemical resistance, and long-term operational durability. The thermal annealing process affects the optical properties of polymers by altering their structural ordering, electronic transitions, and degree of crystallinity, leading to the optimization of characteristics such as transparency and light absorption. The mechanism of this process is explained by the increased electronic delocalization resulting from the enhanced mobility of polymer chains under thermal influence, strengthening of π–π interactions, reduction of defects, and rearrangement of energy levels. The reason for selecting two different materials is to combine their complementary properties to improve the composite's mechanical, thermal, and electrical characteristics.

In the synthesis process, to prepare the polymer composite, GO synthesized by the Hummers method and $FeGaInS_4$ synthesized by the Bridgman method were mixed in an aqueous solution of PVA. The mixture was prepared using the solution casting method and dried at room temperature. The dried samples were then thermally annealed at 85 °C under a 0.02 MPa vacuum for 2 and 4 hours, and the effect of thermal annealing and its duration on the optical properties of the polymer composite was analyzed.

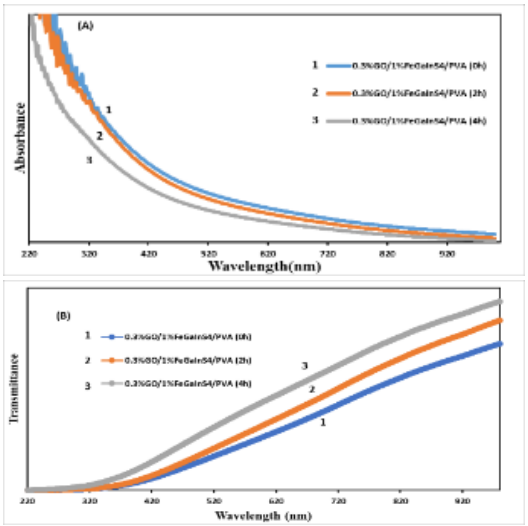

Fig. 1. (a) Absorbance and (b) transmittance spectra of 0.3% GO/1% $FeGaInS_4$/PVA samples: 1 – unannealed (0 h), 2 – annealed for 2 h, and 3 – annealed for 4 h.

The UV spectra of 0.3%GO/1%$FeGaInS_4$/PVS samples - unannealed, and those thermally annealed are shown in Figure 1.

As the duration of thermal annealing increases, the light absorption of the samples decreases, while their transmittance increases. This is associated with the softening of the samples at 85 °C – a temperature close to their glass transition temperature(95-110°C) – and the redistribution of the fillers within the polymer matrix.

THE INFLUENCE OF GAMMA RAYS ON THE STRUCTURE OF Fe_3O_4 NANOPARTICLES

[1]*Hashimov R.F., [2]Abdurahmanova V.A., [1]Aliyeva N.A., [2]Aliyev Y.I.

[1]Institute of Physics, Ministry of Science and Education, Azerbaijan

[2]Azerbaijan State Pedagogical University, Azerbaijan

rovi248@gmail.com

All substances existing in nature are subject to external influences. Among these influences, pressure, temperature, and gamma rays occupy a special place. It has been established that these influences radically change the properties of functional materials. In particular, under the influence of pressure and

temperature, both the structure and physical properties of materials undergo radical changes. It is known that nanoparticles differ from others in their structural features. These materials are more resistant to external influences compared to others. However, under the influence of ionizing radiation, such processes as amorphization and rupture of weak chemical bonds can also occur in nanoparticles.

Iron oxide nanoparticles occupy a special place among functional materials. It is known that materials containing Fe atoms have magnetic properties. Therefore, iron-containing materials are of greater interest. It has been established that Fe_3O_4 nanoparticles also have ferromagnetic properties. The value of the specific magnetic moment is M = 33.4 emu/g. When studying the effect of heavy ions, it was determined that the values of the magnetic moments decrease depending on the radiation dose. This process is explained by a partial violation of the long-range magnetic order under the influence of ionizing radiation. However, magnetic properties are present in iron oxide nanoparticles even when irradiated with $\Phi = 3.83\times10^{14}$ ions/cm^2. Although many physical properties of Fe_3O_4 nanoparticles have been studied, the effect of gamma radiation on them has not been studied. In this work, the crystal structures of iron oxide nanoparticles with a size of d = 20-30 nm irradiated with ionizing gamma radiation at doses up to D = 194 kGy, before and after irradiation, are investigated.

The effect of gamma radiation on the structure of iron oxide nanoparticles was studied using X-ray diffraction. The studies, conducted at doses of D = 0-194 kGy, showed that Fe_3O_4 nanoparticles are a fairly stable system to ionizing radiation. Crystallographic parameters of samples irradiated with different doses were determined. The dose dependence of lattice parameters was established, and the mechanism of change in lattice parameters under irradiation was determined. It was shown that the main changes in parameters are observed at doses of D = 0-48.5 kGy. A stable state was already observed in the dose range of D = 145.5-194 kGy. The results obtained in the study of the effect of gamma rays on the structure of Fe3O4 nanoparticles with a size of d = 20-30 nm show that this system is quite stable to external influences. These results further increase the possibilities of using iron oxide nanoparticles.

This work was supported by a grant from the "International Innovation Center for Nanotechnology of the CIS".

INFLUENCE OF MATERIAL SELECTION ON STRESS, DEFORMATION AND MASS IN AUTOMOTIVE REAR WINGS: A FEM-BASED COMPARATIVE ANALYSIS

Dedeoğlu O.
Concept Design Engineer, Karsan Inc, Turkey
orhandedeoglu16@gmail.com

This inquiry examined how the choice of material influences the structural behavior of a car's rear wing when it is exposed to the forces of aerodynamics. The study aimed to use the Finite Element Method (FEM) to investigate the different materials including Al 6061-T6 aluminum alloy, Ti-6Al-4V titanium alloy, and C9021 GV120 high-strength polymer composite to compare the structural performance of these materials by means of stress distribution, total deformation, safety factor, and overall weight, which are interrelated, and to open up a pathway for engineering-driven material choice in design decisions.

The loading conditions were derived from CFD-based aerodynamic coefficients (C_d = 0.4865, $C_l \approx -0.0013$ at a reference speed of 100 km/h). The aerodynamic force calculations were introduced for seven various speeds from 50 to 400 km/h, and the corresponding loading case (F_R = 1482 N), which was the highest, was determined and used for the analysis. The ANSYS Workbench Structural software was employed in the structural simulations. The common elements of the mesh setup were mostly second-order hexahedral (Hex20), and the global element size varied from 20 mm in the panel regions to 5 mm in the areas of high stress gradients, such as mounting feet and chassis joints.

The results that were obtained demonstrate the vital role of material properties in the whole process of the structural response. The titanium alloy, with its modulus of elasticity ($E \approx 110$ GPa), had an insignificant deformation (i.e., ~1 mm) and its safety factor that went beyond 14, which means that it had an excess of stiffness. As a consequence of this, the material was free to have a significant mass of 54 kg, and thus, its cost of production was very limited. The aluminium alloy was the first to indicate the most balanced performance, though it had a deformation of about 2.8 mm, a safety factor of about 9, and a weight of 33 kg, with respect to both structural integrity and manufacturability. However, the C9021 GV120 polymer composite showed remarkable results in weight loss and its a weight of 19 kg and a formation of 9 mm too much, which revealed that the composite was ineffective for keeping aerodynamic surface integrity.

In conclusion, the analyses reveal that the Al 6061-T6 aluminum alloy offers the most favourable balance between strength, weight efficiency, and cost under

high-speed aerodynamic conditions. While titanium alloys are advantageous in specialized high-performance applications, polymer composites are better suited for low-cost prototyping or secondary aerodynamic components. This study establishes a numerically grounded and engineering-informed decision-making basis for material-based structural optimisation in automotive aerodynamic appendages, contributing to the scientific foundation of design verification and material selection processes.

OPTIMIZING THE PERFORMANCE OF Au/(CdTe:PVA)/n-Si JUNCTIONS: INFLUENCE OF CdTe DOPING LEVELS

***Baxtiyarlı E.R., Afandiyeva I.M.**
Baku State University, Azerbaijan
elvinb18104@sabah.edu.az

In this present work, Au/(CdTe: PVA)/n-Si (MPS) structures were fabricated and characterized to study the effects of varying CdTe concentrations (3%, 5%, and 7%) on the electrical and dielectric properties of the junction. The fabrication of the Au/(CdTe:PVA)/n-Si (MPS) structures involved substrate cleaning, deposition of an ohmic contact, spin-coating for the CdTe: PVA interlayer, and thermal deposition of the Au rectifier contact. The C-V, G/w-V, C^{-2}-V, R_s-V, and N_{ss}-V measurements were performed using an HP4192-A impedance analyzer at room temperature and 1 MHz frequency. Series resistance (Rs) was lowest for the 3% CdTe sample, indicating better conductivity and reduced resistive losses, while the 7% CdTe exhibited the highest R_s, suggesting increased resistive losses likely due to defects or scattering at higher CdTe concentrations. The dielectric constant (ε') was highest for the 3% CdTe sample, indicating better charge storage capacity, while the 7% CdTe showed a lower dielectric response due to increased defects.

As shown Fig.1, the 3% CdTe: PVA sample exhibits the lowest capacitance and conductance in the reverse bias, indicating a more stable dielectric response and lower charge transport. The 5% CdTe: PVA sample shows higher capacitance and conductance, suggesting improved dielectric and charge transport properties, making it a balanced choice for devices. The 7% CdTe: PVA sample demonstrates the highest conductance but reduced capacitance, highlighting the trade-off between charge storage and carrier mobility at higher doping concentrations. These results show the significant impact of CdTe concentration on the electrical, dielectric, and interface properties of the Au/(CdTe:

PVA)/n-Si structures. The 3% CdTe sample offers optimal performance with lower series resistance, higher dielectric constant, and fewer interface states, ideal for high-efficiency charge storage.

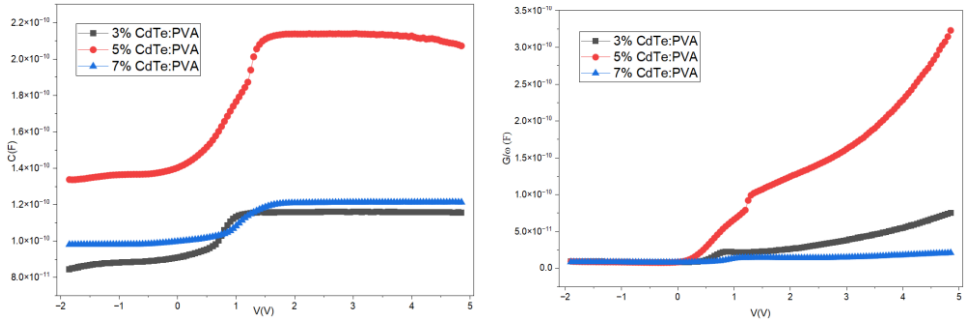

Fig. 1. The C-V and G/ω-V plot of Au/n-Si with 3%,5%,7% CdTe:PVA interfacial layers at 1 MHz

DIELECTRIC PROPERTIES AND AC-CONDUCTIVITY OF Re/n-GaAs SCHOTTKY DIODES IN THE FREQUENCY RANGE OF 1 kHz - 5 MHz

***Afandiyeva I.M., Bakhtiyarli E.R., Akhundov C.G.**
Baku State University, Azerbaijan
elvinb18104@sabah.edu.az

The objective of this study is to investigate the dielectric parameters and ac-conductivity of a Re/n-GaAs Schottky diode fabricated using the PLD method. The choice of contact structure composition is driven by the unique properties of rhenium (Re) and the high electron mobility of GaAs. In addition, Schottky diodes of similar composition have been little studied. The deposition of rectifying contacts, with a thickness between 200 and 250 nm, was carried out on the front surface of an n-type GaAs wafer using the Pulsed Laser Deposition (PLD) method. Rhenium (Re), sourced from Good Fellow with a purity of 99.99%, served as the target material in this process. The substrate and target were placed 40 mm apart during deposition. To ensure a more uniform contact area, both the Rhenium target and the n-GaAs wafer were rotated at a speed of 10-15 revolutions per minute.

In the presented work, based on measurements using the impedance method, the capacitance-voltage ($C-V$) and conductance-voltage (G/ω -V) characteristics in the wide frequency range of 10 kHz – 5 MHz and bias voltage

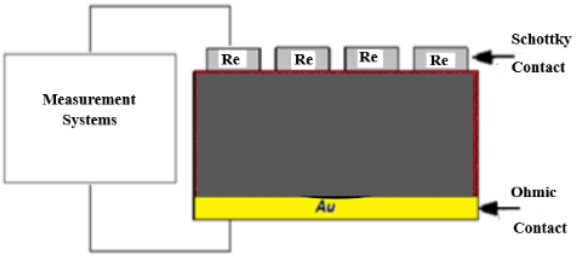

Fig. 1. Cross-sectional view of Re/n-GaAs (MS) Schottky diodes/structures.

from -2 to 5 V, room temperature (T = 300 K), the real ε' and imaginary ε'' parts of the permittivity, the loss tangent (tanδ), and the ac electrical conductivity (σ_{ac}) were calculated. In the frequency range under study, ε' and ε'' change from 2.3E+2 to 1.5E-1 and 3.6E+2 to 3.6E-2, respectively. Large values of ε' indicate a reformation of the covalent bond in the structure. The dependence of the dielectric parameters on the frequency of the test signal reveals the important role of surface states. The tanδ-ln(f) dependence shows a broad peak in the frequency range (70 kHz-2 MHz), the height of which decreases with increasing bias voltage. The frequency dependence of the dielectric loss tangent (tanδ) indicates a complex connection of the equivalent circuit elements. The ac-conductivity (σ_{ac}) decreases non-uniformly with increasing frequency. The change, like the dependence, is due to the predominance of the role of various conductivity mechanisms. The real and imaginary parts of the electric modulus (M' and M″) of Re/n-GaAs SBDs were investigated in detail. By using the of electric modulus formalism (M' and M″), the relaxation process at 1 MHz was obtained.

IN-SITU ABSORPTION SPECTROSCOPIC INVESTIGATION OF AGGREGATION AND CRYSTALLIZATION KINETICS IN PM6: Y6 and PM6:L8-BO ORGANIC PHOTOVOLTAIC SYSTEMS

***Kuvondikov V.O., Urazkulova D.M.**

Institute of Ion Plasma and Laser Technologies, Uzbekistan Academy of Sciences, Tashkent, Uzbekistan
kuvondikov@iplt.uz

Non-fullerene acceptor (NFA)-based organic photovoltaics (OPVs) have emerged as a revolutionary class of devices, with power conversion efficiencies (PCEs) surpassing 18%. Among these, the polymer PM6 donor and the Y6-family acceptors (Y6, Y6-BO, L8-BO) represent one of the most effective material pairings due to their complementary absorption spectra, matched energy levels,

and tunable aggregation tendencies. However, the precise control of aggregation and crystallization kinetics during film formation remains a decisive factor in achieving optimal bulk heterojunction (BHJ) morphology. This study focuses on elucidating these kinetics using in-situ UV–Vis absorption spectroscopy, offering real-time insights into how the PM6:Y6 and PM6:L8-BO blends evolve from solution to solid-state films (shown in the figure).

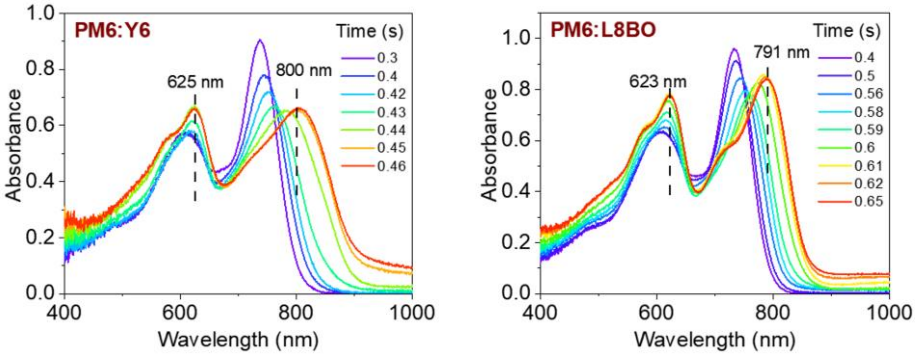

Fig. 1.

For the PM6:Y6 system, the absorption spectrum shows a broad, featureless band spanning 600–850 nm, indicating a predominantly disordered solution state. As the solvent rapidly evaporates, a gradual emergence of the Y6 π–π* transition at ~830 nm is observed, signifying the formation of weak aggregates. In contrast, the PM6:L8-BO solution exhibits sharper absorption features even before full solvent removal, indicating the presence of pre-aggregated supramolecular networks. L8-BO, with its extended alkoxy side chains and reduced solubility, promotes stronger π–π interactions. Both systems exhibit a progressive red-shift in the principal absorption peak (λ_{max}) during spin-coating, directly reflecting enhanced intermolecular ordering and π–π stacking. The larger and faster red-shift in PM6:L8-BO indicates rapid structural reorganization toward a planar π–π stacked morphology. The rate constant for aggregation (k_{agg}), derived from exponential fits of absorbance intensity at λ_{max}, is approximately 0.12 s^{-1} for PM6:Y6 and 0.45 s^{-1} for PM6:L8-BO, confirming a ~4× faster aggregation kinetics in the latter.

This comprehensive in-situ spectroscopic study provides direct evidence linking aggregation kinetics, crystallization behavior, and photovoltaic performance in PM6:Y6 and PM6:L8-BO systems. The PM6:L8-BO blend exhibits faster aggregation, tighter molecular packing, and enhanced crystallinity, leading to superior charge transport and higher device efficiency. The PM6:Y6 blend, though effective, suffers from slower aggregation and less uniform morphology, resulting in reduced crystallinity.

REINVENTING SPR BIOSENSORS WITH 2D MATERIALS: FROM OPTICAL MODELING TO HIGH-THROUGHPUT DIAGNOSTICS

Bellucci S.

[1]National Institute of Materials Physics, Romania; R.A.I.T.88 S.R.L., Roma, Italy
belucci@lnf.inf.it

Rapid, label-free biosensing relies on optical architectures that combine strong plasmonic confinement with highly selective molecular interfaces. We numerically engineered Kretschmann-type SPR biosensors that integrate a noble-metal film, a Si_3N_4 spacer, few-layer 2D materials, and an ultrathin ssDNA receptor layer. Using the transfer-matrix method, we quantified angle shift, refractive-index sensitivity, FWHM, detection accuracy, quality factor, figure of merit, and limit of detection across clinically relevant conditions.

For malaria diagnostics, incorporating Si_3N_4 and monolayer MoS_2 concentrated the evanescent field and enabled clear discrimination of ring, trophozoite, and schizont stages via RBC refractive-index variations. The fully functionalized stack reached ~319°/RIU in early-stage detection and maintained >240°/RIU for later stages while keeping FWHM growth controlled. For viral nucleic-acid sensing, a bilayer-MoS_2 system (Ag 45 nm, Si_3N_4 13 nm, ssDNA 5 nm) achieved 375.01°/RIU and a quality factor near 38 at low target concentration. A graphene/Si_3N_4 variant traded peak sensitivity for an enhanced figure of merit across a wider dynamic range, favoring robust and stable readout. A $MoSe_2$/Si_3N_4 architecture optimized for nanomolar regimes provided 197.70°/RIU at 100 nM, with detection accuracy $\approx 5.24\times10^{-2}$ and a limit of detection $\approx 2.53\times10^{-5}$.

Across all use-cases, metal/spacer thickness, 2D material type and layer count, and receptor-layer thickness define the sensitivity–resolution–attenuation balance. These results highlight actionable design knobs for 2D-material-assisted plasmonic sensing and support the development of compact, selective platforms compatible with scalable fabrication and poised for near-term experimental realization.

Acknowledgement. This work is supported in part by a project funded by Romania's National Recovery a Resilience Plan (PNRR), component C9. Support for the private sector, research, development and innovation "I8. Development of a program to attract highly specialised human resources from abroad in research, development and innovation activities", entitled "Composite materials for the applications in the water management field", ID - 11/ 26.07.2023, contract number 760270/26.03.2024. This work is also supported in part by a project funded by the EU-funded consortium Water4All, with title "Developing innovative solution for mitigation of drought effects (DIME)", 776681. This grant was awarded under the European Union's Horizon 2020 research and innovation program

THE EFFECT OF POLYETHYLENE GLYCOL ON THE ELECTRICAL CONDUCTIVITY OF AQUEOUS SOLUTIONS OF VARIOUS ELECTROLYTES

Rasulzada G.X., *Hesenova X.T.
Baku State University, Azerbaijan
xavarhasanova@bsu.edu.az

Polyethylene glycol (PEG) is a polyether compound that is widely used in chemistry, biology, medicine, and material science. This polymer is formed by the repetition of the ethylene oxide units. The main function of PEG depends on its application, but in general, its primary roles are to act as a water-soluble carrier, binder, and moisturizer.

Studying the effect of PEG on the conductivity of aqueous electrolyte solutions is important for both fundamental science and practical applications. It helps understand ion mobility, solution viscosity, and the electrostatic properties of the system. İn this study, various electrolytes were selected and changes in electrical conductivity were investigated when they were mixed with different concentrations of PEG.

During the study, it was found that at high polymer concentrations, the electrical conductivity of the electrolyte decreases due to an increase in viscosity. However, at very low concentrations (below 1%), the electrical conductivity of the system increases behavior is explained by the fact that in very dilute polyethylene glycol solutions, water molecules in the solution are captured by the polymer, which reduces the hydration layer around the ions and consequently increases their mobility. This effect is attributed to hydrogen bonding interactions between PEG molecules and water, which influence ion hydration.

The addition of PEG increases solution viscosity, reducing ion mobility and conductivity. PEG molecules form complexes with water, decreasing the free ion ability, and conductivity decreases. Divalent and trivalent ions interact more strongly, with conductivity decreasing more significantly.

In conclusion, the results of the observations show that the addition of polyethylene glycol to aqueous electrolyte solutions generally decreases their electrical conductivity, and the effect depends on PEG concentration, molecular weight, and ion type. Temperature is also found to play a significant role in determining the conductivity behavior of the solutions.

IMPACT OF GAMMA IRRADIATION ON THE STRUCTURAL ORDERING AND SURFACE EVOLUTION OF $Cd_{1-x}Fe_xS$ THIN FILMS

[1]Mehrabova M.A., [2*]Mammadli S.N.

[1]Azerbaijan Technical University, Azerbaijan

[2]Institute of Radiation Problems, Ministry of Science and Education, Azerbaijan

sona.huseynli@mail.ru

Solid solutions of $Cd_{1-x}Fe_xS$ (x = 0.03) were synthesized, and the corresponding thin films were fabricated using the molecular beam condensation (MBC) method under high vacuum conditions. The present study investigates the effects of γ-irradiation on the crystalline structure, surface morphology, and compositional uniformity of $Cd_{1-x}Fe_xS$ thin films. Structural characterization using X-ray diffraction (XRD) revealed that the as-deposited films exhibit a polycrystalline nature with prominent diffraction peaks corresponding to the (100), (002), and (101) planes. Exposure to γ-radiation from a ^{60}Co source at doses up to 100 kGy resulted in a notable enhancement of the (101) plane intensity, indicating improved crystallinity and preferred orientation. After 100 kGy, deterioration of properties, crystallinity, and preferred orientation is observed. This radiation-induced reorientation is attributed to lattice defect annealing and atomic rearrangement processes, which contribute to increased grain size and reduced internal strain.

The morphological evolution observed through scanning electron microscopy (SEM) revealed smoother, more compact, and homogeneous surfaces in γ-irradiated samples compared to non-irradiated ones. This transformation suggests that controlled radiation exposure facilitates surface recrystallization and enhances atomic diffusion within the thin-film lattice. Energy-dispersive X-ray spectroscopy (EDX) confirmed a nearly stoichiometric Cd: Fe:S ratio, verifying that the incorporation of Fe ions was uniform and did not lead to impurity phase formation. These results collectively demonstrate that γ-irradiation not only modifies the crystalline order but also stabilizes the microstructure, improving the film's overall structural and surface integrity. Such improvements directly influence the optical and electrical performance of $Cd_{1-x}Fe_xS$ thin films, making them promising candidates for next-generation optoelectronic devices.

Furthermore, the substrate temperature was found to significantly influence the crystallographic phase and grain alignment of the films. Films deposited at T_sub = 470 K displayed polycrystalline characteristics with randomly oriented grains, while those grown at T_sub = 670 K exhibited a monocrystalline structure with enhanced textural uniformity. The combination of optimal

Fe incorporation, γ-irradiation treatment, and substrate temperature control yielded films with superior crystallinity, larger grains, and improved surface morphology. Overall, the study confirms that $Cd_{1-x}Fe_xS$ heterostructures processed under controlled radiation conditions possess enhanced stability and structural coherence, highlighting their potential use in radiation-tolerant solar cell and optoelectronic applications.

TRANSITION-METAL PENTACHALCOGENIDES MATERIAL CLASS AS TOPOLOGICAL INSULATORS: WEYL POINTS, ELECTRONIC STRUCTURE, AND VAN HOVE SINGULARITIES

[1]Koc H., [2,3*]Mamedov A.M., [2]Ozbay E.

[1]Siirt University, Siirt, Turkey
[2]Bilkent University, Turkey;
[3]Baku State University, Azerbaijan
mamedov@bilkent.edu.tr

A large number of binary chalcogenides containing transition metals exhibit various structures and interesting physical properties, which have potential applications in fields such as magnetism, second-order nonlinear optics, and voltage-dependent effects. As for the group IV elements Ti, Zr, and Hf, their chalcogenides have been studied extensively, exhibiting many promising properties, such as superconductivity, cathode applications in solid oxide fuel cells, Pentachalcogenides AX5, and battery electrode materials. The Transition-Metal (A=Zr, Hf; X=Te, Se, and S) are similar to the well-known 3D topological insulators Bi_2Se_3 and Bi_2Te_3. In recent years, due to the outstanding performance and exotic properties of AX5 (including anomalous Hall effect, chiral magnetic effect, and large Zeeman splitting), scientists have turned their attention to the unusual properties of AX5.

In the present investigation, the electronic structure, charge density, optical properties, density of states (partial and total), and elastic parameters of ZrTe(S, Se)5 were calculated using ab initio DFT with GGA. The real and imaginary parts of dielectric functions and, hence, the optical functions such as energy-loss function, the effective number of valence electrons, and the effective optical dielectric constant were calculated, too. It has been observed that the calculated lattice parameter values are in agreement with the values in the literature. The second-order elastic constants were calculated, and the other related quantities have also been estimated. The electronic band structures and

partial density of states for ZrS5, ZrSe5, and ZrTe5 are examined, revealing that all the investigated compounds are narrow-band semiconductors or semimetals. Also, the electron energy loss function (ELS) spectra and charge density of ZrX5 are calculated and interpreted.

Finally, we obtain four types of Van Hove singularities, depending on the sign of Ɛi (i= z, y, and z, Ɛi equal to +1 or -1). The critical points are called: M0 (all Ɛi coefficients of the quadratic expansion are positive, minimum), M1 (two Ɛi coefficients of the quadratic expansion are positive and one negative, saddle point), M2 (two Ɛi coefficients of the quadratic expansion are negative and one positive, saddle point), and M3 (all Ɛi coefficients of the quadratic expansion are negative).

VAN HOVE SINGULARITY AND FERROELECTRICS-BASED WEYL METAMATERIALS

[1]Ozer Z., [2,3*]Mamedov A.M., [2]Ozbay E.

[1]Mersin University, Turkey
[2]Bilkent University, Turkey;
[3]Baku State University, Azerbaijan
mamedov@bilkent.edu.tr

Weyl semimetals are materials in which electrons exhibit linear dispersion in all directions, while being doubly degenerate at a single point, known as a Weyl point, located near the Fermi surface in 3D momentum space. Since the Weyl point or Weyl cone in Weyl semimetals represents a special dispersion of electrons moving in periodic potentials, the question naturally arises as to whether a similar dispersion or the Weyl point for classical waves propagating in artificial periodic structures exists. The study of Weyl points in electronic systems has inspired much recent research in classical systems such as photonic and acoustic lattices. We construct a single-phase three-dimensional structure, an analog of the honeycomb lattice, and predict the existence of Weyl points with opposite topological charges (±1), and the associated gapless topologically protected surface states. Following the developments of Weyl phononic crystals with Weyl points for acoustic waves, we report the theoretical investigation of Weyl points in ferroelectric-based 3D acoustic metamaterials. This study presented a fully continuous, load-bearing, elastic metamaterial capable of indirectionally propagating and topologically protected surface states. The design of the 3D unit cell, inspired by sandwich composites, consisted of a layered prismatic lattice with different cross-sections in which the layers were spaced by solid cylindrical elements and by slanted circular beams connecting

consecutive faces of the prismatic unit cell. The analysis of the lattice dynamics highlighted the existence of Weyl points following the breaking of the z-mirror symmetry and the P-symmetry of the lattice. To gain insight into the mechanism leading to the formation of these degenerate points, we evaluated the topological invariants using ab-initio calculations. This study may serve as a basis for developing composite-like structures with advanced elastic waveguiding capabilities for various applications.

EFFECT OF GAMMA IRRADIATION ON THE OPTICAL PROPERTIES OF GO/PVA/Ag-BASED NANOCOMPOSITES

*Baghirov M.B., Muradov M.B.
Baku State University, Azerbaijan
bmbaghir@gmail.com

In recent years, research on graphene oxide (GO)-based nanocomposites has gained significant attention. Due to its semiconducting properties, GO serves as an effective filler material; furthermore, incorporating metallic nanostructures into such systems expands their potential for advanced functional applications. One notable example is the GO/PVA/Ag-based nanocomposite, the preparation and investigation of which are crucial for understanding its physical and optical properties. These materials exhibit promising potential for use in optoelectronic devices.

In this study, GO was synthesized using a modified Hummers method, while silver nanowires (AgNWs) were prepared via a modified polyol process. The GO/PVA/AgNWs nanocomposites were fabricated through a solution casting technique and subsequently dried at room temperature under ambient conditions. The prepared nanocomposites were exposed to gamma irradiation at doses of 250, 500, and 1500 kGy, using a ^{60}Co source.

To investigate the influence of radiation on the optical properties of the GO/PVA/AgNWs nanocomposites, UV–Vis absorption spectra were recorded for all samples. Figure 1 presents the absorption spectra of the nanocomposites. Figure 1a corresponds to the pristine (non-irradiated) sample, which shows two characteristic plasmon peaks of AgNWs at wavelengths of 357 nm and 394 nm. Figures 1b, 1c, and 1d illustrate the spectra of samples irradiated at 250, 500, and 1500 kGy, respectively. As observed, increasing the radiation dose results in the emergence of a new peak around 290 nm, which is attributed to the formation of C=O bonds induced by radiation exposure. The optical band gap of

the nanocomposites was determined using the Tauc method. It was found that the band gap decreased with increasing radiation dose. Specifically, the pristine sample exhibited a band gap of 5.07 eV, which reduced to 4.98 eV, 4.86 eV, and 3.87 eV for the 250, 500, and 1500 kGy irradiated samples, respectively. This reduction in band gap is attributed to an increase in the number of radiation-induced defects and dislocations. As the irradiation dose increased, the concentration of these defects rose significantly, thereby altering the electronic structure of the nanocomposites.

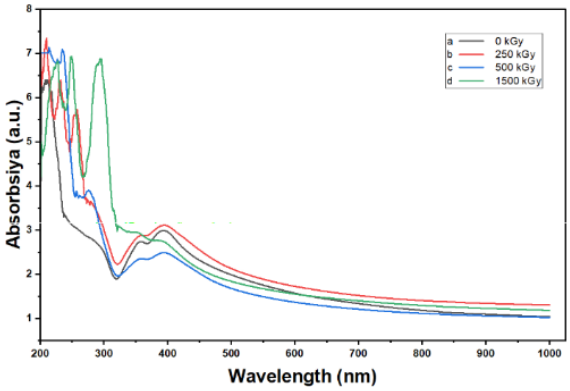

Fig. 1. UV-Vis spectrum of GO/PVA/AgNWs depends on gamma irradiation

COMPARATIVE ANALYSIS OF THE MOLECULAR STRUCTURE OF Ch@Fe_3O_4/GO-BASED NANODRUG DELIVERY SYSTEMS

***Aghayeva Sh.M., Karimova A.H., Mehdiyeva A.R.**
Baku State University, Azerbaijan
shehane999@gmail.com

In recent years, the design and optimization of nanostructured drug delivery systems (DDS) have gained tremendous attention in biomedical and pharmaceutical research, primarily due to the limitations of conventional cancer therapies, such as poor drug solubility, non-specific targeting, and systemic toxicity. Combining Fe_3O_4 nanoparticles and graphene oxide (GO), has emerged as promising multifunctional platform for controlled and targeted drug delivery because of their high surface area, tunable surface chemistry, and excellent magnetic responsiveness. Among various surface functionalization approaches, chitosan (Ch) coating is especially advantageous owing to its biocompatibility, biodegradability, and the presence of reactive amino and hydroxyl groups that enhance drug adsorption and conjugation efficiency.

In this study, a comparative molecular structural analysis was performed

between Ch coated GO-magnetite drug delivery system (Ch@Fe_3O_4/GO) and its drug-loaded form (Ch@Fe_3O_4/GO/Chrysin) using Fourier Transform Infrared (FTIR) spectroscopy. These systems were synthesized via a co-precipitation method followed by surface modification with Ch and GO to enhance their structural integrity and drug loading capacity. The successful coating of Ch and GO was confirmed by the characteristic FTIR absorption bands observed at ~3440 cm^{-1} (O-H and N-H stretching), ~1640 cm^{-1} (C=O and N-H bending), and 1068, 1150 cm^{-1} (C-O-C stretching), while the distinct vibrations around 1620 cm^{-1} corresponded to the C=O and C=C bonds of GO sheets, confirming their integration within the nanocomposite matrix.

Upon chrysin incorporation, new peaks appeared at 1023, 956, 843, and 623 cm^{-1}, attributed to C-O/C-O-C stretching, aromatic C-H vibrations, and Fe-O stretching modes. These spectral shifts and new bands provide clear evidence of strong molecular interactions between chrysin and the Ch@Fe_3O_4/GO carrier through hydrogen bonding and π-π stacking, indicating successful drug loading without compromising the crystalline stability of the Fe_3O_4 magnetic core. Such structural interactions play a crucial role in improving drug loading efficiency and ensuring sustained release behavior, which are key parameters for the effective design of nanocarrier systems.

Overall, the FTIR results demonstrate that the Ch@Fe_3O_4/GO/Chrysin nanosystem exhibits favorable molecular compatibility, chemical stability, and potential responsiveness to physiological conditions. These findings highlight the importance of molecular-level characterization in understanding drug-carrier interactions and underscore the potential of this hybrid nanostructure as a stable, biocompatible, and magnetically responsive drug delivery system for targeted cancer therapy applications.

INFLUENCE OF COOLING MODE ON THE EMISSION SPECTRUM OF HIPS NANOCOMPOSITES

***Aliyeva G.Y., Pashayev B.G., Shirinova H.A., Hasanova M.R.**

Baku State University, Azerbaijan
eliyeva.qenire.0403@gmail.com

The study of the luminescent properties of HIPS-based nanocomposites has gained significant scientific and practical importance in recent years for the development of functional optoelectronic materials. By varying the cooling regime, it is possible to control the internal structure and energy transitions of the

nanocomposites, which enables purposeful tuning of their emission characteristics. Such investigations provide an important foundation for improving polymer-based light-emitting materials, sensors, and energy conversion systems.

In this study, the luminescence properties of HIPS-Silica nanocomposites were investigated. Experimental results have demonstrated that the observed maxima in the studied system indeed correspond to luminescence peaks. For this purpose, excitation light with a wavelength of 370 nm was directed onto the samples, and a luminescence maximum centered at 480 nm was recorded. To obtain more precise results, excitation at 375 nm was applied, which led to the observation of a maximum at 486 nm. For silica, the emission signals observed within the energy range of 2.2–3.1 eV were found to be associated with defect structures of silicon oxide. In particular, within oxygen-deficient centers – such as neutral oxygen vacancies (Si–Si) or in doubly coordinated defect structures (Si–O–Si–O–Si) – the recombination of self-trapped excitons (electron–hole pairs) occurs, resulting in radiative emission within the mentioned energy range.

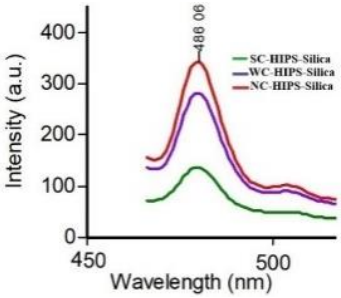

Fig. 1. İnfluence of cooling mode on FL spectrum of HİPS-silica nanocomposite

It has been established that the intensity of the luminescence signal depends on the crystallization regime selected during the formation of the nanocomposite.

THERMAL PROPERTIES OF GeO_2 NANOPARTICLES

*Mammadova N.J., Mammadov H.M., Jafarov M.A.
Baku State University, Azerbaijan
nigarmdva2002@gmail.com

The wide range of industrial and scientific applications of germanium dioxide (GeO_2) nanoparticles (NPs) makes them an interesting research object. The development of effective synthesis methods that can control their structure

and properties, and the need to optimize reaction parameters, necessitate the development and comprehensive study of research in this direction. Understanding the thermodynamic behavior of GeO_2 NPs is essential for optimizing their synthesis and evaluating their stability under varying synthesis temperature conditions. There are various methods for obtaining GeO_2 NPs. Among these methods, fluoride technology has particular importance because it allows obtaining NPs with a higher degree of purity, and it is possible to control the size of the nanoparticles by changing the technological regime.

The basis of this technology is the production of highly pure amorphous GeO_2 by reacting ammonium fluoride (bifluoride) with GeO_2-containing raw materials to obtain ammonium hexafluorogermanium, purifying it by sublimation, and precipitating it with ammonia solution. It is known that the physicochemical properties of amorphous GeO_2 are affected by the raw material, process temperature, pH of the reaction medium, ratio of reagents, addition of coagulant, washing and drying modes, etc.

To obtain GeO_2, the fluoride salt is mixed with a raw material containing 45 % GeO_2, water vapor is evaporated when heated at 100°C for 1 hour, ammonia gas is evaporated when heated at 130°C for 1 hour, hexafluorogermanate is formed when heated at 220°C for 2 hours, then the product is cooled and placed in a sublimator. At 360°C, hexafluorogermanate sublimes, passes to a desublimator, and is collected in a container at 120 °C. We take the collected substance and add 20 % ammonia solution to it. The reaction mechanism for obtaining GeO_2 is as in Equation 1.

$$(NH_4)_2GeF_6 + 4NH_4OH = GeO_2 + 6NH_4F + 2H_2O \qquad \text{(Eq.1)}$$

Final solution washed with distilled water and GeO_2 separates, after drying, a pure white powder is obtained. The obtained GeO_2 was subjected to X-ray structural analysis, its purity was checked, and it was studied using the differential scanning calorimetry (DSC) method. The conducted studies confirmed the correctness of the technological regime of obtaining the technology of GeO_2.

Thus, using simple technology, we obtained 60-80 nm NPs with a high purity (99.99 %) from the raw material.

PHYSICAL METHODS OF INFLUENCING THE CATALYST SURFACE, CHANGING ITS CATALYTIC ACTIVITY USING THE EXAMPLE OF THE METHYL ALCOHOL SYNTHESIS REACTION

***Khimach N.Y., Baran M.M., Kamenskyh D.S., Tkachenko T.V., Yevdokymenko V.O.**

V.P. Kukhar Institute of Bioorganic Chemistry and Petrochemistry of the National Academy of Sciences of Ukraine, Ukraine
vay.77@ukr.net

The relevance of the work is related to the current global situation, namely, the improvement of the process of direct hydrogenation of carbon dioxide to methanol on Cu/ZnO-based catalysts. Without a doubt, copper-based catalysts are still one of the most promising for the direct hydrogenation of CO_2 to methanol in industry. However, they need to be improved to overcome a number of technical problems.

To achieve the set goal, heterogeneous catalysis methods were used, and for analytical control of the conversion process, gas chromatography, chemical and elemental analysis methods were used, and to determine the change in the state of the catalyst surface, low-temperature nitrogen adsorption-desorption methods, FTIR-ATR, XRF, wide-angle X-ray diffractometry, SEM, thermogravimetric analysis, and atomic force microscopy were used.

In accordance with the task, a complete comparative physicochemical analysis of the industrial catalyst before and after the process of hydrogenation of carbon oxides was performed. During the research, it was found that the increase in the activity of the SNM-U catalyst is influenced by such structural and morphological characteristics as the average size of the copper crystallite, the morphology of the catalyst surface, its specific surface area, and thermogravimetric characteristics.

A series of comparative studies of the catalytic characteristics of the industrial granular catalyst SNM-U was conducted using a working gas mixture (molar ratio $CO:H_2:CO_2$ = 1.0:2.92:0.24) of carbon oxides with/without the use of in situ vibration-acoustic oscillations. The results of the studies showed that the use of in situ vibration-acoustic oscillations at a frequency of 30 Hz in the process of hydrogenation of carbon oxides contributes to an increase in the productivity of the SNM-U catalyst for methanol by 2.6 times with an increase in selectivity by 16%. Carrying out the hydrogenation process under conditions of in situ vibration-acoustic oscillations showed that this is one of the promising factors influencing the increase or maintenance of the activity of existing industrial catalysts

precisely during the process.

It was found that vibrational acoustic oscillations activate the catalyst surface by creating anisotropic deformations, namely changes in the electronic properties of the metal catalyst, such as the d-level center of the materials, which in turn facilitates the dissociation of hydrogen atoms on the copper surface and their transfer to the zinc oxide surface. Thus, by adjusting the frequency and shape of vibrational acoustic oscillations, it is possible to control hydrogen spillover, lowering the energy barriers of the limiting stages of the hydrogenation reactions of carbon oxides to methanol.

PHOTOELECTRIC AND RADIATION-DEFECT INTERACTION MECHANISMS IN Yb-DOPED GaS MONOCRYSTALS UNDER GAMMA IRRADIATION

[1*]Mammadova N.P., [2,3]Madatov R.S., [2]Tagiev T.B., [2]Mamishova R.M., [1,2]Khaligzadeh A.Sh.

[1]Baku State University, Azerbaijan
[2]Institute of Radiation Problems, Ministry of Science and Education, Azerbaijan
[3]National Aviation Academy, Department of Applied and General Physics, Azerbaijan
nerminmemmedova955@gmail.com

Because of their high photosensitivity and anisotropic characteristics, layered gallium sulfide (GaS) crystals are interesting materials for optoelectronic applications. However, in ionising settings, structural and radiation-induced flaws can have considerable effects on their performance. It is possible to alter defect structures and improve radiation tolerance by doping with rare-earth elements such as ytterbium (Yb). In this study, we determine the features of the interaction mechanisms between radiation-induced defects, impurities, and structural defects in γ-irradiated GaS(Yb) monocrystals and how these interactions modify the radiation resistance of the crystal. Improving the stability and performance of layered semi-conductors in radiation environments can be achieved by understanding the defect dynamics brought on by Yb-doping and γ-irradiation.

At doses of D = 20, 50, 100, and 200 krad, layered GaS and GaS(Yb) (0.1 at%) monocrystals were exposed to γ-quanta radiation. Under an applied voltage of U = 50 V, photoelectric characteristics were investigated at room temperature (T = 300 K) and low temperature (T = 110 K).

In order to determine the impact of impurity-radiation defect formation on photocurrent intensity and to examine variations in long-wave and short-wave boundaries, the spectral distribution of photocurrent was investigated. To determine the thermal extinction and recombination behaviour of charge carriers, data were analysed before and after irradiation.

The photocurrent spectrum of GaS shows a long-wave boundary at 660 nm at normal temperature (T = 300 K). After Yb doping, this boundary shifts to roughly 700 nm because of the impurity level within the band gap. In GaS(Yb), the highest photocurrent occurs at λ = 475 nm. The creation of donor-type sulfur vacancies (V_S) is indicated by an increase in photosensitivity and a shift in the spectrum toward the impurity region after γ-irradiation at D = 20 krad. The photocurrent increases in the short-wave area ($\lambda \approx 400$ nm) but decreases at longer wavelengths at D = 50 krad, confirming the generation of acceptor-type gallium vacancies (V_{Ga}). The photocurrent typically decreases at higher doses (D = 200 krad), showing that deep recombination centres dominate at high irradiation levels.

The photocurrent maximum shifts from 472 to 476 nm at a lower temperature (T = 110 K), which is in accordance with the Byub theory. The partial substitution of gallium vacancies caused by Yb doping results in a rise in photocurrent intensity. After irradiation, there is a little decrease in sensitivity at D = 20 krad and a noticeable increase at D = 200 krad about λ = 475 nm. This indicates the generation of shallow local levels and reveals how temperature and dose have significant effects on the interactions between impurities and radiation defects.

OPTICAL PROPERTIES OF NEW PP+ZrO_2 / TiO_2 BASED HYBRID NANOCOMPOSITES

***Valiyev S.R., Hajiyeva F.V.**
Baku State University, Azerbaijan
veliyevxsenan@gmail.com

Nanostuctured ZrO_2, recognized as one of the most industrially important transition metal oxides, is extensively employed as a catalyst due to its exceptional physicochemical properties. These include high thermal stability, superior electrical and optical performance, chemical inertness, non-toxicity, as well as notable ion-exchange capacity and redox activity, which collectively enable

its application in advanced catalytic, sensing, and protective material technologies. ZrO_2, on the other hand, is a versatile material renowned for its wide band gap (ranging from 3 to 5.2 eV).

Titanium dioxide (TiO_2) is a widely known semiconductor material for its use in many applications, including solar energy conversion, pollution control, and photocatalysis. TiO_2 is an n-type semiconductor having a wide band gap (3.2 eV for anatase and 3.0 eV for rutile).

Polypropylene composites with metal oxide fillers are now used in different technological fields. Their high physical and chemical stability makes these composites promising materials in areas such as electronics, packaging, and optical devices.

In the presented work, novel hybrid nanocomposites based on isotactic polypropylene (PP), zirconia (ZrO_2), and titanium dioxide (TiO_2) nanoparticles (NP) were synthesized by ex-situ methods. Initially, the PP was dissolved in the organic solvent toluene at 110°C. Then, ZrO_2 NP (35 nm) and TiO_2 NP (20 nm) were added to the PP solution and intensively mixed on a magnetic stirrer for 30 min. The final mixture was dried at room temperature for several days. Then, samples were dried under a vacuum oven at 100°C for 1 hour. Different concentrated PP+ZrO_2+TiO_2 thin films were obtained using 100°C and 10 mPA under hot press. After obtaining the absorbance spectrum of the nanocomposite materials by Ultraviolet-Visible (UV-Vis) analysis, the band gap energy (E_g) was calculated. It is determined that, 3.1 eV for PP + 1 % ZrO_2 + 1 % TiO_2, 2.8 eV for PP + 3 % ZrO_2 + 3 % TiO_2 and 3 eV for PP + 5 % ZrO_2 + 5 % TiO_2.

The decrease in the band gap energy of nanocomposite materials due to the increase in NP content in the polymer is related to the increase in NP size. From PL analysis, it is determined that PP+ZrO_2+TiO_2-based nanocomposites have a wide range of luminescence spectra. PL peaks can be observed at the 419 nm, 443 nm, 484 nm, and 503 nm wavelengths. At the same time, the maximum PL was observed in PP+ 1 % ZrO_2 + 1 % TiO_2 nanocomposites. With the increasing NP content in the polymer matrix, NP size increased; as a result, increasing specific surface area and luminescent centers decreased.

SYNTHESIS AND ELECTRICAL CHARACTERIZATION OF CHITOSAN-BASED GREEN POLYMER NANOCOMPOSITES REINFORCED WITH MULTI-WALLED CARBON NANOTUBES

[1*]Orujova T.I., [1]Gahramanova G.K., [2]Jabbarov R.B.

[1]French-Azerbaijani University (UFAZ) under Azerbaijan State Oil and Industry University, Azerbaijan

[2]Institute of Physics, Ministry of Science and Education, Azerbaijan

tarana.orujova@ufaz.az

The growing need for sustainable and eco-friendly materials has driven extensive research on green polymer nanocomposites. Among various biopolymers, chitosan (CS) has emerged as a promising candidate due to its biodegradability, renewability, and film-forming ability. When reinforced with multi-walled carbon nanotubes (MWCNTs), chitosan-based nanocomposites exhibit enhanced electrical and structural properties, making them suitable for environmental and sensing applications. This study focuses on the synthesis and electrical characterization of CS/MWCNT nanocomposites, aiming to explore their potential as sustainable conductive materials. In the present work, we report the synthesis and characterization of green polymer nanocomposites reinforced with multi-walled carbon nanotubes (MWCNTs) synthesized from three different carbon sources. Biodegradable matrices such as chitosan were selected as the base materials, reflecting a broader trend favoring bio-derived and compostable polymer systems. Structural and chemical analyses, including Fourier Transform Infrared Spectroscopy (FTIR) and Scanning Electron Microscopy (SEM), confirmed strong interfacial interactions between the nanotubes and the polymer chains: the presence of characteristic absorption bands and well-distributed nanotube networks supports the occurrence of effective load transfer and interfacial adhesion. These findings demonstrate that MWCNT-reinforced chitosan biopolymer nanocomposites offer promising potential for applications in biomedical devices and electronic components, where both biodegradability and high performance are required. This study contributes to the advancement of green nanotechnology by offering an environmentally responsible approach to designing high-performance materials.

DIELECTRIC PROPERTIES OF PVA/NiCr-LDH NANOCOMPOSITE FILM

***Ibrahimova Kh.A., Azizov A.A., Balayeva O.O., Eyvazova G.M.**
Baku State University, Azerbaijan
khazangul.ibrahimova1994@mail.ru

Recently, polymer materials based on Layered Double Hydroxides (LDHs) have garnered significant attention for their applications in catalysts, metal removal, biomedical fields, oil/water separation, and supercapacitors.

In this work, we have synthesized a polyvinyl alcohol (PVA) based nickel-chromium layered double hydroxide (NiCr-LDH) nanocomposite film using the sonochemical method. The dielectric properties of PVA/NiCr-LDH nanocomposites were investigated using an impedance analyzer. The dielectric constant, resistivity, dielectric loss (tan δ), and electrical conductivity of the nanocomposite films were determined using dielectric spectrometry measured over a wide frequency range from 120 Hz to 1 MHz and a temperature range from 20 °C to 100 °C under different reaction conditions. The primary dielectric property is the permittivity, which characterizes the response of the material to an applied electric field. The main phenomena that contribute to permittivity are dipolar relaxation, atomic polarization, electronic polarization, and ionic relaxation. Each phenomenon dominates at a different frequency range, as shown in Figure 1.

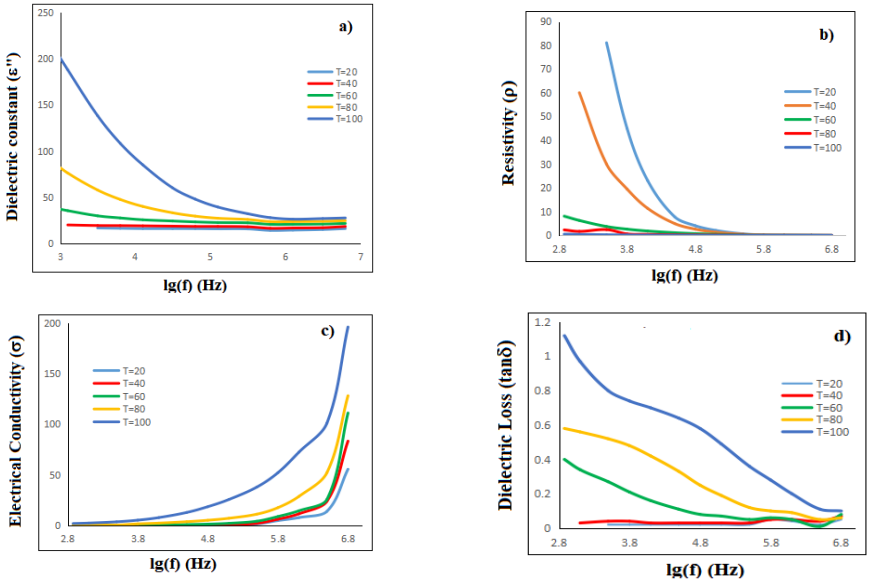

Fig. 1. Frequency dependence of (a) dielectric constant, (b) resistivity, (c) electrical conductivity, (d) dielectric loss of PVA/NiCr-LDH nanocomposite film measured in the temperature range 20-100 °C.

At low frequencies, for example, at 120 Hz, the dielectric constant ε′ increased significantly with temperature, rising from 39.36 at 20 °C to 216.48 at 100 °C, indicating strong polarization effects. As the frequency increased, ε′ decreased; at 1 MHz, ε′ ranged from 16.4 to 27.88. The dielectric loss (tan δ) also varied with frequency and temperature, reaching 0.4–1.12 at 120 Hz and 0.05–0.1 at 1 MHz.This indicates that the LDH layers allow the molecules to move and generate interfacial polarization in the PVA matrix (Maxwell-Wagner-Sillars effect). The nanocomposite exhibited enhanced dielectric properties compared to pure PVA, indicating that NiCr-LDH significantly influences the charge storage and polarization mechanisms. These findings demonstrate the potential of PVA/NiCr-LDH nanocomposites for electronic and dielectric applications.

FUNCTIONALIZED IRON OXIDE NANOPARTICLES FOR OPTIMIZED DRUG DELIVERY APPLICATIONS

***Mehdiyeva A.R., Karimova A.H., Muradov M.B., Nuriyeva S.G., Gahramanli L.R., Eyvazova G.M.**

Baku State University, Azerbaijan
aygun.mehdiyeva.rahman@bsu.edu.az

Optimizing the drug-loading potential of nanoparticles for cancer therapy requires precise control over design parameters, including drug-loading capacity, fabrication methods, and surface functionalization. Superparamagnetic iron oxide nanoparticles are promising candidates for drug delivery due to their magnetic properties, biocompatibility, low toxicity, and functionalization potential for targeted applications. In this study, Fe_3O_4 nanoparticles were synthesized via the co-precipitation method and functionalized with chitosan, followed by glutaraldehyde crosslinking to enhance drug-loading efficiency. The natural anticancer bioflavonoid chrysin was non-covalently loaded onto the modified nanoparticles to improve therapeutic efficacy.

The synthesized and functionalized nanoparticles were characterized using X-ray diffraction (XRD) to determine structural properties, Fourier-transform infrared (FTIR) spectroscopy to analyze molecular interactions, and UV-Vis spectroscopy to assess drug-loading efficiency. XRD analysis using the Debye-Scherrer equation determined the crystallite size as 13 nm for chitosan-modified SPIONs, which increased to 17 nm after crosslinking. UV-Vis spectroscopy revealed a significant improvement in drug-loading efficiency, increasing from 52% to 83%, attributed to the enhanced network structure and functional

sites provided by crosslinked chitosan. FTIR analysis confirmed strong interactions between the crosslinked chitosan and chrysin, as evidenced by shifts in characteristic absorption peaks and changes in vibrational bands, indicating improved drug binding. Comparison of the FTIR spectra of both samples revealed a shift towards lower wavenumbers in the absorption bands (C-H bonds) of chrysin within the 1200-1000 cm^{-1} range for the crosslinked system. The shift of vibrational frequencies towards lower wavenumbers, along with variations in absorption band intensities, suggests stronger intermolecular interactions between the drug and the crosslinked chitosan coating.

In conclusion, these results demonstrate that crosslinked chitosan-modified SPIONs offer a robust platform for drug delivery in cancer therapy. Future studies should focus on their in vitro and in vivo performance, assessing stability, biocompatibility, and therapeutic efficacy.

FUNCTIONAL APPLICATIONS OF GALLIUM SULFIDE (GaS) CRYSTALS IN GAS DETECTORS

[1,2]Madatov R.S., [3]Allahverdiyev S.A., [1,4]Mamishova R.M., [1,3]Khaligzade A.Sh., [1]Sadigli L.E., [1,2]Faradjova U.F.

[1]Institute of Radiation Problems, Ministry of Science and Education, Azerbaijan
[2]National Aviation Academy, Azerbaijan
[3]Baku State University, Azerbaijan
[4]Azerbaijan University of Architecture and Construction, Azerbaijan
rexsane@yandex.ru

Gallium sulfide (GaS), which belongs to the A_3B_6 group of semiconductors, is distinguished by its layered crystal structure, wide band gap, high photosensitivity, and thermal stability. These properties make it an important material for the development of various sensors and optoelectronic devices. At the same time, gallium sulfide (GaS) is considered a promising material in modern sensor technologies due to its high thermodynamic stability in atmospheric air, radiation resistance, and strong sensitivity to gases.

GaS crystals can be fabricated using different technologies (such as vacuum evaporation or epitaxial methods) in the form of thin or thick layers and deposited onto dielectric substrates. This is of great importance for detector technologies in terms of miniaturization and flexibility. GaS materials can exhibit either n-type or p-type conductivity, and changes in conductivity resulting from interactions with gases form the fundamental operating principle of gas sensors.

The structural characteristics of GaS crystals – their layered structure, weak van der Waals interlayer interactions, and high surface reactivity – enhance their sensitivity to gas adsorption, particularly to oxygen. In this regard, a decrease in conductivity is observed when electrons are captured by gas molecules adsorbed on the GaS surface. This change is proportional to the gas concentration and ensures the selective sensitivity of GaS-based sensors to oxygen and other gases.

Research results show that GaS crystals, which are radiation-resistant, thermally stable, and possess strong optical and photosensitive properties, can be used to detect variations in gas concentrations caused by radiation or light exposure. In particular, GaS crystals doped with rare-earth elements (for example, Yb-doped GaS) demonstrate promising results in both photoconductivity and gas sensitivity. This enables the development of highly sensitive, multifunctional sensor systems based on such materials.

SYNTHESIS AND OPTICAL PROPERTIES OF NEW Pr:PVDF/CdS/ZnS – BASED NANOCOMPOSITES DOPED WITH PRASEODYMIUM

***Huseynova S.İ., Hacıyeva F.V.**
Baku State University, Azerbaijan
fhajiyeva@bsu.edu.az

Nanomaterials have attracted extensive interest due to their unique size-dependent physical and chemical properties. Cadmium sulphide (CdS), a II–VI group semiconductor, possesses an optical band gap ranging from 2.42 to 5.0 eV at room temperature and exhibits remarkable physical and chemical stability.

Zinc sulfide (ZnS) is an inorganic compound II–VI semiconductor known for its photoconductivity and photoluminescence. Polyvinylidene fluoride (PVDF) is a functional polymer with a melting point of around -177°C, pronounced piezoelectric and pyroelectric properties, a high dielectric stability, and chemical inertness. Praseodymium (Pr) is a rare-earth element, specifically a soft, silvery metal within the lanthanide series.

In the presented work, novel Pr doped PVDF/CdS / ZnS nanocomposites (Pr: PVDF/CdS/ZnS) were obtained, and their optical properties were studied by Ultraviolet-Visible (UV-Vis.) spectroscopy. For obtaining nanocomposite materials, dissolving the PVDF polymer in dimethylformamide, pre-synthesized CdS particles with particle sizes of 16-25 nm and ZnS nanoparticles with sizes of 3-5 nm were added to this solution in turn and mixed by a magnetic stirrer

for 20 minutes at T= 60 °C. Then, Pr^{3+} particles in different amounts (0.1, 0.5, 1,3,5%) were added to the PVDF/CdS/ZnS system and mixed for 2 hours at a T= 60 °C until a homogeneous mixture was prepared. Then, the mixture was poured into a petri dish and dried at room temperature. The final thin films were obtained from Pr: PVDF/ CdS /ZnS ingots in a press apparatus at the melting temperature of PVDF (180°C). The absorption and emission spectra of the nanocomposites were studied by UV-Vis. spectroscopy, and the bandgap energy was calculated by the Tauc method. It was determined that the bandgap value of the 0.1% Pr/PVDF/CdS/ZnS-based nanocomposite is – 2.15 eV, 0.5%Pr/ PVDF/CdS/ ZnS is – 2.2 eV, 1%Pr/PVDF/CdS/ZnS is - 1.8 eV, 3%Pr/PVDF/ CdS/ZnS is - 2.05 eV, and 5%Pr/PVDF/CdS/ZnS is - 2.4 eV.

SYNTHESIS AND PROPERTIES OF MULTIPHASE NANOCOMPOSITES BASED ON PE+Fe_3O_4+MWCNTs

***Huseynova J.J., Hajiyeva F.V.**
Baku State University, Azerbaijan
jaleguseinzade@gmail.com

The presented work describes the synthesis and investigation of properties of nanocomposites based on Polyethylene (PE), magnetite nanoparticles (Fe_3O_4), and multi-walled carbon nanotubes (MWCNTs). The polyethylene was dissolved in the organic solvent carbon tetrachloride (CCl_4) at a temperature of 70^0C. Subsequently, Fe_3O_4 nanoparticles with particle sizes 5-15 nm were first added to the polymer + CCl_4 solution, followed by MWCNTs with a size of 10 nm. The mixture was stirred on a magnetic stirrer for a total of 2 hours.

The concentration of $e_3O_4$nanoparticles in the polyethylene matrix ranged from 1% to 10%, while the amount of carbon nanotubes was fixed at 1%. The dielectric properties of the PE + Fe_3O_4 + MWCNTs multiphase nanocomposites were investigated. Results from the frequency dependence of dielectric losses showed that the addition of 1% carbon nanotubes to the PE + Fe_3O_4 system leads to a sharp increase in dielectric losses due to the enhanced fraction of the conductive phase. This increase is attributed to the information of a conductive network by the carbon nanotubes.

Due to their high dielectric losses, such composites possess electromagnetic wave shielding properties at ultra-high frequencies, making their wide application in industry possible. Furthermore, the magnetoresistance effect was also observed in the PE + Fe_3O_4 + MWCNTs multiphase nanocomposites.

PHOTOCONDUCTIVITY INVESTIGATION IN GaSe–Ge HETEROSTRUCTURES

***Babayeva A.F., Guseynov A.G., Akhmedova F.Sh., Balayeva L.A.**
Baku State University, Azerbaijan
aybenizbabayevvv@gmail.com

This research focuses on the investigation of the photoconductive and spectral response characteristics of a p–n type GaSe–Ge heterojunction formed at the interface between Gallium Selenide (GaSe) and Germanium (Ge) layers. The heterostructure was fabricated by thermally bonding a Ge layer onto a GaSe crystal grown by the Bridgman method, using a vacuum diffusion bonding technique.

The photoconductivity of the prepared samples was examined using the spectral photoelectric method within the photon energy range of 1.35–2.9 eV (≈ 430–920 nm). The built-in electric field formed at the heterointerface ensures the effective separation of photo-generated charge carriers and their transfer into the Ge layer.

Experimental results revealed that the photoconductivity spectrum exhibits a distinct maximum near 2.15 eV, corresponding to the fundamental bandgap energy of the GaSe layer ($E_g \approx 2.0–2.1$ eV). In the spectral region below 1.8 eV, the photocurrent remains weak, indicating the onset of absorption. At photon energies above 2.3 eV, the photocurrent gradually decreases, with a weak peak observed in the 2.6–2.7 eV range, which may be attributed to the participation of surface and defect states. In the long-wavelength region (around 1.4–1.6 eV), a slight increase in photocurrent indicates the indirect contribution of the Ge layer, corresponding to carrier transfer across the heterointerface.

The obtained results demonstrate that GaSe–Ge heterostructures exhibit high photosensitivity in the visible and near-infrared regions, confir-ming their potential as promising material systems for optoelectronic applications, including photodetectors, photodiodes, and light sensors.

In conclusion, it was established that the photoconductivity process predominantly occurs within the GaSe absorption region, while the Ge layer acts as an indirect component, facilitating carrier transport across the heterointerface and enhancing the overall photoresponse of the heterostructure.

STRUCTURAL ANALYSIS OF SIC AND PP VIA X-RAY DIFFRACTION

***Hamidova S.N., Gahramanli L.R.**
Baku State University, Azerbaijan
hamidova.sevinc.natiq@bsu.edu.az

X-ray diffraction (XRD) analysis was performed to study the crystalline structure of silicon carbide (SiC) nanowires and polypropylene (PP). As shown in Figure 1, the SiC diffraction pattern exhibits sharp peaks at 2θ = 35.6°, 41.5°, 60.0°, 72.0°, and 75.5°, which correspond to the (111), (200), (220), (311), and (222) planes of β-SiC (JCPDS 73-1665). The presence of these well-defined reflections confirms the cubic sphalerite structure and high crystallinity of the synthesized SiC. A minor shoulder near the (111) peak indicates stacking faults, which are commonly observed in nanostructured SiC materials.

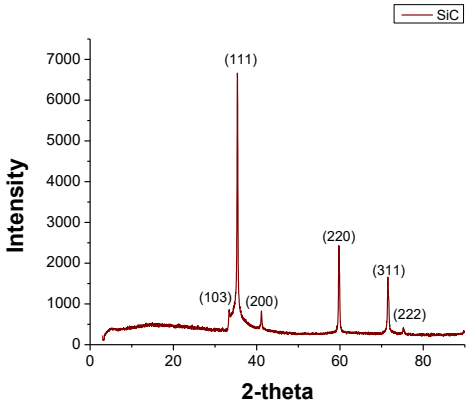

Figure 1. XRD pattern of SiC nanowires

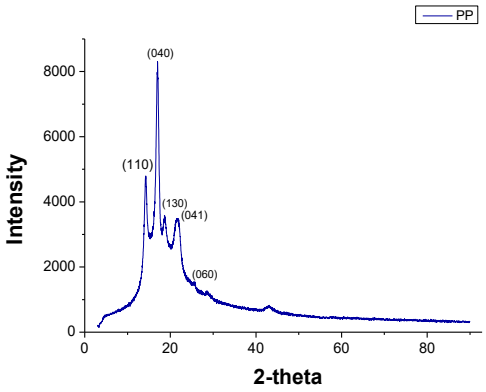

Figure 2. XRD pattern of PP

The XRD pattern of polypropylene, shown in Figure 2, displays distinct reflections at 2θ = 14.2°, 17.0°, 18.5°, 21.6° and 25.5°, which can be indexed to the α-form crystallographic planes (110), (040), (130), (041), and (060), respectively (JCPDS 66-1214). These peaks confirm the semi-crystal-line nature of PP and indicate a predominant α-phase orientation typical for isotactic polypropylene.

The obtained XRD results for both materials demonstrate their well-defined crystalline phases and structural stability, confirming the suitability of SiC and PP for further integration into functional materials and nanocomposites.

MONOLITHIC TiO_2 NANOTUBE DSSC–SUPERCAPACITOR PLATFORM FOR AUTONOMOUS SOLAR-TO-HYDROGEN CONVERSION

[1*]Eminov Sh.O., [2]Gardashov R.G., [1]Gurbanov I.I., [1]Abdullayeva S.H., [1]Jalilova Kh.D., [1]Badalov A.A., [1]Rajabli A.A.

[1]Institute of Physics, Ministry of Science and Education, Azerbaijan
[2]Institute of Geography, Ministry of Science and Education, Azerbaijan
shikhamirem@gmail.com

This study presents a novel, fully integrated energy platform developed by our research team, which synergistically combines solar energy harvesting, electrochemical energy storage, and photoelectrochemical (PEC) water splitting within a single TiO_2 nanotube (TNT)-based architecture. The device leverages anodically synthesized, nitrogen-doped TiO_2 nanotube arrays as a common active material across three subsystems: a dye-sensitized solar cell (DSSC), a supercapacitor, and a PEC cell. This unified material strategy ensures structural compatibility, enhances charge transport, and simplifies fabrication, while also enabling visible-light responsiveness critical for solar-driven applications. By utilizing nitrogen doping, the electronic band structure of TiO_2 is modified, narrowing the bandgap and thereby improving light absorption in the visible region. The vertically aligned nanotube morphology further promotes efficient electron mobility and a large interfacial surface area, facilitating faster redox reactions and superior energy conversion and storage performance. The seamless integration of these three functional components within a shared architecture minimizes interfacial losses, reduces device complexity, and allows for continuous energy flow – from solar energy capture to electrochemical storage and subsequent utilization for hydrogen generation via PEC water splitting. This multifunctional TiO_2 nanotube–based platform thus represents a significant step toward developing compact, self-sustaining, and environmentally friendly energy systems capable of addressing the growing global demand for clean and renewable energy technologies.

A shared Glass/ITO substrate design facilitates direct photocharging of the supercapacitor, eliminating the need for external wiring and reducing system complexity. To overcome the voltage mismatch between the solar cell and the PEC unit, an LTC3108 ultra-low-voltage boost converter is integrated, enabling efficient energy transfer and autonomous hydrogen generation under solar illumination. Morphological and structural analyses confirm the formation of high-quality anatase-phase TiO_2 nanotube films with excellent transparency and uniformity – key attributes for optimal photovoltaic and PEC performance. Prototype testing of the DSSC yielded an open-circuit voltage, validating the

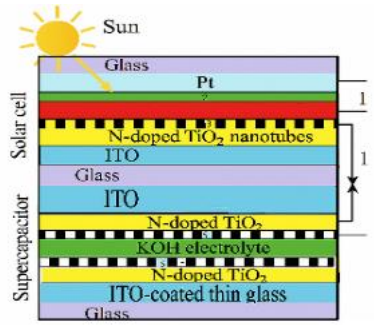

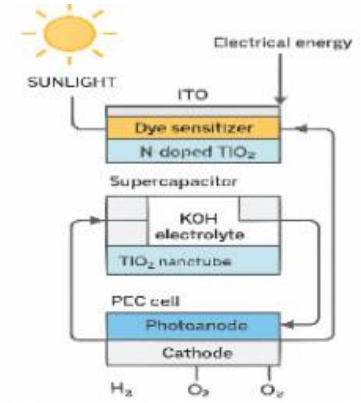

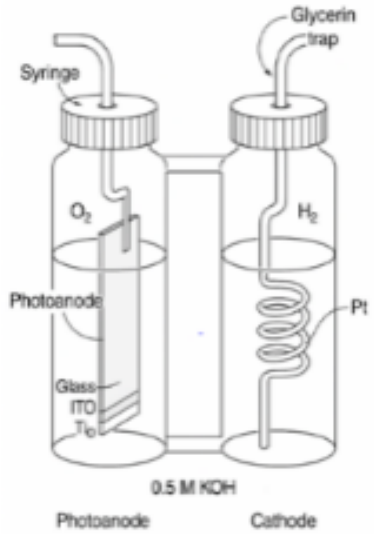

Figures illustrate the schematic design of the electrolyzer with a nanotubed TiO_2 photoanode and the prototype testing of the DSSC.

photovoltaic activity of the TNT-based electrodes. The PEC compartment, powered by the hybrid system, successfully produced hydrogen in alkaline media, demonstrating operational compatibility and energy autonomy. Importantly, the architecture minimizes ion crossover between compartments while maintaining ionic conductivity and device stability.

INVESTIGATION OF SILICON PHOTOMULTIPLIERS IRRADIATED BY GAMMA RAYS

Mammadli A.H.

Institute of Radiation Problems, Ministry of Science and Education, Azerbaijan
arzu.mammadli06@gmail.com

In this study, the electrical properties of silicon photomultipliers (SiPMs) manufactured by Zecotek Photonics Inc., featuring an active area of 3.7 × 3.7 mm^2 and a pixel density of 4450 pixels/mm^2, were investigated. The research object, a SiPM with an internal pixelated structure (model MAPD-3NM2), was examined under the influence of gamma irradiation from a ^{60}Co source at doses of 10 kGy and 40 kGy, focusing on its current–voltage (I–V) and capacitance–voltage (C–V) characteristics.

The experimental results revealed that the dark current increased by factors of 9.4 and 31 at doses of 10 kGy and 40 kGy, respectively, which is attributed to radiation-induced defects in the silicon crystal lattice and at the pixel boundaries. A slight shift in the breakdown voltage – from 52 V to 51.8 V – was observed, explained by radiation-induced variations in the electric field distribution across the p–n junction. Furthermore, the C–V characteristics indicated an approximately 2% decrease in capacitance at 40 kGy, corresponding to an expansion of the space-charge region width.

The obtained results demonstrate that the MAPD-3NM2 photodiodes maintain their stability under high-dose gamma irradiation, indicating their potential applicability in nuclear technologies and radiation-tolerant detector systems.

BOOSTING AQUEOUS ZINC-ION BATTERY PERFORMANCE VIA LANTHANUM-DRIVEN STRUCTURAL ENGINEERING OF HYDRATED VANADATE

[1*]Muhammad Iftikhar Khan, [2]Guozhong Cao

[1]The University of Lahore, Pakistan.
[2]University of Washington, Seattle, USA.
Muhammad.iftikhar@phys.uol.edu.pk

Low carrier mobility and cycling stability of hydrated vanadate (VOH) are enhanced by modifying the regional atomic environments through the chemical pre-insertion of trivalent La ions by a hydrothermal process. The increased

lattice gap and decreased electrostatic interaction between the host crystal in LaVOH and zinc ions facilitate quick electron transfer and Zn^{2+} diffusion. This leads to a high capacity of 410 mAh g^{-1} at 500 mA g^{-1} and improved long-term cycling stability at 4000 mA g^{-1}, with capacity retention exceeding 80% over 3000 cycles, compared to conventional VOH. The introduction of La ions helps prevent structural degradation and promotes sustained electrochemical performance.

THICKNESS-DEPENDENT MECHANICAL PROPERTIES OF EPITAXIAL PMN-PT THIN FILMS STUDIED BY NANO-INDENTATION

[1*]Boota M., [2]Houwman E.P., [3]Sebastiani M., [3]Rossi E., [3]Bemporad E., [2]Rijnders G.

[1]The University of Lahore, Pakistan
[2]University of Twente, The Netherlands
[3] Roma Tre University, Italy
Muhammad.boota@phys.uol.edu.pk

This study examines the thickness-dependent structural and mechanical properties of epitaxial $[Pb(Mg_{1/3}Nb_{2/3})O_3]_{0.67}$-$(PbTiO_3)_{0.33}$ thin films, a high-performance piezoelectric material, deposited on (001)-oriented $SrTiO_3$ substrates with a 100 nm $SrRuO_3$ bottom electrode layer and a 25nm $Pb(Zr_{0.5}Ti_{0.5})O_3$ interfacial layer. Structural characterization confirms phase-pure, (001)-oriented PMN-PT films with very slight in-plane tensile strain. The out-of-plane lattice constant evolves with thickness in the range of 300-1000nm, shifting from values below the bulk value in thinner films to the bulk value for the thickest film. This indicates strain relaxation and defect accumulation. The XRD analysis indicates a transition from a tetragonal to a more bulk-like, rhombohedral lattice symmetry for the thickest PMN-PT layer, which is ascribed to the strain relaxation. Nanoindentation results show that the hardness and elastic modulus exceed those of bulk values, with the thickest film (1000 nm) standing out with the highest modulus (217 ± 17.7 GPa) and hardness (12.04 ± 0.84 GPa) values. This is attributed to the rhombohedral lattice symmetry for this sample. The observed correlation between deeper pop-in events and PMN-PT film thickness signifies the strong effect of strain relaxation and structural defects on mechanical failure mechanisms. These findings highlight the potential to optimize the mechanical response of PMN-PT thin films through thickness control, paving the way for advanced applications in piezoelectric devices.

TRANSFER MATRIX METHOD AS A TOOL FOR PROBING OPTICAL RESPONSES OF A THIN FILM: A THEORETICAL APPROACH

[1*]Muhammad Amin, [1]Muhammad Asif, [2]Khalid Rauf, [2]Afaq Ahmad
[1]The University of Lahore, Lahore, Pakistan
[2]Punjab University, Lahore, Pakistan
wajeeha.shahid@phys.uol.edu.pk

Experimental fabrication of thin films often requires advanced facilities, significant cost, and complex processes. In contrast, the Transfer Matrix Method (TMM) offers a powerful, accurate, and cost-effective theoretical framework for predicting optical behavior before fabrication. By systematically analyzing the influence of key parameters such as film thickness, wavelength, and refractive index on transmission, reflection, and absorption phenomena, TMM minimizes experimental effort while providing critical insights that guide experimental studies and the rational design of optoelectronic devices. Strontium Titanate (STO), a multifunctional perovskite oxide with exceptional dielectric, optical, and electronic properties, is investigated in this work alongside $TiO_2/V_2O_5/TiO_2$ multilayer thin films deposited on glass substrates, a heterostructure widely studied for photonic and optoelectronic applications. For STO thin films with thicknesses of 250 nm and 260 nm, the computed direct band gap values of 3.49 eV and 3.59 eV, respectively, show excellent agreement with reported experimental findings, validating the accuracy of the TMM approach. Similarly, for $TiO_2/V_2O_5/TiO_2$ multilayer stacks, the optical wave propagation behavior is systematically examined, highlighting the impact of layer configuration on transmission, reflection, and absorption spectra. Collectively, these investigations deepen the understanding of both single-layer STO films and complex oxide multilayers, offering valuable guidance for the design and optimization of next-generation STO- and $TiO_2/V_2O_5/TiO_2$-based optoelectronic and photonic devices.

EFFICIENT CONSTRUCTION OF TWO-DIMENSIONAL LAYERED MATERIALS AND THEIR MULTIFUNCTIONAL APPLICATIONS

Asif Hussain
The University of Lahore, Lahore, Pakistan
wajeeha.shahid@phys.uol.edu.pk

The efficient construction of two-dimensional (2D) porous carbon-based layered materials, specifically graphitic carbon nitride (g-C_3N_4) and bismuth

oxyhalides (BiOX, X = Cl, Br, I), exhibits remarkable potential in multifunctional applications, such as photocatalytic, electrocatalytic, and supercapacitors. In this study, we focused on synthesizing and characterizing these 2D materials through innovative techniques to enhance their structural and electronic properties. 2D g-C_3N_4 provides a highly tunable platform for solar energy conversion to organic fuels and environmental remediation. Furthermore, BiOX exhibits excellent photocatalytic and photoluminescent properties due to its unique layered structure, high electron mobility, and strong anisotropic interactions. Our findings revealed that the 2D morphology, coupled with the inherent semiconductor properties of g-C_3N_4 and BiOX, results in improved charge separation efficiency, extended light absorption, and superior stability. The enhanced performance of materials in various photocatalytic applications, such as pollutant degradation, CO_2 reduction, H_2 production, batteries, and supercapacitors, validates the significance of 2D nanomaterials. Moreover, their ease of synthesis and adaptability in various device architectures make them promising candidates for scalable, low-cost, and high-efficiency optoelectronic systems. Conclusively, this work underscores the potential of these 2D layered materials as building blocks for next-generation sustainable energy applications.

TIME SERIES ANALYSIS BASED ON COMPUTER VISION FOR THE EXTRACTION OF THE TIME PERIOD OF A SIMPLE PENDULUM

Nasir Mehmood

The University of Lahore, Pakistan
wajeeha.shahid@phys.uol.edu.pk

Computer vision (CV) is one of the branches of AI that plays a vital role in retrieving useful information from data. Despite its wide implementation, there still exists a need for a simplified approach in the field of feature extraction and data retrieval. Here, we explore the employment of an automatic visual analysis tool for the extraction of the simple pendulum time period merely from time series analysis based on CV. Various direct and indirect methods are employed, including real-time measurement of the oscillations, estimation through visual analysis of experiment videos, and finally, using the CV technique to generate the time series graphs. The CV-generated graphs are then analyzed through fast Fourier transform (FFT) in order to find out the oscillation frequency and finally the time period of the oscillations. A comparison of the results from all of the implemented methods for time period estimation shows that the CV

technique provides a level of accuracy within a reasonable range. However, the major advantage of this technique is its minimal human intervention. The results of this study pave the way for future employment of CV-based methodologies in the field of feature extraction from the input visual data, useful for experimental analysis.

STRAIN-DRIVEN ELECTRONIC AND THERMOELECTRIC MODULATION IN $Ba_2XReO_6(X = Y, Sc)$ OXIDES DOUBLE PEROVSKITES

[1*]Sadia Nazir, [2]Noor N.A., [1]Syed Tauseef Hussain, [3]Sohail Mumtaz

[1]University of Lahore, Pakistan
[2]University of Sargodha, Pakistan
[3]Gachon University, Republic of Korea
Sadia.nazir@phys.uol.edu.pk

Oxide-based double perovskites subjected to biaxial strain reveal significant insights into their electronic and magnetic properties, making them strong candidates for spintronic applications. This study investigates the structural, electronic, magnetic, optoelectronic, and thermoelectric properties of $Ba_2XReO_6(X = Y, Sc)$ under biaxial strain using the WIEN2k software. The lattice constant has increased from 10.01 to 10.53 Å due to the substitution of Y with Sc in the optimized face-centered cubic lattice. Their thermodynamic stability is supported by calculated enthalpy of formation values of -1.46 eV for Ba_2YReO_6 and -1.33 eV for Ba_2ScReO_6 The observed bandgap values are 0.94 eV for Ba_2YReO_6 and 0.32 eV for Ba_2YReO_6 using the GGA method, which increases to 2.25 eV and 0.93 eV, respectively, when the GGA+mBJ method is applied. Incorporating Hubbard's potential in the range of 1-5 eV further enhances the bandgap from 2.38 eV (@1eV) to 2.58 eV (@5eV) for Ba_2YReO_6 and from 0.96 eV (@1eV) to 1.09 eV (@5eV) for Ba_2ScReO_6. Compressive strain consistently reduces the bandgap, while tensile strain increases the bandgap up to 3%, but further application of tensile strain to 5% decreases the bandgap for Ba_2YReO_6 The magnetic moments and spin magnetization density at iso-values of ±0.05 eÅ show slight variations under strain. Biaxial strain ranging from 0 to 4% was utilized alongside the GGA+mBJ potential to calculate the optoelectronic and thermoelectric properties, highlighting their potential for applications in transport and energy harvesting.

SOLAR-SIMULATED PHOTOCATALYSIS WITH MoS_2@WO_3 HETEROSTRUCTURES: AN EFFICIENT STRATEGY FOR RhB DEGRADATION

Wajeehah Shahid
The University of Lahore, Pakistan
wajeeha.shahid@phys.uol.edu.pk

In this study, a novel hydrothermal ex situ synthesis approach was employed to synthesize MoS_2/WO_3 heterostructures, utilizing two distinct molar ratios of 1:1 and 1:4. The successful implementation of a 'bottom-up' assembly method resulted in the synthesis of heterostructures with spherical and flaky shapes. Comprehensive structural, morphological, compositional, and bandgap characterizations were conducted through XRD, EDX, SEM, UV-Visible spectroscopy, and FTIR analysis. These analyses provided valuable insights into the agglomerated nature of MoS_2/WO_3 heterostructures, elucidating their potential applications in photocatalysis. Subsequently, the prepared heterostructures underwent testing for RhB photodegradation under solar light irradiation. The percentage efficiency of MoS_2/WO_3 composites after 30 minutes of irradiation was 91.41% for the 1:1 ratio and 98.16% for the 1:4. Similarly, the percentage efficiency of 1:1 MoS_2/WO_3 heterostructures after 60 minutes of exposure was 92.68%, while for the 1:4, it was 98.56%. Extending the exposure time to 90 minutes, the percentage efficiency was 92.41% for 1:1 and 98.48% for 1:4 composites. Furthermore, these heterostructures exhibited stability over three cycles, Moreover, indicating their future applications for other photocatalytic applications.

NOBIOMATERIALS IN THE TREATMENT OF CANCER - AN OVERVIEW

*__Saman Mumtaz, Fazal-e-Aleem__
The University of Lahore, Pakistan
Samanmumtaz698@gamil.com

Cancer is a leading cause of death worldwide. Nanobiomaterials are an emerging platform in oncology. These materials are natural, synthetic, and hybrid materials. Nanomaterials refer to structures with at least one dimension between 1 and 100 nanometers (nm). Nanobiomaterials are highly significant because they have unique properties, such as reactivity, strength, and surface area, which are utilized in health care, electronics, cancer treatment, and environmental

science. Types of nanobiomaterials include lipid-based, polymeric, inorganic nanoparticles, protein/DNA-based nano-structures, and hybrid nanocomposites utilized in cancer treatment. Nanobiomaterials enable more effective and targeted therapies by enhancing the immune system, improving drug delivery, facilitating gene therapy, and enhancing photothermal therapy (light-based therapy), as well as advancing theranostics (imaging contrast agents used in CT scans, MRI, and NIR). They can overcome the critical barriers in the traditional cancer therapy. By using special nanoscale materials to replicate natural tissues, distribute medications, and alter tissues, nanobiomaterials will play a key role in the development of targeted therapies and diagnostics. New developments are making the nanobiomaterial safer, smarter, and better. They are getting closer to actual cancer therapies and individualised care because of improved design. Our talk will mainly cover these aspects.

MULTILAYER CHALCOGENIDE GLASS NANOSTRUCTURES: TOWARDS THE FORMATION OF HIGH-EFFICIENCY DIFFRACTIVE OPTICAL ELEMENTS

[1]*Meshalkin A., [1]Achimova E., [1]Abaskin V., [1]Losmanschii C., [1]Botnari V., [1]Muntean D., [2]Toy M.F.

[1]Moldova State University, Moldova;
[2]Istanbul Medipol University, Istanbul, Turkey
alexei.meshalkin@ifa.usm.md

Chalcogenide glassy semiconductors, particularly in the form of thin films, are of significant interest due to their wide range of photoinduced phenomena, which makes them attractive as recording media for optical and holographic information storage. When exposed to actinic laser irradiation, these materials undergo substantial modifications of their optical properties, including changes in refractive index, absorption coefficient, and solubility. Such transformations allow the direct inscription of amplitude–phase structures with high spatial resolution. Nevertheless, in homogeneous recording media the achievable refractive index modulation is typically limited to ~0.1, which constrains the maximum diffraction efficiency of thin phase gratings to about 10%. In order to increase efficiency further, deeper phase modulation is required, which is often realized through selective etching of the recorded pattern. While effective, this additional post-processing step complicates fabrication and reduces technological flexibility.

In the present study, we demonstrate that nanostructuring of chalcoge-

nide glass films within the As–S–Se system, in combination with polari-zation holographic recording, enables the direct one-step formation of relief–phase structures during the writing process itself. This approach eliminates the need for post-exposure chemical treatment, thus simplifying fabrication and ensuring greater reproducibility. Using this method, diffraction gratings with efficiencies as high as 33.9% were successfully obtained. The role of polarization configurations of the recording beams was systematically investigated, and optimal conditions leading to maximum diffraction efficiency were identified.

Structural analysis of the recorded gratings using atomic force microscopy revealed a well-developed surface relief with depths up to 500 nm. Such pronounced surface modulation is directly correlated with enhanced diffraction efficiency. Furthermore, the dependence of relief depth on both the grating period and laser exposure was examined, showing clear trends consistent with theoretical predictions. Numerical modeling of diffraction efficiency as a function of surface relief depth demonstrated good agreement with experimental data, further validating the proposed mechanism.

These findings underscore the potential of multilayer nanostructured chalcogenide glasses for the development of high-efficiency diffractive optical elements. The demonstrated single-step recording approach provides a promising pathway toward practical, scalable, and efficient fabrication of advanced diffractive devices for photonic applications.

Acknowledgment: This work was carried out within the framework of the projects 24.80013.5007.3TR and 25.80015.5007.02POE, funded by the Moldova National Agency for Research and Development, and 123N774 project, funded by TUBITAK (The Scientific and Technological Research Council of Turkey).

STUDY OF AZOMETHINES, NITROBENZYLIDENE CHLOROACETAMIDE, AND *n*-AMINOACETOPHENONE *N* (2-HYDROXYETHYL) ETHYLENEDIAMINE AS MULTIFUNCTIONAL ADDITIVES

Aminova B., *Ibragimova T., Almammadova A., Qahramanova K., Mammadova G., Qasimli G., Babaeva H.

Institute of Additive Chemistry, Ministry of Science and Education, Azerbaijan
ibragimovatarana66@gmail.com

As is known from the literature, azomethines (Schiff bases) are produced by the reaction of aromatic aldehydes and ketones with amines. Motor oils, cutting fluids, and fuels deteriorate over time, becoming contaminated by microorganisms, which leads to a reduction in their performance properties.

Therefore, in order to protect them, we have synthesized a number of additives that improve both the composition and efficiency of petroleum products, as well as metal complexes of these additives, which are widely used in medicine for the production of antibiotics.

Azomethine nitrobenzylidenechloroacetamide

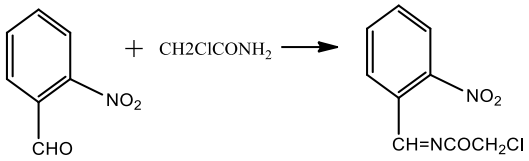

Azomethine N-aminoacetophenone N (2-hydroxyethyl) ethylenediamine

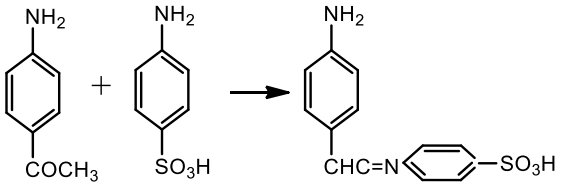

The antimicrobial properties of the obtained additives were determined by the zonal diffusion method in accordance with ГОСТ 9.085-78, ГОСТ 9.052-88 and ГОСТ 9.024-74. Cladosporium resinae, Aspergillus niger, Penicillium chrysogenum were used as mold fungi, and Mycobacterium phlei and Pseudomonas aeruginosa, were used as bacteria, which are widespread in petroleum product.

CONVERSION TECHNOLOGY GRAPHENE OXIDE TO REDUCED GO

***Ahmadova N., Babayeva M.**
Baku State University, Azerbaijan
agmedova07@gmail.com

Graphene oxide (GO) is a single-atomic-layer of graphite consisting of several oxygenated functional groups, and it has attracted significant attention due to its unique properties such as good mechanical flexibility, large specific surface area, higher thermal-chemical stability, and excellent electrical conductivity. RGO is currently the most promising nanomaterial for various electronic devices, including sensors that can be synthesized by the thermal reduction method. In the presented study, GO was synthesized by the Hummers method. For the reduction process, 25 mg of GO was dispersed in 50 mL of distilled water, and the solution was homogenized via sonication for 1 hour.

Then, the pH of the mixture is altered to 10-11 utilizing 0.1 M NaOH solution. For the reduction process, 200 mg of NaBH4 is dissolved in 10-20 mL of distilled water, then added dropwise to the main GO mixture under magnetic stirring. The process is performed by stirring the final mixture for 1 hour at 95 °C. The obtained solid product is purified by washing 1-3 times with ethanol and then 2-3 times with distilled water to get a pure RGO. To determine structural changes after the reaction, the X-ray Diffraction method (XRD) The XRD is used to determine the crystallographic structure, providing information about the crystal phase and interlayer spacing (d) of GO and RGO. The XRD pattern of GO (Fig. 1a) shows a sharp peak at 2Θ=10.44° corresponding to the (001) plane with a d-spacing of 0.85 nm, indicating a higher amount of hydrophilic oxygen-containing functional groups that break π bonding and increase interlayer distance, confirming a correct oxidation process. Nevertheless, after reducing GO, the 2Θ peak at 10.44° shifts to 2Θ=24.49° corresponding to the (002) plane for RGO (Fig a.b). In this case, the d-spacing decreases to the value of 0.36 nm, showing that graphitic structure has been recovered. This decrease confirms the detachment of the oxygen-containing functional groups from GO. Both GO and RGO show a peak at 43° corresponding to the plane of (100), indicating irregular stacking of graphene sheets known as turbostratic disorder of carbon materials.

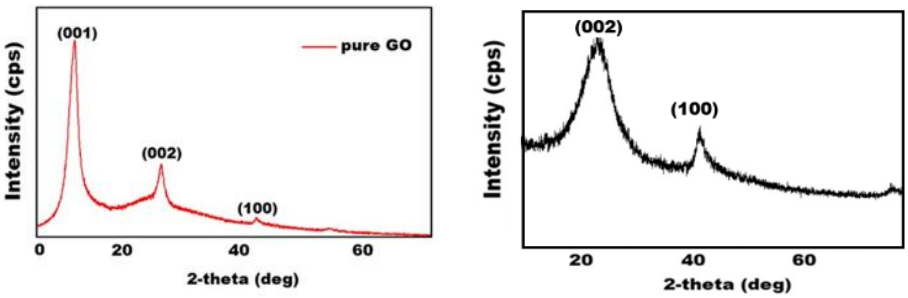

Figure 1. Diffraction pattern of a) GO and b) rGO

As can be seen from the figure, the higher amount of hydrophilic oxygen-containing functional groups in the diffraction pattern of GO was not detected in the rGO sample. Thus, the technology used was a convenient method to easily convert GO to rGO.

THE MECHANISM OF OZONE FORMATION IN THE MICRODISCHARGE CHANNEL IN THE BARRIER DISCHARGE

Alakbarov Sh.Sh.
Baku State University, Azerbaijan
shahinalakbarov@bsu.edu.az

Despite extensive research and application of ozone, the mechanism of ozone formation in a gas discharge remains poorly understood. Given that the main physical and chemical processes in a gas discharge occur in the microdischarge channel, it is clear how important it is to study the mechanism of ozone formation in the microdischarge channel.

According to literature, barrier discharge ozonizers operating in pulsed mode are considered the most effective, with efficiency reaching $\sim 0{,}2\ kg/kVt \cdot h$ (at a discharge pressure of $\sim 1{,}4\ atm$). Calculations show that under such conditions, the efficiency of ozonizers should be at least half that. This discrepancy is resolved by taking into account the additional pressure created in the channel due to the high currents flowing through it.

Ozonizers operating in pulsed mode are known to have a voltage drop of $\approx 2\ kV$ per mm of discharge region. In this case (1 atm, temperature 300 K), numerous microdischarges with a duration of 10–50 ns and an energy of 5–10 μC occur between the barriers. Considering that the channel diameter is 0.3–1 mm, and the amount of charge transferred during a microdischarge is $2–10 \cdot 10^{-10}$ C, then the current density in the microdischarge channel is 100 A/cm^2.

Considering that the charges transferred during the microdischarge form a disk-shaped spot with a diameter of 15–17 mm on the dielectric barrier, and that the microdischarge channel is sharp, it is known that the electric field is distributed unevenly in the axial and radial directions of the microdischarge. Thus, when a large current flows through the channel as a pulse, a magnetic field is created around the channel. The positively charged ions moving in this field are acted upon by the Lorentz force, directed toward the channel axis. In this case, the pressure distribution in the radial direction from the channel axis has the form:

$$-dp = \frac{dF_L(r)}{S} = \frac{q_{(+)} v dB(r)}{S}$$

$$= \frac{q_{(+)}}{S} \cdot \sqrt{\frac{2eU}{m_i}} \cdot \frac{jds}{2\pi r} = \frac{jq_{(+)}}{S} \cdot \sqrt{\frac{2eU}{m_i}} \cdot dr \qquad (1)$$

Here F_L – is the Lorentz force, S – is the area of the lateral surface of the channel,

$q_{(+)}$ – is the charge of positively charged ions, e – is the charge of an electron, U – is the voltage drop across the discharge gap, m_i – is the mass of positively charged ions, j – is the current density in the channel, ds – is the elementary area over which charges move in a magnetic field, r – is the distance from the channel axis. Moreover, if we take into account that $j = P/B$

$$\frac{dp}{p} = \frac{pq_{(+)}}{BS} \cdot \sqrt{\frac{2eU}{m_i}} \cdot dr = -\frac{2\pi q_{(+)}}{Si} \cdot \sqrt{\frac{2eU}{m_i}} \cdot rdr \qquad (2)$$

From here

$$p = p_0 \cdot exp\left(-\frac{\pi q_{(+)} r^2}{Si} \cdot \sqrt{\frac{2eU}{m_i}}\right) = p_0 \cdot exp\left(-\frac{\pi q_{(+)} r^2 \tau}{SQ} \cdot \sqrt{\frac{2eU}{m_i}}\right) \qquad (3)$$

According to the pressure inside the channel

$$p_0 = p \cdot exp\left(\frac{\pi q_{(+)} r^2 \tau}{SQ} \cdot \sqrt{\frac{2eU}{m_i}}\right) \qquad (4)$$

Calculations based on this expression show that the pressure inside the channel is ~10 atm.

THERMOPHYSICAL INVESTIGATION OF NANOCRYSTALLINE h-BN UNDER NEUTRON IRRADIATION

Abbasov N.R.

Nuclear Research Department of IDDA, Azerbaijan
nicat.rpi@gmail.com

Neutron-dose-resolved thermo-physical data for nanocrystalline h-BN are essentially missing, despite h-BN's growing use in high-temperature, radiation-exposed systems. This study provides an integrated DSC/DTA/TG map of G(T), H(T), S(T), and mass-loss kinetics from 300–1270 K after controlled neutron flux, directly linking dose to thermal response. The results show preserved global stability but clear, dose-dependent heat-flow and DTG features consistent with $^{10}B(n,\alpha)^{7}Li$ transmutation and defect reorganization. These dose-resolved parameters are immediately usable for materials screening and lifetime modeling in nuclear components, shielding, and space-radiation environments.

Nanocrystalline hexagonal boron nitride (h-BN) nanoparticles were irradiated in a research reactor over flux from 1.6×10^{15} to 2×10^{17} n·cm^{-2} to quantify how neutron exposure modifies their thermo-physical response. Using

simultaneous DSC/DTA/TG between 300–1270 K during both heating and cooling, we derived Gibbs free energy, enthalpy, and entropy before and after irradiation. TG/DTG reveal irradiation-dependent, step-like differential mass changes superimposed on a low-temperature desorption regime that largely vanishes by ≈750 K. Across all doses, G(T) remains negative and exhibits similar temperature dependence, with small irradiation-induced deviations, indicating preserved global thermodynamic stability despite local rearrangements. Enthalpy and entropy increase quasi-linearly with temperature, at higher flux a subtle feature emerges near ∼770 K, consistent with transmutation-driven compositional changes and defect production. The thermal signatures, together with spectroscopic evidence from prior work, support a neutron-assisted reorganization of bonding motifs in BN – plausibly involving vacancy formation, Li/^{12}C buildup via B-mediated (n,α)/(n,γ) paths, and an accompanying shift in local BN stoichiometry – that perturbs heat-flow and mass-loss kinetics without destabilizing the bulk thermodynamic landscape. These results provide a compact, dose-resolved map of the thermal behavior of neutron-exposed h-BN nanoparticles and offer practical parameters for materials selection and lifetime modeling in nuclear and other high-radiation environments.

4-STUDY OF THE ANTIMIBROMIC PROPERTIES OF DIMETHYLAMINO-BENZYLIDENE THIOSEMICARBAZIDE COPPER ACETATE SALT

***Gasimli G.R., Babayev E.R., Mammadova P.Sh., Aminova B.M., Ibrahimova T.M., Almammedova A.E., Gahramanova K. R., Mammadova G.A.**

Institute of Additive Chemistry, Ministry of Science and Education, Azerbaijan
gulshengasımlı@gmail.com

Schiff base has been known by its name “Schiff” ever since Hugo Schiff first described it almost 160 years ago. The utilization of *Schiff bases* as ligands in *metal complexes* has demonstrated significant advancement in the field of *coordination chemistry*. A Schiff *base* is a carbonyl-containing aldehyde or *ketone* with a nitrogen-based counterpart. It is formed by condensing a *primary amine* with the *carbonyl group* and replacing it with an *imine* group called *azomethine*.

The reaction of 4-dimethylaminobenzylidene with copper acetate salt (2:1) was synthesized. The reaction of 4-dimethylaminobenzylidene thiosemicarbazide Schiff base with copper acetate salt gave 4-dimethylaminobenzylidene thiosemicarbazide copper acetate salt.

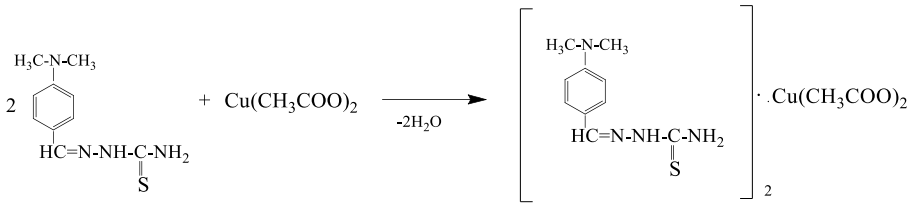

The additive is multifunctional and is applied to lubricating and cooling fluids (LCF), fuels, increasing their antimicrobial properties, resistance to corrosion, oxidation and wear. The additive we purchased has been proven to be of high quality. It has been confirmed by IR spectroscopy.

These compounds were determined to have antimicrobial properties by the zonal diffusion method in accordance with GOST 9.052-88 and GOST 9.023-74. Cladasporium resinae, which is widely distributed in oils and petroleum products and is an aggressive destroyer of them, was used in these studies.

Thus, the obtained compound of 4-dimethylaminobenzylidene thiosemicarbazide copper acetate salt at a concentration of 0.5% shows high properties in A-95 gasoline with bactericidal properties of 2.3-3.4 cm, fungicidal properties of 2.4-2.4 cm with a diffusion zone. The fuel itself does not have antimicrobial properties.

THE COMPLEX EFFECTS OF ORGANIC AND INORGANIC SALT ADDITIVES ON RHEOLOGICAL, ELECTRICAL, AND OPTICAL PROPERTIES ON AGAROSE-BASED HYDROGELS

Asadova A.H.
Baku State University, Azerbaijan
aynurasadova19@gmail.com

This study examines the complex effects of various organic and inorganic salts on the physicochemical properties of agarose-based hydrogels. The samples were modified with inorganic salts (NaCl, $CaCl_2$, KCl, KBr) and organic salts (sodium tartrate and sodium succinate). Rheological, electrical, and optical properties were systematically analyzed. Inorganic salts decreased the elasticity of the gels but enhanced their ionic conductivity, while organic salts improved the thermal stability and optical transparency of the hydrogels. The results indicate that both the type and concentration of salts can be effectively used to fine-tune the physicochemical properties of agarose hydrogels, making them suitable for biomedical and sensor applications.

PHYSICS OF GRAPHENE-BASED NANOSTRUCTURES: STUDY OF PROPERTIES

***Jafarov S., Hesenli E., Ismayilova Z.**
Nakhchivan State University, Azerbaijan
seyfadjafarov@gmail.com

In this article, graphene is treated as a special object, the properties of its electronic structure are presented in the light of the general concept of extraordinary phenomena caused by quantum phase transitions caused by persistent symmetry breaking. First, the violation of the spin symmetry of the electron system of graphene is related to the correlation of its excess pz-electrons. In order to determine the physical properties of carbon nanostructures (graphene, multi-walled carbon nanotubes) and to use them in the future to create devices based on them, suspensions were obtained for their controlled deposition. It was determined that the studied carbon nanostructures have good thermal and electrical conductivity. Thermal conductivity coefficients were determined for multilayer graphene and commercial multiwalled carbon obtained by the presented method. The structure of multilayer graphene sheets was studied using transmission electron microscopy. Using a modified Langmuir-Blodgett method, the possibility of creating thin, transparent, high-conductivity phnazic substrates based on multilayer graphene has been demonstrated order to determine the physical properties of carbon nanostructures (graphene, multiwalled carbon nanotubes) and to use them in the future to create devices based on them, suspensions were obtained for their controlled deposition. One method of obtaining graphene - graphite etching in the liquid phase - has been studied and described in detail. The distribution law for the lateral dimensions and thicknesses of the graphene sheets obtained by this method was determined. The method of placing single carbon nanostructures on the electrodes – dielectrophoresis - is demonstrated, its main features affecting the density and quality of the applied structures (amplitude of the applied voltage, application frequency and time, as well as the concentration of the suspension) are demonstrated. of applied carbon nanostructures) were determined.

DEPENDENCE OF REFLECTION AND EXTINCTION COEFFICIENT OF Nano-Si-Nanocomposite ON TYPE OF POLYMER MATRIX

***Surkhayli A.E., Shirinova H.A., Pashayev B.G., Jafarov M.A.**
Baku State University, Azerbaijan
afsana.surxayli@bsu.edu.az

Nanocomposite systems synthesized by incorporating nanosized particles exhibit superior optical, thermal, mechanical, and structural properties compared to conventional polymers. In these nanocomposites, optical behavior is mainly characterized by the refractive index (n) and extinction coefficient (k).

In this study, the optical properties of composites prepared by adding silicon (Si) nanoparticles at equal weight fractions (1.5 and 3%) to thermoplastic matrices with different molecular structures – polystyrene (PS) and polyvinyl chloride (PVC) – were investigated. The optical parameters of Si–PS and Si–PVC nanocomposites were analyzed within the wavelength range of 200–1200 nm using the ellipsometry method. Polystyrene is an amorphous, nonpolar, and transparent polymer. Its nonpolar nature limits its dielectric constant and interaction with light; however, this property makes PS a suitable candidate for modification with nanosized functional additives. Polyvinyl chloride, on the other hand, is a polar polymer with an approximate crystallinity degree of 10%. For both polymers, the refractive index generally ranges between 1.5 and 1.6. Experimental measurements revealed that, in both normal and anomalous dispersion regions, increasing the Si nanoparticle content from 1.5% to 3% in Si–PS nanocomposites led to only a slight increase in both the refractive and extinction coefficients. In contrast, a different tendency was observed for the Si–PVC system. The energy dependence curves of the refractive index showed anomalous dispersion near the absorption edge for both concentrations (1.5% and 3%) of Si–PVC nanocomposites. In this region, the refractive index values were determined as $n = 1.665$ for the Si(1.5%)–PVC nanocomposite and $n = 1.655$ for the Si(3%)–PVC sample. In the Si(3%)–PVC nanocomposite, defects created by the filler within the polymer's supramolecular structure cause light to propagate not through a homogeneous optical medium but through regions with locally varying density. This leads to a decrease in the effective optical density and, consequently, a reduction in the refractive index. The extinction coefficient, however, exhibited an increasing trend with rising nanoparticle concentration in both normal and anomalous dispersion regions. These results can be explained by the intensified aggregation of Si nanoparticles at a 3% concen-

tration in the Si–PVC composite system, which reduces the degree of dispersion and introduces defects into the polymer's supramolecular structure. The observed differences in optical behavior are also attributed to the distinct forbidden energy band gaps of PS and PVC polymers. Specifically, the band gap width of PS is approximately 4 eV, while that of PVC is around 5 eV. This difference affects the interaction mechanisms of the materials with light and their optical conductivity properties, leading to the distinct dispersion behaviors observed in the refractive and extinction coefficients.

PHOTOCONDUCTIVITY PROPERTIES OF GaS_xSe_{1-x} (x = 0.6) SINGLE CRYSTAL

***Jahangirova S.A., Abasova A.Z. Hasanova L.H., Mammadov E.Z.**
Baku State University, Azerbaijan
sonacahangirova@bsu.edu.az

Gallium selenide (GaSe) and gallium sulfide (GaS), belonging to the AIII–BVI group, form continuous solid solutions over the entire composition range. Various structural modifications are observed for all values of x, and crystallization in the β-modification occurs only when x ≥ 0.6. The dependence of the lattice parameters on composition (x) reveals that the a-parameter varies linearly with x, following Vegard's law regardless of the crystal structure, whereas the c-parameter exhibits a sharp variation.

In this study, the spectral characteristics of the GaS_xSe_{1-x} (x = 0.6) single crystal were investigated. The measurements were carried out using non-polarized light. The applied electric field was oriented parallel to the crystal layers, while the incident light was directed perpendicular to them.

Analysis of the spectral dependence of photoconductivity at different temperatures shows that the photoconductivity spectrum of the GaS_xSe_{1-x} (x = 0.6) single crystal decreases sharply in the short-wavelength region. This behavior indicates that surface recombination processes play a significant role in the studied crystal. The maximum of the photoconductivity spectrum coincides with the intrinsic luminescence maximum of the GaS single crystal.

A general feature of the spectral characteristics of the investigated solid solution is that the photoconductivity increases and the frequency range broadens as the temperature decreases.

ELECTROCHEMICAL PROPERTIES OF CERAMIC-POLYMER BASED PKR-3M COMPOSITE STUDIED BY EIS METHOD

Mehdiyeva N.
Karabakh University, Azerbaijan
nargiz.mehdiyeva@karabakh.edu.az

In this study, the electrochemical properties of the PKR-3M composite, consisting of ZnO nanoparticles dispersed in a Polycarbazole polymer matrix, were systematically investigated using Electrochemical Impedance Spectroscopy (EIS). The main objective was to evaluate the composite's electrical conductivity, dielectric behavior, relaxation mechanisms, and frequency-dependent response under alternating current (AC) excitation. Nyquist and Bode plot analyses revealed the presence of a single dominant relaxation process, primarily governed by intragrain conductivity. The semicircular Nyquist plot indicated a well-defined resistive-capacitive behavior, while the Bode plot confirmed the frequency-dependent reduction of impedance magnitude and phase shift. Dielectric constant measurements showed a decrease from approximately $\varepsilon' \approx 12.5$ at low frequencies to $\varepsilon' \approx 8.2$ at high frequencies, highlighting polarization effects at the grain boundaries. The temperature-dependent conductivity followed an Arrhenius-type behavior, enabling the calculation of the activation energy for charge transport in the composite. The results demonstrate that the synergistic combination of ZnO ceramic nanoparticles and Polycarbazole polymer matrix enhances dielectric stability, reduces energy loss, and improves electrical performance. These findings suggest that PKR-3M is a promising candidate for advanced applications in sensors, capacitors, energy storage devices, and electronic components, offering both high conductivity and mechanical stability.

PLASMON ENGINEERING IN GERMANENE, SILICONE ALLOTROPES AND GRAPHENE DERIVATIVES: A FIRST-PRINCIPLES STUDY

Vacacela G.C.
University of Calabria, Italy; Universidad Ecotec, Ecuador
cvacacela@ecotec.edu.ec

In this talk, we will present a unified ab initio investigation of collective charge excitations in low-dimensional group-IV and carbon-based nano-structures, with emphasis on how geometry and environment can be used as control

parameters for plasmon engineering. Using time-dependent density-functional theory within the random-phase approximation, complemented where necessary by Bethe–Salpeter–level corrections, we first analyze synthesized germanene nanosheets, both freestanding and supported on realistic substrates. The coexistence of linear (Dirac-like) and parabolic electronic bands in germanene is shown to give rise to infrared massless plasmons (with optical and acoustic branches) and to distinct massive plasmons associated with different families of heavy carriers. We demonstrate that their dispersion, spectral weight and damping can be finely tuned by substrate, strain and carrier concentration.

We then address flat-to-buckled allotropes of silicene and germanene, establishing quantitative links between lattice deformation, dielectric screening and plasmonic response. In particular, flat germanene emerges as an unconventional two-dimensional conductor in which Dirac fermions and metal-like carriers coexist at the Fermi level, supporting strong intraband plasmon modes in the far-infrared that are highly sensitive to externally imposed stress or strain.

Finally, we extend this framework to periodic planar arrays of narrow graphene nanoribbons. For zigzag and armchair ribbons, we predict distinct intraband and interband plasmons whose dispersions interpolate between one- and two-dimensional behavior and span energies from the terahertz /infrared to the visible. Their properties are shown to be strongly dependent on ribbon width, edge geometry, carrier injection and electronic temperature. Taken together, these results provide design rules for tailoring plasmon modes in realistic 2D and quasi-1D platforms for future nano-optics and optoelectronic applications.

ENHANCED ADSORPTION OF AIRBORNE RADIOISOTOPES BY A GRAPHENE-BASED MULTILAYER FILTRATION CARTRIDGE

Tene T.

Universidad Técnica Particular de Loja, Ecuador
tbtene@utpl.edu.ec

A graphene-based air filtration device was developed and evaluated for removing radioisotopes from air in gaseous and aerosolized forms. The device consists of three sequential layers, activated carbon (AC), graphene oxide (GO), and reduced graphene oxide (rGO), assembled in a cylindrical cartridge with air-permeable membranes. AC serves mainly to reduce humidity, while GO and

rGO, with their high surface area and tunable surface chemistry, adsorb radioactive species such as radon-222 (Rn-222) and iodine-131 (I-131). GO is synthesized from graphite via chemical oxidation, and subsequent reduction with ascorbic acid yields rGO. GO, rGO, and commercial AC are characterized by UV–Vis spectroscopy, FTIR, X-ray diffraction, and thermogravimetric analysis to confirm structural, chemical, and thermal properties relevant to adsorption.

Gaseous Rn-222 performance is studied in a closed two-chamber system with a natural radon source at secular equilibrium, using 3 g of each adsorbent separately. Adsorption capacities of 0.16 Bq/mg (AC), 0.77 Bq/mg (GO), and 1.13 Bq/mg (rGO) are obtained, corresponding to removal efficiencies of 7.1%, 32.5%, and 49.8%, respectively, relative to the no-adsorbent case. When combined in an optimized AC–GO–rGO configuration, the device removes ~85% of the accumulated Rn-222 activity in the closed chamber. Radioactive aerosol removal is assessed using I-131 in saline solution in a sealed chamber. Without filtration, the exposure rate follows the expected exponential decay; with the GO/rGO/AC cartridge, the decay curve becomes steeper, indicating active aerosol removal and yielding an effective adsorption rate of ~0.31 mR/h per hour. Overall, GO and rGO provide a substantial improvement over conventional activated carbon, and their integration with AC in a compact cartridge offers a practical strategy for mitigating airborne radioactivity in indoor environments such as residences, hospitals, and nuclear medicine facilities.

COMPARATIVE ANALYSIS OF SIMULATION AND EXPERIMENTAL RESULTS OF CdS/$Cd_{1-x}Mn_xTe$ HETEROJUNCTIONS FOR SOLAR CELL APPLICATIONS

[*1,2]Mehrabova M.A., [1]Safarov N.Y.

[1]Azerbaijan Technical University, Azerbaijan

[2]Institutue of Radiation Problems, Ministry of Science and Education, Azerbaijan

metanet.mehrabova@aztu.edu.az

This study presents a comparative analysis of simulated and experimental performance metrics for nCdS /p$Cd_{1-x}Mn_xTe$ heterojunction solar cells with manganese concentrations ranging from x=0.1 to x=0.4. The structural, morphological, and optical properties of the materials were examined using X-ray diffraction (XRD), scanning electron microscopy (SEM), ultraviolet–visible (UV–VIS) spectroscopy, photoelectrochemical (PEC) measurements, and electrometric techniques.

Using the SCAPS-1D (version 3.3.12) simulation software, the electrical

characteristics of these structures were modeled and validated against experimentally fabricated devices. The incorporation of manganese (Mn) atoms into the CdTe absorber layer enables bandgap engineering, allowing for tunable optical and electronic properties. As Mn concentration increases, the bandgap of p-$Cd_{1-x}Mn_xTe$ expands from 1.45 eV to approximately 1.65 eV, leading to an enhanced open-circuit voltage (Voc) and reduced parasitic absorption in the short-wavelength region. The n-CdS window layer exhibits high transparency and favorable conduction band alignment, promoting efficient carrier separation and minimizing recombination losses at the interface.

Simulation results show that the quantum efficiency (QE) increases sharply near 520 nm across all Mn concentrations, attributed to optimal photon absorption and carrier collection in the active region. The overall power conversion efficiency (η) improves with increasing Mn content up to an optimal range ($x \approx 0.1–0.2$), beyond which defect-induced recombination limits further enhancement. These findings highlight the potential of Mn-doped CdTe absorbers for improving the spectral response and efficiency of CdS/CdTe-based solar cells.

This work contributes to the development of high-efficiency, tunable heterojunction solar cells and provides a basis for further experimental optimization and device engineering.

DEVELOPMENT OF FOAM CONCRETE COMPOSITION BASED ON COMPOSITION ADHESIVES

Guvalov A.A.

Azerbaijan Architecture and Construction University, Azerbaijan
abbas.guvalov@azmiu.edu.az

One of the most important issues facing builders today is energy saving, ecology and creating comfortable living conditions. The use of foam concrete in the construction of buildings and structures can make a significant contribution to solving this problem. A significant increase in the efficiency of foam concrete is possible through the use of composite adhesives containing mineral additives. The use of both natural and man-made components as mineral additives in foam concrete will expand the raw material base, reduce the consumption of the energy-intensive and high-cost adhesive component - Portland cement, and control the processes of structure formation depending on the type of materials produced. Therefore, the purpose of the study is to develop an efficient foam

concrete composition using a composite adhesive (KY) obtained on the basis of the tras.

When developing the composition of foam concrete, concrete with a density of D600 and D800 and a compressive strength of not less than 1.5 MPa was considered as the most optimal brand. Mikroair-220 was used as a foam-forming component.

Studies have shown that the strength indicators of foam concrete samples obtained on the basis of a composite adhesive containing 20% and 30% tras are 13-20% higher than those of cement-based samples. This is due to the monodisperse distribution of macropores due to puzzolanization and an increase in the viscosity of foam concrete (according to the Suttard viscometer).

When the amount of tras in the KY is increased to 40%, the strength of foam concrete decreases by 20-28% compared to cement-based samples, and by 48% compared to samples with a 30% tras content. The decrease in the strength of foam concrete is due to a decrease in the clinker fraction in the adhesive.

The results of microscopic analysis showed that the pores of the KY-based foam concrete with a 20% tras content are mainly closed. When the amount of tras is increased to 30%, the size of the pores decreases slightly. When the amount of tras is 20-30%, the surface of the pores becomes more homogeneous. This is due to the deeper hydration of clinker minerals and the filling of microvoids with new compounds formed as a result of the pozzolanic reaction. When the trace amount reaches 40%, new large pores with a non-uniform surface are formed, which indicates a high total porosity. The collapse of the pore walls, as well as their merging, is observed, which leads to the occurrence of the sedimentation process and a decrease in the homogeneity of the microstructure. Thus, the compositions prepared in the research work allow the production of foam concrete with the following characteristics: density – 600–800 kg/m^3; compressive strength limit -2.0-3.0 MPa; thermal conductivity – 0.11–0.14 W/(m·°S); shrinkage 2.3-2.7 mm/m. Based on the obtained indicators, foam concrete meets the requirements set by regulatory documents for construction and thermal insulation materials: density grade D600-D800, strength class B1.5-B2, frost resistance grade F25, and shrinkage when dry not exceeding 3 mm/m.

THE ROLE OF ION MIGRATION AND HYSTERESIS IN PEROVSKITE SOLAR CELLS: MODELING CHARGE TRAPPING AND RELEASE MECHANISMS VIA DRIFT-DIFFUSION

***Najafzade N.E., Mammadov F.**
Azerbaijan National Aerospace Agency, Azerbaijan
necefzadenurlan@gmail.com

Metal-halide perovskite solar cells (PSCs) promise high efficiency at low cost, but their commercial viability is hindered by operational instability, most notably the anomalous current-voltage (J-V) hysteresis. This phenomenon is widely attributed to the mixed ionic-electronic conductivity of the perovskite material. In this work, we develop a comprehensive numerical model based on the drift-diffusion (D-D) framework that explicitly couples the transport of electronic charge carriers (electrons, holes) with the migration of mobile ionic species (e.g., iodide vacancies). We simulate the device operation under transient conditions, replicating forward and reverse voltage sweeps. Our model demonstrates that hysteresis is a direct consequence of mobile ion accumulation at the perovskite/transport-layer interfaces. This pile-up of ionic charge screens the internal electric field, alters the energy bands at the contacts, and – most critically – modulates the occupation and activity of electronic trap states.

We show that the coupling between ion distribution and trap-assisted recombination at the interfaces is the primary physical mechanism governing the scan-rate-dependent J-V curves. The model quantitatively links key physical parameters, such as ion mobility (μi) and trap density (Nt), to the hysteresis index, providing a clear pathway for device engineering to mitigate this instability.

SURFACE PROCESSES OF CsCl INTERACTION WITH BARIUM ISLANDS: ROLE OF EDGE ATOMS AND TEMPERATURE FACTOR

Abdullayev T.Sh., *Sarmasov S.N.
Baku State University, Azerbaijan
suleymansarmasov@bsu.edu.az

The interaction between two-dimensional barium islands and CsCl molecules on the surface of a graphite monolayer deposited on a rhenium substrate (Re–2DGF) has been investigated. Special attention is given to the role of edge atoms and the effect of temperature on the catalytic dissociation of CsCl. The

experiments were carried out under ultra-high vacuum conditions using a static magnetic mass spectrometer, thermodesorption spectroscopy, and ion spectral analysis. These methods allowed the identification of the adsorption and decomposition mechanisms of molecules at the graphite–rhenium interface.

It has been shown that barium atoms on the Re–2DGF surface can exist either as two-dimensional islands or as individual chemisorbed atoms, significantly influencing their interaction with CsCl. At elevated temperatures (1150–1400 K), the edge atoms of the barium islands exhibit pronounced catalytic activity, enabling a two-step exchange mechanism of CsCl dissociation with the formation of BaCl, $BaCl_2$, and Cs^+ ions. The island edges function as active catalytic centers whose reactivity increases proportionally with the CsCl molecular flux.

At lower temperatures (T < 800 K), the catalytic activity decreases sharply due to chlorine accumulation on the island edges, leading to their deactivation. Short-term annealing at high temperatures (~1400 K) restores the activity through chlorine desorption, indicating the reversible nature of adsorption and surface diffusion processes.

Thus, the catalytic properties of barium islands are governed by their phase state and the chemical composition of their edge atoms. At high temperatures, they act as efficient centers for dissociation, while at low temperatures their activity becomes limited. These findings are important for understanding surface chemistry involving alkaline-earth metals on carbon substrates and for the development of catalysts designed for halide dissociation processes. The revealed temperature dependence of activity emphasizes the necessity of precise thermal control during catalyst operation under extreme conditions.

DENSITY FUNCTIONAL THEORY PERSPECTIVE ON THE TRICLINIC SYSTEM OF $NiFe_2O_4$

***Sadıgova A.A., Mammadova S.O.**

Institute of Physics, Ministry of Science and Education, Azerbaijan
amidesadiqova@gmail.com

The various research groups explored experimentally the structural, optical, and magnetic behaviours of inverse spinel and mixed spinel $NiFe_2O_4$. Note that the number of ab initio density functional theory based on the structural optoelectronic and magnetic properties of $NiFe_2O_4$ is restricted. The majority of the first principle studies reported to appreciate the structural, electronic, and

magnetic properties of NiFe2O4 take into account the calculations of full potential.

In this report, the structural and electronic properties of $NiFe_2O_4$ were investigated using the ab initio density functional theory. Exchange–correlation energy with Hubbard correction (SGGA +U) was estimated using the Perdew–Burke–Ernzerhof spin generalized gradient approximation. SGGA +U formalism is useful for investigating the semiconducting and ferrimagnetic properties of $NiFe_2O_4$. The anti-parallel spin configuration of tetrahedrally and octahedrally occupied Fe atoms helped to understand the ferrimagnetic property of $NiFe_2O_4$. Spin-polarized band structure calculations of the triclinic system of $NiFe_2O_4$ occur in an indirect band gap of 2.27eV (Fig.1 b). Figure 1 illustrates the atomic and electronic structure of the $NiFe_2O_4$.

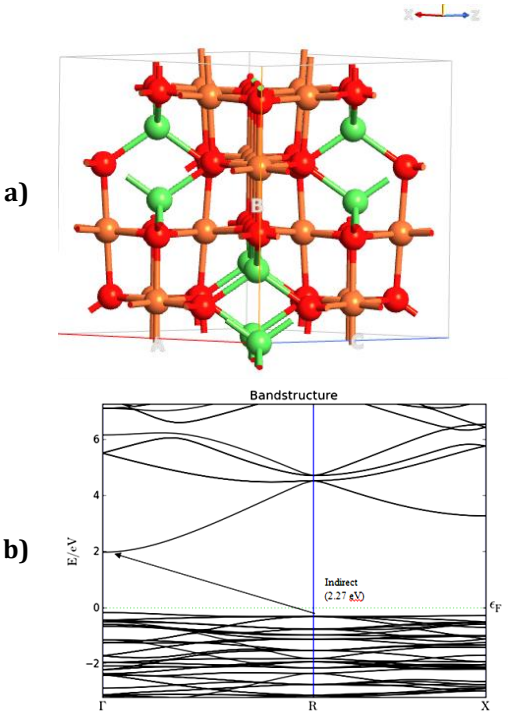

Fig. 1. a) atomic and b) electronic band structure for the triclinic system of $NiFe_2O_4$.

The $NiFe_2O_4$ refers to a crystal structure that consists of 56 atoms, out of which 24 atoms are transition metals of Ni and Fe in a specific arrangement. Relaxed and optimized cell parameters of the triclinic system of $NiFe_2O_4$ with the lattice parameter a=8.48Å are in good agreement with experimental and theoretical calculations.

OPTICAL AND STRUCTURAL CHARACTERIZATION OF Ga_2O_3 THIN FILMS DEPOSITED BY RF MAGNETRON SPUTTERING AT DIFFERENT OXYGEN RATIOS

***Hopoğlu H., Tüzemen Şenadim E.**
Sivas Cumhuriyet University, Türkiye
akalan23@hotmail.com

Gallium oxide (Ga_2O_3) is one of the materials widely investigated for optoelectronic applications, especially UV detector technologies, due to its wide bandgap semiconductor nature and high transmittance in the deep-ultraviolet region. Producing Ga_2O_3 in thin-film form is important because the optical and structural properties of the material are highly sensitive to processing parameters.

In this study, Ga_2O_3 thin films were deposited by RF magnetron sputtering at different oxygen ratios (1%, 2%, and 3% O_2). To evaluate the effects of thermal treatment, the fabricated films were annealed in air at 850°C for 1.5 hours.

Cross-sectional images were obtained by scanning electron microscopy (SEM) to determine the thicknesses of the films. For optical characterization, the transmittance spectra of the films were measured using a spectrophotometer, and these data were used to calculate the energy band gap values.

As a result, it was observed that variations in oxygen ratio and the annealing process produced notable effects on the optical properties of the films.

This work was supported by the Scientific Research Project Fund of Sivas Cumhuriyet University, Turkey, under the project number F-2025-736.

OPTİCAL PROPERTİES OF ZnSe FİLMS DEPENDİNG ON ANNEALİNG FOR OPTİC APPLİCATİONS

***Bulut E.E., Tüzemen Şenadım E.**
Sivas Cumhuriyet University, Türkiye
2025Zincceleumhuriyet.edu.tr

Zinc Selenide (ZnSe) is a good candidate for highly transparent optical components. It is used to create II-VI light-emitting diodes and diode lasers. Its refractive index ranges from 2.67 to 2.40 between 550 nm and 10.6 μm. ZnSe is a semiconductor with an average band gap of 2.70 eV at 25°C. It also has a melting point of 1525°C and a cubic crystal structure. It can be found as the input optic in the new series of "in-ear" clinical thermometers, often seen as a small

yellow window in everyday life.

When considering the use of ZnSe thin films in solar cell technology, ZnSe is one of the strongest candidates for replacing cadmium sulfide (CdS) among Cd-free buffer layers. In addition to its environmental advantages, the wider band gap of ZnSe (approximately 2.7 eV) compared to CdS (approximately 2.4 eV) contributes to the photocurrent density by increasing the transmittance of blue light. Furthermore, because ZnSe exhibits a good lattice match with the $Cu(In,Ga)(S,Se)_2$ composition, various solar cell structures using ZnSe thin films as buffer layers have been reported in the literature, such as CIGS (copper-Indium-Gallium-Selenide), dye-sensitized solar cells (DSSC), and CdTe-based photovoltaic devices.

In this study, ZnSe was produced on glass substrate using an RF magnetron sputterin system. The produced films were annealed at different temperatures. The transmittance and absorbance of all films were measured with an optical spectrophotometer. Based on these data, the energy band gap of the ZnSe film before annealing was found to be approximately 443 nm = 2.799 eV.

FLUORIDE-DERIVED SYNTHESIS OF SiO_2

*Ahmadov Kh.I., Pashayev B.G., Rahimli A.M., Aliyev L.P., Mammadov V.U.
Baku State University, Azerbaijan
xaqan.ahmadov@bsu.edu.az

Silicon dioxide (SiO_2), commonly known as silica, is one of the most abundant and versatile materials in both natural and industrial contexts. Its unique physicochemical properties, such as high thermal stability, chemical inertness, optical transparency, and tunable surface chemistry, make it an essential material in diverse applications ranging from catalysis and ceramics to electronics, biomedical engineering, and nanotechnology. The functional versatility of SiO_2 arises from its ability to form highly ordered frameworks, porous structures, and nanoscale morphologies, which can be precisely tailored for specific applications. Consequently, the development of efficient and controllable synthesis methods for SiO_2 remains a critical focus of materials research.

In this study, SiO_2 nanoparticles were synthesized by fluoride driven synthesis method. To evaluate the effects of thermal treatment, samples were prepared and annealed at different temperatures.

The thermal properties of the synthesized SiO_2 samples were examined using Differential Scanning Calorimetry (DSC). The measurements were condu-

cted to identify thermal events such as endothermic and exothermic transitions, assess thermal stability, and provide insight into structural changes occurring with temperature.

This thesis demonstrates that fluoride-driven synthesis is an effective and environmentally friendly method for producing high-purity, amorphous SiO_2 with controllable morphology and particle size. The fluoride-assisted approach enables precise structural tuning and efficient precursor utilization, making it a sustainable route for silica preparation.

Overall, this study confirms that moderate, controlled incorporation of fluoride-mediated SiO_2 provides both structural and functional advantages, establishing a solid foundation for future development of advanced silica-based materials.

STRUCTURAL AND SURFACE QUALITY ENHANCEMENT OF InGaAs LAYERS THROUGH TMIN FLOW ENGINEERING FOR QCL DEVICES

Özbakir F.K., Yolcu G., Perkitel I., Altuntaş I., *Demir I.
Sivas Cumhuriyet University, Turkey
idemir@cumhuriyet.edu.tr

In this study, the influence of trimethylindium (TMIn) flow on the structural and morphological properties of InGaAs layers – crucial components in quantum cascade laser (QCL) heterostructures – was systematically investigated. Six samples were grown under identical growth temperature, TMGa, and AsH_3 flow conditions. In contrast, only the TMIn flow was varied to isolate its effect on In incorporation, lattice matching, and interface quality relevant to QCL active-region engineering.

X-ray diffraction (XRD) measurements revealed a systematic shift of the InGaAs peak toward lower 2θ values with increasing TMIn flow, indicating higher In incorporation. The narrowest full width at half maximum (FWHM) values were obtained at intermediate TMIn levels, suggesting an optimum In composition for achieving improved crystalline quality and better lattice matching to the surrounding layers in QCL structures.

Atomic force microscopy (AFM) analyses showed that samples grown with low TMIn flow exhibited rougher island-like surface features, whereas intermediate TMIn values resulted in enhanced coalescence and minimized root-mean-square (RMS) roughness. At higher TMIn flow rates, increased roughness associated with In-rich clustering was observed, which may degrade interface

smoothness and lead to enhanced interface scattering in QCL devices.

Overall, the results demonstrate that optimizing TMIn flow enables the growth of InGaAs layers with reduced FWHM values and smoother surfaces, both of which are essential for high-performance QCL epitaxy.

Acknowledgments. This study is supported by the Scientific Research Project Fund of Sivas Cumhuriyet University, Turkey, under Project No. MRK-2024-004 and TÜBİTAK under Project No. 22-AG-074.

LOW-DEFECT InP/GaAs BUFFER LAYERS ON SI FOR MONOLITHIC PHOTONIC INTEGRATION

***Tariverdiev S., Demir I.**

Sivas Cumhuriyet University, Turkey

samirtariverdiyev@cumhuriyet.edu.tr

In the context of exponential growth in global data traffic, silicon photonics has established itself as a key platform for creating high-performance and energy-efficient data transmission systems. One of the main challenges on this path remains the integration of efficient light-emitting devices based on III-V group materials with silicon substrates. This work is dedicated to developing a monolithic integration technology via direct epitaxial growth of high-quality InP/GaAs heterostructures on silicon. The primary focus was on minimizing dislocation density and achieving optimal surface morphology, which is critically important for the subsequent creation of reliable electrically pumped lasers.

To address the stated tasks, the Metalorganic Chemical Vapor Deposition (MOCVD) method was employed. Optimization of GaAs buffer layers on silicon substrates with various orientations was conducted. To relax mechanical stresses at the GaAs/InP interface, InGaAs transition layers were developed and studied.

As a result, the feasibility of obtaining InP buffer layers with low defect density and a smooth surface was demonstrated. Comprehensive structural and optical analysis confirmed the high crystalline quality of the grown layers.

CONDENSED MATTER

DATABASE OF PHOSPHORESCENCE, RAMAN SCATTERING, AND INFRARED TRANSMISSION SPECTRA OF CRUDE OIL OF THE ABSHERON PENINSULA OF AZERBAIJAN

Pashayev A.M., Asgarov K.A., Musayev A.A., *Allahverdiyev K.R.
Azerbaijan National Academy of Aviation, Azerbaijan
kerim.allahverdi@gmail.com

The present research determines the feasibility of using phosphorescence, Raman, and Fourier Transform IR spectroscopy (FTIR) as a substitute for traditional crude oil petroleum geochemical methods for determining the characteristics of crude oil and various methods for determining the source of a crude oil leak. It is known that there are 12 Oil and Gas Producing Companies (OGPC) in the Republic of Azerbaijan, including 8 owned by Azerbaijan and 4 owned by Joint Stock Companies (JSC). Experience shows that in most cases of an oil spill, it is desirable to have more than one experimental method to determine the source of the alleged spill of crude oil and its properties. In our previously published articles, we describe the results of the phosphorescence, Raman scattering, and IR transmission spectra of a crude oil sample taken from 12 OGPC of the Azerbaijan Republic. All obtained results are used to create pf Database of phosphorescence, Raman scattering, and FTIR spectra of crude oil produced by OGPC of the Republic of Azerbaijan.

RESONANCE EMISSION OF InSe NANOPARTICLES BEYOND THE FUNDAMENTAL ABSORPTION EDGE

[1*]Salmanov V.M., [1]Guseynov A.G., [1]Jafarov M.A., [2]Ibragimov G.B., [1]Mamedov R.M.[1], [1]Akhmedova F.Sh., [1]Jafarli Kh.E.
[1]Baku State University, Azerbaijan
[2]Institute of Physics, Ministry of Science and Education, Azerbaijan
vagif_salmanov@yahoo.com

In the depth of the continuous spectrum of many semiconductors, absorption peaks are observed that can be interpreted as exciton states associated with minima of bands deeper than the bands forming the fundamental absorption edge. The formation of such states and their stability have not been studied

sufficiently, so the study of absorption beyond the fundamental absorption edge is of considerable interest. To conduct such studies, it is necessary to have thin crystals with a relatively small value of the absorption coefficient above the edge, the absence of surface defects, and powerful laser radiation with a tunable frequency in a wide energy range. In our opinion, layered InSe crystals are a convenient object for such experiments. Previously, we observed resonant radiation in the region of the continuous spectrum of InSe crystals. It was found that the detected radiation is associated with the presence of a "saddle" point in InSe corresponding to a hyperbolic exciton. Detection and study of hyperbolic excitons in InSe nanoparticles is of great interest, since in nanoparticles with sizes of several nanometers, the study of the features of the zone structure in the depth of the continuous spectrum of InSe is a unique opportunity. This work is devoted to the experimental study of the absorption and luminescence spectra of InSe nanoparticles beyond the fundamental absorption edge. InSe nanoparticles were synthesized by laser ablation in a liquid medium. From the absorption spectrum, it is seen that the absorption maximum corresponds to the energy of ~ 4.30 eV, exceeding the band gap of InSe nanoparticles approximately twice (Eg = 2.15 eV). When InSe nanoparticles were excited by the 2nd harmonic of a Nd: YAG laser ($\hbar\omega$=2.34 eV), luminescence with an energy corresponding to the absorption energy of nanoparticles (~4.30 eV) was detected. The comparatively large half-width of the emission line (~300 meV) of InSe nanoparticles is noteworthy, whereas this value for the edge luminescence of crystals is only a few meV. In addition, the intensities of both lines turned out to be almost the same, despite a large shift of the luminescence spectrum of nanoparticles to the short-wave region of the spectrum by ~2.15 eV. In InSe crystals, the emission intensity beyond the absorption edge turned out to be four orders of magnitude lower than the emission intensity of a parabolic exciton at the absorption edge. Thus, the results obtained in this work, in particular, the stability and significant half-width of the absorption and luminescence lines of InSe nanoparticles located in the short-wavelength region of the spectra, at distances commensurate with the width of the forbidden band of the nanoparticles, can be more consistently interpreted from the point of view of the concept of a hyperbolic exciton.

FEATURES OF ELECTRICAL CONDUCTIVITY OF SINGLE CRYSTALS OF CADMIUM-MERCURY-TELLURIUM SOLID SOLUTIONS IN STRONG ELECTRIC FIELDS

[1*]Abdinov A.Sh., [1]Amirova S.I., [2]Babayeva R.F., [1]Ragimova N.A., [1]Rasulov E.A.

[1]Baku State University, Azerbaijan
[2]Azerbaijan State Economic University, Azerbaijan
abdinov-axmed@yandex.ru

The low effective mass and high mobility of charge carriers, the tunability of composition and corresponding band gap over a wide range, as well as the possibility of controlled modification of defect parameters and surface processes through various methods, make $Cd_xHg_{1-x}Te$ crystals a highly promising material for solid-state physics and solid-state electronics.

In this work, we present the results of our experimental investigations on the peculiarities of the electrical conductivity of this semiconductor in strong electric fields, under conditions of carrier heating induced by the applied field. The studied objects were undoped $Cd_xHg_{1-x}Te$ single crystals ($0.30<x<0.90$) of both n- and p-type conductivity, grown by the Bridgman method. Carrier heating was achieved by subjecting the samples to rarely repeated microwave electric field pulses with a frequency of 10^{10} Hz.

The measurements were performed in the ranges of sample temperature T0=77÷300 K and microwave electric field strength Ê=5·101÷4·103 V/cm. The dependence of the electrical conductivity of the investigated samples on the applied microwave electric field strength (Ê) was experimentally determined, along with the kinetics of excess conductivity induced by the strong microwave field at different T_0 values. It was established that, within the considered temperature interval T_0, when the applied microwave field strength exceeded a certain critical threshold (Êcr), the specific conductivity (σ) of the studied $Cd_xHg_{1-x}Te$ samples exhibited changes relative to their initial value (σ_0). The sign of this change (increase or decrease in σ) was found to depend on the conductivity type, composition (value of x), temperature, and the magnitude of Ê. At lower T_0, nearly all studied samples demonstrated $\sigma>\sigma_0$, whereas at higher T_0, a decrease in σ relative to σ_0 was observed. In both regimes, the dependence of $|\sigma-\sigma_0|/\sigma_0$ on Ê followed a power-law behavior.

Analysis of the obtained results revealed that the observed σ(Ê) dependence in the studied $Cd_xHg_{1-x}Te$ crystals is directly associated with carrier heating by the applied electric field and reflects a drift rather than a concentration

mechanism. At lower T_0 and moderate field strengths Ê, the charge carriers can be regarded as "warm." However, with further increases in Ê, the carriers experience stronger heating and enter the "hot" carrier regime, where the σ(Ê) dependence exhibits the characteristic behavior expected for hot carriers heated by an electric field.

DEFECT STATES OF PEROVSKITES $A'_{0.5}A''_{0.5}MnO_3$

***Jabarov S.H., Hakhverdiyeva Z.E.**

Institute of Physics, Ministry of Science and Education, Azerbaijan
sakin@jinr.ru

Studies conducted on $Nd_{0.5}Ca_{0.5}MnO_3$, $Nd_{0.5}Sr_{0.5}MnO_3$, and $Pr_{0.5}Ca_{0.5}$ MnO_3 perovskites revealed that ionic substitution significantly affects the crystal and defect structures. According to the XRD results, all samples were synthesized in an orthorhombic symmetry consistent with the Imma space group. Due to the large ionic radius of Sr, the lattice volume of the $Nd_{0.5}Sr_{0.5}MnO_3$ sample was the highest (V = 225.985 Å^3), followed by Pr-doped (221.890 Å^3) and Ca-doped (219.874 Å^3) samples. Raman spectroscopy demonstrated the influence of ionic composition on local symmetry and Jahn–Teller distortions. The Pr-based composition sample exhibited stronger phonon resonance and higher structural ordering. In the PALS analysis, the $Nd_{0.5}Sr_{0.5}MnO_3$ sample showed the highest positron mean lifetime (τ_{mean} = 0.233 ns), reflecting increased defect volume and reduced local electron density. The lowest values of τ_{mean} = 0.207 ns and τ_2 = 0.765 ns were observed in the $Pr_{0.5}Ca_{0.5}MnO_3$ sample. The two-state positron trapping model confirmed that the Sr-doped sample exhibited the highest trapping rate (k_d = 21 ns^{-1}) and the largest defect size indicator ($\tau_2 - \tau_b$ = 0.698 ns), confirming the highest defect density. These results were supported by DBAS and EMD analyses, which revealed that the $Pr_{0.5}Ca_{0.5}MnO_3$ composition preserves the strongest Mn d-orbital character and most coherent eg electron environments. The reduced local electron density in the Sr-doped sample may indicate electron redistribution from defect sites, potentially influencing charge transport mechanisms. In conclusion, the ionic composition directly influences the structural integrity, the preservation of Mn d-orbital character, and the localization of eg electrons around Mn sites. These findings demonstrate that tuning the A-site ion balance enables regulation of the structural and functional properties of perovskites.

THEORETICAL QUANTUM CHEMICAL MODELING OF THE STABILITY OF MANGANESE BORIDES UNDER EXTREME PRESSURES

Bazarbek A.
Eurasian National University, Kazakhstan
asyl.bazar.92@gmail.com

Hard and superhard materials with strict hardness criteria (HV > 20 and > 40 GPa) play a key role in various industrial applications, stimulating active research and development. In recent years, transition metal borides have attracted attention as promising materials with unique combinations of physical properties such as high strength, wear resistance, and electrical conductivity. The largest volumetric compression modules among transition metal borides are OsB_2 (361 GPa) and ReB_2 (359 GPa), and the hardest is WB5 with a Vickers hardness of 45 GPa, which classifies it as a superhard material.

Most transition metal borides, which have excellent mechanical properties such as high hardness, are typically formed at high pressures and are characterized by specific stoichiometry and structure. Although significant progress has been made recently in the prediction and synthesis of new borides in Ti–B, Sc–B, Fe–B, Ni–B, Zr–B, etc. systems, but the Mn–B system has not been sufficiently studied at high pressures, despite advances in the study of nitrides and borides of other transition metals. This study is devoted to the theoretical assessment of the thermodynamic stability and mechanical properties of manganese borides over a wide range of pressures and temperatures (0-200 GPa and 0-2000 K).

In the present study, the calculation of the search for stable crystal structures was carried out using evolutionary algorithms implemented in the USPEX software package. All calculations were carried out within the framework of density functional theory using the VASP software package.The lattice dynamics method within the quasi–harmonic approximation was used to account for the temperature effect and construct phase P-T diagrams. Phonon calculations were performed using the finite shift method and the supercellular approach implemented in the Phonopy program, with a supercell size of 2×2×2. In this case, the cut-off energy threshold was increased to 800 eV.

A convex hull diagram was used to assess the stability of compounds relative to their decomposition into an isochemical mechanical mixture. These data are necessary to assess the comparative stability of the studied compounds. During the study, we identified two stable compounds on the manganese–enriched side of the Mn-B binary system: Mn_2B and MnB. Both borides remain stable over the entire pressure range under consideration. Six stable compounds

were predicted on the boron-enriched system side: Mn_3B_4, Mn_2B_3, MnB_2, MnB_3, MnB_4, and MnB_6. It should be noted that six of these compounds are classified as solid materials.

The results obtained in the course of this study are of fundamental importance and make a significant contribution to the study of transition metal compounds with light elements.In addition, the data obtained can serve as a basis for determining the priorities of further theoretical and experimental research.

THE INFLUENCE OF A UNIFORM MAGNETIC FIELD ON DISCHARGE DEVELOPMENT IN A LONG TUBE WITH VARIABLE DISTRIBUTED CAPACITANCE

Agayev M.N.
Baku State University, Azerbaijan
mustafaagayev1950@gmail.com

The present study provides a detailed experimental investigation into the influence of a uniform magnetic field on the spatiotemporal evolution of electrical discharge in a long dielectric tube possessing a variable distributed capacitance. To the authors' knowledge, this work represents the first systematic analysis of discharge dynamics in such a configuration. Experiments were performed in inert gases (argon and helium) under pre-ionized conditions and within a pressure range of 0.2–9 Torr. A sinusoidal voltage U(t) was applied between the ignition electrode (IE) and a series of ring-shaped electrodes forming a uniformly distributed capacitive system along the tube length. Under these conditions, gas breakdown was observed to occur twice during each voltage oscillation period: first, during the rising phase of U(t), corresponding to wall charging, and second, during the falling phase, associated with wall discharge.

The paper presents comprehensive results demonstrating how an externally applied longitudinal magnetic field alters the principal discharge characteristics, including breakdown initiation, propagation behavior, and current–voltage dynamics. The findings elucidate the fundamental role of magnetic confinement in modifying electron trajectories and plasma formation processes in extended capacitive discharge systems.

The experimental setup consists of a cylindrical glass gas-discharge tube with a total length of 0.9 m and an internal diameter of 0.3 m. The tube was filled with argon gas at a pressure of P = 0.28 Torr. Argon was selected due to its widespread use in fluorescent lamp technology, for which the present

discharge system serves as a simplified physical model.

Along the entire length of the tube, aluminum foil electrodes were arranged as ring-shaped plates. Each plate has a width of 3×10^{-2} m, and the inter-plate spacing is 1×10^{-2} m. The first three rings were directly attached to the surface of the glass tube, whereas dielectric spacers of varying thickness – ranging from 2×10^{-4} m to 1×10^{-8} m – were inserted between the remaining plates and the tube wall. This configuration ensured that the distributed capacitance gradually decreased along the tube length in the direction away from the ignition electrode. The ratio between the capacitance of the first plate, C1, and that of the final plate, Cn, was approximately 20:1, thereby forming a controlled gradient of capacitive coupling along the discharge path.

To examine the influence of a non-uniform magnetic field on the ionization front velocity, specialized measurements were conducted based on the temporal shift of voltage pulses detected within the plate circuit. During these tests, portions of the electrode array were positioned within the non-uniform field region near the output of a solenoid. The solenoid was displaced axially relative to the discharge tube such that several electrode plates were located at its terminal zones. It was determined that the propagation velocity of the ionization front remained unchanged even when traversing regions of non-uniform magnetic induction near the solenoid's entrance and exit. The non-uniform magnetic region was experimentally found to extend approximately 8 cm into the solenoid from each end, ensuring that several plates were indeed within the gradient zone.

Further analysis demonstrated that modifying the distributed capacitance along the tube's axis did not produce any significant change in the ionization front velocity, provided that the initial capacitance values (C_0) – from which the discharge wave originates – were identical. In both configurations, where the capacitance was made to either increase or decrease uniformly, the observed results consistently indicated that, under all tested discharge conditions, the ionization front velocity was independent of the applied magnetic field induction.

SURFACE IONIZATION OF BARIUM ATOMS ON THE (100) CRYSTALLOGRAPHIC SURFACE OF MOLYBDENUM IN HIGH VACUUM

Orujov A.K., *Jafarova A.V.
Baku State University, Azerbaijan
ariforucov@bsu.edu.az

When a flux of atoms or molecules impinges on the surface of a high-temperature metal, positive or negative ions may be formed depending on the physical and chemical properties of the surface (surface ionization). Let the flux of atoms incident on the metal surface by ν, the flux of neutral atoms desorbing from the surface by ν_0, and the flux of positive ions by ν^+. It is clear that $\nu = \nu_0 + \nu^+$. The degree of surface ionization is defined as $\alpha = \nu^+/\nu_0$, and the surface-ionization coefficient as $\beta = \nu^+/\nu_0 = \nu^+/(\nu_0 + \nu^+)$. The parameters satisfy $0 < \alpha < \infty$. Theoretically, α is calculated by the expression

$$\alpha = \frac{Q^+}{Q_0}\, exp\left(\frac{e(\varphi - V)}{kT}\right),$$

where Q^+/Q_0 is the ratio of the statistical weights of the ionic and atomic states, eφ is the work function, and eV is the ionization energy of the atoms.

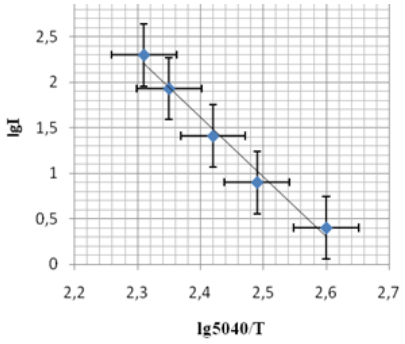

Figure. Dependence of the barium ion current on the inverse value of the sample temperature.

To study the surface ionization of barium atoms, a flux of barium atoms from a Knudsen cell was directed onto the surface of a molybdenum ribbon in a sector-type mass spectrometer under high-vacuum condition ($P = 10^{-9}$ Torr). In the case of difficult ionization, when $e(V - \varphi) \gg kT$, the current intensity.

$$I^+ = e\nu S\frac{Q^+}{Q_0} exp\left[\frac{e(\varphi - V)}{k\,T}\right].$$

Using this expression, the work function was determined from the slope of the dependence $lnI^{+}(5040/T)$, where $tg\alpha = e(\varphi - V)/k$. The obtained value $e\varphi = (5{,}1 \pm 0{,}05)eV$, agrees well with the known data. Since the ionization energy of the barium is $eV = 5{,}21\ eV$, the condition $e(\varphi - V) \ll kT$ is satisfied for the molybdenum surface. This value of the work function for molybdenum corresponds to its (100) crystallographic face and agrees well with the values obtained by other methods. The variation if the barium ion current with temperature indicates partial ionization of the barium atoms.

NONRECIPROCAL TRANSPORT PHENOMENA AND DIODE EFFECT IN SUPERCONDUCTORS

*Askerzade I.N., Yerin Y.
Ankara University, Türkiye
National Research Council, Italy
imasker@eng.ankara.edu.tr

The discovery of the superconducting diode effect has opened a new frontier in nonreciprocal quantum transport. Unlike conventional diodes, which rely on dissipative semiconducting mechanisms, the dııd effect enables dissipationless current flow in one direction and resistive response in the opposite. This unique functionality arises when both inversion symmetry and time-reversal symmetry are broken in superconducting systems, leading to asymmetric current-voltage characteristics and finite diode efficiency. In this talk, firstly introduce the concept of nonreciprocal transport and the definition of the supercurrent diode effect. We then outline several “recipes” and demonstrate key ingredients for engineering superconducting diodes, including polar superconductors with spin–orbit coupling, finite-momentum superconductors, Josephson junctions and SQUIDs with unconventional current phase relations, and systems exploiting asymmetric vortex dynamics. Special emphasis is placed on our recent theoretical contributions to multiband superconductors, where broken time-reversal symmetry produces novel rectification effects, and on Josephson junctions based on fractal superconductors, where fractional-order Ginzburg-Landau theory provides a powerful tool to describe nonlocality (fractality) and emergent diode behavior. Finally, we discuss the state-of-the art of efficiency of superconducting diodes across different material materials and platforms, and comment on potential device applications in quantum electronics.

A SPECTRAL METHOD FOR INVESTIGATING THE SECOND HARMONIC GENERATION (SHG) SPECTRUM

***Kasumova R.J., Ahmadova A.R.**
Baku State University, Azerbaijan
ranaqasimova@bsu.edu.az

The investigation of various nonlinear interaction models in metamaterials provides critical insight into the capabilities of these engineered media with unconventional optical properties and allows for the identification of their potential applications. In the present study, we focus on second harmonic generation (SHG) in a metamaterial exhibiting both quadratic and cubic nonlinearities under ordinary–ordinary (oo) scalar phase matching, assuming that the medium behaves as left-handed solely at the pump frequency ω_1. For the analysis of nonstationary SHG, a spectral approach is conventionally employed. By solving these spectral equations, the amplitude of the SH field can subsequently be determined from the calculated spectral components. The study of various nonlinear interaction models in metamaterials provides a comprehensive understanding of the capabilities of these artificial media with unconventional optical properties and allows for the identification of their potential applications. In this work, we investigate second harmonic generation (SHG) in a metamaterial exhibiting both quadratic and cubic nonlinearities under ordinary–ordinary (oo-e scalar phase matching). It is assumed that the medium behaves as a left-handed material solely at the pump frequency ω_1. In the analysis of nonstationary second harmonic generation (SHG), a spectral approach is commonly employed. Within this framework, the differential equation governing the field amplitudes is transformed, leading to an equation for the spectral amplitudes. By solving this spectral equation, the amplitude of the second harmonic field can subsequently be determined from the calculated spectral components. It is well known that ultrashort pulses are characterized by a relatively broad frequency spectrum, where the spectral width Δω is related to the pulse duration τ through the relation $\Delta\omega \geq 1/\tau$. To implement the spectral approach, the SH field amplitude $A_2(z,\mu)$ is expressed in the form of a Fourier integral.

$$A_1(\mu) = \int_{-\infty}^{\infty} \Phi_1(\xi) e^{i\xi\mu} d\xi$$
$$A_2(z,\mu) = \int_{-\infty}^{\infty} \Phi_2(z,\Omega) e^{i\Omega\mu} d\Omega, \Omega = \omega - 2\omega_1 \quad (1)$$

Next we introduce the function

$$\Lambda_2(z,\Omega) = \Phi_2(z,\Omega)e^{-i(\nu\Omega-\gamma_{21}I_{1l})z+i(\nu'\Omega+\gamma_{21}I_{1l})z}$$

and the generalized detuning is introduced

$$\varphi = \Delta - \nu\Omega + \gamma_{21}I_{1l},\ \ \varphi' = \Delta + \nu'\Omega + \gamma_{21}I_{1l}.$$

Then, equation (3) can be rewritten in the form:

$$\frac{\partial\Lambda_2}{\partial z} = \left[\frac{d\Phi}{dz} - i(\nu\Omega + i\gamma_{21}I_{1l})\Phi_2\right] e^{-i(\nu\Omega-\gamma_{21}I_{1l})z-i(\nu'\Omega+\gamma_{21}I_{1l})z} \qquad (2)$$

After performing the successive transformations, the spectral amplitude of the second harmonic is obtained as:

$$|\Phi_2(z,\Omega)|^2 = \frac{\left(\gamma_2 A_{1l}^2\ \tau_1 z\right)^2}{8\pi} e^{-\frac{\Omega^2\tau_1^2}{4}} sinc^2\frac{(\nu\Omega + \Delta + \Delta^{NL})}{2} z, \qquad (3)$$

where $\Phi_2(z,\Omega)$ – the amplitude of the second harmonic spectrum, $\nu = u_2^{-1} + |u_1|^{-1} - \omega_1$ Relation for the group velocities in a material with a negative refractive index at the corresponding frequency, $\Omega = \omega - \omega_2$ – the central frequency of the fundamental radiation, τ_1 – At the input of the medium, the fundamental radiation is represented by a Gaussian pulse with amplitude $A_1(z = l, t) = A_{1l}\ exp(-t^2/\tau_1^2)$. In conclusion, analyzing the SHG process through frequency spectrum analysis provides a clear and precise understanding of the fundamental interaction mechanisms.

THE FABRICATION OF PHOTONIC SENSORS-BASED Al/(AgZnO:rGO-PVA)/Al VIA CONTROLLING SOLAR PHOTON INTENSITIES IN THE WIDE RANGE OF VOLTAGE AND ILLUMINATION INTENSITIES

Şemsettin Altındal
Gazi University, Ankara, Türkiye
altundal@gazi.edu.tr

In this study, Al/(AgZnO:rGO-PVA)/Al photodiodes were produced and then both their electric and optoelectronic parameters, charge transport mechanisms (CTMs) investigated by using the current-voltage (*I-V*) characteristics both in dark and under illumination range of 0-100 mW/.cm^{-2} at room-temperature (RT). Their capacitance/conductance-voltage (C/G-V) measurements were performed at 1 MHz. Firstly, some fundamental electrical parameters of them were extracted from thermionic emission (TE) model by utilizing I-V, C-V, and G/w-V characteristics. Secondly, their photosensitivity (S), photo

responsivity (R), and photo detectivity (D*) values were found as function of voltage under each illumination intensity. These parameters were found to be quite sensitive to light intensity as well as applied bias voltage, so they can be successfully used in photonic sensor applications instead of conventional metal /semiconductor (MS) structures with/without insulator layers grown by traditional methods. The open-circuit voltage (V_{oc}), short-circuit current (I_{sc}) and filling factor (FF) values calculated from the I-V curve for 100 mW/cm^2. The voltage dependent resistance (R_i) and energy dependent profile of interface-states (N_{ss}) were obtained from the forward-bias I-V measurements. Thirdly, the density of doping donor-atoms (N_d), barrier-height (Φ_B(CV)), Fermi-energy (E_F), depletion layer (Wd), and maximum electric-field ($\mathbf{e}_{max}$) were also calculated from the reverse bias C^{-2}-V plot at 1 MHz.

ADVANCEMENTS AND APPLICATIONS OF THE FRENKEL-POOL EFFECT IN ORGANIC SEMICONDUCTORS

Qaraev E.S., *Ragimov R.Sh.

Baku State University, Azerbaijan
rahimrahimov@bsu.edu.az

In modern organic electronics, the study of thin-film structures and their electrical contact properties is of great importance for improving the performance of microelectronic devices. This work systematically investi-gates the generation and transport of charge carriers in organic semiconductor films under the influence of the Frenkel-Pool (FP) effect. The study was conducted on metal–semiconductor–metal (M–S–M) thin-film structures through the analysis of their current–voltage characteristics. The absence or minimal presence of high-resistance electrode barriers created favourable conditions for studying linear and nonlinear current-voltage dependencies.

Experimental results showed that at low voltages, the current increases linearly with voltage, whereas at higher voltages, a nonlinear increase is observed. It was established that the nonlinear growth is associated with the FP effect, where thermally trapped charge carriers are more easily released under the applied electric field. In weak fields, the current-voltage dependence is characterized by two activation energies: 0.5 eV and 0.7 eV (in kT units), where 0.5 eV corresponds to the depth of dominant traps and 0.7 eV represents intrinsic conductivity. These results are in good agreement with literature data. In strong fields, the rapid current increase is explained by the reduction of trap barriers according to the FP theory.

The film thickness was approximately 0.72 μm, and the FP barrier values derived from the experiments were in good agreement with theoretical calculations. Conductivity dependence on voltage in FP coordinates at different temperatures showed that in weak fields, conductivity is almost voltage-independent, while in strong fields, it increases by several orders of magnitude. This demonstrates good agreement between experimental data and theoretical modeling.

These findings contribute to a better understanding of the role of material selection and electrode interfaces in designing organic semiconductor devices. They allow prediction of charge carrier behaviour in thin films under an electric field and improve the efficiency of microelectronic active elements.

INFLUENCE OF RELATIVE HUMIDITY ON THE OPTICAL PARAMETERS AND CONDUCTIVITY OF FREE-STANDING POROUS SILICON FILMS

Mammadov H.M., *Sarmasov S.N.

Baku State University, Azerbaijan
suleymansarmasov@bsu.edu.az

The sensitivity of the optical and electrical characteristics of free-standing porous silicon (PS) films to porosity and relative humidity (RH) is investigated. The films were produced by anodizing p-Si(111) in an HF electrolyte under illumination; the typical thickness was ∼5–10 μm, and porosity varied within ∼30–90%. A portion of the samples was detached from the substrate to eliminate contributions from the Si-substrate/PS interface. Transmission spectra T(λ) were recorded at room temperature; the absorption coefficient α(hν) was calculated from paired measurements, and the band-gap width E_g was determined by linear fitting of the Tauc regions. The resistivity ρ was measured both along and across the pore axis to reveal the geometric anisotropy of conduction.

It is shown that increasing porosity leads to a monotonic blue shift of the absorption edge and a quasi-linear increase of E_g in the 30–90% range (typically from ≈1.4 to ≈1.9 eV). These trends are consistent with a quantum-confinement model in nanostructured silicon networks and with the growth of specific surface area. Electrical data demonstrate an increase of ρ with porosity and a difference between ρ∥ and ρ⊥, reflecting the directional channel morphology.

The effect of moisture manifests itself as (i) an additional rise in E_g when RH increases from ∼40 to ∼90%, and (ii) a time-dependent evolution of optical and electrical parameters during exposure to a humid atmosphere. The observed changes are interpreted in terms of diffusion of H/O-containing species

and water into the pore system, followed by the formation of surface Si–H and Si–O bonds. The dominance of Si–H passivation accounts for the enhanced blue shift and the increase in resistance due to a reduction in the density of surface states. The partial reversibility of the spectral effects after removing the samples from the humidity chamber indicates a dynamic adsorption–desorption balance and underscores the role of surface chemistry. Taken together, the results support the concurrent action of two mechanisms governing PS optics/luminescence – quantum confinement and surface-complex processes – with humidity "retuning" their relative contributions.

Practically, the findings show that E_g, resistivity anisotropy ρ, and response time constants can be engineered by selecting porosity (≈60–70%) and controlling RH. This provides a basis for calibrating and improving the stability of humidity sensors as well as optoelectronic and photonic devices based on PS, where surface–environment interactions are critical. Future work should include in-situ monitoring of Si–H/Si–O bond formation and a parametric decomposition of the contributions from water-vapor partial pressure, temperature, and pore-size distribution.

STUDY OF THE CRYSTAL STRUCTURE OF $TlIn(S_{1-x}Se_x)_2$ SEMICONDUCTOR COMPOUNDS BY X-RAY DIFFRACTION

Sharifov R.R., *Dashdemirov A.O., Abiyev A.S.
Azerbaijan State Pedagogical University, Azerbaijan
dashdamirovarzu@gmail.com

The compound $TlInS_2$ is one of the most studied semiconductors. The main reason this compound is of widespread interest is its diverse physical properties. Because it exhibits both semiconducting and ferroelectric properties, it has potential applications in modern electronics. Recent research has focused on synthesizing new compounds via cation-cation and anion-anion substitution in semiconductor crystals and studying their physical properties. This research makes it possible to control the physical properties of crystals by slight changes in their chemical composition. Therefore, in previous studies, new materials were obtained and characterized via atomic substitution in materials with known physical properties. Although the crystal structure and physical properties of $TlInS_2$ have been studied, the changes that occur during cation-cation and anion-anion substitution remain insufficiently understood. In this work, $TlIn(S_{1-x}Se_x)_2$ (x = 0-0.4) compounds were synthesized by partially replacing S

atoms in the $TlInS_2$ compound with Se atoms, and the structure of the obtained polycrystals was studied.

There are many methods for studying the structure of crystals. Each of these methods has its own advantages and disadvantages. The choice of an appropriate research method depends on the shape and chemical composition of the sample. X-ray diffraction is used to study the structure of chalcogenide semiconductors. This method allows for highly accurate determination of the phase analysis and crystallographic parameters of crystals. X-ray diffraction was used to study the crystal structure of $TlInS_2$, $TlIn(S_{0.9}Se_{0.1})_2$, $TlIn(S_{0.8}Se_{0.2})_2$, $TlIn(S_{0.7}Se_{0.3})_2$ and $TlIn(S_{0.6}Se_{0.4})_2$ compounds. The studies were carried out on a D8 ADVANCE diffractometer (Bruker, Germany). The parameters of this diffractometer were: 40 kV, 40 mA, Cu Kα radiation, λ = 1.5406 Å. X-ray diffraction spectra obtained at room temperature were analyzed using the Rietveld method in the FullProf program. Miller indices and crystallographic parameters were determined from the diffraction maxima.

Analysis of the obtained spectra revealed that all samples are single-phase. Their crystal structure corresponds to monoclinic symmetry with the space group C2/c. Previous studies indicate that the crystal structure of $TlInS_2$ corresponds to monoclinic symmetry. The crystal structure of $TlInSe_2$ corresponds to tetragonal symmetry. As can be seen, although S and Se atoms have similar chemical properties, they form different properties in the compounds. In $TlIn(S_{1-x}Se_x)_2$ (x = 0-0.4), the tetragonal phase cannot form due to the lower concentration of Se atoms. Consequently, the structure of each of the obtained compounds corresponds to monoclinic symmetry, consistent with $TlInS_2$.

THERMAL PROPERTIES OF THE CHALCOGENIDE SEMICONDUCTOR Cu_2NiTe_2

[1]Aliyev Y.I., [2*]Guliyeva Kh.M.

[1]Azerbaijan State Pedagogical University, Azerbaijan
[2]Institute of Physics, Ministry of Science and Education, Azerbaijan
q.xeyale84@mail.ru

The physical properties of semiconductor materials change with temperature. This is because the concentration of free charge carriers in the system increases with increasing temperature. This leads to significant changes in electronic processes. Therefore, the thermal properties of each semiconductor material must be studied. A number of methods exist for studying the thermal

properties of crystals. Among these methods, Differential Scanning Calorimetry (DSC) and Thermogravimetric Analysis (TGA) occupy a special place. There are certain difficulties in studying the thermal properties of chalcogenide semiconductors. Since these compounds are non-oxide materials, an oxide layer forms on the surface with increasing temperature. To prevent this, the thermal properties of chalcogenide semiconductors are studied in vacuum conditions. When conducting studies in vacuum conditions, the mass of the samples does not change. Therefore, TGA studies are impossible. However, by analyzing the DSC spectra, it is possible to study the processes of evaporation, decomposition, phase transitions, and melting occurring in the system. In this paper, the thermal properties of the compound Cu_2NiTe_2, which has interesting physical properties, are investigated. Although many properties of this compound have been studied, its thermal properties at high temperatures have not yet been investigated.

The thermophysical properties of the Cu_2NiTe_2 compound were studied at high temperatures using the DSC method. The DSC measurements were carried out using the DSC3 STARe Systems manufactured by METTLER TOLEDO and temperature-corrected MULTISTAR sensors. The standard adiabatic calorimetry was performed in the temperature range from 20 °C up to 1000 °C at a heating rate of 5 °C/min in argon atmosphere at a flow rate of 20 mL·min−1 (which is previously calibrated with indium). The cooling process was achieved with the help of the NITROGEN UN 1977 REFRIGERATED LIQUID analyzer cooling system and "digital temperature controller". The error of weight determination did not exceed 1.02% at 20°C and 1% at 1000°C.

The thermal properties of the Cu_2NiTe_2 compound were studied in the temperature range T = 20–1000 °C. Eight thermal effects were observed in this temperature range. These effects occurred at temperatures of T = 147 °C, 310 °C, 360 °C, 495 °C, 664 °C, 580 °C, 885 °C, and 958 °C. The transition occurring at T = 147 °C was explained by the release of water molecules from the sample. Other effects occurring at higher temperatures were explained by the rupture of bonds formed by gas molecules within the sample and the release of gases from the sample. It was found that the hexagonal system is sufficiently stable with respect to temperature, and no phase transition occurs in the specified temperature range.

THE DEPENDENCE OF THE ELECTRICAL CONDUCTIVITY OF $FeGaInSe_4$ ON FREQUENCY AND TEMPERATURE

[1*]Niftiyev N.N., [1]Dashdemirov A.O., [1,2]Mammadov F.M., [1]Aghayeva R.M., [3]Muradov, M.B.

[1]Azerbaijan State Pedagogical University, Azerbaijan,
[2]Institute of Catalysis and Inorganic Chemistry, Ministry of Science and Education, Azerbaijan
[3]Baku State University, Azerbaijan
namiq7@bk.ru

In this study, the frequency and temperature dependence of the AC electrical conductivity of $FeGaInSe_4$ crystals were investigated. The $FeGaInSe_4$ compound was obtained by combining cubic $FeGa_2Se_4$ (space group $F\bar{4}3m$) and trigonal $FeIn_2Se_4$ (space group R3m) in a 1:1 ratio. X-ray diffraction analysis revealed that $FeGaInSe_4$ crystallizes in the trigonal system (space group R3m) with lattice parameters a = 0.39290(1) nm and c = 3.8542(6) nm.

Figure 1 shows the frequency dependence of electrical conductivity at various temperatures (T, K: 1 – 190, 2 – 210, 3 – 230, 4 – 250, 5 – 270, 6 – 300). At low frequencies, the conductivity remains nearly constant, while at higher frequencies it gradually increases according to the relation $\sigma \sim fS$. At 190 K, in the range $2\times10^5 \div 10^6$ Hz, the parameter s = 0.54, whereas at 240 K, s = 0.37. The decrease of s with increasing temperature corresponds to the Correlated Barrier Hopping (CBH) model, where charge carriers hop between localized states over potential barriers as temperature rises.

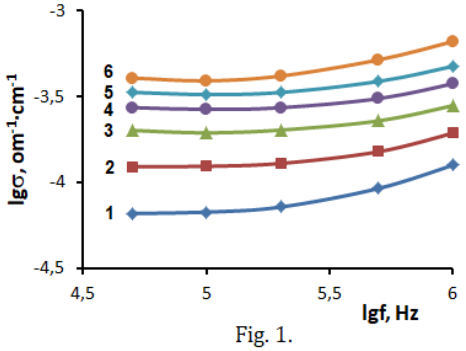

Fig. 1.

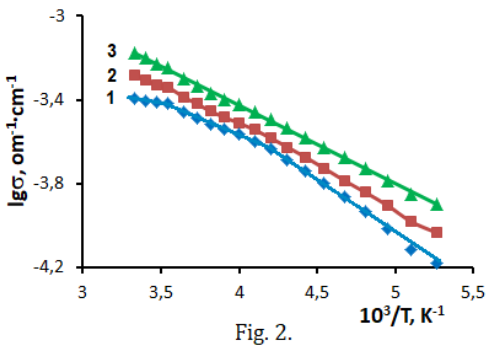

Fig. 2.

Figure 2 presents the temperature dependence of electrical conductivity at different frequencies. The σ(T) relationship exhibits thermally activated behavior following the Arrhenius law: $\sigma \sim exp(-E_a/kT)$. In the frequency range of $5\times10^4 \div 2\times10^5$ Hz, the logσ – $10^3/T$ plots consist of three linear regions with

different slopes, while at 106 Hz, a single linear region is observed. The activation energy at 106 Hz is E_a = 0.076 eV.

In the low-temperature region (190–240 K), the activation energy decreases with increasing frequency from 0.10 to 0.076 eV, consistent with the CBH model. In the intermediate temperature region (240–280 K) and the high-temperature region (280–300 K), the activation energy increases within the ranges of 0.067–0.076 eV and 0.015–0.076 eV, respectively.

The electrical conductivity in the $FeGaInSe_4$ compound is characterized by a mixed band-hopping mechanism.

INTRINSIC AND EXTRINSIC INSTABILITIES IN MULTIMINIMA ENERGY SPECTRUM SEMICONDUCTORS

Alizada N.
Baku State University, Azerbaijan
alizadanarmin81@gmail.com

Semiconductors with a multiminimal energy spectrum exhibit complex transport behavior arising from the coexistence of several equivalent energy valleys. Such materials are of growing interest due to their unique nonlinear responses to external perturbations and their potential applications in high-frequency and high-power electronic devices.

The present study aims to analyze both intrinsic and extrinsic instabilities in semiconductors characterized by multiple conduction band minima. The focus is placed on understanding how carrier redistribution and intervalley scattering contribute to the onset of nonequilibrium states under varying external electric and magnetic fields.

A theoretical approach based on the Boltzmann transport equation was applied to model carrier dynamics and evaluate critical parameters of instability formation. Analytical results were supported by numerical simulations that revealed strong sensitivity of the system to temperature fluctuations and field intensity.

The findings indicate that intrinsic instabilities originate from intervalley electron transitions, while extrinsic ones are mainly influenced by impurity concentration and lattice deformation. These results provide new insights into the control of electronic transport processes in advanced semiconductor materials and may guide the design of next-generation electronic and optoelectronic devices.

LUMINESCENCE AND DEFECT STATES OF $NaBi(MoO_4)_2$ CRYSTAL

Darvishov N.H., Rustamov F.A., Mamedov M.Z., Gasanly N.M.
Baku State University, Azerbaijan
n_darvishov@mail.ru

The optical and electronic properties of $NaBi(MoO_4)_2$ were investigated. It was carried out the photoluminescence (PL), absorbance and thermally stimulated current (TSC) measurements. The absorbance spectrum analysis showed a bandgap energy of 2.94 eV, indicative of the material's potential for optoelectronic applications. The presence of hole defect centers was obtained by TSC measurements and provided information concerning charge transport mechanisms. At temperatures of 69.3 and 127.5 K, it was observed two TSC peaks. The activation energies (0.05 and 0.14 eV) correspond to trap centers.

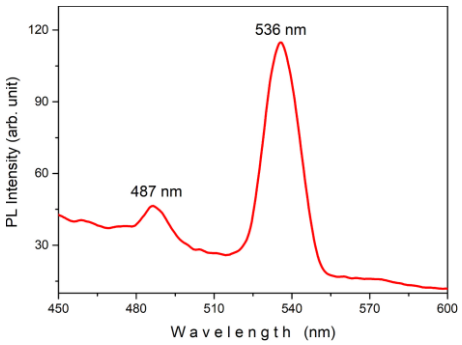

Figure. The PL spectrum of $NaBi(MoO_4)_2$ crystal

PL measurements were carried out to obtain information about the emission characteristics of $NaBi(MoO_4)_2$ crystal. The PL spectrum of the crystal shows two distinct peaks at wavelengths of 487 nm and 536 nm, as shown in the Figure. The peaks of the blue and green regions of the visible spectrum are observed around 487 nm and 536 nm, respectively. The different emission peaks can be attributed to various energy levels or defect states within the crystal. In $NaBi(MoO_4)_2$, bismuth (Bi) can exhibit strong luminescent properties due to its electronic structure. The observed peaks may involve transitions related to Bi^{3+} ions. The PL properties suggest that $NaBi(MoO_4)_2$ has potential applications in optoelectronic devices, such as light-emitting diodes (LEDs) or laser materials, particularly in the visible range. The specific wavelengths of the emission peaks imply that this material can be useful in devices requiring blue and green emissions.

FERROELECTRIC-PARAELECTRIC PHASE TRANSITION IN $BaTiO_3$ and $PbTiO_3$ PEROVSKITES AT HIGH TEMPERATURES

***Huseynov R.E., Mammadov A.I., Mehdiyeva R.Z., Huseynova E.R.**
Institute of Physics, Ministry of Science and Education, Azerbaijan
r.e.huseynov@gmail.com

Perovskite materials are the most studied complex oxides. Their ferroelectric, semiconducting, and ferromagnetic properties generate interest in their further study. The most studied perovskite compounds are the classical ferroelectrics $BaTiO_3$ and $PbTiO_3$. Possessing ferroelectric properties under normal conditions, they are widely used in modern electronics. It has been established that, under the influence of temperature and pressure, these compounds undergo a ferroelectric-parallel phase transition from the tetragonal phase to the cubic phase. Despite the extensive study of the structural aspects of this phase transition, the thermodynamic parameters remain insufficiently understood. Temperature is known to be the physical parameter with the greatest impact on the environment. As temperature increases, the nature of the physical processes occurring in materials also changes. Therefore, it is important to study functional materials at high temperatures. In this paper, the thermophysical properties of $BaTiO_3$ and $PbTiO_3$ compounds are investigated.

The experiments were conducted on a German-made STA 449 F3 Jupiter® thermal analyzer (STA – Simultaneous Thermal Analyzer). This instrument enables simultaneous TG-DTA and TG-DSC analysis. It operates in a temperature range from room temperature to 1500 K and provides heating rates in the range of 0.001–50 K/min. Cooling was accomplished using a Julabo F25 circulation cooling system. The thermal behavior of the samples during the experiment was recorded using Proteus Analysis software, which was used to calculate the kinetic parameters of the reactions. Argon was used as an inert atmosphere to prevent the accumulation of combustion and condensation products formed during the reactions in the system.

During the studies conducted in the temperature range T = 300–850 K, differential scanning calorimetry (DSC) and thermogravimetric analysis (TGA) spectra were obtained. Analysis of the spectra revealed that, despite the similarity of the chemical composition and structure of the compounds, their thermophysical properties differ significantly. It was established that in the $BaTiO_3$ compound at a temperature of T = 386 K, a phase transition occurs corresponding to the ferroelectric–paraelectric phase transition observed during the tetragonal-cubic structural transformation. In the $PbTiO_3$ compound, this phase

transition was detected at higher temperatures. From the DSC spectrum, it was found that the phase transition occurs at a temperature of T = 754 K. This transition also corresponds to the ferroelectric–paraelectric phase transition observed during the tetragonal-cubic structural transformation. It is evident that, despite the similarity of the chemical composition and crystal structure, the thermodynamic properties of the compounds differ significantly. Incorporating Pb atoms into the crystal creates a more stable system. Therefore, the phase transition occurs at a higher temperature. However, more energy is required to achieve the phase transition.

CRYSTAL STRUCTURE OF AgCuS THIN FILMS

[1]Bagirova H.I., [2]Hakhverdiyeva Z.E., [2]Nazarov A.M., [3*]Aliyev Y.I.

[1]Azerbaijan University, Azerbaijan
[2]Institute of Physics, Ministry of Science and Education, Azerbaijan
[3]Azerbaijan State Pedagogical University, Azerbaijan
yusifafshar@gmail.com

The physical properties of functional materials depend on their production methods and structural features. Therefore, it is essential to study the processes of production and phase formation of these materials. As research methods have evolved, these studies have become more precise. Chalcogenide semiconductors occupy a special place among functional materials. These compounds can form various structures depending on the bonds formed by the metal and chalcogen atoms and the valence of the metal atoms. Therefore, phase formation processes in these compounds have been extensively studied recently. The observed variability of the valence of metal atoms sometimes leads to the formation of two-phase systems. Due to the variable valence of copper atoms, such cases have been observed in structural studies conducted in Cu–X (X = S, Se, Te) systems. Therefore, it is important to study the structure, phase transitions, and phase formation processes of these materials.

It has been established that thin layers exhibit certain differences in many material properties. However, to obtain multifunctional systems of small dimensions, it is necessary to study the properties of thin layers as well. It is known that producing thin layers of complex systems poses certain technological challenges. Therefore, it is necessary to obtain thin layers of systems with the highest symmetry elements. Results obtained during structural studies revealed that the AgCuS compound, obtained with equal concentrations of Ag and

Cu, possesses the highest symmetry elements in the Ag-Cu-S system. When studying thin layers of the Ag-Cu-S system, it is also advisable to study epitaxial layers of AgCuS. For this purpose, thin layers of the silver-copper-sulfate system were obtained, and their surface structure was studied.

Thin layers of the AgCuS compound were produced using a specialized technology. One of the key requirements for epitaxial layer production is the use of high-purity evaporation sources. To obtain thin layers of the Ag-Cu-S system, polycrystalline AgCuS was used as the evaporation source for the epitaxial layers. The epitaxial layers were produced using molecular beam condensation (MBC) using a UVN-71P-3 setup in a vacuum of $(1\text{-}2)\cdot10^{-4}$ Pa.

The crystal structure of an AgCuS thin film with a thickness of h = 1 μm was studied using X-ray diffraction. The resulting X-ray spectrum was compared with the X-ray spectrum of the AgCuS compound, and the crystal structure of the thin film was determined. It was found that the crystal structure of the thin film corresponds to an orthorhombic syngony with the space group Cmcm. This structure corresponds to the crystal structure of the AgCuS compound. A single-phase system was formed in the thin film. It is known that structure plays a special role in the formation of physical properties. Therefore, the crystal structure should be controlled during the production of each system. The correspondence of the crystal structure of the Ag-Cu-S thin film to the crystal structure of the AgCuS compound indicates the formation of physical properties characteristic of crystals in thin films.

INFLUENCE OF Mn (MANGANESE) ION CONCENTRATION ON THE HEAT CAPACITY OF DILUTED MAGNETIC SEMICONDUCTOR SUPERLATTICES

Mahmudov M.M., *Damirov R.Y.
Baku State University, Azerbaijan
mehdimahmudov@bsu.edu.az

When investigating transport phenomena as well as the magnetic and optical properties of diluted magnetic semiconductors, it is essential to understand the distribution of charge carriers within the energy bands, the density of states, and the relationship between carrier concentration and the Fermi level. In the presence of a strong magnetic field, the carrier energy spectrum undergoes significant modification, leading to changes in the density of states. This, in turn, governs all thermodynamic quantities, particularly the entropy, heat capacity and related physical characteristics. To determine the field and

temperature dependence of various physical coefficients, it is therefore necessary to establish the dependence of the chemical potential on the magnetic-ion concentration, magnetic field strength, and temperature. Moreover, once the entropy is known, the thermopower can be directly evaluated.

This paper presents a theoretical investigation of the heat capacity of an electron gas in diluted magnetic semiconductor superlattices. The results show that in such superlattices, the heat capacity depends strongly on the impurity-ion concentration, magnetic field strength, and exchange interaction energy. At temperatures up to 50 K and magnetic fields up to 3 T, the specific heat of diluted magnetic semiconductors is considerably higher than that of nonmagnetic counterparts. The excess heat capacity arises from the magnetic contribution of manganese ions. When the manganese ion concentration exceeds 0.2, the heat capacity varies linearly with temperature. As the manganese concentration increases further, the temperature dependence of the heat capacity becomes non-monotonic, exhibiting a pronounced maximum whose position depends on both the manganese concentration and magnetic field strength. The emergence of this maximum is associated with a phase transition from the paramagnetic to the antiferromagnetic state. At very low temperatures and when the concentration of manganese ions is greater than 0.3, the heat capacity is independent of the magnetic field and varies with temperature as T^{-2}. In zero magnetic field, the heat capacity decreases monotonically with temperature. As the manganese concentration increases, the influence of the magnetic field on the heat capacity diminishes. This behavior can be attributed to the clustering of manganese ions into larger aggregates at lower field strengths, which leads to the release of spins from manganese ion clusters and the eventual disappearance of weakly coupled spins.

DENSITY OF STATES EFFECTIVE MASS OF $(AgSbTe_2)_{0.9}(PbTe)_{0.1}$

[1,2*]Ragimov S.S., [3]Hashimova N.N., [2]Aliyeva A.I., [4]Pashayev G.P.

[1]Baku State University, Azerbaijan
[2]Institute of Physics, Ministry of Science and Education, Azerbaijan
[3]Azerbaijan State Oil and Industry University, Azerbaijan
[4]Military Institute named after Heydar Aliyev, Azerbaijan
sadiyar.raqimov@bsu.edu.az

The ternary compound $AgSbTe_2$ is a good thermoelectric material. As is known, the thermoelectric materials are used for the conversion of thermal energy into electricity and for solid-state cooling. The thermoelectric energy conversion efficiency parameter depends on the Seebeck coefficient, electrical

conductivity, and thermal conductivity.

Thermoelectric parameters of semiconductors with a complex conduction- or valence-band structure depend on the energy position of the band extrema, the effective carrier masses, and the scattering mechanisms involved. In many solid solutions, the relative positions of extrema in the conduction or valence band depend on composition. This offers considerable possibilities for properly choosing the degree of doping and the solid solution composition, which optimize the combinations of contributions to the carrier transport from different bands and bring about an increase in the thermoelectric efficiency. In thermoelectric materials, the effective mass (m*) reflects the band curvature, and doping is found to affect the effective mass. The estimation of effective mass provides helpful information to understand the doping effect and improve the TE performance, as so md* directly influences the S and electrical conductivity.

This work is devoted to the estimation of the density of states (DOS) effective mass (md*) of $(AgSbTe_2)_{0.9}(PbTe)_{0.1.}$ The Hall coefficient and thermal power of $(AgSbTe_2)_{0.9}(PbTe)_{0.1}$were measured. It was observed that the sign of the Hall coefficient indicates the electronic type. It differs from the positive sign of the thermoelectric power. The different signs of the thermoelectric power and the Hall coefficient signs are the result of electrons and holes participation in conductivity. Different signs of the Hall coefficient and thermoelectric power were previously observed in $AgSbTe_2$.

The carrier concentration measured by the Hall effect and the experimentally measured S enable us to calculate the density of states (DOS) effective mass (md*). According to the thermoelectric power and the carrier concentration was estimated effective mass of holes in the $(AgSbTe_2)_{0.9}(PbTe)_{0.1}$ ($md^*=0.46m_0$). This value of effective mass is in agreement with the value of the effective mass for $AgSbTe_2$ ($md^*=0.61m_0$). The decrease of effective mass value for $(AgSbTe_2)_{0.9}(PbTe)_{0.1}$ is due to the decrease of carrier concentration.

INFLUENCE OF $BiSe_3Te_6$ SEMICONDUCTOR COMPOUND STRENGTH PROPERTIES OF LOW-DENSITY POLYETHYLENE

Gafarova D.M., *Askerova G.Z.

Azerbaijan University of Architecture and Construction, Azerbaijan
esgerovagunel1985@gmail.com

This study investigates the effect of $BiSe_3Te_6$ semiconductor fillers on the mechanical and electrical strength properties of low-density polyethylene

(LDPE) composites. These composites were prepared using hot pressing at 15 MPa for 10 minutes, and their electrical and mechanical strengths were tested at room temperature. Results show that the addition of $BiSe_3Te_6$ significantly enhances both electrical and mechanical strengths, with the optimal filler content providing the best performance. However, increasing the filler content beyond this optimal point leads to a decline in strength, which is attributed to excessive rigidity and internal stresses. The observed improvement in strength is due to the formation of a fine spherulite structure in the polymer, which enhances crystallization and packing density of structural elements. Additionally, the introduction of the optimal semiconductor additive helps reduce the rate of strength degradation during electrical aging, demonstrating the stability of the modified composite under electrical stress. These findings suggest that $BiSe_3Te_6$ can effectively modify the properties of LDPE for advanced electret and piezoelectric applications, but careful optimization of the filler content is crucial for maintaining material performance.

INTRABAND OPTICAL TRANSITIONS IN QUANTUM DOTS

***Usibli G.A., Gadirova I.R.**
Baku State University, Azerbaijan
gunayyusibli@gmail.com

Optical methods are the most powerful and universal methods for studying quantum dots. They can provide information about the energy spectrum of the elementary excitations, for example, the energy spectra of electrons and phonons. Optical methods allow for determining the chemical composition and sizes of quantum dots.

In this work, the intraband optical transitions in the conduction band of the cubic symmetry semiconductor quantum dots have been investigated. Rectangular-shaped quantum dots have been considered on the assumption that the potential well has infinitely high walls. Mathematical expressions for the optical susceptibility, the absorption coefficient, and the refractive index change have been obtained for the group of identical quantum dots. For this dipole, momentum matrix elements were calculated.

The selection rules for the intraband transitions are determined by the Kronecker delta so that only one of three quantum numbers changes for each single-photon transition; optical transitions occur only between electron states for which the sum of the quantum numbers is an odd number.

The specificity of the electron-photon interaction causing the intraband transitions is the dependence of its matrix elements on the size of the quantum dot. The dipole momentum matrix elements are proportional to the linear sizes of the quantum dot. Unlike the one-dimensional quantum well and quantum wire in quantum dots, the intraband transitions are possible in any direction of the light wave polarization vector.

Mathematical expressions for the optical susceptibility, the absorption coefficient, and the refractive index changes appear as the sum of the terms, each of which describes a separate single-photon transition. The optical function spectra are the set of lines, each of which corresponds to a single-photon transition, obeying the selection rules. As the linear sizes of the quantum dot decreases, the optical function spectra move to the high energy region and their amplitudes decrease.

THE ROLE OF THE SPECTROPHOTOMETRIC METHOD IN STUDYING THE OPTICAL PROPERTIES OF LIQUID MIXTURES

Abdullayev A.P., Huseynov H.I., Babayev N.M., *Musazada I.V., Asgarova G.Z.

Azerbaijan University of Architecture and Construction, Azerbaijan
esgerovagunel1985@gmail.com

When monochromatic light falls on a substance, part of the light is absorbed and part is emitted. The intensities of the incident and emitted rays are measured and analyzed by spectrophotometry. Based on these analyses, information can be obtained about the optical properties of the solution.

The dependence of the optical densities of aqueous solutions of copper sulfate ($CuSO_4 \cdot 5H_2O$) and potassium dichromate ($K_2Cr_2O_7$) on wavelength and concentration was studied.

Copper sulfate is blue, and potassium dichromate is orange. It has been found that the optical density of copper sulfate increases in the orange-red region of the wavelength range. (Figure 1) As the concentration of the mixture increases, the maximum value of the optical density also increases and shifts to the left. The blue mixture transmits blue light without absorbing it, while orange-red light is absorbed. Most likely, molecules that absorb orange-red light emit additional blue-green light.

In a solution containing potassium dichromate ($K_2Cr_2O_7$), absorption is observed in the wavelength range of 420-520 nm (Figure 2). This interval

corresponds to the blue-blue color. As the concentration of the mixture increases, the maximum value of absorption also increases, and the maxima shift to the right. The optical density maxima of the blue-colored copper sulfate mixture are observed in the orange-red region, and the optical density maxima of the orange-colored copper sulfate are observed in the blue-blue region.

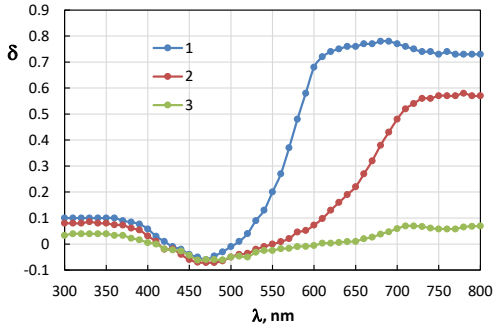

Figure 1. Dependence of the optical density of a mixture of copper sulfate ($CuSO_4 \cdot 5H_2O$) in water on the wavelength. The amount of the mixture in water in parts: 1 – 0.1; 2 – 0.01; 3 – 0.001

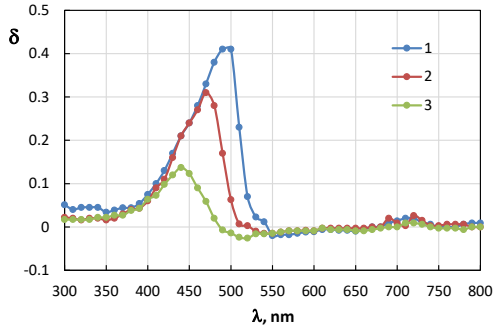

Fig. 2. Dependence of the optical density of a mixture of potassium ($K_2Cr_2O_7$)in water on the wavelength. The amount of the mixture in water in parts: 1 – 0.1; 2 – 0.01; 3 – 0.001.

As the concentration of the mixture increases, the maximum value of absorption also increases, and the maxima shift to the right. Thus, the maxima of the blue copper sulfate mixture are observed in the orange-red region, and the maxima of the orange potassium dichromate mixture are observed in the blue-blue region.

DETERMINATION OF CHARACTERISTIC SEMICONDUCTOR PARAMETERS IN THE $TlInS_2$-$TlEuS_2$ SYSTEM OF SOLID SOLUTIONS

***Ağabalayeva A.A., Nurullayev Y.Q.**
Baku State University, Azerbaijan
ayselagabalayeva6@gmail.com

The modern development of the electronic industry requires not only the search for new semiconductor materials in the field of solid-state physics but also a more detailed study of the physical properties of existing compounds. In this regard, the investigation of the electrophysical characteristics of compounds synthesized based on $TlInS_2$(Se_2, Te_2) ternary systems is of particular scientific interest. These compounds belong to the class of AlllBlllC2Vl-type semiconductors, which crystallize in the tetragonal syngony. Their crystal structure contains two structural units, with the tetrahedron considered as the fundamental chemical unit. Compounds of this class and their solid solutions are widely used in the fabrication of detectors for near-infrared, X-ray, gamma, and neutron radiation, as well as in solar energy conversion devices. The quaternary compound $TlInEuSe_2$ exhibits a metallic luster and a dark-gray color; upon prolonged exposure to air, it becomes coated with a thin grayish film. In the present work, the temperature dependences of the electrical conductivity, Hall coefficient, and thermoelectric power of solid solutions in the $TlInS_2$–$TlEuS_2$ system have been studied in the temperature range of 300–1000 K. From Hall effect measurements, it was established that at a 1:1 ratio of the initial components, congruently melting quaternary compounds of the $TlInEuSe_2$ type are formed, while within the range of 0–9 mol% $TlEuS_2$, regions of solid-solution formation exist. It was determined that in both solid solutions and quaternary compounds, thallium atoms behave as monovalent, whereas indium and europium atoms exhibit trivalent states. Increasing the europium content leads to an elevation in the melting temperature of the solid solution. The Tl_2InEuS_2 quaternary compounds and $TlIn_{1-x}Eu_xS_2$ solid solutions crystallize in the tetragonal system, similar to the initial $TlInEuS_2$ compounds. The temperature dependence of the electrical conductivity, Hall coefficient, and thermoelectric power was measured in the 100–1000 K range. In the studied samples, impurity conduction dominates at low temperatures, while intrinsic conduction is observed above 600 K. Based on the temperature dependence of the conductivity, the width of the forbidden band (band gap) was determined.

ENERGY SPECTRUM AND WAVE FUNCTIONS OF ELECTRONS AND HOLES IN SEMICONDUCTOR-BASED QUANTUM WIRE

Ismayilov T.H., *Amirova L.F.
Baku State University, Azerbaijan
lamanamirova26@gmail.com

Lasers based on low-dimensional quantum systems have many advantages over conventional semiconductor lasers. One of them is that their frequency can be tuned. Thus, the frequency of the light emitted by the laser can be changed depending on the size of the system. Since the number of states to be inverted in such systems is much smaller than in semiconductor lasers, the threshold current density is significantly lower. Due to the different dependences of the state densities on energy, not only does the value of the threshold current in such lasers change, but also its temperature dependence. It becomes weaker, as a result of which continuous radiation is obtained not only at room temperature, but also at higher temperatures. In addition, it is easier to create inverse occupancy in these systems. Therefore, such lasers are very economical, operate with a smaller current, and give more light per unit of energy consumed. To calculate the parameters of such lasers, it is necessary to know the energy spectrum and wave functions of the current carriers

In connection with the above, in this work, the energy spectrum and wave functions of charge carriers (electrons and holes) in a semiconductor-based quantum wire were found from the solution of the Schrödinger equation, as well as the density of states was also calculated. Numerical calculations were performed for the density of states in a number of different semiconductor-based quantum wires, and energy dependence curves were constructed.

INTRABAND OPTICAL ABSORPTION IN GaAs SEMICONDUCTOR SUPERLATTICES

Ibaeva R.Z.
Institute of Physics, Ministry of Science and Education, Azerbaijan
raidaibaeva@gmail.com

The tunable electrical and optical properties of semiconductor superlattices, which are made up of alternating layers of various materials like GaAs and AlAs, have garnered a lot of attention. Minibands and minigaps are created as a

result of the periodic potential along the growth direction, altering the optical response in contrast to bulk semiconductors. When designing infrared and terahertz optoelectronic systems, such as quantum cascade lasers and detectors, intra-band optical absorption – which takes place between subbands within the same miniband – is crucial.

The GaAs well width and the AlAs barrier width are represented by a and b, respectively, in a one-dimensional GaAs/AlAs superlattice with period d=a+b. Within the effective mass approximation, the Kronig–Penney model describes the transport of electrons along the growth direction. The following is the Schrödinger equation in Eq.1:

$$\left[-\frac{\hbar^2}{2m^*(z)}\frac{d^2}{dz^2}+V(z)\right]\psi(z)=E\psi(z), \qquad (1)$$

where $m^*(z)$and $V(z)$are the position-dependent effective mass and potential energy. Solving the dispersion relation yields the miniband energy spectrum $E(k_z)$, from which the optical transition probabilities are obtained.

A theoretical analysis of intraband optical absorption in GaAs/AlAs superlattices has been performed. The superlattice period, barrier height, and miniband parameters all have a significant impact on the absorption spectra. In order to optimize superlattice structures in tunable infrared optoelectronic devices, the work offers helpful insights.

STUDY OF THE ELECTRICAL CONDUCTIVITY OF A TWO-DIMENSIONAL ELECTRON GAS IN A SEMI-PARABOLIC QUANTUM WELL WITH COULOMB FIELD SCREENING BY REMOTE IMPURITY IONS

[1*]Huseynov H.I., [2]Mahmudov M.M., [2,3]Jahangirli Z.A., [1]Abdullayev A.P.

[1]Azerbaijan University of Architecture and Construction, Azerbaijan
[2]Baku State University, Azerbaijan
[3]Institute of Physics, Ministry of Science and Education, Azerbaijan
huseynov.h.i@mail.ru

Recently, asymmetric quantum wells with broken inversion symmetry have attracted growing attention compared to their symmetric counterparts. The study of asymmetric quantum wells has become crucial in modern micro- and nanoelectronics, as these structures enable both the design of novel miniaturized devices and the enhancement of existing device performance. An asymmetric quantum well can be created by applying an external influence, such as

an electric or magnetic field.

In this paper, we theoretically investigate the electrical conductivity of a two-dimensional electron gas in a semi-parabolic quantum well scattered by remote ions. Based on the obtained analytical expressions, the dependence of the electrical conductivity on the potential and the quantum well width, as well as on the conduction electron concentration and the number of subbands, has been investigated. When calculating the kinetic coefficients in two-dimensional electron systems, the reference point is the energy spectrum, which for conduction electrons in a semi-parabolic quantum well has the form:

$$\varepsilon = \frac{\hbar^2}{2m}\left(k_x^2 + k_y^2\right) + \hbar\omega_s\left(2n + \frac{2}{3}\right), \quad (1)$$

here m is the electron effective mass, $k_x^2 + k_y^2$ are the components of the wave vector in the quantum well plane, ω_s is the frequency of the semi-parabolic potential in a quantum well, $n = 1,2,3, \ldots$ are the quantum numbers.

At very low temperatures, approximately T = 10 K, impurity ions behave as scattering centers. Electrical conductivity depends strongly on the quantum well parameters: the quantum well potential and width, as well as the concentration of conduction electrons and the number of subbands whose bottoms are below the Fermi levels. In nonparabolic quantum wells, the number of such subbands typically does not exceed 2÷3. The electrical conductivity of the electron gas in a semi-parabolic quantum well, when screened by distant ions, increases in magnitude with decreasing quantum well width and changes sign, becoming negative. However, at relatively large quantum well widths, it becomes positive. This increase is due to the electron localization effect and reduced electron scattering. As the electron concentration increases, the electrical conductivity increases. The greater the potential, the faster it increases, and at a certain value of the electron concentration, the numerically constructed graphs intersect. Furthermore, the analysis shows that, under remote impurity scattering, the relative electrical conductivity increases in magnitude with the quantum well potential, undergoes a sign reversal, and becomes negative. For a small number of occupied subbands, the electrical conductivity remains negative; as the number of subbands increases, its absolute value grows accordingly.

These results demonstrate that the interplay between quantum confinement, remote impurity scattering, and screening effects plays a crucial role in determining the transport properties of asymmetric quantum wells.

SIZE EFFECT OF $BaTiO_3$ NANOPARTICLES ON THE OPTICAL PROPERTIES OF CHIRAL PHASE LIQUID CRYSTAL

[1*]Mammadov N.M., [1]Humbatov Sh.A., [2]Imamaliev A.R.

[1]Baku State University, Azerbaijan

[2]Institute of Physics, Ministry of Science and Education, Azerbaijan

memmedovan2003@gmail.com

In recent years, incorporating ferroelectric nanoparticles into liquid crystalline matrices has become a key strategy for enhancing electro-optic performance and tunability. In this study, the influence of $BaTiO_3$ nanoparticle size on the optical birefringence and threshold voltage of a chiral smectic C* liquid crystal-2-methylbutyl 4-(4-decyloxybenzylideneamino) cinnamate (DOBAMBC) – was systematically investigated. $BaTiO_3$ nanoparticles with mean diameters of 100–500 nm were ultrasonically dispersed in the LC host to achieve homogeneous composites. The experimental methodology combined polarized optical microscopy (POM), electro-optical transmission measurements, and dielectric spectroscopy to assess phase behavior, birefringence, and threshold voltage variations.

$BaTiO_3$ particle size (nm)	**Optical birefringence (Δn)**	**Threshold voltage (Vth, V)**
100	0.185	6.2
200	**0.213**	**4.8**
300	0.205	5.3
400	0.191	6.8
500	0.176	7.5

The results show a clear size-dependent trend, with the 200 nm $BaTiO_3$-doped sample exhibiting the highest birefringence (Δn = 0.213) and lowest threshold voltage (V_{th} = 4.8 V), indicating enhanced ferroelectric coupling and electro-optic efficiency. This optimum performance is attributed to a balance between surface polarization effects and nanoparticle–LC compatibility. Conversely, smaller particles disrupted the helical order, while larger ones caused optical scattering. The findings highlight the critical role of nanoparticle dimension in tuning liquid crystal–ferroelectric interactions for photonic device applications.

MECHANISM OF BLUE LUMINESCENCE FORMATION IN ZnS CRYSTALS DUE TO DONOR–ACCEPTOR PAIR RECOMBINATION

[1]Mammadli Ch.A., [1*]Huseynov C.I., [2]Abbasov I.I., [2]Asadullayeva S.G.

[1]Azerbaijan State Pedagogical University,
[2]Azerbaijan State Oil and Industry University,
cahangirhuseynov1958@gmail.com

The photoluminescence (PL) properties of ZnS single crystals excited by a 325 nm (≈3.82 eV) ultraviolet laser at room temperature (300 K) were investigated in the wavelength range of 350–690 nm. The PL spectrum exhibits a dominant blue emission band centered at 463 nm (≈2.68 eV) with a narrow full width at half maximum (FWHM) of 15–18 nm, indicating high crystalline quality and uniform distribution of electronic states. The blue emission is attributed to donor–acceptor pair (DAP) recombination involving donor-type sulfur vacancies (V_S) and acceptor-type zinc vacancies ($V_{Zn''}$). Calculations based on the DAP model yielded a donor–acceptor separation of 0.5–3.4 nm and a combined defect energy ($E_D + E_A$) of approximately 1.00 eV, consistent with effective radiative recombination within the ZnS band gap. Additional weak bands in the 535–675 nm range are associated with deep-level defects and d–d transitions of metal ions (Cu^+, Mn^{2+}, Fe^{3+}). These results confirm that the observed luminescence originates primarily from donor–acceptor pair transitions and provide valuable insights into the defect-related optical processes in ZnS crystals, which are promising for UV–blue light-emitting and photodetector applications.

THE NEGATIVE CAPACITANCE, AN ANOMALOUS PEAK IN THE C-V PLOT, AND VOLTAGE-DEPENDENT PROFILE OF INTERFACE TRAPS AND SERIES RESISTANCE IN Au/(CdTe: PVA)/n-Si STRUCTURE

[1*]Guchlu C.S., [2]Demirci A.

[1]Gazi University, Ankara-Türkiye
[2]PROTEK Technology Solutions Trans. & Cons. Serv. Ind. & Trade Ltd. Co., Türkiye
cigdemguclu@gazi.edu.tr

In this present study, Au/(CdTe: PVA)/n-Si structures have been fabricated, and then capacitance-voltage (C-V) and conductance-voltage (G/ω-V) measurements of them were performed at low and high frequencies in a wide range of voltage at room temperature. The C-V plots at low frequency show a

negative capacitance (NC) and an anomalous peak, but both the NC and peak disappear at high frequency. Therefore, such behavior at low frequency was explained by the existence of interface traps and surface/dipole polarization. Because at lower frequencies, the lifetimes of interface traps (D_{it}) are considerably lower than the measured period (T=1/2pf). In addition, dipoles have enough time to rotate around their own axis. The voltage-dependent profile of Dit was extracted from the low-high frequency capacitance method developed by Nicollian & Brews by using a 1kHz and 1 MHZ C-V plot. The average value of D_{it} was found at about $3x10^{11}$ $eV^{-1}.cm^{-2}$ which is very suitable for such devices. The voltage-dependent profile of series resistance (Rs) was also extracted from the C-V and G/w-V plot at 1MHz, and it was considerably changed by the applied bias voltage. At low frequencies, while the value of C gives a peak, the value of G/W reaches a maximum value, and such behavior of them is called "Inductive behavior". In other words, the maximum value of G corresponds to the minimum capacitance. All experimental results indicate that the impedance measurements are considerably dependent on frequency and voltage, especially at lower frequencies, because of D_{it}, Rs, and the interfacial layer. Therefore, they must be considered in the calculation of electrical parameters and conduction mechanisms.

This study was supported by Scientific and Technological Research Council of TÜRKİYE (TÜBİTAK) (Project Number 121C396).

RADIATION EFFECTS ON THE PARAMETERS OF MICRO-PIXEL AVALANCHE PHOTODIODES UNDER FAST NEUTRON IRRADIATION

Akbarov R.A.

Institute of Radiation Problems, Ministry of Science and Education, Azerbaijan;
Department of Nuclear Research of IDDA, Azerbaijan
ramilakbarow@gmail.com

Micro-pixel avalanche photodiodes (MAPD/SiPM) are widely used in fields such as medical imaging, laser ranging, particle physics, and aerospace applications due to their ability to detect extremely weak optical signals with internal gain. However, operation in environments with intense ionizing radiation requires an understanding of radiation-induced degradation mechanisms.

This study aimed to investigate the effect of fast neutron irradiation (E > 1 MeV) on MAPD structures with different pixel geometries. Three types of devices were tested: MAPD-3NM (deep pixel layout) and MPPC S12572-10P

(surface pixel layout).

Before irradiation, devices were sorted based on dark current and photoresponse amplitude. Breakdown voltages were determined by differentiation of the dark current–voltage characteristics.

Neutron irradiation was performed at the IBR-2 pulsed reactor (Joint Institute for Nuclear Research, Dubna). Samples were positioned at three different distances from the irradiation channel output, resulting in fluences of 1.28×10^{12}, 3.73×10^{12} and 9.68×10^{12} n/cm^2 (1 MeV equivalent). Fluence values were verified using calibrated silicon planar detectors.

After irradiation, dark current values increased by 2–3 orders of magnitude for all photodiode types, while breakdown voltage shifted to higher values. At fluences near 1×10^{13} n/cm^2, the dark current increased by a factor of 2855 and the breakdown voltage increased by 1.4% relative to pre-irradiation values. Comparative analysis demonstrated that the studied MAPD devices exhibit 11 times higher radiation tolerance in terms of dark current growth compared to foreign commercial SiPM detectors.

The obtained results demonstrate that MAPD devices with deep pixel architecture retain functional parameters under high neutron fluence and can be recommended for applications in radiation-intensive environments.

EXCITATION OF UNSTABLE WAVES IN CONDUCTING MEDIA IN THE PRESENCE OF A CONSTANT TEMPERATURE GRADIENT

*Veliyeva G.V., Hasanov E.R.
Baku State University, Azerbaijan
veliyevaagunay@gmail.com

We will consider isotropic semiconductor compounds such as GeAu with two types of charge carriers (electrons and holes), the lattice which is active or passive this is these states can capture free charges (recombination) or emit free charges (generation) depending on temperature. At room temperature (T = 300 K), singly and doubly negative charged centers are more active. Multiplying the latter scalarly and vectorially by b, we obtain $b^2 = \Omega\tau << 1$ and $\vec{x}(1+b^2) = \vec{a} + [\vec{b}\vec{a}] + \vec{b}(\vec{b}\vec{a})$, respectively (where Ω refer to the Larmor frequency, the collision time of charge carriers). The electric field takes on the following value

$$\vec{E} = -\frac{[\vec{V}\vec{H}]}{c} - \Lambda'[\vec{\nabla}T\vec{H}] + \frac{c}{4\pi\sigma} rot\vec{H} -$$

$$-\frac{c\sigma'}{4\pi\sigma^2}\left[rot\vec{H},\vec{H}\right]+\frac{T}{e}\left(\frac{\nabla n_+}{n_+^0}-\frac{\nabla n_-}{n_-^0}\right)+\Lambda\nabla T \qquad (1)$$

(where, $\Lambda'=(\alpha'\sigma-\alpha\sigma')/\sigma^2$ refer to the Nernst-Ettingshausen coefficient). Linearizing the last equation, we obtain

$$\left(1-\frac{2\vec{k}\vec{V}_0}{\omega}+\frac{2\omega_T}{\omega}+\frac{ic^2k^2}{2\pi\sigma\omega}\right)\vec{E}'=\frac{T\vec{k}}{e}\left(\frac{n_+'}{n_+^0}-\frac{n_-'}{n_-^0}\right)+\gamma\Lambda_0\vec{\nabla}T\frac{\vec{E}'\vec{E}_0}{E_0'^2}$$

At $\mu >> \mu_+$, we obtain to determine the oscillation frequency of the excited waves

$$\omega^2+\left[kv_-+i\big(\nu_-+\nu_+(0)\big)-i(\omega_++\omega_-)-\frac{\beta}{\varphi}(\Omega_++\Omega_-)\right]-$$

$$-k^2v_+v_-+\frac{\beta}{\varphi}\big(kv_-\delta_++i\Omega_+\nu_-+\Omega_-kv_+-i\Omega_-\nu_+(0)\big)=0$$

Then after some calculations

$$(1-i)\omega^3+\big(-i\widetilde{\omega}_++kv_-+i\tilde{\delta}+\omega_++\omega_-\big)\omega^2+$$

$$+\left[2kv_-\widetilde{\omega}_++\widetilde{\omega}_+\big(i\tilde{\delta}+\omega_++\omega_-\big)-k^2v_+v_-+\Omega_1^2+i\Omega_2^2\right]\omega_++$$

$$+kv_-\widetilde{\omega}_+^2+\widetilde{\omega}_+(\Omega_1^2+i\Omega_2^2)=0$$

is obtained. Given $\delta_+\nu_-=\delta_-\nu_+(0)$ the frequency of thermomagnetic waves, $\omega_T=-Tk^2\mu_+/e$.

The electromagnetic regiment has the value:

$$E_0=\frac{\mu_-\delta_++\mu_+\delta_-}{k\mu_-\mu_+}=\frac{\Omega_++\frac{\mu_+}{\mu_-}\Omega_-}{k\mu_+}.$$

$\omega_0=(\widetilde{\omega}_T/2)\left(x/\sqrt{2}-1\right)$ the increment for the frequency of the excited waves is obtained from the dispersion equation

$$\omega^2+\frac{1+i}{2}(-i\widetilde{\omega}_T+kv_-+\omega_T+\omega_-)\omega+$$

$$+(1+i)kv_-\omega_T+\frac{1+i}{2}\widetilde{\omega}_T(\omega_T+\omega_-)=0.$$

Thus, in GeAu semiconductor compounds, hydrodynamic waves are generated with a frequency $Tk^2\mu_+/e+\omega_T+\omega e/2=\vec{k}\vec{v}_0$ depending on the frequency of the electromagnetic waves and of the waves excited by holes.

PHASE TRANSITIONS AND BAND INVERSION IN $Pb_{1-x}Sn_xTe$ SOLID SOLUTIONS: EXPERIMENTAL AND THEORETICAL ASPECTS

***Sarmasov S.N., Ragimov R.Sh.**
Baku State University, Azerbaijan
suleymansarmasov@bsu.edu.az

This study presents the results of a comprehensive investigation into phase transitions in $Pb_{1-x}Sn_xTe$ solid solutions, which belong to the class of narrow-gap IV–VI semiconductors. Samples with varying Sn concentrations were synthesized via direct melting followed by annealing, ensuring the formation of homogeneous solid solutions. Structural characterization was performed using X-ray diffraction, confirming a cubic NaCl-type structure without secondary phases. Electrical measurements using the four-probe method, along with optical spectroscopy and photoluminescence, allowed for tracking the evolution of the bandgap width and identifying characteristic features near the phase transition region.

The results demonstrated that increasing the Sn concentration leads to band inversion, accompanied by pronounced changes in the electronic and optical properties of the material. The observed anomalies in the temperature dependence of electrical conductivity and heat capacity are explained by the contribution of electron–phonon interactions and anharmonic effects in the lattice dynamics. Additionally, it was established that topologically protected states form on the sample surfaces, confirmed by photoelectron spectroscopy methods. The obtained data are in good agreement with contemporary theoretical models and highlight the key role of phase transitions in shaping the physical properties of $Pb_{1-x}Sn_xTe$. Moreover, we show that controlled composition tuning (x), targeted doping, and strain engineering enable optimization of carrier density and mobility for device-relevant operation. A graded $Pb_{1-x}Sn_xTe$/PbTe architecture is promising for band alignment and reduced contact losses in IR photonic stacks.

The practical significance of this work lies in the fact that the revealed patterns can be utilized in the design of new materials for infrared optoelectronics, thermoelectric converters, and spintronic devices.

INFLUENCE OF TMAl AND SiH_4 PRECURSOR FLOW RATES ON THE STRUCTURAL AND ELECTRONIC CHARACTERISTICS OF LATTICE-MATCHED InAlAs USED IN QUANTUM CASCADE LASERS

Alkrdy A., Sür Ö., Ünal D.H., Koçak M.N., *Demir I.
Sivas Cumhuriyet University, Turkey
idemir@cumhuriyet.edu.tr

Quantum cascade lasers (QCLs) are unipolar semiconductor devices that rely on intersubband transitions within multiple quantum well structures, allowing their emission wavelength to be engineered through precise layer design. Their high output power, efficiency, and tunability make them indispensable for mid-infrared technologies. In lattice-matched InGaAs/InAlAs QCLs grown on InP, InAlAs serves as the barrier layer, providing strong carrier confinement, enhanced electron transport, and controlled tunneling characteristics – making the optimization of its growth conditions essential for maximizing device performance.

In this study, the influence of arsine (AsH_3) flow rate on the structural, morphological, and electrical properties of lattice-matched InAlAs layers grown by metal–organic vapor phase epitaxy (MOVPE) was systematically investigated. Adjusting the AsH_3 flow modifies the effective V/III ratio during growth, thereby directly influencing group-V availability, indium incorporation, and the resulting alloy composition. Comprehensive material characterization was performed using high-resolution X-ray diffraction (HR-XRD) to assess lattice matching and compositional shifts, atomic force microscopy (AFM) to analyze nanoscale surface morphology, Raman spectroscopy to probe phonon behavior and strain state, and Hall effect measurements (HEMS) to evaluate carrier concentration and transport properties. The findings provide critical insights into the epitaxial growth optimization of InGaAs/InAlAs heterostructures, particularly for quantum cascade laser (QCL) applications where precise control of composition, interface quality, and doping is essential for device performance.

Acknowledgments. This work is based on results obtained during the ongoing Ph.D. thesis of Merve Nur Koçak, titled “Development of Short- and Mid-Wavelength Quantum Cascade Lasers”. Merve Nur Koçak is supported by the YÖK (Council of Higher Education) 100/2000 Ph.D. Scholarship Program and The Scientific and Technological Research Council of Turkey (TÜBİTAK) 2211/A Program. This study supported by The Scientific Research Project Fund of Sivas Cumhuriyet University, Turkey under the project number MRK-2024-004 and The Scientific and Technological Research Council of Turkey (TUBITAK) under the project number 22AG074.

THE NEGATIVE DIELECTRIC, ELECTRIC MODULUS, LOSS TANGENT (tanδ), AC CONDUCTIVITY (σ_{ac}), AND NYQUIST ARCS IN THE Au/(CdTe:PVA)/n-Si STRUCTURES AS FUNCTION OF FREQUENCY AND VOLTAGE

[1*]Demirci A., [2]Güçlü Ç.Ş.

[1]PROTEK Technology Solutions Trans. & Cons. Serv. Ind. & Trade Ltd. Co., Türkiye

[2]Gazi University, Türkiye

demircia@gmail.com

The value of complex dielectric (ε*(f)=ε'-iε''), complex electric modulus (M*(f)=M'+iM"), loss-tangent (tanδ=ε"/ε'), AC-conductivity (σ_{ac}), Nyquist-plots of the prepared Au/(CdTe:PVA)/n-Si SDs were calculated from the measured capacitance/conductance values as function of frequency and voltage. To obtain more information frequency and voltage dependence of them, the C-V-f and G-V-f measurements were performed at various frequency in voltage-range of -2V/6V by 50mV steps at room temperature. Experimental results indicate that all parameters as strong functions of frequency/voltage. The changes observed in these parameters are more effective, especially at low frequencies in inversion and depletion regions. Interestingly, negative-dielectric behavior was observed in the ε'-V plots at lower-frequencies in the inversion region. Conversely, the ε' value tends to a minimum in this region, while the ε" value tends to a maximum. This behavior is referred to "negative-dielectric" or "inductive-behavior" in the literature and is generally attributed to the presence of interface traps/states, series resistance of the structure, and majority carrier injection. The value of ε' was changed from 174.5 (at 0.1kHz) and 35.5 (at 1MHz) which is 46 times higher than the maximum value of traditional SiO_2 (3.8), so it can be more storage of electronic-charges or energy storage.

This study was supported by Scientific and Technological Research Council of TÜRKİYE (TÜBİTAK) **(Project Number 121C396).**

BIOPHYSICS

THE IMPACT OF WASTE FROM THE GADABAY DEPOSIT ON THE ENVIRONMENT

[1*]Guliyeva A.A., [2]Rafiyeva H.L., [2]Jafarova N.M.

[1]Institute of Catalysis and Inorganic Chemistry, Ministry of Science and Education, Azerbaijan

[2]Baku State University, Azerbaijan

aybeniz.quliyeva.72@mail.ru

The mining industry, ferrous and non-ferrous metallurgy, as well as enterprises for the production of rare and precious metals, are concentrated in the western region of the republic, in the Dashkasan-Gadabay economic district. Implementing a set of measures to address the environmental problems inherited from the long-term development of the mining industry in independent Azerbaijan is an important task. By the 21st century, the global volume of mineral extraction had reached 650 billion tons; hundreds of billions of tons of overburden, soil, and earth are moved for their recovery. Human geological activity surpasses natural processes in scale and leads to a sharp deterioration of the environmental situation on mining lands and adjacent territories. Mass explosions in open-pit mines have become routine and represent major sources of dust and toxic gases. As a rule, during a powerful explosion, the dust-gas cloud disperses 200–250 tons of dust within a radius of 2–4 km from the epicenter, causing environmental pollution in the surrounding areas. Mineral resources, almost all of which are practically non-renewable, are far from being fully utilized by modern mining. In most countries, 12–15% of ferrous and non-ferrous metal ores remain underground or are discarded into waste dumps. The so-called planned losses of coal amount to 40%, and oil – on average – to 56%. In the development of polymetallic ores, usually only one or two metals that are in particular demand at the moment are extracted, while the remaining associated metals are discarded together with the host rock. In the extraction of potash salts and mica, up to 80% of raw materials remain in waste dumps. Mineral resources, almost all of which are practically non-renewable, are far from being fully utilized by modern mining. Air dustiness and the sharp deterioration of living conditions are exacerbated by the weathering of rocks stored in dumps. Research and pilot-scale testing of these wastes have shown that they can serve as excellent raw materials for porous concrete aggregates, building bricks and ceramics, plaster and masonry mortars, crushed stone, and other construction materials. Their use is also promising as clay raw material for the production of hollow

building ceramics and agloporite – a lightweight porous aggregate for concrete. Coal beneficiation aimed at reducing its sulfur content results in the formation of carbonaceous pyrite (FeS_2), containing 42–46% sulfur and 5–8% carbon. Carbonaceous pyrite is a potential raw material for sulfuric acid production. Its use together with another large-scale industrial waste – iron sulfate ($FeSO_4$), produced during the manufacture of titanium dioxide (TiO_2) pigment – allows for the generation of SO, for subsequent sulfuric acid production (CO_2). Soil and surface water contamination with heavy metals sharply increases in areas adjacent to mine dumps. In the extraction of polymetallic ores, and for the soil cover in uranium mining regions, high concentrations of radionuclides are characteristic.

ECOLOGICAL ASSESSMENT OF THE ENVIRONMENTAL IMPACT OF HEAVY METALS IN THE WASTE GENERATED BY THE METALLURGICAL INDUSTRY

*Jafarova N.M., Hajiyeva S.R., Bayramov G.I.
Baku State University, Azerbaijan
nailajafarova@bsu.edu.az

The article primarily presents ecological analytical studies on the waste generated in the production areas of the Baku Steel Company. It was determined that during various steel casting and processing operations in several production areas of the enterprise, different types of waste are formed in gaseous-aerosol, liquid, and solid states, each with distinct compositions and properties. Based on our preliminary scientific research, the actual composition and concentration levels of harmful substances released into the atmosphere at different times in both the working and sanitary protection zones were identified. Initially, the actual concentrations of gaseous emissions formed in the working area of this production site were determined using the Dräger Tubes LLG, a flexible and mobile gas detection device. The actual concentrations of inorganic substances with ecotoxic properties emitted into the ambient air from the Electric Arc Steel Melting Furnace (EASMF) area of the Baku Steel Company were determined, primarily in the working area, particularly near the electric arc furnace. The article also provides scientific explanations of the negative environmental and human health impacts caused by heavy metals present in the industrial waste formed in the production areas of this enterprise.

The measurements were conducted using the aforementioned portable

device, with flexible analyses carried out in a circular pattern at a 10-meter radius around the EASMF. The results are presented in Table 1.

Table 1. Analysis Results of Ecotoxic Inorganic Substances Emitted into the Atmosphere from the Electric Arc Steel Melting Furnace (EASMF)

Names of Inorganic Substances with Ecotoxic Properties	**Maximum Allowable Concentrations (MAC) of these substances, mg/m³**	**Measured Concentrations in the Electric Arc Steel Melting Furnace (EASMF)**
Hg	0.0003	0.5ppm (4.10 mg/m³)
Cu	0.002	1ppm (2.59 mg/m³)
Ni	0.001	1ppm (2.40 mg/m³)
Pb	0.0003	1ppm (8.47 mg/m³)
Zn	0.05	2ppm (5.34 mg/m³)

Furthermore, it can be stated that many of the inorganic substances with ecotoxic properties listed in Table 1, even when undergoing various transformations during the process, lead to the formation of numerous harmful compounds. During the recycling process of steel equipment, cast iron, and even non-ferrous metals classified as scrap metal, a variety of complex metallic compounds are formed as a result of the high-temperature decomposition of many components used in the process (such as coal, coke, ferromanganese, and ferrosilicomanganese). During the cooling of these alloys, a portion of the metals that have separated from the main alloy enters the composition of the cooling water, thereby generating industrial wastewater. In the Electric Arc Steel Melting Furnace (EASMF) area, the amount of ecotoxic and harmful substances in the water used for cooling steel alloys, which is then reused, increases significantly. For this reason, the application of multi-stage physical and chemical treatment methods to purify the recycled industrial wastewater can be considered essential in preventing the emergence of environmentally stressful conditions in the working zone of the facility.

QUANTITATIVE STUDY OF PETROCHEMICAL AND POLYCYCLIC AROMATIC HYDROCARBON (PAH) POLLUTION IN LAKE ZABRAT ABSHERON PENINSULA

[1*]Hajiyeva S.R., [1]Aliyeva T.I., [2]Huseynov E.Y., [1]Jafarova N.M.

[1]Baku State University, Azerbaijan

[2]Azerbaijan State University of Oil and Industry, Azerbaijan

sevinchaciyeva@bsu.edu.az

This study presents a quantitative analysis of petroleum hydrocarbon contamination and polycyclic aromatic hydrocarbons (PAHs) in bottom sediments of Lake Zabrat, located on the Absheron Peninsula. The investigation employed gas chromatography and n-hexane extraction methods. Results indicate the presence of C7–C11 hydrocarbons with a maximum total concentration of 7.7 mg/l detected by gas chromatography in samples from station St 26. PAH analysis revealed the presence of 2-bromonaphthalene, fluorene, and phenanthrene with total concentrations up to 0.563 μg/l. These findings indicate anthropogenic impact associated with industrial and urban sources, providing important data for ecosystem assessment and environmental monitoring of the region. The objective of this study is to quantitatively assess the level of petrochemical contamination and the concentration of polycyclic aromatic hydrocarbons (PAHs) in the water of Lake Zabrat, located on the Absheron Peninsula. The analysis is based on gas chromatography and solvent extraction methods, aiming to determine the extent of anthropogenic impact and evaluate the current ecological condition of the aquatic environment. Amid rapid urbanization and industrial development on the Absheron Peninsula, the risk of hydrocarbon and related anthropogenic pollution in water bodies is increasing. Lake Zabrat, situated in an area subject to intense human activity, is particularly vulnerable to contamination by petroleum hydrocarbons and PAHs – persistent, toxic, and potentially carcinogenic compounds. Assessing their concentrations in lake water is crucial for identifying pollution sources, evaluating ecological risks, and supporting the development of effective environmental monitoring and protection strategies. The results of the chemical analysis of water samples collected from Lake Zabrat, including concentrations of petroleum hydrocarbons and polycyclic aromatic hydrocarbons (PAHs), are presented in Table 1. The data provide quantitative insight into the levels of both volatile and semi-volatile hydrocarbon compounds in the lake water, highlighting spatial variations in contamination across the sampled stations.

Table 1. Content of Petroleum Hydrocarbons and Polycyclic Aromatic Hydrocarbons (PAHs) in Water Samples from Lake Zabrat

Lake		St 24	St 25	St 26
Field number	Unit	912	4772	4773
TPH Zabrat				
C7H16	mg/l	1,5	3,0	3,0
C8H18	mg/l	0,8	1,5	1,0
C9H20	mg/l	1,5	2,0	0,5
C10H22 + C11H24	mg/l	<0,5	0,5	1,7
C12H26 + C15H32	mg/l	<0,5	<0,5	1,5
C16H34 +C20H42	mg/l	<0,5	<0,5	<0,5
C21H44 +C30	mg/l	<0,5	<0,5	<0,5
Total hydrocarbons by GC	mg/l	3,3	7,0	7,7
Total extractable Hydrocarbons by n-hexan extraction	mg/l	5,8	11,0	9,5
PAH				
Naphtalene	mkq/l	<0.02	<0.02	<0.02
Acenaphtylene	mkq/l	<0.02	<0.02	0,025
Anthracene	mkq/l	<0.02	<0.02	<0.02
Fluoranthene	mkq/l	<0.02	<0.02	<0.02
Naphthalene, 2-bromo-	mkq/l	0,171	0,237	0,148
Fluorene	mkq/l	0,049	0,059	0,049
Phenanthrene	mkq/l	0,195	0,267	0,173
Acenaphthene	mkq/l	<0.02	<0.02	<0.02
Pyrene	mkq/l	<0.02	<0.02	<0.02
Benz[a]anthracene	mkq/l	<0.02	<0.02	<0.02
Chrysene	mkq/l	<0.02	<0.02	<0.02
Total	mkq/l	0,415	0,563	0,395

EXPRESSION AND PURIFICATION CYTOCHROME C-LIKE DOMAIN OF THE HUMAN BK CHANNEL

Aliyeva T., Aliyeva A., Gudratova F., Mahmudova S., Gasimov K., Yusifov T.*
Institute of Biophysics, Ministry of Science and Education, Azerbaijan
Talehy671@gmail.com

The highly conductant, calcium-activated, voltage-gated BK channel (MaxiK; Slo1) was the first ion channel identified as susceptible to heme modulation. Human BK channels are widely expressed in human tissues. Recently, we found that the linker region between RCK1/RCK2 domains forms a cytochrome c-like

structure. But this newly identified cytochrome c-like domain has not yet been structurally characterized. To better understand the structure and function of this important region (598IAS...LSG718), we expressed and purified it from E. coli as a soluble protein.

Expression: M15[pREP4] bacterial cells were transformed with the recombinant pQE-30-Cytc plasmid. Protein expression was induced with 1 mM IPTG. Cells were cultured at 37°C in 1 liter of Luria-Bertani (LB) medium containing 100 mg/ml ampicillin. Cells were incubated for another 1 hour at 28°C and collected by centrifugation.

Purification: The cell pellet was resuspended in 5 volumes of Tris-buffered saline with imidazole (25 mM Tris-HCl, 150 mM KCl, 5-10-20 mM imidazole) and protease inhibitor cocktail (1 tablet/50 ml extraction solution, Roche Applied Science) and lysed by sonication. The supernatant was loaded onto a 5-ml nickel-nitrilotriacetic acid-agarose column, and the protein was eluted with elution buffer (25 mM Tris-HCl, 150 mM KCl, 150 mM imidazole, pH 8.0) containing a 150 mM imidazole gradient, according to the manufacturer's instructions.

Quality assessment: The purity of protein samples was analyzed by 12.5% SDS-PAGE. SDS-PAGE analysis of the purified cytochrome sample revealed a single band with a molecular weight just above 15 kDa, consistent with the expected molecular weight of the expressed protein (15.3 kDa). Further analysis of the purified cytochrome by electron absorption spectrometry revealed high purity of the Cytc domain protein, as measured by electron absorption spectrometry.

Functional property: Interestingly, spectral analysis of the purified cytochrome c domain revealed the presence of heme in the protein, confirming its affinity for the cytochrome c domain, and the human BK channel is a hemoprotein. In other words, heme is a natural ligand for this ion channel, binding to it non-covalently.

INTERPLAY BETWEEN BIOELECTRICAL AND EGFR SIGNALING PATHWAYS AS A NOVEL APPROACH IN CANCER THERAPY

Seyyabli A., Aliyeva G., Gudratova F., Gasimov K., Yusifov T.*
Institute of Biophysics, Ministry of Science and Education, Azerbaijan
Talehy671@gmail.com

Lung cancer is the second most prevalent cancer, with non-small cell lung cancer (NSCLC) comprising 85 percent of cases and representing the leading

cause of cancer-related mortality. The epidermal growth factor receptor (EGFR) regulates processes critical to tumor progression. EGFR tyrosine kinase inhibitors (EGFR-TKIs), including erlotinib, are standard treatments for metastatic NSCLC. However, most NSCLC cases with EGFR mutations that initially respond to EGFR-TKIs ultimately develop resistance and relapse. Consequently, alternative therapeutic strategies for NSCLC are required. One emerging approach targets bioelectrical signals mediated by ion channels in cancer cells. Evidence indicates that combining first-line therapies with ion channel modulators can reduce required chemotherapy doses and associated adverse effects. KCa3.1 ion channels have multiple roles in NSCLC, including prognostic significance and promotion of disease progression. Both in vitro and in vivo studies demonstrate that inhibition of KCa3.1 using blockers such as senicapoc or TRAM-34 reduces tumor migration, invasion, proliferation, and growth. Additionally, combining senicapoc with erlotinib enhances drug sensitivity, particularly under hypoxic conditions.

Recent research has examined how KCa3.1 channels in the inner mitochondrial membrane contribute to the resistance of NSCLC cells to EGFR-TKI therapy. Meta-analyses of microarray data indicate that KCa3.1 channel expression in erlotinib-resistant NSCLC cells correlates with genes involved in integrin and apoptotic pathways. To assess the impact of mitochondrial KCa3.1 channels on these pathways, both erlotinib-sensitive and erlotinib-resistant NSCLC cells were analyzed. Cell adhesion to the extracellular matrix was measured using single-cell force spectroscopy, and apoptosis was quantified with fluorescence-based assays. The findings show that inhibition of KCa3.1 channels with senicapoc in erlotinib-resistant NSCLC cells increases cell adhesion by upregulating β1-integrin expression, a process dependent on mitochondrial reactive oxygen species (ROS) release. Enhanced adhesion subsequently reduces NSCLC cell migration within a three-dimensional matrix.

These studies propose a model in which KCa3.1 channel inhibition helps overcome erlotinib resistance in NSCLC. Senicapoc operates through two distinct mechanisms. First, inhibition of mitochondrial KCa3.1 channels induces the release of reactive oxygen species (ROS), which promotes cancer cell apoptosis. Second, ROS release increases β1-integrin expression, enhancing adhesion to the extracellular matrix (ECM) and reducing the motility of erlotinib-resistant NSCLC cells. Additionally, senicapoc impairs cell migration by inhibiting plasma membrane KCa3.1 channels and preventing local volume changes at the cell's posterior. Thus, modulation of KCa3.1-mediated bioelectrical signals may represent a novel therapeutic concept for the treatment of NSCLC and overcoming resistance to EGFR TKIs

NOVEL MECHANISM OF CANCER DEVELOPMENT IDENTIFIED

[1*]Gasymov O.K., [1]Bakhishova M.J., [1,2]Melikova L.A., [2]Aliyev J.A.

[1]Institute of Biophysics, Ministry of Science and Education, Azerbaijan
[2]National Center of Oncology, Ministry of Health, Azerbaijan
oktaygasimov@gmail.com

Here we present a joint scientific study conducted by researchers from the Institute of Biophysics of the Ministry of Science and Education and the National Oncology Center of the Ministry of Health. This study aimed to identify structural differences related to the lipid composition of healthy and lung cancer cell membranes. Fourier Transform Infrared (FTIR) spectroscopy was applied to analyze the temperature-dependent changes in the spectral bands at 2848 cm^{-1} and 2916 cm^{-1} – sensitive to the "trans" and "gauche" conformations of the CH_2 groups within lipid molecules. These spectral regions correspond to the symmetric and asymmetric stretching vibrations of the CH_2 groups, respectively, and provide valuable information regarding the conformational order of lipid chains.

The results demonstrate that, unlike the lipids of cancer cells, those of healthy cells undergo a highly cooperative transition, characterized by simultaneous conformational changes of lipid molecules across the membrane. In contrast, cancer cell lipids exhibit a non-cooperative or stepwise transition, in which conformational changes occur in a less synchronized manner. Moreover, the transition temperatures observed in cancer cell membranes are significantly lower than those in healthy cells. The free energy values associated with the trans–gauche structural transitions differ markedly between cancerous and adjacent healthy cells, further confirming the distinct biophysical properties of their lipid components.

The molecular packing of lipid molecules is determined primarily by their conformational state. The packing density of fatty acid chains can be effectively monitored using the CH_2 scissoring band, which reflects lateral interactions among hydrocarbon chains. In healthy cells, the 1465 cm^{-1} band of CH_2 vibrations splits into two distinct components (at 1462 and 1472 cm^{-1}) due to strong coupling effects between adjacent lipid molecules. This splitting is indicative of dense, ordered, and orthorhombic packing of fatty acid chains. In contrast, cancer cells display no such band separation, implying that their lipid molecules are arranged in a more disordered and fluid manner. Overall, the FTIR data clearly suggest that the physical state and molecular organization of lipids differ substantially between healthy and cancerous cells. These findings underscore

that FTIR spectral bands corresponding to CH_2 symmetric and asymmetric stretching and CH_2 scissoring vibrations possess significant potential as reliable diagnostic markers for identifying and differentiating lung cancer tissues based on their molecular structural characteristics.

Interestingly, in some cells that are morphologically classified as healthy, lipids exhibit structural transitions similar to those of cancer cells. Conversely, no cancer cells display the lipid structural transitions typical of healthy cells.

Our findings show that metabolic changes can occur before morphological changes, and may represent one of the initial events triggering malignant transformation. While such conclusions have been suggested theoretically in the literature, they have been experimentally demonstrated for the first time through our research. This result is of particular importance in diagnostics, since diagnosis based solely on morphology may be insufficient for some patients. Therefore, alongside morphological analysis, determination of the metabolic profile at the cellular level is necessary for cancer diagnostics. At the same time, the results indicate that environmental factors influencing metabolic changes significantly affect the initiation and progression of cancer.

THE ROLE OF CONGO RED IN THE DETERMINATION OF AGGREGATES IN SILK FIBROIN SOLUTION

Mammadzada A.M.

İnstitute of Biophysics, Ministry of Science and Education, Azerbaijan
aidamammadzada92@gmail.com

The accumulation of toxic protein aggregates underlies many age-related pathologies. Neurodegenerative disorders, such as Parkinson's disease, Alzheimer's disease, and amyotrophic lateral sclerosis, affect an increasing number of individuals worldwide and are expected to become major healthcare and economic challenges in the near future.

Silk fibroin, as shown previously, can be proposed as a model protein to study the inhibition of fibrillation, owing to its similarities with amyloid-forming proteins. Amyloids are characterized by their ability to bind Congo Red (CR), one of the most commonly used amyloid-specific dyes. In Alzheimer's disease, senile plaques that bind the dye CR are a characteristic feature of the condition. This finding reveals that CR can interfere with β-amyloid fibril formation, bind to preformed fibrils, and prevent in vitro cytotoxicity.

The CR dye has been widely used to detect amyloid aggregates in tissues

and *in vitro* because of its ability to bind to amyloid-like proteins adopting a β-sheet conformation. Changes in CR absorbance monitored at 540 nm at regular time intervals are presented in gradual increase in absorbance was observed, consistent with the interaction of CR with amyloid-like aggregates. To visualize β-amyloid aggregates in the SF solution, CR staining was performed and analyzed using polarized light microscopy with crossed polarizers. Under these conditions, amyloid fibrils exhibit characteristic green birefringence, indicating that the bound CR molecules are specifically aligned along the fibril axis. In contrast, randomly oriented or unbound CR molecules do not produce birefringence. CR assays were conducted under the same experimental conditions as those used for circular dichroism (CD) spectroscopy. Upon binding, CR exhibits a characteristic red shift in its absorption maximum (λmax), with the most pronounced change typically observed around 540 nm.

A solution of SF (20 μM) was titrated with increasing concentrations of CR (2–40 μM). The plot of the area-normalized absorption spectra indicated the existence of two isosbestic points. The narrow width of the isosbestic point at approximately 564 nm (0.21 nm) is consistent with the presence of only two species: free CR and the CR–amyloid complex. These data suggest that CR selectively detects amyloid aggregates of SF, with no evidence of non-amyloid intermediates. The spectral analyses demonstrate that CR binds selectively to amyloid aggregates of SF, forming a distinct CR–amyloid complex characterized by well-defined isosbestic points. These findings confirm the utility of CR as a reliable probe for detecting amyloid structures without interference from non-amyloid intermediates.

QUANTUM-CHEMICAL PROPERTIES OF Fe-Ile-Trp DIMER COMPLEX

*Rahimzade S.G., Akverdieva G.A.
Baku State University, Azerbaijan
sararahimzada@bsu.edu.az

Metal complexes of the biologically active Ile-Trp dipeptide are formed by coordinating the Ile-Trp dipeptide with metal ions, most notably iron (Fe(II)). These complexes demonstrate potential for medical use because of their immunostimulating and immunomodulating effects, as well as their ability to treat iron and immune deficiencies.

We performed DFT/B3LYP calculations, using the 6-31+G(d,p) basis set, on the complex of iron (Fe) with the dimeric dipeptide Ile-Trp. In this compound,

two dipeptides, each consisting of isoleucine (Ile) and tryptophan (Trp), are bound together and chelated by iron. This type of complex is not a common, well-studied molecule and is formed through coordination between the iron ion and specific functional groups – carboxyl and amino groups. Within the framework of the study, the energies of frontier molecular orbitals, energy gap, chemical reactivity descriptors, atomic charge distribution, dipole moment, and polarizability were calculated for the Fe-Ile-Trp dimer compound.

The data obtained allowed for the accurate characterization of the stable molecular structure of the studied system. The calculations revealed that the nature of the mentioned substituent facilitates the formation of two stable, concave ring-shaped cavities through coordination bonds between C16–Fe89, N34–Fe89, C60–Fe89, and N78–Fe89. In addition, the effect of hydrogen bonds on the geometric structure of the complex was also observed. Hydrogen bonds N21H22 ··· O6, N21H22 ··· O44, N65H66 ··· O50, N65H66 ··· O88 were observed between the hydrogen atom of the amide groups and the oxygen of the carbonyl and carboxyl groups of the monomers.

To identify the locations of electrophilic and nucleophilic sites, or potential molecular interaction zones, the molecular electrostatic potential (MEP) maps of this complex were analyzed. The results allowed for an identification of the potential reactive sites of this compound and assessment of the Fe substituent's reactivity and the resulting chemical properties, including its catalytic and biochemical activity.

OPTICAL AND STRUCTURAL ANALYSES OF THE SERICIN – RHODAMINE 6G INTERACTION

Aytaj J.M.

Institute of Biophysics, Ministry of Science and Education, Azerbaijan
a.k134@hotmail.com

The study of sericin-Rhodamine 6G interactions is of great importance for understanding the structural and functional properties of these materials. In the present study, the sericin protein, which is produced by *Bombyx mori* (silkworm) during silk formation, was found to interact specifically and strongly with the Rhodamine 6G (laser dye) molecule to form a complex. As a result of the studies conducted, a hypochromic effect and induced circular dichroism (ICD) were observed during binding in the sericin- Rhodamine 6G complex.

The specificity and binding stoichiometry of the interaction properties of

sericin and Rhodamine 6G molecules were studied by titration experiments. Titration experiments were carried out using the ultraviolet-visible spectroscopy method. As a result of the experiments, it was shown that as the concentration of sericin protein increases (0-40μM), the Rhodamine 6G absorption intensity decreases sequentially. This decrease occurs as a result of the hypochromic effect and directly indicates the interaction between Rhodamine 6G molecules and sericin protein molecules. Since the molecules form a complex with each other, the conformational restriction of Rhodamine 6G occurs, and as a result, the π-π* transition responsible for its absorption line causes the hypochromic effect (decrease in absorption) based on the overlap of the π-orbitals in the xanthene ring system. The dissociation constant was calculated as a result of the titration experiment. As a result, the dissociation constant Kd= 0.8 μM was determined based on the interaction of sericin with Rhodamine 6G, which characterizes a fairly strong binding. As complementary experiments, the concentration of RHD 6G was varied while keeping the concentration of sericin protein constant (15μM). According to the results of this study, as the concentration of Rhodamine 6G increases, the hypochromic effect is observed to be stronger, but after reaching a certain limit, the system enters the saturation phase and the absorption changes plateau. The calculated Kd=11.6 μM, n=2.3 demonstrates positive cooperativity. Thus, the conducted studies show that the interaction of Rhodamine 6G with sericin protein occurs through the hypochromic effect, where the binding is quite strong (Kd = 0.8 μM) and is characterized by 1:1 stoichiometry. These results not only clarify the basic mechanisms of protein–dye interaction, but also indicate the potential role of sericin as a matrix in bio-optical materials and various photofunctional applications in the future.

In the present study, Circular Dichroism (CD) spectroscopy was applied to monitor the interaction between sericin and Rhodamine 6G complex. The circular dichroism spectra of the sericin- Rhodamine 6G complex in the visible light range are shown, along with the absorption and circular dichroism spectra of free Rhodamine 6G. In the free state, the Rhodamine 6G molecule shows a weak CD signal because its periphery is symmetrical. However, as shown in the figure, when it is combined with a protein to form a complex, the periphery of Rhodamine 6G becomes asymmetric and an induced circular dichroism (ICD) phenomenon occurs. The result shows that while the CD maximum of the free Rhodamine 6G molecule is at 520.5 nm, it exhibits a red shift to 525 nm upon interaction with sericin. The absorption of the complex is observed at 528 nm. These shifts and absorption changes indicate the specificity of the protein-dye complex.

Cu^{2+}–Silk FIBROIN INTERACTIONS: IMPACT ON MONOLAYER VISCOELASTICITY

***Suleymanova L.M., Gasymov O.K.**

Institute of Biophysics, Ministry of Science and Education, Azerbaijan
leman.dashdemirova@mail.ru

Copper ions (Cu^{2+}) are essential cofactors in numerous enzymes and, therefore, contribute significantly to diverse biological processes. They bind to a variety of proteins through coordination with the side chains of His, Cys, Met, Asp, and Glu, and such interactions can stabilize protein structure and enhance overall stability. Nevertheless, the presence of free Cu^{2+} can also exert toxic effects on organisms. Specifically, unbound Cu^{2+} generates reactive oxygen species (ROS) through Fenton-like reactions, which in turn damage proteins, DNA, and lipids. Given this dual role, the maintenance of Cu^{2+} homeostasis is of critical importance and must be tightly regulated. Indeed, deficiency, excess, or misregulation of Cu^{2+} has been implicated in a wide range of human diseases. Cu^{2+} ions have been shown to play an important role in amyloid protein aggregation and, therefore, neurodegenerative diseases, such as Alzheimer's, Parkinson's, prion, etc., diseases. It has been shown that Cu^{2+} may accelerate the nucleation and oligomerization rate of amyloid peptides. It has been shown that Cu^{2+}-induced protein aggregates are more toxic than fibrils.

Our previous studies indicate that fibroin extracted from silk cocoons shows a tendency to form β-amyloids. Several aggregation-related properties, such as temperature and pH dependence, resemble those of functional amyloids. Therefore, silk fibroin serves as a useful model for studying both the mechanisms of aggregation and their inhibition.

In this study, we used electron paramagnetic resonance (EPR) and circular dichroism (CD) spectroscopies to identify Cu^{2+} coordination sites in silk fibroin, as well as to examine binding-induced changes in protein secondary structure. Using Langmuir monolayer techniques, we obtained silk fibroin monolayers, and with a vibrating barrier at different frequencies (10 mHz–500 mHz), we investigated their dynamic properties in the presence and absence of Cu^{2+}.

EPR spectra of SF: Cu^{2+} films at room temperature exhibit three well-resolved out of four $A_{\parallel}$ hyperfine components. The following EPR spectral parameters for SF:Cu^{2+} films were obtained: SF:Cu^{2+} (1:1) ($g_{\parallel}$ = 2.273, $g_{\perp}$ = 2.053, $A_{\parallel}$ = 517.0 MHz); SF:Cu^{2+} (1:5) ($g_{\parallel}$ = 2.283, $g_{\perp}$ = 2.060, $A_{\parallel}$ = 510.3 MHz); and SF:Cu^{2+} (1:15) ($g_{\parallel}$ = 2.299, $g_{\perp}$ = 2.062, $A_{\parallel}$ = 487.8 MHz). Interestingly, the EPR spectral parameters for films SF: Cu^{2+} (1:1) and SF: Cu^{2+} (1:5) are very similar

to those of Cu^{2+} bound to the murine prion protein fragment mPrP(58–91). By contrast, the parameters of the SF: Cu^{2+} (1:15) film resemble those of mPrP(121–131). Cu^{2+} ions occupy different binding sites at higher concentrations. The EPR parameters of Cu^{2+} in SF: Cu^{2+} (1:1) and SF: Cu^{2+} (1:5) are consistent with the coordination of the Cu^{2+} ion by two oxygen and two nitrogen atoms (2O2N). In contrast, the parameters of SF: Cu^{2+} (1:15) are consistent with the coordination of the Cu^{2+} ion by one oxygen and three nitrogen atoms (1O3N).

CD studies indicate that Cu^{2+} binding partially induces β-structure formation. However, the random-coil conformation remains dominant. This finding implies that Cu^{2+}-induced aggregation does not lead to the formation of β-amyloid.

Langmuir trough experiments indicate that Cu^{2+} ions bind to the silk fibroin monolayer, and the induced structural changes increase its elastic properties. The data support the hypothesis that Cu^{2+}-induced aggregation is more toxic, since it does not lead to β-amyloid formation.

INTERACTIONS OF IRON IONS WITH FUNGAL MELANINS

Bagirov R.M.
Baku State University, Azerbaijan
rafiqbagirov@bsu.edu.az

Recently, the synthesis and investigation of certain structural characteristics of complex compounds of biometals with biologically active ligands have attracted considerable attention from researchers.

The present work reports and discusses the results of experimental studies on the complex formation of iron ions with melanins extracted from the fungus associated with European beech (Fagus sylvatica) and birch (Betula) chaga, which exhibit high antioxidant activity.

Melanins were isolated using alkaline extraction followed by precipi-tation in an acidic medium. To identify the extracts, their IR and EPR spectra were recorded. Analysis of the IR and EPR spectral parameters showed good agreement with analogous data reported in the literature, allowing us to conclude that the isolated pigments are indeed melanins. Complexes of iron ions with fungal melanins were obtained by incubating freshly isolated melanin in a solution of (^{57}Fe) SO_4 at room temperature. The incubation time was varied from 5 minutes to 2 hours.

It was established that the obtained precipitates (complexes) possess a complex Mössbauer spectrum, consisting of at least four partial spectra: two doublets and two sextets with broadened lines of relaxation origin. The central, more intense broad doublet (δİ = 1.31 mm/s, ΔE = 3.08 mm/s) is characteristic of high-spin (HS) Fe^{2+} complexes. The less intense, narrow central doublet (δİ = 0.50 mm/s, ΔE = 0.87 mm/s) corresponds to paramagnetic HS Fe^{3+} complexes. The parameters of the sextet partial spectra (δİ = 0.65 mm/s, ΔE = 0.23 mm/s, B_eff = 50.2 T and δİ = 0.51 mm/s, ΔE= 0.34 mm/s, B_eff = 55 T) are also characteristic of HS Fe^{3+} complexes. Comparative analysis of all partial spectral parameters indicates that iron ions in the complex have an octahedral ligand environment, suggesting that fungal melanins act as weak-field ligands toward iron ions.

The simultaneous presence of magnetic and doublet partial Mössbauer spectra in the sample is likely associated with a heterogeneous distribution of iron-binding centers in the melanin polymer. For two or more closely spaced Fe^{3+} ions (for instance, those forming polynuclear clusters with $n \geq 2$), rapid relaxation due to effective spin–spin interactions results in the observation of doublet partial spectra. In the case of spatially well-separated Fe^{3+} ions, spin–spin interactions are significantly weakened, resulting in relaxation spectra with diffuse hyperfine structure. The sextet with an effective magnetic field of ~55 T likely corresponds to Fe^{3+} ions bound to carboxyl groups, while the sextet with a smaller field (~50 T) corresponds to structures where amino or imino groups of melanin also participate in the coordination of Fe^{3+}.

Thus, the obtained results demonstrate that fungal melanins can effectively bind iron ions in both divalent and trivalent states. Importantly, fungal melanins, similar to those of animal and plant origin, are capable of directly binding pro-oxidant Fe^{2+} ions and oxidizing them to Fe^{3+}, which is inactive in pro-oxidant reactions, followed by complex formation. The activity of both these processes increases with rising pH of the reaction medium and under illumination of the suspension with visible light.

SPATIAL STRUCTURE AND CONFORMATIONAL PROPERTIES OF PENTAPEPTIDE MOLECULE Np5

[1*]Ismailova L.I., Akhmedova S.R.[2], Akhmedov N.A.[1]

[1]Baku State University, Azerbaijan

[2]Azerbaijan Technical University, Azerbaijan

lara.ismailova.52@mail.ru

Recently, the pentapeptide Leu-Lys-Glu-Lys-Lys (Np5) was synthesized. It was found to have anti-inflammatory activity in vitro and in vivo. The molecule is non-toxic, has a simple structure, and is not immunogenic. All this makes the molecule suitable for the development of an anti-inflammatory drug. It is known that a synthetic pentapeptide Leu-Lys-Glu-Lys-Lys (LKEKK) corresponding to the sequences 16–20 of human thymosin-α1 and 131–135 of human interferon-α2 binds with high affinity to the membrane, s small intestinal mucosa.

The knowledge of the structural and functional properties of peptide molecules is of great practical importance for medicine and pharmacology. This scientific work is devoted to studying the spatial structure and conformational possibilities of the pentapeptide Np5. It is known that short linear peptides in solutions do not have a fixed spatial structure. The amino acid sequence and physicochemical properties of the solvent determine the set of low-energy conformations of the peptide molecule. The three-dimensional structure of the synthetic peptide Np5 is studied by the method of theoretical analysis. The potential function of the system is chosen as the sum of non-valent, electrostatic and torsional interactions and the energy of hydrogen bonds. Non-valent interactions were estimated using the Lennard-Jones potential. Electrostatic interactions were calculated in the monopole approximation using Coulomb's law with partial charges on atoms. The energy of hydrogen bonds was estimated using the Morse potential.

The conformational possibilities of the pentapeptide LKEKK were studied in fragments. First, the conformational properties of two tripeptides, LKE and EKK, were determined. The three-dimensional structure of the tripeptides was studied based on the low-energy conformations of the corresponding amino acid residues. The addition of the tripeptides allowed us to calculate the spatial structure of the all pentapeptide molecule. As can be seen from the amino acid sequence, the molecule includes polyatomic, positively and negatively charged amino acid residues. The results of the calculation of the Np5 molecule showed that there is a sharp energy differentiation between the shapes, forms of the main chain, and conformations.

Conformations of twelve shapes fall into a large energy interval (0-10)

kcal/mol. Conformations of shape f f f e turned out to be sterically impossible, and conformations of shapes f e f f, e e f e, e f f e are high-energy. The energy range (0-6) kcal/mol includes conformations of five forms of the main chain: BBBBB, RRBBB, RBBBB, RRBRR, RBRBB. Thus, the spatial structure of the pentapeptide molecule Np5 can be represented by twelve structural types, and it can be assumed that the molecule carries out its physiological functions precisely in these structures. Theoretical conformational analysis of the pentapeptide molecule Np5 led to a structural organization of the molecule that does not exclude the implementation of many functions by the molecule that require strictly specific interactions with various receptors.

THE EFFECT OF HYPERTHERMIA AND ALKALIZATION ON THE DISTRIBUTION DYNAMICS OF ANTI-CANCER AGENTS IN LUNG CANCER

[1*]Bakhishova M.J., [1]Aslanov R.B., [1,2]Melikova L.A., [1]Gasymov O.K.

[1]Institute of Biophysics, Ministry of Science and Education, Azerbaijan

[2]National Center of Oncology, Ministry of Health, Azerbaijan

matanat.baxishova93@gmail.com

In several types of cancer, the lipids – the main structural components of cell membranes – differ sharply from those in healthy cell membranes. This compositional difference confers distinct physicochemical properties upon cancer cells. The presented work was carried out within the framework of a collaboration between the Institute of Biophysics of the Ministry of Science and Education and the National Oncology Center of the Ministry of Health. Human lung tissues were collected immediately after surgery from lung carcinoma patients in accordance with the principles of the Declaration of Helsinki and approved by the review board of the Azerbaijan National Oncology Center. To investigate the characteristics of human lung normal and carcinoma cell membranes, the spin label 2,2,6,6-tetramethylpiperidine-1-oxyl (TEMPO) was employed and studied using electron paramagnetic resonance (EPR) spectroscopy. Since the TEMPO spin label exhibits no binding affinity toward proteins, it enables the selective evaluation of membrane lipids.

The primary goal of this study is to identify potential approaches for cancer therapy based on cell membrane properties and thus contribute to the advancement of personalized medicine. The experiments were con-ducted at two pH values, 6.2 and 7.3, corresponding to the microenvironmental conditions of

cancerous and healthy cells, respectively. Additionally, TEMPO partitioning experiments were carried out within the temperature range of 273–317 K to examine the influence of local hyperthermia, which is often applied alongside chemotherapy. Hyperthermia refers to the controlled elevation of temperature in a specific region, organ, tissue, or even the entire body through the application of heat. This method is primarily used to target malignant tumors and the surrounding tissues and structures. The results show that the partition coefficient of the TEMPO spin label in cancer cell membranes is significantly higher compared to that in neighboring healthy cells. As the temperature increases, the partition coefficient of TEMPO also rises in both normal and carcinoma samples. However, within the studied temperature range, the partition coefficient remains consistently higher in cancer cells than in normal ones. Data obtained using C12SL, a spin-labeled analog of lauric acid, indicate that the membrane dynamics of cancer cells increase with temperature, which may represent a possible mechanism underlying the enhanced partitioning of the TEMPO spin label. The calculated free energy values for TEMPO partitioning at pH 6.2 and 7.3 show that, at pH 7.3, the process requires approximately 30% less energy.

The above-mentioned results pertain to a patient who had not received radiation or chemotherapy prior to the surgical procedure. Furthermore, the TEMPO partitioning experiments were extended to four additional samples. In all cases, the general partitioning characteristics of TEMPO were similar, but the partition coefficients varied depending on the sample. The benefits of alkalization and/or hyperthermia may not be observed universally. These findings are highly valuable from the standpoint of personalized medicine, as they may help predict whether local hyperthermia and alkalization could serve as effective complementary therapies for patients undergoing chemotherapy.

SPATIAL STRUCTURE OF THE H–Ala–Val–Pro–Tyr–Pro–Gln–Arg–OH MOLECULE

Karimli Y.Q., Akhmedov N.A.[1]
Baku State University, Azerbaijan
yasaman.karimli.g@gmail.com

The heptapeptide molecule H–Ala–Val–Pro–Tyr–Pro–Gln–Arg–OH belongs to the group of bioactive peptides formed as a result of the enzymatic degradation of β-casein, one of the milk proteins. β-casein is the main protein of milk and contains many biologically active fragments. These fragments become active only

when released under the action of specific enzymes. The studied heptapeptide molecule is one of these fragments.

The spatial structure of the H–Ala–Val–Pro–Tyr–Pro–Gln–Arg–OH heptapeptide molecule was studied by dividing it into fragments. In the first approximation, the spatial structures of the N-terminal H–Ala–Val–Pro–Tyr tetrapeptide fragment and the C-terminal Tyr–Pro–Gln–Arg–OH tetrapeptide fragment were investigated based on the low-energy conformations of the corresponding amino acid residues. The calculation of the spatial structure of the N-terminal tetrapeptide fragment shows that differentiation occurs according to the energies of shapes, main-chain forms, and conformations. For each of the four possible shapes of the tetrapeptide fragment, three conformations of the main chain were considered. Therefore, conformations of twelve main-chain forms were calculated for the tetrapeptide fragment. The lowest-energy conformation of each main-chain form was selected. The relative energies of these conformations vary within the range of (0)–(8.0) kcal/mol, and all of them were chosen as initial variants for calculating the spatial structure of the heptapeptide molecule.

The spatial structure of the C-terminal Tyr–Pro–Gln–Arg–OH tetrapeptide fragment was studied based on the low-energy conformations of the corresponding amino acid residues. Since the R-form of the main chain of the amino acid residue preceding the Pro residue is high in energy, the conformations of eight main-chain forms belonging to four shapes of the tetrapeptide fragment were calculated. The calculations show that strong differentiation occurs according to the energies of shapes, main-chain forms, and conformations. The lowest-energy conformation of each main-chain form was selected. The relative energies of these conformations vary within the range of (0)–(12.0) kcal/mol, and they were chosen as initial variants for calculating the spatial structure of the heptapeptide molecule.

At the final stage, the spatial structure of the heptapeptide molecule was calculated based on the low-energy conformations of its N-terminal and C-terminal tetrapeptide fragments. The set of low-energy conformations of the molecule, the interaction energies stabilizing them, and the values of the dihedral rotation angles were determined.

SPATIAL STRUCTURE OF THE β-CASOMORPHIN-9 MOLECULE

*__Akhmedov N.A., Ismailova L.I., Agayeva L.N., Godjayev N.M.__
Baku State University, Azerbaijan
namiqabdulavval@mail.ru

Casomorphins are opioid peptides derived from casein, the main protein of milk, during the digestion process. These peptides are produced as a result of enzymatic cleavage in the gastrointestinal tract and are capable of exerting morphine-like physiological effects. The spatial structures of various casomorphin molecules, which contain four to eight amino acid residues and are obtained from food, have been studied by theoretical conformational analysis. In this study, the three-dimensional spatial structures and conformational possibilities of the bovine β-casomorphin-9 (Tyr1-Pro2-Phe3-Pro4-Gly5-Pro6-Ile7-Pro8-Asn9) molecule were investigated using theoretical conformational analysis. The potential energy of the system was expressed as the sum of non-valent, electrostatic, torsional, and hydrogen bond interaction energies.

The β-casomorphin-9 molecule was obtained by adding an Asn residue to the β-casomorphin-8 molecule. The spatial structure of β-casomorphin-9 was calculated based on the low-energy conformations of β-casomorphin-8 and the Asn9 fragment. The β-casomorphin-9 molecule consists of amino acid residues with diverse structural characteristics: two large and flexible aromatic residues (Tyr1 and Phe3); four proline residues (Pro2, Pro4, Pro6, Pro8); one glycine residue (Gly5) with high conformational freedom; one isoleucine residue (Ile7) with limited conformational flexibility; and one polar residue (Asn9) with a side chain capable of hydrogen bonding. As a result, the β-casomorphin-9 molecule adopts a highly compact spatial structure. Such compact conformations are possible only for certain spatial orientations of the four proline residues. The computational results showed that the shapes, backbone conformations, and energy distributions of β-casomorphin-9 are strongly differentiated in terms of energy. The low-energy conformations of the molecule, their relative energies, and the contributions of various interaction energies are presented in Table 1.

As seen from Table 1, six conformations of the main peptide backbone correspond to low-energy states. Three of these differ from the other three only by the conformation of the C-terminal dipeptide fragment (Pro8–Asn9). The side chains of Ile7 and Asn9 possess a certain degree of conformational flexibility, which affects the molecule's overall dynamics. Therefore, it can be assumed that the physiological activity of β-casomorphin-9 may be lower compared to other β-casomorphin analogues, as its compact conformation limits structural

adaptability. The study also determined the low-energy spatial structures of β-casomorphins, the interaction energies responsible for their stabilization, the roles of intra- and inter-residual interactions in spatial organization, and the values of the dihedral torsion angles.

Table 1. Energy contributions of non-valent (Unv), electrostatic (Uel), torsional (Utors) interactions and relative (Urel) energies of the optimal conformations of the β-casomorphin-9 molecule.

№	Shapes	Conformation	Unv	Uel	Utors	Utotal	Urel
1	efeffeee	B2BL3RRBB32BB31	-32.2	-1.0	4.0	-29.2	0.0
2	efeffeef	B2BL3RRBB32RR31	-31.6	-1.3	4.5	-28.5	0.7
3	ffeeeeef	R3RB1RLBB32 RR31	-27.6	-2.4	4.0	-25.9	3.3
4	ffeeeeee	B3RB1RLBB32 BB31	-26.0	-2.5	4.5	-23.9	5.3
5	eeefefef	B1BB2BLRB12 RR31	-28.3	-1.8	4.8	-25.3	3.9
6	eeefefee	B1BB2BLRB12 BB31	-27.6	-1.8	5.2	-24.2	5.0

SPATIAL STRUCTURE OF ANALOGUES OF THE RUBISCOLIN-5 MOLECULE

*__Agayeva L.N., Karimli Y.G.__
Baku State University, Azerbaijan
leylaagayeva@bsu.edu.az

The H-Tyr1-Pro2-Leu3-asp4-Leu5-OH rubiscolin-5 molecule is an opioid peptide obtained from food. The spatial structure of the molecule was studied by theoretical conformational analysis and was shown to have eight low-energy conformations. Its various analogues were synthesized by Sobolezyk M., Perlikowska R. The spatial structures of the analogues [Met3], [Met5], and [Met3], [Phe5]-rubiscolin-5 were studied by theoretical conformational analysis. The [Met3], [Met5]-rubiscolin-5 analogue was obtained by replacing the third amino acid residue Leu3 and the fifth amino acid residue Leu5 in the natural rubiscolin-5 molecule with the methionine amino acid residue. The spatial structure of the analogue was studied based on the low-energy conformations of the natural rubiscolin-5 molecule. The low-energy conformations of the analogue are shown in the table; the values of their dihedral rotation angles correspond to the natural molecule. Based on the distribution of the energies of the conformations in both molecules, it can be assumed that this analogue can also perform certain functions of the natural molecule and can be proposed for synthesis and for studying the physiological functions of the molecule.

Table 1. Energy contributions of non-valent (Unv), electrostatic (Uel), torsional (Utors) interactions and relative (Urel) energies of the optimal conformations of the β-casomorphin-9 molecule.

№	Shapes	Conformation	Unv	Uel	Utors	Utotal	Urel
1	efee	B3RB21B3B33	-16.2	-4.2	3.5	-16.8	0.9
2	efff	B2RR22R3R33	-16.6	-3.5	2.7	-17.4	0.3
3	efef	B3RB33R3R33	-17.7	-4.4	4.5	-17.7	0
4	eeef	B2BB21R1R32	-15.7	-0.4	2.6	-13.6	4.1
5	effe	B3RR22B3B32	-14.9	-0.3	2.1	-13.1	4.6
6	eefe	B1BR23B1B33	-13.9	1.4	2.7	-12.9	4.8
7	eeff	B1BR22R3R33	-14.2	0.7	1.7	-11.9	5.8
8	eeee	B1BB21B1B33	-16.1	0.2	2.5	-13.3	4.4

The [Met3], [Phe5]-rubiscolin-5 analog was obtained by replacing the Leu3 amino acid residue in the third position with the Met amino acid residue, and the Leu5 amino acid residue in the fifth position with the Phe amino acid residue. The results of the calculations show that the low-energy conformations of this analog and the natural rubiscolin-5 molecule, the values of their dihedral rotation angles, and the spatial arrangement of the atoms are consistent. Therefore, it can be assumed that the [Met3], [Phe5]-rubiscolin-5 analog can perform certain functions of the natural rubiscolin-5 molecule and can be proposed for the synthesis and study of its physiological functions.

THE SPATIAL STRUCTURE OF THE N-TERMINAL TETRAPEPTIDE FRAGMENT OF THE ALBUTENSIN A MOLECULE

Ismayilzada M.T., Agayeva L.N.
Baku State University, Azerbaijan
leylaagayeva@bsu.edu.az

Albutensin A is a bioactive peptide formed as a result of the proteolytic cleavage of the serum albumin molecule. This molecule belongs to the group of albumin-derived peptides and possesses vasodilatory (vessel-widening) properties. The main function of Albutensin A is to participate in the regulation of blood pressure and the enhancement of blood flow to internal organs. It acts on endothelial cells of the vascular wall, stimulating the secretion of nitric oxide (NO), which causes relaxation of the blood vessels. The molecule has the structure H-Ala1-

Leu2-Lys3-Ala4-Trp5-Ser6-Val7-Ala8-Arg9-OH, and the spatial structure of the A-protein molecule has been confirmed by theoretical conformational analysis through the separation of its fragments. This research focuses on the N-terminal of H–Ala–Leu–Lys–Ala tetrapeptide fragment of the molecule, studying its spatial structure based on the low-energy conformations of the corresponding amino acids. According to the amino acid sequence of the fragment, the N-terminal region and the side chain of lysine are positively charged, while leucine and lysine possess multi-atomic and highly rotatable side chains. Therefore, numerous conformations of the tetrapeptide fragment were calculated to explore its conformational possibilities. The results of the calculations show that differentiation occurs according to conformational energies. The lowest-energy conformation for each form of the main chain was selected, and their shapes, as well as the contribution energies, along with their total and relative energies, are presented in Table 1.

Table 1. Energy contributions of non-valent (Unv), electrostatic (Uel), torsional (Utors) interactions and the relative energy (Urel) of the optimal conformations of the H–Ala–Leu2–Lys3–Ala4 fragment of the Albutensin A molecule.

№	Shape	Conformation	Unv	Uel	Utors	Utot	Urel
1	eff	$B_2\ R_{32}R_{2122}\ R_2$	-13.5	10.2	2.9	-0.4	0
2	efe	$B_2\ R_{32}\ B_{2122}\ B_2$	-11.6	8.5	2.8	-0.3	0.1
3	eee	$B_2\ B_{21}\ B_{2322}\ B_2$	-11.4	8.2	3.1	-0.1	0.3
4	fff	$R_2\ R_{32}\ R_{1222}\ R_2$	-14.0	11.7	2.7	0.3	0.4
5	fee	$R_2\ B_{12}\ B_{2322}\ B_2$	-11.4	8.9	3.2	0.8	1.2
6	fef	R_2 B21 R32 R_2	-13.0	11.6	2.3	0.9	1.3
7	eef	B_2 B32 R32 R_2	-12.0	9.9	3.7	1.6	2.0
8	ffe	$R_2\ R_{32}\ B_{1222}\ B_2$	-10.5	10.3	1.8	1.6	2.0

Electrostatic and nonvalent interaction energies play a crucial role in the formation of conformations. Within the energy range of 0–2.0 kcal/mol, eight conformations corresponding to eight distinct shapes were identified. These conformations were selected as initial models for studying the spatial structure of the Albutensin A molecule.

POLYPHENOLS FROM QUINCE LEAVES: EXTRACTION, CHARACTERIZATION, AND BIOLOGICAL

[1*]Madrakhimova S.D., [2]Matmuratov B.Ya., [2]Yunuskhuja Yu.T., [1]Matchanov A.D.

[1]Institute of Bioorganic Chemistry, Academy of Sciences of the Republic of Uzbekistan, Uzbekistan;
[2]Tashkent Medical University, Tashkent, Uzbekistan
bioorganic86@mail.ru

We extracted the leaves of quince, and qualitative reactions specific to total polyphenols were performed on the leaves with certain reagents. An aqueous extract of the plant leaf turned a solution of $FeCl_3$ green, a qualitative reaction to an aromatic ring. We observed a color change from orange to light red when we experimented with a 1% vanillin solution in hydrochloric acid. This reaction is characteristic of condensed polyphenols, namely anthocyanidins (catechins). Total polyphenols were isolated from quince leaves using extraction methods and organic solvents (acetone, chloroform, ethyl acetate) known in the literature. Studies were conducted to investigate the medicinal properties of an extract isolated from the leaves of quince on the mitochondrial membrane status of mouse cells. An extract isolated from the leaves of quince showed antioxidant and membrane-active properties and had a corrective effect on the state of the mitochondrial membrane. It can be concluded that the substances extracted from quince leaves are highly biologically active substances.

COMPARATIVE CONFORMATIONAL ANALYSIS OF TWO ANTIMICROBIAL TETRAPEPTIDES FRFR AND WRWR

[*]Agaeva G.A., Agaeva U.T., Godjaev N.M.

Baku State University, Azerbaijan
gulshenagaeva@bsu.edu.az

Many antimicrobial peptides are synthesized in the body by the immune system in response to infection with foreign bacteria, viruses or fungi. These peptides are considered promising antibiotics, due to a wide range of antimicrobial properties and the ability to kill bacteria with drug resistance. However, the large size of such peptides did not contribute to their pharmaceutical development. Therefore, many studies have been conducted to identify effective

short antimicrobial peptides. Thus, showed antimicrobial activity in short tetrapeptides consisting of natural amino acids. The ultrashort linear antimicrobial tetrapeptides FRFR-NH2 and WRWR-NH2 have potent and rapid antimethicillin-resistant Staphylococcus aureus (MRSA) activity. It is known that FRFR-NH2 and WRWR-NH2 peptides tend to bind with the membrane surface in a monomeric form and cover the membrane surface in a carpet-like manner. Therefore, these results provide an advanced microscopic understanding of how hydrophobic interactions or hydrophobic residues affect the antimicrobial activity and mechanism of antimicrobial peptides (AMPs). As the results of the study showed, tetrapeptide monomers, interacting with membranes, completely cover their surface.

To study the mechanism of interaction of these tetrapeptides with the surface of membranes, it is necessary to know the conformational behavior of the peptide molecule, as well as the parameters of the electronic structure of its stable conformational states. Conformational changes of the molecule lead to the movement of some atomic groups relative to others and this changes the electronic distribution and geometric parameters, as a result of which the nature of the interaction and the binding properties of the molecule change.

To determine the mechanism of interaction of the tetrapeptides FRFR and WRWR with membranes in the present work, conformational features were investigated using molecular modeling methods. The study showed that the conformational behavior of each tetrapeptide can be described by a set of low-energy conformations with a similar semi-folded shape of the peptide chain. Conformational analysis of the tetrapeptides made it possible to determine the nature of the forces stabilizing the energetically preferred spatial structures of the molecules, and energetically preferred regions of the values of dihedral angles; the values of the energy contributions of interactions between residues were also determined. The mutual arrangement of residues and their side chains in low-energy conformations of the tetrapeptides WRWR and FRFR was also revealed. Based on the obtained values of dihedral angles, molecular models of stable conformations of the tetrapeptides FRFR and WRWR were constructed, the comparison of which made it possible to identify structural features important for the design of drugs suitable for clinical use.

STUDY OF THE DIPEPTIDE FRAGMENT OF BIOLOGICALLY ACTIVE MOLECULE

***Abbasova G.D., Haciyeva L.S.**
Baku State University, Azerbaijan
lalahaciyeva@bsu.edu.az

Conformational changes within a molecule play an essential role in the structural organization of peptide compounds. In living organisms, peptides act as carriers of biological information. The transmission of information from one cell to another regulates the vital activity of the organism.

Cells synthesize specific types of proteins, and the interactions and precise functioning of these proteins contribute to the coordination of overall physiological processes.

The study of the spatial structure and adaptive potential of complex molecules enables a better understanding of the molecular mechanisms underlying physiological processes in living cells and organisms. The diverse biological functions of peptides are directly related to their three-dimensional and spatial organization. A detailed investigation of the principles of three-dimensional structure and spatial configuration, as well as of the biological functions of natural peptides and proteins, provides the foundation for the design of their synthetic analogues. Therefore, structural studies of peptides should include not only experimental research but also theoretical calculations using advanced technologies and computer-based modeling methods. Theoretical conformational analysis is a molecular modeling approach that allows for the evaluation of the conformational possibilities of a peptide molecule and determination of its energetic and geometrical parameters.

As the object of this research, the structure H-Val^{1}-Ser^{2}-Glu^{3}-Asn^{4}-Leu^{5}ψ ($CH(OH)CH_2$) Val^{6}–Ile^{7}–Val^{8}–OH, designated U-85548e according to international nomenclature, was selected. This inhibitor consists of eight amino acids, seven of which are natural, while the fifth amino acid, Leu, is non-standard. Based on its conformational potential, this inhibitor represents a complex molecular system. According to the developed methodology, complex peptide molecules are divided into di-, tri-, and tetrapeptide fragments to study their spatial properties, and the stable conformations of each fragment are analyzed separately. The above inhibitor was divided into seven dipeptide fragments. When examining the spatial structure of the Val^{6}–Ile^{7} dipeptide fragment, the study was conducted based on the stable conformations of the constituent amino acids Val and Ile. This fragment is composed of the essential amino acid valine

(Val) and the aliphatic α-amino acid isoleucine (Ile).

The conformational variability of a molecule may lead to different intramolecular interactions and cause variations in the energetic characteristics of its functional groups.

For the Val^6–Ile^7 dipeptide fragment, a total of 246 conformations were calculated. The relative energies (in kcal/mol) are distributed as follows: 13 conformations fall within the 0–1 kcal/mol range, 16 within 1–2 kcal/mol, and 25 within 2–3 kcal/mol. The remaining ones correspond to higher-energy states. Analysis shows that the electrostatic energies of nearly all conformations are approximately the same. This results from the non-polar nature of the side chains of Val and Ile. The torsional energy is also relatively constant, around 2 kcal/mol, indicating an absence of significant internal strain. The low-energy conformations of the molecule are predominantly stabilized by non-valent interactions. The obtained values can be used in the calculation of tri- and tetrapeptide fragments.

CONFORMATIONAL BEHAVIOR OF β-AMYLOID (25–35) PEPTIDE IN DIFFERENT ENVIRONMENTS: STRUCTURAL INSIGHTS INTO AGGREGATION PROPENSITY

[1*]Najafova G.Z., [2]Agaeva G.A.

[1]French-Azerbaijani University (UFAZ) under the Azerbaijan State Oil and Industry University, Azerbaijan.

[2]Baku State University, Azerbaijan

gulshenagaeva@bsu.edu.az

Understanding the structural determinants that govern amyloid β-peptide aggregation is crucial for elucidating the molecular mechanisms of Alzheimer's disease. The short fragment Aβ-(25–35), which retains the neurotoxicity and aggregation behavior of the full-length peptide, was examined under different physicochemical conditions to evaluate its conformational adaptability and stability. By integrating experimental and computational results obtained in aqueous, lipid, and organic environments, this work demonstrates how external conditions modulate the balance between ordered (α-helical, β-sheet, β-turn) and disordered structural states. In lipid systems mimicking biological membranes, the peptide preferentially adopts flexible yet partially helical structures, while in aqueous and organic media, it remains largely disordered. The comparative analysis highlights that the presence of cholesterol and hydrophobic interfaces

promotes β-structure formation, suggesting an environment-dependent pathway toward aggregation. The unified interpretation of these findings reveals that Aβ-(25–35) exhibits strong conformational polymorphism driven by its surroundings. Understanding this structural adaptability provides valuable insight into the early stages of amyloid fibril formation and contributes to the rational design of anti-aggregation strategies for Alzheimer's disease.

THE EFFECT OF SOME ELECTROLYTES ON THE STRUCTURAL TEMPERATURE OF WATER

Masimov E.A., Aliyev E.Z., *Teymurova J.Z.
Baku State University, Azerbaijan
jalateymurova98@gmail.com

Water is one of the most important and unique substances in nature. Its molecular structure and physical properties change under the influence of dissolved substances, especially electrolytes. In this study, the structural temperature (Tstr) of aqueous solutions containing inorganic salts such as sodium nitrite ($NaNO_2$), sodium nitrate ($NaNO_3$), sodium dichromate ($Na_2Cr_2O_7$), and sodium dihydrogen phosphate (NaH_2PO_4) was determined using an optimization method based on the viscosity–temperature dependence. Experimental results showed that the 1/(T–Tstr) dependence provides a more accurate correlation than 1/T. It was found that all investigated salts increase the structural temperature of water, indicating their water-structuring effect. These findings help to better understand how electrolytes influence the hydrogen-bond network and dynamic properties of water.

The concept of structural temperature of water was first introduced by Bernal and Fowler to describe the structural state of liquid water. Later, Ueberreiter proposed a different interpretation of this concept based on the temperature dependence of viscosity using Vogel's empirical equation. The structure of water refers to parameters such as the number, energy, density, and length of intermolecular hydrogen bonds, their spatial configuration, and the average kinetic energy of water molecules. A change in any of these parameters indicates a change in the structural organization of water. For any aqueous solution with a given concentration (Ci), there exists a temperature (Ti) at which the selected physicochemical property of pure water coincides with that of the solution at room temperature; this temperature was defined by the authors as the "structural temperature." In the present study, the

temperature dependence of the viscosity of 10% aqueous solutions of inorganic salts ($NaNO_2$, $NaNO_3$, $Na_2Cr_2O_7$, NaH_2PO_4) was measured using an SVM3000 Stabinger viscometer. Based on the obtained experimental data, the structural temperature (Tstr) was determined by applying the optimization method to the viscosity–temperature relationship. The results showed that the 1/(T–Tstr) dependence provides a more accurate correlation than 1/T. The structural temperatures were found to be 139K for pure water, 173K for $NaNO_2$, 155K for $NaNO_3$, 148K for $Na_2Cr_2O_7$, and 146K for NaH_2PO_4. It was established that when Tstr(solution) > Tstr(water), the solute acts as a water-structuring substance. Therefore, all investigated salts increase the structural temperature of water, confirming their structure-forming effect.

THE ROLE OF INTRAMOLECULAR RESONANCE HYDROGEN BONDING IN THE FORMATION OF INTERMOLECULAR HYDROGEN BONDS IN MONO- AND DIMERIC COMPLEXES OF THE (Z)-N, N-Diethyl-3-oxo-2-(2-phenylhydrazineylidene) PROPANAMIDE $C_{13}H_{17}N_3O_2$ MOLECULE

***Demukhamedova S.D., Aliyeva I.N.**

Baku State University, Azerbaijan

svetlanabest@mail.ru, irada_aliyeva@bsu.edu.az

In recent years, considerable interest has focused on studying the role and mechanisms of the transformation of intramolecular hydrogen bonds (H-bonds) into intermolecular ones, leading to the formation of more stable molecular complexes. This process is particularly characteristic of resonant hydrogen bonds (RAHBs), which are more susceptible to such transitions in reactive molecules. The formation of a resonant hydrogen bond, in which the electron density is distributed throughout the RAHB system, affects not only the strength and nature of the bond but also significantly influences the overall physical and chemical properties of molecules.

The paper describes the mechanism of transformation of the intramolecular resonance hydrogen bond in the structure of the newly synthesized molecule (Z)-N, N-diethyl-3-oxo-2-(2-phenylhydrazineylidene) propanamide ($C_{13}H_{17}N_3O_2$) into an intermolecular hydrogen bond during the formation of its dimeric complex, both in the gas phase and under aqueous conditions. The molecule under study was synthesized in the Laboratory of Fine Organic Synthesis at Baku State University through the reaction of N-substituted hydrazones with CCl_4 in the presence of a CuCl catalyst. Theoretical investigations were carried out using a non-empirical quantum chemical method within the framework of

Density Functional Theory (DFT) using the hybrid B3LYP potential in an extended 6-31+G(d,p) basis set, which includes polarization and diffuse functions.

Based on the analysis of energy characteristics, chemical bond parameters, redistribution of electron density as a result of interatomic interactions and calculations of reactivity descriptors in optimized structures of the studied molecule, the role of the intramolecular resonant H-bond in the formation of the intermolecular hydrogen bond responsible for the stabilization of the dimeric complex was described. The calculations were carried out in several successive stages of computer modeling using the GAUSSIAN-09 software package. To interpret the obtained results, we used the convenient and functional graphical interface CaussView 6.0.16, which allows us to process and visualize numerous optimized structural parameters, in particular, frontier molecular orbitals, and to construct distribution surfaces of the molecular electrostatic potential of the studied molecules, with the help of which we can clearly determine the sites of possible nucleophilic and electrophilic attacks.

The study also included an analysis of natural bond orbitals (NBOs) for the monomeric molecule and its dimeric complex in an aqueous medium. The purpose of the NBO calculation was to study conditions favorable for the formation of H-bonds, intermolecular hybridization, and to describe the delocalization of electron density in the structure of the studied compounds. The calculated data include bond populations, energies, and the main delocalization interactions during hydrogen bond formation, allowing one to identify the type of atoms they belong to (the same, adjacent, or located at a distance).

These results can be useful for quantitative assessment of the contribution of intermolecular hydrogen bonds to the stability of the studied compounds and their complexes.

SPATIAL STRUCTURE AND REACTIVITY OF T7 PEPTIDE BASED ON THEORETICAL STUDIES

***Hajiyeva Sh.N., Abbasova G.D., Aliyeva I.N., Veliyeva L.I.**
Baku State University, Azerbaijan
shahlahaciyeva@bsu.edu.az

Studies carried out in recent years have shown that the development of effective drugs used in the treatment of oncological diseases is based on finding ways to deliver medicinal agents to the affected areas of tissues and organs. These investigations include studies using liposomes modified with the T7 peptide (T7-MLP@DTX/SchB) to improve the effectiveness of treatment for drug-

resistant breast cancer. The T7 peptide, with the chemical formula $C_{41}H_{60}N_{14}O_9$, has demonstrated tumor targeting specificity in preclinical studies for the treatment of solid tumors such as glioblastoma, liver cancer, and breast cancer.

Previously, we used molecular mechanics methods and quantum chemical calculations with semiempirical potential functions to investigate the spatial and electronic structure of the T7 peptide (HAIYPRH) and studied the molecular dynamics of the peptide molecule in an aqueous environment. In this study, we used quantum chemical calculations of the peptide's electronic characteristics, taking into account the electron energies, frontier orbital energy differences (HOMO and LUMO), dipole moment values, and other parameters. We described the key reactivity descriptors and analyzed charge density transfer pathways on the functional groups of the T7 peptide atoms. Visualization of molecular orbitals and electrostatic potential distributions in two- and three-dimensional images provided a clear picture of the changes in the electronic characteristics of the molecule during structure optimization.

The electronic structure of the T7 peptide was calculated based on the coordinates of the equilibrium nuclear configurations obtained by optimizing the molecular geometry in the MM+ semiempirical molecular mechanics potentials using the Polak-Ribiere algorithm with an accuracy of 0.001 kcal/mol. The obtained data formed the basis for calculating the electronic structure of the molecule using the PM3 semiempirical quantum chemical method, taking into account all valence electrons. The HyperChem 8.6 software package available on the Hypercube Corporation website (http://www.hyper.com/) was used for the calculations.

The calculated HOMO-LUMO energy gaps in various conformational states confirmed the stability of the structures with the folded form of the peptide chain. The presence of a proline residue at position 5 of the amino acid sequence, as well as the effective non-valent interactions of the Tyr4 and Arg6 side chains not only with each other but also with the main chain atoms, contributes to the additional stabilization of such structures. The formation of hydrogen bonds between hydrogen atoms and electronegative oxygen atoms of the main and side chains of such conformations stabilizes the low-energy conformational states of the molecule. Thus, the presence of a proline residue in the T7 peptide structure limits the conformational mobility and flexibility of the polypeptide chain, which facilitates the formation of stable folded structures and ensures high selectivity of interaction with the protein target.

The results of the study can be used for molecular modeling of the process of peptide binding to the transferrin receptor.

COMPARATIVE ANALYSIS OF METHANOL, ETHANOL, AND PROPANOL SOLUTIONS BASED ON STRUCTURAL TEMPERATURE MEASUREMENTS

***Gurbanova F.G., Hasanov A.A.**
Baku State University, Azerbaijan
fidan.qurbanova@outlook.com

The study presents a comparative investigation of methanol (C_1), ethanol (C_2), and 1-propanol (C_3) aqueous solutions using the Structural Temperature Method (STM), which provides insight into the molecular ordering and hydrogen-bond network behavior in mixed liquids. The structural temperature (T_s) reflects the energetic stability and degree of organization within the hydrogen-bonded water structure influenced by solute molecules.

In this research, aqueous solutions of the three alcohols were prepared at different concentrations (0.5–3.0 mol·L^{-1}). The measurements were carried out using a precision thermostat system (±0.01 °C accuracy). The **temperature of maximum density (T_md)** was determined for each concentration, and the corresponding structural temperature was calculated according to the relation:

$$T_S = T_{H_2O} + \Delta T$$

where $T_{H_2O} = 3.98°C$ is the temperature of maximum density of pure water, and ΔT presents the deviation caused by the solute.

The results demonstrate that methanol solutions exhibit a *negative* shift ($\Delta T < 0$), classifying methanol as a structure-breaker due to the dominance of its hydrophilic –OH group, which disrupts water's hydrogen-bonded framework. Ethanol shows an intermediate behavior: at low concentrations, it behaves as a weak structure-maker, but at higher concentrations (above 1 mol·L^{-1}), the growing hydrophobic influence of the ethyl group leads to a decrease in T_s. Conversely, 1-propanol produces a *positive* shift ($\Delta T > 0$), acting as a structure-maker, indicating the formation of a more ordered, low-density water network stabilized by hydrophobic interactions.

A clear correlation was observed between the alkyl chain length (nC) and the structural temperature, expressed by the empirical equation:

$$\Delta T = a\ln(n_C) + b$$

where a and b are constants determined experimentally (a = 1.25, b = –2.10). This relationship confirms that the transition from hydrophilic to hydrophobic dominance is gradual and chain-length dependent.

The comparative analysis reveals that the structural role of monohydric alcohols shifts from destructive (methanol) to constructive (propanol) as the hydrocarbon chain length increases. These findings contribute to a deeper understanding of solute–solvent interactions, hydrophobic hydration, and molecular ordering in binary liquid systems. The method provides a reliable thermodynamic tool for exploring structural changes in aqueous organic solutions relevant to biophysics and molecular chemistry.

MOLECULAR-LEVEL MECHANISMS OF IONIC HYDRATION AND PHASE BEHAVIOR IN PEG–CITRATE SYSTEMS

[1]*Shahbazova G.M., [2]Masimov E.A.

[1]Baku State University, Azerbaijan

[2]Institute of Physics, Ministry of Science and Education, Azerbaijan

shahbazova.gunel@mail.ru

Aqueous biphasic systems (ABS) based on polyethylene glycol (PEG) and sodium citrate have attracted growing attention due to their ability to separate biomolecules and ions efficiently. However, the molecular mechanisms governing ion hydration and phase behavior remain insufficiently understood. This work investigates the influence of ion hydration and polymer–water interactions on the structural and thermodynamic properties of the PEG–$Na_3C_6H_5O_7$–H_2O system.

The binodal curves of the PEG–$Na_3C_6H_5O_7$–H_2O system were deter-mined using the titration method. Densities and viscosities of both phases were measured by vibrating-tube densimetry and the Ostwald viscometer, respectively. The structural temperature (T_{str}) was calculated from viscosity–temperature data according to the Masimov–Zaslavsky hydration model. Hydration numbers were derived to quantify the structuring effect of water around ions and polymer chains.

The results indicate that increasing sodium citrate concentration enhances phase separation by strengthening ion–polymer interactions and decreasing polymer solubility. The obtained structural temperature values differ for upper and lower phases, reflecting distinct molecular organization levels. Correlations between T_{str}, viscosity, and hydration number confirm that ionic hydration plays a dominant role in determining the system's stability.

The study demonstrates that the molecular behavior of PEG–$Na_3C_6H_5O_7$–H_2O biphasic systems is strongly dependent on hydration phenomena and ion–polymer interactions. The concept of structural temperature provides a valuable tool for elucidating molecular mechanisms in aqueous biphasic systems and optimizing their separation performance.

METABOLIC IMPLICATIONS OF RADIOACTIVE IODINE THERAPY IN TOXIC ADENOMA PATIENTS: A COMPREHENSIVE ASSESSMENT OF LEPTIN, LIPID PROFILE, AND INSULIN SENSITIVITY

Mammadova A.E.
Azerbaijan Medical University, Azerbaijan

Background: Toxic adenoma, a benign autonomously functioning thyroid nodule, can lead to persistent hyperthyroidism that disrupts multiple metabolic pathways, including lipid metabolism, adipokine secretion, and glucose-insulin homeostasis. Radioactive iodine (RAI) therapy is a widely accepted definitive treatment for toxic adenoma, effectively restoring euthyroidism. However, the metabolic consequences of transitioning from a hyperthyroid to a euthyroid or hypothyroid state post-RAI – particularly regarding serum leptin levels, lipid profile changes, and insulin sensitivity – remain insufficiently characterized.

The primary aim of this study was to evaluate the metabolic effects of RAI therapy in patients with toxic adenoma by assessing longitudinal changes in leptin concentrations, lipid parameters, body mass index (BMI), and insulin resistance. Understanding these alterations is crucial, as they may contribute to elevated long-term cardiometabolic risk, requiring proactive clinical management in endocrine and nuclear medicine practice.

Methodology: This was a prospective observational study conducted at the Oncology Clinic of Azerbaijan Medical University and National Oncology Hospital between 2023 and 2025. The study enrolled 37 patients (aged 25–65 years) diagnosed with toxic adenoma who were scheduled to undergo radioactive iodine (RAI) therapy. Biochemical measurements were performed both at baseline (before RAI therapy) and 12 months post-treatment. Statistical analysis was conducted using SPSS version 26.0.

Results: At the 12-month follow-up, 76.2% of patients achieved a euthyroid state following radioactive iodine (RAI) therapy. A statistically significant increase in serum leptin levels was observed compared to baseline (median change; $p = 0.041$), despite only a modest and statistically nonsignificant increase in body mass index (BMI).

Analysis of the lipid profile revealed a trend toward increased LDL-C and triglyceride levels, with a concurrent decrease in HDL-C, though these changes did not reach statistical significance in the small sample. Total cholesterol levels increased slightly post-treatment. Regarding insulin sensitivity, there was a mild increase in HOMA-IR values, indicating a tendency toward greater insulin resistance post-treatment, although this change did not achieve statistical

significance ($p > 0.05$).

Correlation analysis revealed a moderate negative correlation between the decline in free thyroxine (FT4) and the rise in leptin levels ($r = -0.42$, $p < 0.05$), as well as a positive correlation between leptin and BMI ($r = 0.45$, $p < 0.01$). These findings suggest that leptin alterations may be partially mediated by thyroid hormone decline and changes in body composition.

Conclusion: This study demonstrates that radioactive iodine (RAI) therapy, while effective in restoring thyroid function in patients with toxic adenoma, is associated with notable metabolic alterations, particularly in leptin regulation and lipid profile dynamics. The significant post-treatment increase in leptin levels and the unfavourable trends in lipid parameters suggest that the transition from a hyperthyroid to a euthyroid or hypothyroid state may elevate cardiometabolic risk, even in the absence of overt weight gain.

INVESTIGATING THE RHEOLOGICAL AND THERMAL PROPERTIES OF DISOL AND TRISOL SOLUTIONS

Bagirova A.A.
State Border Service Military Hospital, Azerbaijan
aynurbagirova84@icloud.com

Disol is an isotonic solution containing 6 g of $NaCl$ and 2 g of CH_3COONa per 1 liter. Trisol, on the other hand, is an isotonic solution composed of 5 g of $NaCl$, 1 g of KCl, and 1 g of $NaHCO_3$ per 1 liter. These solutions exert hemodynamic effects in the body, prevent blood thickening, and improve capillary circulation, thereby facilitating the removal of toxic substances (such as toxins resulting from food poisoning or El-Top cholera). They are also used to prevent dehydration of the body. It should be noted that Disol and Trisol solutions are highly dilute. Therefore, the salts contained in these solutions dissociate almost completely in water, producing free ions. When these solutions enter the bloodstream, chemical processes occurring in the presence of these ions (anions and cations) contribute to the detoxification of blood. Based on the above, it can be concluded that investigating certain physicochemical properties of these solutions may be beneficial in medical practice.

In the present study, the dynamic viscosity (η), density (ρ), and electrical conductivity (σ) of the isotonic solutions disol and trisol were experimentally determined at normal atmospheric pressure within the temperature range of 20 – 50°C. The experimental results show that, with increasing temperature, the

dynamic viscosity and density of both solutions decrease, while their electrical conductivity increases. Based on the temperature dependence of the viscosity and density of the investigated substances, the activation parameters of viscous flow ($\Delta G_\eta^{\neq}$, $\Delta H_\eta^{\neq}$, $\Delta S_\eta^{\neq}$) and the thermal expansion coefficient (α_p) were calculated. Furthermore, using the experimental values of dynamic viscosity and electrical conductivity, the Walden rule ($\eta\sigma = const$) was examined.

It was determined that, for both disol and trisol, the activation parameters of viscous flow ($\Delta G_\eta^{\neq}$, $\Delta H_\eta^{\neq}$, $\Delta S_\eta^{\neq}$) decrease with increasing temperature, and the values of all three parameters are very close to each other within the examined temperature range. It should be noted that the activation Gibbs energy of viscous flow ($\Delta G_\eta^{\neq}$) represents the work performed during the transition of ions to an activated state in the solution. The activation enthalpy of viscous flow ($\Delta H_\eta^{\neq}$) characterizes the solution from an energetic standpoint, whereas the activation entropy of viscous flow ($\Delta S_\eta^{\neq}$) describes the structural changes occurring within the solution. The observed decrease in the activation entropy of viscous flow with rising temperature in isotonic solutions of disol and trisol is likely associated with the disruption of the solution's structure.

Studies show that, for both disol and trisol, the thermal expansion coefficient increases with rising temperature. However, at any given temperature, the thermal expansion coefficient of disol is slightly higher than that of trisol. It was also determined that, for both solutions, the product ησ does not remain constant with temperature, indicating that the Walden rule is not satisfied within the investigated temperature range.

THEORETICAL AND HIGH ENERGY PHYSICS

ION DISTRIBUTION FUNCTION IN ELASTIC COLLISIONS OF PARTICLES IN PLASMA

Huseynov T.Kh.
Baku State University
tarlanhuseynov@bsu.edu.az, tarlanhuseynov57@gmail.com

In numerous studies on low-temperature gas discharges, the collision cross sections of neutral atoms with charged particles specific to the plasma environment have been determined. However, the corresponding modifications in the shape of the ion velocity distribution function (IVDF) have not been systematically investigated. In most prior works, the IVDF in gas-discharge plasmas has been assumed to conform to the Maxwellian form.

Our investigation demonstrates that, during elastic scattering of charge carriers by neutral gas atoms, as well as in resonant charge-exchange processes, the IVDF undergoes significant deviations from the Maxwellian distribution. Specifically, we established that resonant charge transfer constitutes the dominant mechanism in ion–neutral collisions within certain gases. In such interactions, the ion, while conserving its energy and momentum during the collision, transfers its charge to the neutral atom via a tunneling-mediated process.

On the basis of the fundamental mechanisms of ion–neutral interactions, the following conditions for the existence and formulation of the IVDF can be postulated:

– The motion of neutral gas atoms follows a Maxwellian distribution;

– The ions propagate in a medium of low degree of ionization;

– Resonant charge neutralization serves as the principal mechanism governing the shape of the IVDF;

– Plasma parameters exhibit no gradient along the axial (longitudinal) direction.

The latter condition is of particular significance, since the presence of axial gradients would render the IVDF dependent on the longitudinal coordinate. Although the mathematical treatment of such cases is in principle straightforward, it necessitates the imposition of physically consistent boundary conditions along the Z-axis.

The ion velocity distribution function was investigated in relation to charge-carrier scattering by neutral atoms in a gas-discharge plasma and to resonant charge-neutralization phenomena. It was established that the ion velocity

acquired over a mean free path in a given medium exhibits non-Maxwellian characteristics whenever it exceeds the thermal energy scale of the neutral atoms. Under strong electric fields, both the mean and root-mean-square ion velocities are governed by the energy condition at which the most probable ion velocity converges to that of the neutral species. Furthermore, under ambipolar diffusion conditions in gas discharges, as well as during elastic electron–neutral collisions, the experimentally measured ion velocity distribution functions reveal pronounced deviations from Maxwellian statistics, in contrast to the behavior observed in the presence of a purely axial electric field.

PARAMETRIC INSTABILITY OF PLASMA WITH EXCITATION OF LOW-FREQUENCY ION AND HIGH-FREQUENCY ELECTRON OSCILLATIONS

*Mammadov F.E., Akberov E.M., Gurbanov I.I., Aliev A.A., Aliev S.A., Eminov Sh.O., Khalilov A.J.

Institute of Physics, Ministry of Science and Education, Azerbaijan
mammadov.f.e@gmail.com

The interaction of electromagnetic fields with plasma leads to the emergence of parametric instabilities. The study of such processes is important for the development of plasma heating methods, as well as devices in which plasma is used to generate and convert various waves, etc. The effect of a high-frequency (HF) electric field on a magnetized plasma in the pump frequency range $\omega_{pi} \ll \omega_0 \ll \omega_{pe}$ ($\omega_{pi,e}$ – are the ion and electron frequencies, ω_0 - is the frequency of the external field) is accompanied by the excitation of longitudinal hydrodynamic oscillations in the plasma.

Our experiments have shown that applying a high-frequency field to plasma leads to parametric instability of lower-hybrid electron and low-frequency ion oscillations. A low-pressure arc discharge was ignited in a cooled brass chamber between the cathode and anode. The plasma column was maintained in a uniform longitudinal magnetic field with an intensity of up to 200 oE. A high-frequency electric field $\vec{E}$ perpendicular to the magnetic field $\vec{H}$ was created using a plasma capacitor. The capacitor was supplied with high-frequency voltage from an external generator with a tunable frequency [$\omega_0/2\pi \approx (7 \div 40)$ MHz], which made it possible to obtain an alternating voltage Ũ of up to ~300 V on the capacitor. The plasma parameters and high-frequency oscillations were recorded using cylindrical probes.

The imposition of an HF field on the plasma leads to instability of the decay

type with the excitation of a low-frequency branch of plasma oscillations, characteristic of systems with effective Cherenkov damping of electrons. The experiments established the excitation threshold of oscillations based on the magnitude of the pump field strength, which indicates the parametric nature of the instability.

Experiments have shown that applying an HF field to a plasma leads to parametric instability. In the studied pump frequency range $\omega_{pi} \ll \omega_0 \ll \omega_{pe}$, the parametric instability of lower-hybrid electron and low-frequency ion oscillations is considered using a theory of the [2]. In the case of $\gamma \gg \omega_0$, the line width of the high-frequency oscillations is large and the corresponding low-frequency spectrum differs significantly from the ion-sound spectrum. In this case, the spectrum of oscillations in the low-frequency region has a set of satellite frequencies of both lower and higher values than the pumping frequency. In our experiments, the case $\gamma \gg \omega_0$ is realized. In this case, the threshold of parametric instability is expressed by the following formula (γ-decrement of attenuation of ion-acoustic waves)

$$E_{thres}^2/4\pi n_e T_e = 16\omega_0\gamma/\omega_{pe}^2$$

where E_{thres} - threshold value of the excitation intensity of parametric instability.

Thus, in the described experiments, when an HF field is applied to the plasma, a parametric instability of the decay type is realized with the excitation of a low-frequency branch of oscillations and oscillations in the region of the pump frequency.

MACHINE LEARNING FOR PARTICLE SIGNAL SELECTION

Khalilova Sh.G.
Baku State University, Azerbaijan
shahlaganbarova@gmail.com

High-energy physics experiments such as ATLAS and CMS at the Large Hadron Collider analyze vast amounts of data obtained from proton collisions at energies of 13 TeV. Identifying rare signals – events associated with new physical processes or particles – requires effective background filtering. Traditional threshold-based selection methods are insufficiently sensitive. This paper explores the use of machine learning (ML) algorithms to improve event selection and signal identification accuracy.

The purpose of this paper is to evaluate the effectiveness of various machine learning algorithms in analyzing detector data and identifying signals

from rare processes.

1. Studying the distribution characteristics of signal and background event features.

2. Implementing and training classification models (Random Forest, XGBoost, neural networks).

3. Comparing classification quality using precision, recall, and AUC metrics.

4. Optimization of model hyperparameters and feature importance analysis.

5. Evaluation of the applicability of the developed methods to real LHC experiment data.

This study utilized data from simulated proton-proton collisions with specified event characteristics. The analysis was performed using the Python libraries scikit-learn, TensorFlow, and XGBoost. ROC curves and the F1-score metric were used to evaluate classification performance.

A comparison of various models showed that machine learning methods outperform traditional signal selection algorithms. The best results were demonstrated by the gradient boosting algorithm (XGBoost), which provided a 20% increase in classification accuracy with the same level of background suppression. Neural networks demonstrated high adaptability to increasing input data dimensionality, which is especially important when analyzing multidimensional features from detectors.

The use of machine learning methods significantly improves the efficiency of data analysis in high-energy physics experiments. Machine learning algorithms improve event selection, reduce the impact of statistical noise, and speed up data processing. Future work plans to use deep neural networks and convolutional architectures to analyze spatial energy distributions in calorimeters.

PHYSICS-INFORMED NEURAL NETWORK MODELLING OF THE SCHRÖDINGER EQUATION FOR THE COULOMB POTENTIAL AND QUANTUM HARMONIC OSCILLATOR

***Alizada M.R., Nuriyev R.A., Alazova S.D., Muradova S.T.**

Baku State University, Azerbaijan

mohsunalizade@gmail.com, mohsun.alizada@bsu.edu.az

This paper investigates the generality of physics-informed neural networks (PINNs) for solving the stationary Schrödinger equation. Unlike traditional grid methods, PINN approximates the wave function $\psi(x)$using a neural

network $\psi_{NN}(x;\theta)$ whose parameters $\theta$are optimized to minimize a composite loss function. This function includes the residual of the differential equation itself, calculated on a set of collocation points, as well as terms responsible for satisfying physical constraints – boundary conditions and wave function normalization. This approach allows one to find the eigenvalues and eigenfunctions of a system without the need for spatial discretization.

The effectiveness of the method was demonstrated in its application for the determination of the energy spectrum of the hydrogen atom and the quantum harmonic oscillator (QHO). For both systems, the discrete energy levels obtained using PINN demonstrate excellent agreement with their known theoretical relationships. As shown in Figure 1, the calculated values exactly fit a hyperbolic curve $E_n \propto -1/n^2$for the hydrogen atom and a linear relationship $E_n \propto (n + 0.5)$ for the QHO.

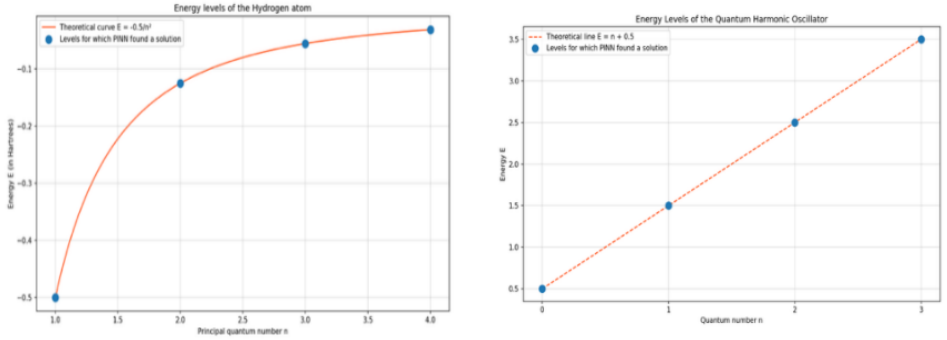

a **b**

Comparison of energy levels obtained by PINN (dots) with theoretical curves (line) for a hydrogen atom (a) and a quantum harmonic oscillator (b).

Furthermore, the wave functions found by the neural network are virtually indistinguishable from their analytical counterparts. The model correctly reproduces the shape, symmetry, and required number of nodes for each quantum state, successfully handling both the singular Coulomb potential of the hydrogen atom and the parabolic oscillator potential.

The study confirms that PINN is a powerful, accurate, and flexible tool for solving eigenvalue problems in quantum mechanics. The method's ability to produce correct results for systems with fundamentally different potentials opens up prospects for its application to more complex problems where analytical solutions are unknown.

PHYSICS-INFORMED NEURAL NETWORK MODELLING OF NONLINEAR QUANTUM SIZE EFFECTS IN SEMICONDUCTOR NANOWIRES

[1*]Alizada M.R., [2]Tanriverdili K.V., [3]Ibragimov G.B.

[1]Baku State University, Azerbaijan

[2]Azerbaijan Technical University, Azerbaijan

[3]Institute of Physics, Ministry of Science and Education, Azerbaijan

mohsun.alizada@bsu.edu.az, mohsunalizade@gmail.com

Physics-Informed Neural Networks (PINNs) are used to model nonlinear quantum size effects in semiconductor nanowires by solving the stationary Schrödinger equation with a nonlinear potential:

$$V(R) = V_0 + \frac{\alpha}{R^n} + \beta\left(1 - e^{-(R/R_c)^2}\right) + \frac{\gamma}{R} e^{-(R/R_s)^2},$$

where α, β, γ, n are material-dependent parameters, and R_c, R_s characterize deformation and surface interaction scales. PINNs minimize the residual

$$\mathcal{N}[\psi] = -\frac{\hbar^2}{2m^*}\frac{1}{r}\frac{d}{dr}\left(r\frac{d\psi}{dr}\right) + V(R)\psi - E(R)\psi = 0,$$

subject to boundary and normalization constraints. A 4–6 layer network jointly learns $\psi(r;R)$ and $E(R)$ using Adam and L-BFGS optimizers ($\eta = 10^{-3}$), enabling direct eigenvalue computation without discretization.

The method accurately reproduces size-dependent energy levels in nanowires. For large radii, PINN results converge to analytical confinement models, while at small radii, deformation and surface terms cause a nonmonotonic $E(R)$ dependence absent in traditional models. Fig. 1 shows close agreement with analytical results at large R and notable nonlinear deviations below $R < 3$ nm due to strain and boundary effects.

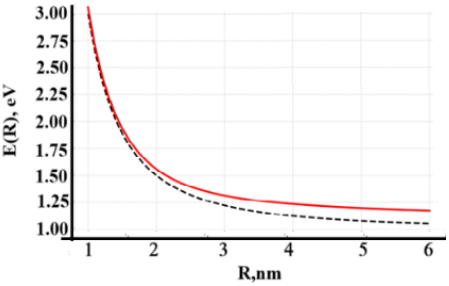

Fig. 1.

The study confirms that PINNs provide a robust and physically consistent tool for modeling nonlinear quantum size effects in semiconductor nanowires. The method accurately captures confinement, deformation, and surface phenomena beyond analytical limits and can be extended to temperature-dependent and time-evolving nanostructures.

SOME SOLUTIONS OF THE MHD EQUATIONS FOR A SINGLE-LIQUID COLLISIONLESS PLASMA OF ANISOTROPIC SOLAR WIND FOR SMALL DISTANCES FROM THE SUN AND THE PROBLEM OF PLASMA MASS ACCELERATION

Bashirov M.M., *Ahmedova K.N.
Baku State University, Azerbaijan
mbashirov@bsu.edu.az

This study presents solutions to the Magnetohydrodynamic (MHD) equations for an anisotropic, collisionless solar wind plasma, focusing on small distances from the Sun. By evaluating constants, mathematical expressions for solar wind velocity as a function of radial distance were derived and analyzed. Results indicate that plasma ejected from the Sun's surface initially achieves a maximum speed ratio of $v/v_0 = 30$, followed by deceleration up to a distance of $x = 3.3 - 3.7R$. Beyond this, the plasma accelerates, reaching $v/v_0 = 10$, and moves away from the Sun with increasing momentum. Magnetic repulsion, verified by Parker Solar Probe data, is not uniformly stronger than gravity for all ejected plasma masses, varying with plasma properties, active regions, and ejection dynamics. A change in the magnetic field direction within the separated plasma contributes to its acceleration. These particular solutions within MHD theory, incorporating heat flux and thermal pressure anisotropies and acknowledging singularities, characterize the complex dependence of solar wind speed on radial distance and thermal velocities, aiding in constructing global numerical solutions and understanding plasma acceleration. The core equations utilized include: $r^2B = C_1$, $r^2\rho V = C_2$. The energy equation is:

$$\frac{V^2}{2} + \frac{1}{\rho}\left(P_\perp + \frac{3}{2}P_\parallel\right) + \frac{1}{\rho V}\left(S_\perp + \frac{1}{2}S_\parallel\right) - \frac{GM}{r} = \frac{C_5}{C_2}$$

And the dimensionless differential equations are:

$$\left(\frac{Y}{X} - 1\right)\frac{dX(x)}{dx} - 2\frac{dY(x)}{dx} + \frac{4}{x^3}Z(x) - \frac{2\overline{g}}{x^2} = 0$$

$$\left(\overline{C}_6 - Z(x)\right)\frac{dX(x)}{dx} + \left(Y(x) - X(x)\right)\frac{dZ(x)}{dx} - \frac{2}{x^3}Z^2(x) = 0$$

$$\left(\frac{Y(x)}{X(x)} - 1\right)\frac{dY(x)}{dx} + \frac{4}{3}\left(\overline{C}_5 + \frac{\overline{g}}{x} - \frac{\overline{C}_6}{x^2} - \frac{3}{4}X(x) - \frac{3}{2}Y(x)\right) \times$$

$$\times \frac{1}{X(x)}\frac{dX(x)}{dx} + \frac{2}{3x^2}\left(\frac{2\overline{C}_6}{x} - \overline{g}\right) = 0$$

Here, $x = r/R$, $X = V^2/v_0^2$, $Y = u_\parallel^2/v_0^2$, $Z = x^2u_\perp^2/v_0^2$, with $\overline{C}_5$, $\overline{C}_6$, and $\overline{g}$ representing dimensionless constants related to physical parameters.

For specific constants ($C_5 = 245$, $C_6 = 3246$), solutions for $X(x)$ were obtained, with $B(C,x)$ and $N(C,x)$ as intermediate terms. The primary real solutions for $X(x)$ are:

$$X1(x) = \frac{1}{18x^2}N(C,x) + \\ + \frac{8}{9}\frac{(245x^2 + x - 3246)^2}{N(C,x)} + \frac{2}{9}\frac{245x^2 + x - 3246}{x^2},$$

$$X2(x) = -\frac{1}{36x^2}N(C,x) \\ - \frac{4}{9}\frac{(245x^2 + x - 3246)^2}{N(C,x)} + \frac{2}{9}\frac{245x^2 + x - 3246}{x^2},$$

where C is an integral constant determined by initial conditions, for example, $C \approx 10^7$ when $X(x = 1) = 1$.

MODELING PROMPT PHOTON PRODUCTION IN PROTON-PROTON COLLISIONS AT NICA SPD ENERGIES USING PYTHIA 8.3

Alizada M.R.

Baku State University, Azerbaijan

mohsun.alizada@bsu.edu.az, mohsunalizade@gmail.com

Prompt photon production in pp collisions at 10 GeV NICA energies was simulated in PYTHIA 8.3. In the simulation, we use 500,000 prompt photon production events and use the parton distribution function.

According to PYTHIA 8.3 simulations at NICA energies, the Compton scattering process ($qg \to q\gamma$) is the dominant mechanism for prompt photon production, contributing 51.27% to the total cross-section, while quark-antiquark annihilation accounts for 47.72%. This highlights the importance of the proton's gluon content. A comparison with theoretical FeynCalc calculations shows similar qualitative behavior for differential cross-sections against transverse momentum (p_T) and scattering angle (Cosθ), but quantitative differences exist.

Figure 1 compares the total cross-section for prompt photon production versus center-of-mass energy ($\sqrt{s}$), as calculated by PYTHIA 8.3 and FeynCalc.

It clearly illustrates the key discrepancy between the models at lower energies, suggesting potential limitations of the PYTHIA 8.3 model for the NICA experiment.

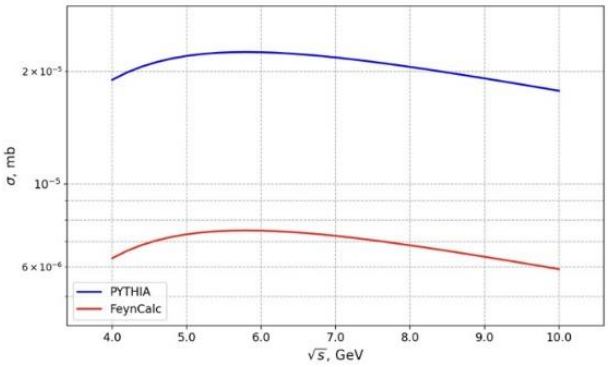

Fig. 1.

Simulations confirm that Compton scattering dominates prompt photon production at NICA energies, but reveal discrepancies with FeynCalc's theoretical calculations at low energies. These findings underscore the critical need for experimental data from NICA's SPD to constrain and refine the models.

PHYSICS-INFORMED NEURAL NETWORK APPROACH TO SOLVING THE SCHRÖDINGER EQUATION FOR THE VAN DER WAALS POTENTIAL IN A HARMONIC TRAP

*Alizada M.R., Rajabov M.R., Alazova S.D., Muradova S.T.
Baku State University, Azerbaijan
mohsun.alizada@bsu.edu.az, mohsunalizade@gmail.com

Solving the Schrödinger equation for realistic potentials, such as the van der Waals (vdW) interaction, requires robust numerical methods. This work utilizes Physics-Informed Neural Networks (PINNs), a modern mesh-free approach, to find the ground state of a particle in a combined vdW and harmonic trap potential $V(r) = -C_6/r^6 + (1/2)m\omega^2 r^2$. The neural network, representing the wavefunction $\psi(r)$, is trained by minimizing the energy expectation value $\langle \hat{H} \rangle = \langle \psi \mid \hat{H} \mid \psi \rangle$ according to the variational principle. To overcome convergence issues arising from the dual-well nature of the potential, a curriculum learning strategy was employed, ensuring convergence to the physically correct ground state.

A parametric study was conducted by varying the trap frequency ω. The

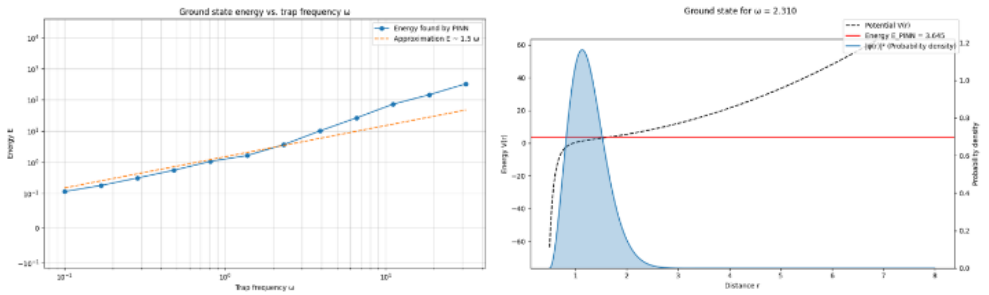

a) **b)**

Fig. 1

results (Fig. 1(a)) show a physically correct monotonic increase in the ground state energy E. The calculated energies accurately match the theoretical harmonic oscillator asymptote ($E \sim 1.5\omega$) in the strong confinement limit. The corresponding wavefunction for an intermediate ω (Fig. 1(b)) is shown to be correctly localized in the potential well.

This study demonstrates that PINNs, when combined with advanced training strategies, are an accurate and robust method for solving complex quantum eigenvalue problems. The excellent agreement with theoretical limits validates the approach and highlights its potential for systems where analytical solutions are unavailable.

PHYSICS AT FUTURE CIRCULAR ELECTRON-POSITRON COLLIDER

[1]*Dadashova A., [2]Huseynov N.

[1]CEPC, China

[2]CERN, Switzerland

dadashovaa0225@gmail.com

The discovery of the Higgs boson at the LHC marked the beginning of a new era in high-energy physics. The natural next step after the LHC and High-Luminosity LHC (HL-LHC) is to conduct precision measurements of the Higgs boson's properties and to explore physics beyond the Standard Model (BSM). Electron-positron colliders are particularly well-suited for this task, and several projects – such as the ILC, CLIC, and FCC-ee – have been proposed over the last two decades. In 2012, China proposed the Circular Electron-Positron Collider (CEPC), a 100 km circumference facility. Designed as an e+e- Higgs factory, the CEPC will enable unprecedented precision in Higgs measurements, verify predictions of electroweak theory, and advance flavor physics, QCD, and BSM searches. Following an upgrade to increase its beam energy, the CEPC will also

be capable of top-quark pair production and could later be converted into a proton-proton collider. The project is currently finalizing its technical design for the accelerator and is nearing completion of the baseline detector configuration. A proposal is expected to be submitted to the Chinese government for approval in the fall of 2025, with a decision anticipated in early 2026.

SEMILEPTONIC $\Xi_c \to \Xi$ DECAYS: AN LCSR VIEW ON THE EXPERIMENT-LATTICE TENSION

Tahmasib M.A.
Middle East Technical University, Ankara, Turkey
taliev@metu.edu.tr

The semileptonic decay $\Xi_c \to \Xi l\nu$ are studied within light-cone sum rules framework. Firstly, the weak transition form factors are calculated by using the Ξ_c baryon distribution amplitudes. Using these results for the form factors, the branching ratios of the corresponding channels are estimated. The obtained results on branching ratios are good agreement with lattice calculations, while being larger than the current experimental measurements.

THE EIGENVECTORS OF THE 5D DISCRETE FOURIER TRANSFORM IN NEWTONIAN BASIS REVISITED

Atakishiyev N.M.
Baku State University, Azerbaijan
natigata@bsu.edu.az

The eigenvalues λ_n and eigenvectors f_n of the 5D discrete number operator $N_5 = A_5^T A_5$ are evaluated systematically. Because the eigenvalues λ_n are represented by distinct non-negative numbers, the number operator N_5 has been used to classify eigenvectors of the 5D discrete Fourier transform Φ_5, thus resolving the ambiguity caused by the well-known degeneracy of the eigenvalues of the discrete Fourier transform Φ_N. A procedure for sparsification of the intertwining operators A_5 and A_5^T has been formulated, which made it possible to construct the discrete analog of the well-known continuous-case formula $\psi_n(x) = \frac{1}{\sqrt{n!}}(a^\dagger)^n\,\psi_0(x)$. In addition, a discrete analog of the eigenvectors f_n of the continuous case formula $\psi_n(x) = c_n^{-1}\,H_n(x)\,\psi_0(x)$, $c_n = \sqrt{2^n n!}$, has been

established in terms of the Newtonian basis polynomials $\mathcal{P}_n(X_5), n \in Z_5$, times the lowest eigenvector f_0. The methodology developed not only deepens the understanding of the discrete Fourier transform but also paves the way for advanced numerical methods in spectral analysis.

THE CP STRUCTURE OF THE TOP QUARK-HIGGS YUKAWA COUPLING IS PROBED THROUGH AN ANALYSIS OF ttH/tH EVENTS

*Huseynov N.A., Tropina A.D.
CERN, Switzerland
nazim.huseynov@cern.ch

Investigation of the interaction between the Higgs boson and the top quark is of high priority interest. The large mass of the top quark of approximately 173.3 GeV requires that it couples strongly to the Higgs boson in the SM. Consequently the top quark is suspected to play a special role in the electroweak symmetry breaking. The Yukawa coupling of the top quark can be measured directly through the inclusive cross-section of the associated production of the Higgs boson with a top-quark pair (ttH). The measurement of the Higgs boson production cross-section in association with a single top quark (tH) and the kinematic properties of tH and ttH events can also provide information about the CP nature of the coupling. In the SM the Higgs boson is a scalar and its interactions are CP-even. The pure pseudoscalar hypothesis with CP-odd interactions with weak vector bosons and fermions has been excluded. However, it remains experimentally allowed that the Higgs boson is a CP-mixed state, which arises in extended Higgs sectors, and would provide a new source of CP-violation beyond the SM.

A NEW POTENTIAL AND A MODEL OF THE LINEAR HARMONIC OSCILLATOR WITH THE POSITION-DEPENDENT MASS

Nagiyev Sh.M.
Institute of Physics, Ministry of Science and Education, Azerbaijan
shakir.m.nagiyev@gmail.com

Potential models play a key role in the theoretical description of the physical and chemical properties of composite microsystems such as molecules and atoms, atomic nuclei and hadrons, and the motion of microparticles in external potential fields within the framework of nonrelativistic or relativistic quantum

mechanics. The study of potential models is reduced to finding solutions to the quantum wave equations of Schrödinger, Klein-Gordon, or Dirac for a specific type of interaction potential. There are various exact or phenomenological potential functions. These include, in addition to the Coulomb and oscillatory potentials, for example, the Kratzer, Morse, Eckart, Manning-Rosen, Pöschl-Teller, Hulthen, Woods-Saxon, Hartmann, Hautot, Quesne potentials (see). In this paper, a new exactly solvable potential in the form of a semi-infinite well

$$V(x) = \frac{M(x)\omega_0^2}{2}\left(\frac{e^{\alpha x}-1}{\alpha}\right)^2 = \frac{2m_0\omega_0^2}{\alpha^2}\sinh^2\frac{\alpha x}{2}, \quad -\infty < x < \infty$$

is proposed for a linear harmonic oscillator, where the parameter $\alpha > 0$ is related to the range (to the radius) of the potential. This potential can be called a modified oscillator potential, since it contains anharmonic terms. In the limit $\alpha \to 0$, the anharmonic terms disappear. Using the new potential, two oscillator models with a constant mass $M(x) = m_0 = \text{const}$ and with a position-dependent mass $M(x) = m_0\exp(-\alpha x)$ were constructed within the Schrödinger equation. The energy spectrum and wave functions for the constructed models were found. Their wave functions are expressed in terms of Bessel polynomials and Laguerre polynomials, respectively

$$\psi_n^{(0)}(x) = C_n^{(0)} e^{(\frac{\lambda_0^2}{\alpha^2}-\frac{1}{2})\alpha x} e^{-\frac{\lambda_0^2}{\alpha^2}\exp(\alpha x)}\, y_n\left(\frac{\alpha^2}{\lambda_0^2}e^{-\alpha x}; -\frac{2\lambda_0^2}{\alpha^2}\right), \quad \lambda_0 = \sqrt{\frac{m_0\omega_0}{\hbar}}, \quad (1)$$

$$\psi_n(x) = C_n e^{-(\sqrt{\lambda_0^4/\alpha^4+1/4}+\frac{1}{2})\alpha x} \exp\left[-\frac{\lambda_0^2}{\alpha^2}\exp(-\alpha x)\right] \times$$

$$L_n^{\sqrt{4\lambda_0^4/\alpha^4+1}}\left(2\frac{\lambda_0^2}{\alpha^2}e^{-\alpha x}\right). \quad (2)$$

The corresponding energy spectra are determined by the formulas:

$$E_n^{(0)} = \hbar\omega_0\left(n+\frac{1}{2}\right) - \frac{\hbar^2\alpha^2}{2m_0}\left(n+\frac{1}{2}\right)^2, n = 0, 1, 2, \dots, N$$

$$N = [\lambda_0^2/\alpha^2 - 1/2], \quad (3)$$

$$E_n = \hbar\omega_0\left[n + 1/2 + \sqrt{1/4 + \lambda_0^4/\alpha^4} - \lambda_0^2/\alpha^2\right], n = 0, 1, 2, 3, \dots \quad (4)$$

Thus, for the first oscillator model, the number of levels is finite. In (3) angular brakets represent the integer part of the number. Consequently, for at least one bound state to exist, the parameter α must satisfy the inequality $\alpha <$

$\lambda_0\sqrt{2/3}$. The energy spectrum and wave functions have the correct limit as $\alpha \to 0$. As a result, we obtain the following limit relations for the Bessel and Laguerre polynomials

$$\lim_{\nu\to\infty} 2^n \nu^{\frac{n}{2}} y_n\left(e^{-x/\sqrt{\nu}}/\nu\,; -2\nu + 2\sqrt{\nu}x_0\right) = H_n(x + x_0). \tag{5}$$

$$\lim_{\nu\to\infty} n!\,\nu^{-\frac{n}{2}} L_n^{2\nu+2\sqrt{\nu}x_0}\left(2\nu e^{-x/\sqrt{\nu}}\right) = H_n(x + x_0). \tag{6}$$

We believe that the three-dimensional version of the new potential $V_0(r) = \frac{m_0\omega_0^2}{2}\left(\frac{e^{\alpha r}-1}{\alpha}\right)^2$, $0 < r < \infty$ will allow us to construct a more realistic model for those systems whose properties are described using the harmonic oscillator potential.

DIPOLE AND QUADRUPOLE RADIATION OF THE SEMICONFINED QUANTUM WELL MODEL OF THE OSCILLATOR-SHAPED PROFILE

Jafarova A.M.

Institute of Physics, Ministry of Science and Education, Azerbaijan
a.jafarova@physics.science.az

We thoroughly discuss the possible change of the dipole and quadrupole radiation of the quantum well problem under the semi-infinite confinement effect. The stationary Schrödinger equation describing the model is exactly solvable in the position representation, and its wave function of the stationary states is expressed through the Laguerre polynomials. But the surprising behavior of the model is related to its energy spectrum, which completely overlaps with the non-relativistic harmonic oscillator linear energy spectrum. The second important property of the semiconfinement model is its exact solvability even under the suddenly attached homogeneous external field. Therefore, we found that both dipole and quadrupole radiation for this model can still be computed exactly, although the model generalizes the known harmonic oscillator potential in its profile, also additionally exhibits a semiconfinement effect.

We found analytical expressions of the dipole and quadrupole moments matrix elements, which depend on the confinement parameter. We show the impact of this parameter on the behavior of the computed matrix elements and radiation level. Additionally, we compute limit relations, which completely recover the non-relativistic harmonic oscillator when the confinement parameter tends to infinity.

This study, gathering together semiconfinement, spatially varying effective mass, and external field as an efficient mechanism, can play an important role in the detailed study of the optical characteristics of low-dimensional semiconductors. The obtained findings provide valuable guidelines for the optimization of quantum-well-based optoelectronic devices, including modulators, infrared detectors, and terahertz emitters.

p–p SCATTERING IN THE REGGE–EIKONAL MODEL

***Abdulvahabova S.G., Bayramova T.**
Baku State University, Azerbaijan
sacidaabdulvahabova@bsu.edu.az

In this work, a theoretical study of proton–proton (p–p) collisions at high energies is carried out within the framework of the Regge pole approach. The corresponding hadronic potential has a Gaussian shape with a cutoff at large distances.

The application of two-particle unitarity conditions and analytic continuity in the high-energy region allows an effective treatment of the scattering amplitude structure in the impact parameter plane. The scattering amplitude obtained by the eikonalization method satisfies the unitarity condition and the Froissart–Martin bound. In the eikonal approximation, we assume that the hadron wave function diagonalizes the interaction matrix.

The study shows that the amplitude must have poles whose positions depend on the variable t. The Regge trajectory exhibits threshold singularities. Regardless of the specific form of the trajectory or the scattering amplitude, a threshold singularity in t leads to an exponential asymptotic decrease of the impact parameter amplitude, and the p–p diffraction cone changes its slope. The slope of the differential cross sections at small t shows a slight peculiarity but retains the same properties throughout the investigated energy range. In the Oriar region, with increasing energy, the increase in the slope in the diffraction peak shows that it becomes easier for particles to scatter with low transverse momenta. Such behavior of the slope enables further study of fine features of various cross sections. A large diffraction cone slope may be associated with a large radius of hadronic interaction and provides important information about the behavior of the hadronic interaction potential at large distances.

In the future, by including the dual amplitude, it may be possible to extend the asymptotic Regge pole model to the low-energy region.

STUDY OF THE HIGGS BOSON IN THE $H \to b\bar{b}$ DECAY CHANNEL USING VARIOUS MACHINE LEARNING ALGORITHMS

Ahmadov F.N.

Institute of Physics, Ministry of Science and Education, Azerbaijan
fahmadov@jinr.ru

The Higgs boson, with a mass of 125 GeV, measured in the ATLAS and CMS experiments, decays into a pair of bottom quarks with a probability of about 58%. Therefore, this decay channel is of great importance for studying the properties of the Higgs boson and setting constraints on new physics. However, it is very difficult to separate two b-jet signal events from the large QCD background. Therefore, instead of gluon-gluon fusion, which has an order of magnitude larger cross section, the associated production of a Higgs boson with a vector boson (VH where V = W or Z) is used to study the $H \to b\bar{b}$ decay process. Although the associated production of VH and the decay of $H \to b\bar{b}$ have been observed in experiments, the measurement uncertainty is large, especially in the high transverse momenta region. To achieve accurate measurements, in addition to increasing the number of events, it is also necessary to improve the algorithms.

In recent years, LHC experiments have been actively using machine learning algorithms in data analysis. Common algorithms used in LHC experiments are Boosted Decision Tree (BDT), Neural Networks and Transformer. In this work, the performance of the mentioned algorithms in VH(bb) analysis was evaluated and compared. Monte Carlo events, generated by the Powheg and Sherpa generators were used for training. The same variables were used as input variables for all algorithms. Up to one million signals and the same number of background events were used for training. For BDT, the hyper-parameter setting that had already been optimized in the ATLAS VH(bb) analysis was used. Therefore, to confirm the best performance of the selected setting in BDT, only the nearest neighbouring hyper-parameter values were tested. The hyper-parameters of Artificial Neural Networks (ANN) and Deep Neural Networks (DNN) models were optimized. Hyper-parameter optimization of the Transformer model has not yet been performed because it performs well with a large number of low-level variables. After training on Monte Carlo events using these four models, it was found that for the VH(bb) process, the ANN demonstrated the highest performance. But given the Transformer's great potential, after optimizing its hyper-parameters and using new variables, the situation will change in its favour.

THE $T_{cc}^{+}(3875)$ RESONANCE IN HOT MEDIUM

***Damen S., Süngü J.Y., Veliev E.V.**
Department of Physics, Kocaeli University, Izmit, Türkiye
ahmaddamen1967@gmail.com

We investigate the spectroscopic properties of the exotic doubly charmed state $T_{cc}^{+}(3875)$ within the framework of Thermal QCD Sum rules. The T_{cc}^{+} resonance, discovered by the LHCb Collaboration in 2021, with quantum numbers $J^P = 1^+$, is analyzed as a hadronic molecule composed of D^0 and D^{*+} mesons. Employing a molecular interpolating current, we evaluate the two-point correlation function by incorporating non-perturbative condensate contributions up to dimension six. The thermal behavior of both the mass and meson decay constant is extracted from the resulting sum rules as functions of temperature.

Our numerical analysis reveals remarkable stability of these quantities under temperature variations up to $T \simeq 120$ MeV. Beyond this point, both the mass and decay constant decrease significantly with increasing temperature. At the deconfinement temperature ($T \simeq 155$ MeV), the mass is reduced to approximately 35% of its vacuum value, while the decay constant drops to about 65% of its vacuum value. At zero temperature, we obtain $m_{T_{cc}^{+}} = (3863 \pm 15)$ MeV and $f_{T_{cc}^{+}} = (3.42 \pm 0.047) \times 10^{-3}\text{GeV}^4$, in excellent agreement with experimental measurements and other theoretical predictions. The decay width of the T_{cc}^{+} resonance is calculated using finite-width formalism, yielding results consistent with LHCb data.

The investigation of thermal effects on the T_{cc}^{+} provides valuable insights into QCD phase transitions, chiral symmetry restoration, and the properties of hot and dense strongly interacting matter. These findings serve as useful input for future experimental searches in heavy-ion collision experiments at RHIC, LHC, and future facilities such as FAIR and NICA.

THE ROLE OF THE COULOMB EFFECT IN PROTON POLARIZATION

Ahmedov R.
Azerbaijan State University of Oil and Industry, Azerbaijan
ahmedov.rasim@asoiu.edu.az

This paper investigates polarization effects associated with proton scattering on nuclei, taking into account the Coulomb interaction. Taking into account the Coulomb interaction is used not only to determine the influence of the Coulomb interaction on the value of polarization, but also to understand the role of

interactions involved in the dynamics of collisions.

The incident proton wave function is assumed to consist of fully symmetric S-states, so that the corresponding interaction is diagonal in the proton spin states.

The study shows that in the absence of pre-asymptotic corrections, we obtain zero polarizations. Depending on the spin transfer interference from positive and negative scattering angles, the polarization has different signs. Due to the phase shift between the Coulomb and nuclear interactions, a spin distribution occurs, which affects the spin-dependent amplitudes.

The parameters of the spin flip amplitude allow us to obtain a wide range of results for the polarization effects of elastic p-N scattering at high energies.

AN ESTIMATION OF ELLIPTIC FLOW AT THE RHIC AND LHC ENERGIES

***Tabassam U., Zainab R., Abbas Safdar**
COMSATS University Islamabad Campus, Pakistan
uzma.tabassam@comsats.edu.pk

The Relativistic Heavy Ion Collider (RHIC) and the Large Hadron Collider (LHC) allow scientists to study different collision systems such as p–p, p–Pb, Au–Au, and Pb–Pb. These collisions help us explore the fundamental nature of matter under extreme conditions. One of the main goals of heavy-ion collisions is to investigate the quark–gluon plasma (QGP), a special state of matter believed to exist at very high energy densities, where quarks and gluons are no longer confined inside hadrons.

A key signal of QGP formation is the elliptic flow (v_2), which reflects the collective motion of the produced particles. In this work, the elliptic flow is studied using the EPOS4 Monte Carlo event generator. EPOS4 is the latest version of the model and includes improved features, such as a more realistic initial-state description and full hydrodynamic evolution.

We simulated v_2 for Au–Au, Xe–Xe, and Pb–Pb collisions at both RHIC and LHC energies and compared the results with experimental data. The dependence of v_2 on centrality and transverse momentum (pT) in EPOS4 supports the presence of strong collective flow effects in heavy-ion collisions. However, the model tends to slightly underestimate the experimental results, possibly due to limitations in its hydrodynamic treatment or the modeling of final-state effects.

THE PRODUCTION OF HIGGS BOSONS Ahh IN POLARIZED e^-e^+-COLLISIONS

Abdullayev S.K., *Gojayev M.Sh., Alizada M.R.
Baku State University, Azerbaijan,
macidqocayev@bsu.edu.az

In this work, the process of the production of three Higgs bosons Ahh in arbitrarily polarized electron-positron collisions is investigated: $e^-e^+ \to Ahh$. Within the framework of the Minimal Supersymmetric Standard Model, a general expression for the differential effective cross-section is obtained.

If the e^-e^+-pair is longitudinally polarized, it follows that the positron and the electron must have opposite helicities during annihilation: $\lambda_2 = -\lambda_1 = \pm 1$. As a result of this process $e^-e^+ \to Ahh$ has a left-right spin asymmetry:

$$A_{LR} = \frac{1 - 4x_W}{1 - 4x_W + 8x_W^2}, \qquad (1)$$

where $x_W = \sin^2 \theta_W$ – is the parameter Weinberg.

It follows from formula (1) that the left-right spin asymmetry A_{LR} depends only on the Weinberg parameter x_W. When this parameter is set to x_W=0.2315, the asymmetry is A_{LR} =0.14.

With a transverse polarized e^-e^+-pair, the process $e^-e^+ \to Ahh$ has transverse spin asymmetry A_φ. This asymmetry depends on energy x_A, x_1, x_2 and the angles of flight of Higgs bosons θ_A, θ_1 and θ_2.

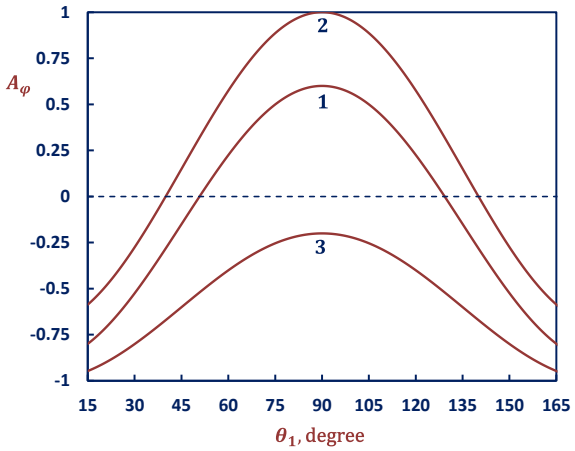

Fig. 1. Dependence of asymmetry A_φ on the angle θ_1 at different φ:
1) $\varphi = \pi/4$,
2) $\varphi = \pi/2$,
3) $\varphi = \pi$ (curves 1, 2, 3 respectively).

Calculations show that the transverse spin asymmetry A_φ at the beginning of the angular spectrum θ_1 is negative, with the growth of the angle θ_1, it increases and reaches its maximum value at θ_1=90° and further growth of the

angle θ_1 leads to a decrease in the asymmetry. The transverse spin asymmetry is sensitive to the azimuthal angle of departure of Higgs bosons φ.

The experimental study of the process $e^-e^+ \to Ahh$ with transversely polarized e^-e^+-pair is of special interest. This allows you to get valuable information and three-boson interaction constants λ_{hhh}, λ_{Hhh} and λ_{hAA}.

PRODUCTION OF HIGGS BOSONS AhH IN POLARIZED e^-e^+-ANNIHILATION

Abdullayev S.K., *Gojayev M.Sh., Alizada M.R.
Baku State University, Azerbaijan
macidqocayev@bsu.edu.az

Within the framework of the Minimal Supersymmetric Standard Model, the process of production of three Higgs bosons AhH in arbitrarily polarized electron-positron annihilation was studied: $e^-e^+ \to AhH$. In the case of a longitudinally polarized electron-positron pair, the differential effective cross section of the process is determined by the following expression:

$$d\sigma(\lambda_1, \lambda_2) \sim [g_L^2(1-\lambda_1)(1+\lambda_2) + g_R^2(1+\lambda_1)(1-\lambda_2)] \cdot F_1, \qquad (1)$$

where λ_1 and λ_2 are the helicities of the electron and positron, g_L and g_R are the left and right coupling constants of the electron with the vector Z-boson.

From formula (1), it follows that during annihilation, the electron and positron must have opposite helicities: $\lambda_2 = -\lambda_1 = \pm 1$. If the electron has left-handed helicity ($\lambda_1 = -1$), then the positron, accordingly, must have right-handed helicity ($\lambda_2 = +1$); combinations $e_L^- e_R^+$ or, conversely, $e_R^- e_L^+$ are possible. Consequently, the process $e^-e^+ \to AhH$ is characterized by left-right spin asymmetry:

$$A_{LR} = (g_L^2 - g_R^2)/(g_L^2 + g_R^2) = (1 - 4x_W)/(1 - 4x_W + 8x_W^2), \qquad (2)$$

where $x_W = \sin^2 \theta_W$ is the Weinberg parameter. It is clear that the left-right spin asymmetry A_{LR} depends only on the Weinberg parameter x_W and, with the experimental value of this parameter x_W=0.2315, it is equal to A_{LR}=0.14.

If the electron-positron is transversely polarized, then in we determine the expression for the transverse spin asymmetry:

$$A_\varphi = \frac{2 g_L g_R}{g_L^2 + g_R^2} \cdot \frac{F_2}{F_1}, \qquad (3)$$

where F_1 and F_2 are functions on the variables x_A, x_1, x_2, θ_A, θ_1, θ_2.

Figure 1 shows the dependence of the transverse spin asymmetry A_φ on the Higgs boson emission angle θ_1 for x_A =0.6, $x_1 = x_2$ =0.7 and different values of the azimuthal angle φ. As can be seen from the figure, for $\varphi = \pi/4$, the transverse spin asymmetry is practically independent of the angle θ_1 and is approximately A_φ ≈0.4. For $\varphi = \pi/2$, with increasing angle θ_1, The asymmetry increases and, reaching its maximum value at θ_1 =90°, further increase of the emission angle leads to its decrease. For the azimuthal angle $\varphi = \pi$, the opposite dependence is observed: with increasing angle θ_1, the value of the transverse spin asymmetry decreases, reaches a minimum value at θ_1 =90°, and with further increase of θ_1, it increases again.

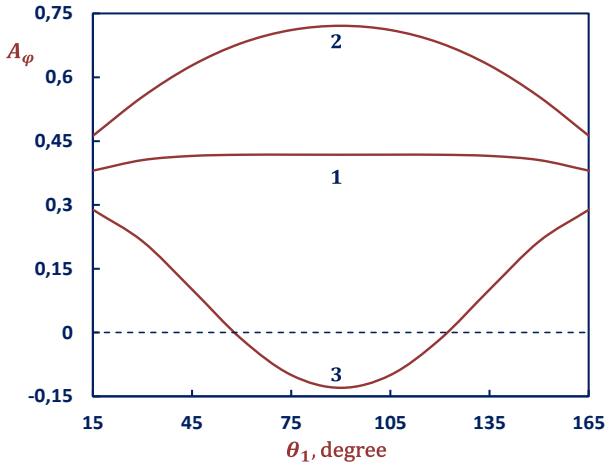

Fig. 1. Dependence of asymmetry A_φ on angle θ_1 for different values of φ:
1) $\varphi = \pi/4$;
2) $\varphi = \frac{\pi}{2}$;
3) $\varphi = \pi$ (curves 1, 2, 3 respectively).

It seems that the experimental study of the $e^-e^+ \to AhH$ process with transversely polarized electron-positron beams is of great interest, since the measurement of the transverse spin asymmetry can provide valuable information on the three-boson interaction constants λ_{Hhh}, λ_{HHh}, λ_{HAA} и λ_{hAA}.

STUDY OF THE PROCESS $e^-e^+ \to AHH$

Abdullayev S.K., *Gojayev M.Sh., Alizada M.R.
Baku State University, Azerbaijan
macidqocayev@bsu.edu.az

Here, we consider the process of production of three Higgs bosons AHH during the annihilation of an arbitrarily polarized electron-positron pair: $e^-e^+ \to AHH$. Within the framework of the Minimal Supersymmetric Standard Model, a general expression for the differential effective cross section of this

process is obtained. In the case of a longitudinally polarized electron-positron pair, the spin vectors are represented as follows: $\vec{\xi}_1 = \vec{n}\lambda_1, \vec{\xi}_2 = -\vec{n}\lambda_2$, where λ_1 and λ_2 are the helicities of the electron and positron, $\vec{n}$ is the unit vector directed along the electron momentum. In this case, the differential effective cross section of the process $e^-e^+ \to AHH$ is given by the formula

$$d\sigma(\lambda_1, \lambda_2) \sim [g_L^2(1-\lambda_1)(1+\lambda_2) + g_R^2(1+\lambda_1)(1-\lambda_2)] \cdot F_1, \qquad (1)$$

g_L and g_R are the left and right coupling constants of the electron with the vector Z-boson.

From the formula (1) it follows that the left-polarized electron e_L^- annihilates with the right-polarized positron e_R^+ and vice versa, the right-polarized electron and the left-polarized positron annihilate: $e_R^- e_L^+$. As a result, the process $e^-e^+ \to AHH$ has left-right spin asymmetry:

$$A_{LR} = \frac{g_L^2 - g_R^2}{g_L^2 + g_R^2} = \frac{1 - 4x_W}{1 - 4x_W + 8x_W^2}, \qquad (2)$$

where $x_W = \sin^2\theta_W$ is the Weinberg parameter. It is clear that the left-right spin asymmetry A_{LR} depends only on the Weinberg parameter. For this parameter x_W=0.2315, the asymmetry is A_{LR} =14%.

In the case of a transversely polarized e^-e^+-pair $\vec{\xi}_1 = \vec{\eta}_1, \vec{\xi}_2 = \vec{\eta}_2$, where $\vec{\eta}_1$ and $\vec{\eta}_2$ – are the transverse components of their spin vectors. In this case, let us determine the transverse spin asymmetry A_φ, caused by the transverse polarizations of the e^-e^+-pair:

$$A_\varphi = \frac{2g_L g_R}{g_L^2 + g_R^2} \cdot \frac{F_2}{F_1}, \qquad (3)$$

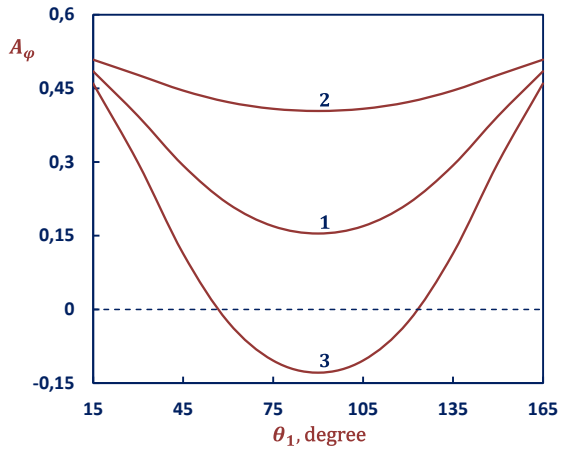

Fig. 1. Dependence of the asymmetry A_φ on the angle θ_1 for different φ:
1) $\varphi = \pi/4$,
2) $\varphi = \pi/2$,
3) $\varphi = \pi$ (curves 1, 2, 3 respectively).

F_1 and F_2 −are functions at the variables $x_1, x_2, x_A, \theta_1, \theta_2, \theta_A$.

At x_A =0.6, $x_1 = x_2$ =0.7 and different values of the azimuthal angle φ (1) $\varphi = \pi/4$, 2) $\varphi = \pi/2$, 3) $\varphi = \pi$), graphs of the dependence of A_φ on the angle θ_1 were constructed, the results are presented in Fig. 1. As can be seen from the figure, with an increase in the angle θ_1, the transverse spin asymmetry decreases, reaching a minimum value at θ_1 =90°, after which it begins to increase. The figure also shows that at $\varphi = \pi/2$, the transverse spin asymmetry reaches its greatest value, and at $\varphi = \pi$, its smallest.

An experimental study of the process $e^- e^+ \to AHH$ with transversely polarized beams of electrons and positrons will allow us to obtain information about the constants of the three-boson interaction λ_{HHh}, λ_{HHH} and λ_{AHH}.

HYDRO+TSALLIS MODELING AND COLLECTIVE DYNAMICS IN HIGH-MULTIPLICITY PP COLLISIONS AT $\sqrt{s}$ = 7 TeV

[1*]Muhammad Ajaz, [2]Haifa I. Alrebdi, [1]Murad Badshah

[1]Abdul Wali Khan University, Pakistan

[2]Princess Nourah bint Abdulrahman University, Saudi Arabia

ajaz@awkum.edu.pk

The transverse-momentum (p_T) distributions of charged pions ($\pi^+ + \pi^-$) have been examined for ten multiplicity classes of proton–proton collisions at $\sqrt{s}$=7TeV up to p_T=20GeV/c. Two phenomenological approaches were employed: the Tsallis–Pareto function and a newly proposed hybrid model combining the Boltzmann-Gibbs Blast-Wave (BGBW) and Tsallis–Pareto forms (Hydro + Tsallis). Spectra were fitted using a minimum-χ^2 method, and the hybrid model yielded a superior description of the data. From these fits, parameters such as the Tsallis temperature (T), non-extensivity index (q), kinetic freeze-out temperature (T_0), transverse flow velocity (β_T), normalization constant (N_0), and mean transverse momentum ($\langle p_T \rangle$) were extracted. Derived thermodynamic quantities – including energy density, entropy, and pressure – show a consistent rise with increasing charged-particle multiplicity, while T_0, q, and transport coefficients decrease. These trends indicate enhanced collective behavior and partial thermalization in high-multiplicity pp events, suggesting QGP-like effects even in small collision systems.

THE INVERSE COMPTON EFFECT AS A POSSIBLE MECHANISM FOR PARTON ACCELERATION

Alizada M.R., *Suleymanov M.K.
Baku State University, Azerbaijan
mais.suleymanov@bsu.edu.az

The possibility of parton acceleration resulting from inverse parton–parton scattering is considered. When a lower-energy parton collides with a higher-energy parton (or with a group of coherently interacting partons), it may gain additional energy through a mechanism analogous to the inverse Compton effect. Using the Monte Carlo code PYTHIA 8.316, we estimate the probability of such a process occurring in high-energy hadron–hadron and nucleus–nucleus collisions. These studies are important for understanding the mechanisms responsible for the generation of high- and ultra–high-energy particles, which is crucial for explaining the origin of ultra-relativistic cosmic rays.

RECENT THEORETICAL DEVELOPMENTS ON THE STRANGE EXOTIC STATES

Amirli S.I.
Baku State University, Azerbaijan
seljanamirli@gmail.com

Over the past few years, there has been progress on the theoretical investigation of the nature of φ(2170), whose internal structure is controversial. A number of interpretations have been proposed, such as an excited vector meson, a hybrid meson, or a tetraquark nature. We study the tetraquark nature of φ(2170) within the dynamical diquark model by applying spin and isospin-dependent interactions in the Hamiltonian. The model parameters are determined by taking advantage of experimental data and the results from lattice QCD and QCD sum rules. Our calculation supports its $qs\bar{q}\bar{s}$ nature and the necessity of including the spin-dependent terms in the Hamiltonian. Furthermore, we also present the model prediction for the I=1 partner of φ(2170), which should be investigated in experiments like BESIII, Jefferson Lab, or the upcoming EIC.

IMPROVED FOUR-PARAMETER EXPONENTIAL–TYPE POTENTIAL

[1*]Badalov V.H., [2]Badalov S.V.

[1]Baku State University, Azerbaijan
[2]University of Bayreuth, Bayreuth, Germany
badalovvatan@yahoo.com

We analyze a four-parameter exponential-type potential that unifies many widely used molecular models and yields new solvable forms through suitable parameter choices. By appropriate tuning, one recovers a family of exponential-type molecular potentials and clarifies interrelations among them.

The four-parameter exponential-type potential energy is given by

$$V(r) = P_1 + \frac{P_2}{1 - e^{-\alpha r}} + \frac{P_3}{(1 - e^{-\alpha r})^2}, \tag{1}$$

where P_1, P_2, P_3 and α are four adjustable parameters.

Using the relationship between the force constant, equilibrium separation, and dissociation energy, we recast it as

$$V(r) = P_1 - D_e e^{2\alpha r_e} + D_e e^{2\alpha r_e} \left(1 - \frac{1 - e^{-\alpha r_e}}{1 - e^{-\alpha r}}\right)^2, \tag{2}$$

where r_e is the equilibrium bond length and D_e is the dissociation energy of the molecule. By choosing an available value of the shifting P_1 potential parameter, it is possible to agree on experimental and theoretical values. To achieve a choice that the value of the potential energy takes $V(r_e) = -D_e; (V(\infty) = 0)$ and $V(r_e) = 0; (V(\infty) = D_e)$, the shifting potential parameter P_1 must be equal to the following expression, respectively : $P_1 = D_e(e^{2\alpha r_e} - 1)$ and $P_1 = D_e e^{2\alpha r_e}$. As a result, we obtain Newing potential and Deng–Fan potential (Schiöberg potential, improved Manning-Rosen potential), respectively:

$$V(r) = -D_e + D_e \beta^2 \left(\frac{1 - e^{-\alpha(r - r_e)}}{\beta - e^{-\alpha(r - r_e)}}\right)^2, \beta = e^{2\alpha r_e} \tag{3}$$

and

$$V(r) = D_e \left(1 - \frac{e^{\alpha r_e} - 1}{e^{\alpha r} - 1}\right)^2. \tag{4}$$

INTRABAND OPTICAL TRANSITIONS IN QUANTUM DOTS

***Usibli G.A., Gadirova I.R.**
Baku State University, Azerbaijan
iradaqadirova@bsu.edu.az

Optical methods are the most powerful and universal methods for studying quantum dots. They can provide information about the energy spectrum of the elementary excitations, for example, the energy spectra of electrons and phonons. Optical methods allow for the determination of the chemical composition and sizes of quantum dots.

In this work, the intraband optical transitions in the conduction band of the cubic symmetry semiconductor quantum dots have been investigated. Rectangular-shaped quantum dots have been considered on the assumption that the potential well has infinitely high walls. Mathematical expressions for the optical susceptibility, the absorption coefficient, and the refractive index change have been obtained for the group of identical quantum dots. For this dipole, momentum matrix elements were calculated.

The selection rules for the intraband transitions are determined by the Kronecker delta so that only one of the three quantum numbers changes for each single-photon transition; optical transitions occur only between electron states for which the sum of the quantum numbers is an odd number.

The specificity of the electron-photon interaction causing the intraband transitions is the dependence of its matrix elements on the size of the quantum dot. The dipole momentum matrix elements are proportional to the linear sizes of the quantum dot. Unlike the one-dimensional quantum well and quantum wire in quantum dots, the intraband transitions are possible in any direction of the light wave polarization vector.

Mathematical expressions for the optical susceptibility, the absorption coefficient, and the refractive index changes appear as the sum of the terms, each of which describes a separate single-photon transition. The optical function spectra are the set of lines, each of which corresponds to a single-photon transition, obeying the selection rules. As the linear sizes of the quantum dot decreases, the optical function spectra move to the high energy region and their amplitudes decrease.

ENERGY SPECTRUM OF A PARTICLE WITH POSITION-DEPENDENT EFFECTIVE MASS IN A NEW HYPERBOLIC POTENTIAL

[1]Nagiev Sh.M., [2*]Nahmadov I.A.

[1]Institute of Physics of The Azerbaijan National Academy of Science, Azerbaijan
[2]Baku State University, Azerbaijan
ibrahimnehmedov246@gmail.com

The idea of position-dependent effective mass is a current approach in order to give an exact solution to the one-dimensional Shrödinger equation. This approach helps us to solve the confined harmonic oscillator problem. The origin of the mass dependence of position can be understood by the band structure of solid compounds, which varies by position. In that case, we will replace the kinetic term of the Hamiltonian of the linear harmonic oscillator with the Ben-Daniel-Duke kinetic energy operator

$$\frac{\hat{P}_x^2}{2m_0} \to \hat{P}_x \frac{1}{2M(x)} \hat{P}_x \tag{1}$$

One can easily show that this operator is Hermitian. Therefore, we get the following equation below

$$\left[\hat{P}_x \frac{1}{2M(x)} \hat{P}_x + V(x)\right]\psi = E\psi \tag{2}$$

In our case, the new hyperbolic potential has the form:

$$V(x) = \frac{1}{2} M(x)\omega^2 \left(\frac{e^{\alpha x} - 1}{\alpha}\right)^2. \tag{3}$$

By approaching $\alpha \to 0$ this potential will recover to the potential of a linear harmonic oscillator. Position-dependent effective mass has the form of $M(x) = m_0\, e^{-\alpha x}$.

To solve this equation, we will use substitution $z = e^{-\alpha x}$. After some simplifications we will get Laguerre differential equation. Finally, we will obtain the Energy spectrum as follows

$$E_n = \hbar\omega\left(n + \frac{1}{2}\right) + \frac{\hbar\omega}{2}\sqrt{1 + \frac{4m_0\omega^2}{\alpha^4\hbar^2}} - \frac{m_0\omega^2}{\alpha^2}. \tag{4}$$

In the $\alpha \to 0$ limit case, our energy spectrum will recover to the linear energy spectrum of a harmonic oscillator.

NUCLEON GENERALIZED PARTON DISTRIBUTIONS AT FINITE TEMPERATURE WITHIN THE SOFT-WALL AdS/QCD MODEL

[1*]Akbarova N.J., [2]Allahverdiyeva M.N., [1]Mamedov Sh.A.

[1]Baku State University, Azerbaijan

[2]Institute of Physics, Ministry of Science and Education, Azerbaijan

nerminh236@gmail.com

The nucleon generalized parton distributions (GPDs) of quarks are investigated at zero skewness within the framework of the soft-wall AdS/QCD model at finite temperature. For the finite-temperature case, the soft-wall model was extended by introducing a temperature-dependent thermal dilaton field. Also, the temperature dependence in such a model was achieved by considering the dilaton constant as a temperature-dependent one. The present work is based on a matching procedure of sum rules relating the electromagnetic form factors to GPDs at finite temperatures. We plotted the temperature dependence of these quantities and observed a decrease in their peaks as the temperature increased.

SOLUTION OF THE RADIAL SCHRÖDINGER EQUATION FOR THE 5-PARAMETER EXPONENTIAL-TYPE POTENTIAL

Mahmudova G.V., *Badalov V.H.

Baku State University, Azerbaijan

gulyamahmud04@gmail.com, badalovvatan@yahoo.com

The radial Schrödinger equation for the s - state with the 5-parameter exponential-type potential has been analytically solved using the Nikiforov–Uvarov (NU) method. The corresponding energy eigenvalues and eigenfunc-tions have been obtained. It has also been established that the number of energy levels in this quantum system under such a potential is finite.

The general form of the 5-parameter exponential-type potential energy function is given as

$$V(r) = P_1 + \frac{P_2}{q + \mathrm{e}^{\alpha r}} + \frac{P_3}{(q + e^{\alpha r})^2}, \qquad (1)$$

where P_1 , P_2 , P_3 are parameters that characterize the depth and width of the potential, α is the screening parameter, and q is the deformation parameter, with $q \neq 0$. Variations in each of these parameters affect the shape, depth, and

radial range of the potential. In particular cases, with appropriately chosen parameter values, this potential reduces to well-known forms such as the constant potential, Coulomb potential, Hulthén potential, Woods–Saxon potential, Morse potential, Rosen–Morse potential, and Manning–Rosen potential.

The radial Schrödinger equation for the 5 -parameter exponential-type potential follows as

$$\frac{d^2u(r)}{dr^2}+\frac{2\mu}{\hbar^2}\left[E-P_1-\frac{P_2}{q+e^{\alpha r}}-\frac{P_3}{(q+e^{\alpha r})^2}-\frac{\hbar^2 l(l+1)}{2\mu r^2}\right]u(r)=0, \qquad (2)$$

where $\hbar = h/2\pi$ is the reduced Planck constant, μ denotes the reduced mass and l is the orbital quantum number.

By solving the equation (2) for the s-state ($l = 0$) using the Nikiforov–Uvarov method, the following expression for the energy spectrum has been obtained:

$$E_n = P_1 - \frac{\alpha^2\hbar^2}{8\mu}\times$$
$$\left[\frac{\frac{2\mu}{\alpha^2\hbar^2q^2}(qP_2+P_3)}{\pm\sqrt{\frac{1}{4}+\frac{2\mu P_3}{\alpha^2\hbar^2q^2}}-n-\frac{1}{2}}-\left(\pm\sqrt{\frac{1}{4}+\frac{2\mu P_3}{\alpha^2\hbar^2q^2}}-n-\frac{1}{2}\right)\right]^2 \qquad (3)$$

Here, the $\pm$ sign in front of the square root corresponds to the cases $q > 0$ and $q < 0$, respectively.

GRAVITATION, AN EFFECTIVE INTERACTION OF SPINORS?

Rainer M.

ENAMEC Institute Würzburg, Germany; Middle East Technical University, Turkey; Baku State University, Azerbaijan

martin.rainer@enamec.de, martin.rainer@bsu.edu.az

Newtonian gravity arises as the nonrelativistic, static, weak-field limit of some Lorentzian spacetime geometry solving the generally covariant Einstein equations for a given matter field configuration. The breakdown of relativistic quantum (field) theory at small distances approaching the Planck length suggests that the underlying Lorentzian geometry is modified at small distances. The thermodynamic correspondence, e.g., for black holes or other horizons, suggests that Lorentzian spacetime is an effective geometric description of an ensemble of more fundamental constituents. The independent derivation of the area law of the Bekenstein-Hawking entropy by string theory and loop quantum

gravity is an indication that some geometric properties of spacetime do not depend on the nature of its fundamental constituents (in leading order).

Whether, on a fundamental scale, gravity has its own classical or quantum constituents, or it is just an effective theory, deriving from expectation values of quantum matter operators (like in spinor gravity or causal fermion systems), is still open.

We compare some very different classical and quantum approaches to spacetime geometry, which, however, all derive it in one way or another from spinors.

HIDDEN-STRANGNESS TETRAQUARKS WITHIN DYNAMICAL DIQUARK MODEL

Jafarzade Sh.
Arizona State University, USA
sjafarz2@asu.edu

This study investigates whether certain short-lived particles observed in high-energy experiments – specifically resonances below 2.6 GeV such as $\phi(2170)$, $f_2(2340)$, and X(2370) – can be understood as exotic forms of matter made of four quarks, known as tetraquarks. While most known particles are built from either two or three quarks, recent discoveries suggest more complex combinations may exist. We explore this possibility using a theoretical framework called the dynamical diquark model, which has previously explained similar states containing heavier quarks. Our approach models the interaction between two tightly bound quark pairs (diquark and anti-diquark) using techniques from quantum mechanics, particularly solving the Schrödinger equation with realistic interaction potentials. To account for the influence of nearby two-hadron thresholds (for example, the $\Lambda\Lambda$ threshold) that are closed at the resonance energies, we employ a diabatic formalism. This allows virtual mixing between compact tetraquark configurations and hadron–hadron channels, providing a more complete description of resonance formation and mass shifts. The mass spectra of the predicted tetraquark states are computed and compared to experimental observations. We find strong evidence that some observed resonances align well with our predictions. For instance, the $f_2(2340)$ resonance matches the properties expected of a tetraquark made entirely of strange quarks, while the $\phi(2170)$ fits better as a mixed-flavor tetraquark involving strange and light quarks. These results support the idea that exotic hadronic matter exists not only in systems involving heavy quarks but also in the lighter, strange sector. This work contributes to a

growing body of evidence for exotic states in the strong nuclear force and extends a unified theoretical framework to new energy regions. By combining the dynamical diquark model with a diabatic treatment of closed thresholds, it offers concrete predictions that can be tested at facilities such as BESIII and Jefferson Lab, with implications for how we classify matter beyond the traditional quark model.

GRAVITATION AND SPACETIME: EMERGENT FROM SPINOR INTERACTIONS – HOW?

Rainer M.

ENAMEC Institute Würzburg, Germany; Middle East Technical University, Turkey; Baku State University, Azerbaijan
martin.rainer@enamec.de, martin.rainer@bsu.edu.az

Newtonian gravity arises as the nonrelativistic, static, weak-field limit of some Lorentzian spacetime geometry solving the generally covariant Einstein equations for a given matter field configuration. The latter has a local description in the spinor basis of Penrose. The breakdown of relativistic quantum (field) theory at small distances suggests that, the Lorentzian geometry is to be modified below some regularization length. The thermody-namic correspondence, e.g. for black holes or other horizons, indicates that, Lorentzian spacetime is an emergent geometric description of an ensemble of more fundamental constituents. The independent derivations of the area law of the Bekenstein-Hawking entropy by string theory and loop quantum gravity show that, (some) properties of spacetime do not depend on the nature of its fundamental constituents (in leading order).

Whether, on a fundamental scale, spacetime gravity has its own classical or quantum constituents (like e.g. in loop quantum gravity), or it is just an effective theory, deriving from expectation values of quantum matter operators (like in spinor gravity or causal fermion systems), this is still open.

We compare some very different classical and quantum approaches to spacetime geometry, all deriving in one way or another from spinors, and comment on questions for future research in order to clarify their relations.

A NEW VIEW ON COSMOLOGY BY USING JAKOBI'S EQUATION FROM CLASSICAL MECHANICS

Isayeva E.A.

Institute of Physics, Ministry of Science and Education, Azerbaijan
eaisaeva@mail.ru

The Jacobi's theorem. If we find the complete integral $S(x, y, z, t, \alpha, \beta, \gamma)$, where α, β, γ are arbitrary non-additive constants for the Jacobi's differential equation

$$\frac{1}{2m}\left[\left(\frac{\partial S}{\partial x}\right)^2 + \left(\frac{\partial S}{\partial y}\right)^2 + \left(\frac{\partial S}{\partial z}\right)^2\right] + V(x, y, z, t) = \frac{\partial S}{\partial t},$$

then the equations $\partial S/\partial\alpha = a$, $\partial S/\partial\beta = b$ and $\partial S/\partial\gamma =$ c, where a, b, c are three arbitrary constants, determine one of the possible motions in the force field $V(x, y, z, t)$. Here the momentum components at time t at the point x, y, z are

$$p_x = mv_x = -\frac{\partial S}{\partial x}, p_y = mv_y = -\frac{\partial S}{\partial y}, \; p_z = mv_z = -\frac{\partial S}{\partial z}$$

The experimental body m is under the action of the force field V. For example, only N_1 of all N affect the body m, N_2 are not.

Today's astrophysicists speak of the existence of dark matter and dark energy. Let's say the experimental body m is placed in their environment. We can represent them graphically. On axis Ox – dark energy N_2, on axis Oy – dark matter N_1. The angle of Universe state ray Ok on xOy plane is its state. The Universe is being expensed, $\alpha < 45°$. So, we consider that arbitrary α, β, γ are N_1, N_2 and α. The refore for us $S(x, y, z, t, N_1, N_2, \alpha)$.

Let's use the formalism of Jacobi: $\partial S/\partial N_1 = a$, $\partial S/\partial N_2 = b$ and $\partial S/\partial\alpha =$ c. Our α plays role of total energy E and $\alpha \neq \alpha(t)$. Therefore $S(x, y, z, t, N_1, N_2, \alpha) = \alpha t - S1(x, y, z, N_1, N_2, \alpha)$.

Then the Jacobi equation is:

$$\frac{1}{2m}\left[\left(\frac{\partial S_1}{\partial x}\right)^2 + \left(\frac{\partial S_1}{\partial y}\right)^2 + \left(\frac{\partial S_2}{\partial z}\right)^2\right] + V(x, y, z, t) = \alpha,$$

where $\partial S/\partial\alpha = t - \partial S_1/\partial\alpha = c = const = t_0$. Therefore $\partial S_1/\partial\alpha = t - t_0$. Thus, the secondary constants $a = \partial S_1/\partial N_1$ and $b = \partial S_2/\partial N_2$ determine the trajectory in space. The constant $c = \partial S_1/\partial\alpha = t - t_0$ describes the movement along this trajectory and in it there is only time. In fact, although the particular values of N_1 and N_2 will determine the ray of state for us, the global α will describe

to us the changes in the ray itself. Let's consider the case $V = 0$ – no force field, for example, no gravity. Then

$$\frac{1}{2m}\left[\left(\frac{\partial S_1}{\partial x}\right)^2 + \left(\frac{\partial S_1}{\partial y}\right)^2 + \left(\frac{\partial S_1}{\partial z}\right)^2\right] = \alpha.$$

We can get $S_1 = \sqrt{2m\alpha}(N_1 x + N_2 y + \sqrt{N^2 - N_1^2 - N_2^2}\, z)$, where $N = N_1 + N_2$. Let's find the secondary constants

$$a = \frac{\partial S_1}{N_1} = \sqrt{2m\alpha}\left(x - \frac{N_1}{\sqrt{N - N_1^2 - N_2^2}} z\right),$$

$$b = \frac{\partial S_1}{N_2} = \sqrt{2m\alpha}\left(y - \frac{N_2}{\sqrt{N - N_1^2 - N_2^2}} z\right)$$

and

$$\mathrm{c} = \frac{\partial S_1}{\partial \alpha} = \frac{m}{\sqrt{2\alpha}}\left(N_1 x + N_2 y + \sqrt{N^2 - N_1^2 - N_2^2}\, z\right) = t - t_0 .$$

Then $\alpha = m^2(N_1 x + N_2 y + \sqrt{N^2 - N_1^2 - N_2^2}\, z)^2 / 2(t - t_0)^2$.

We see $\alpha = 0$ when 1) $N = 0$, 2) x, y and $Z = 0$, 3) $m = 0$ and 4) $t \to \infty$. That mean there is no dark matter, there is only dark energy. These 4 cases help us to make deep analyses for history of Universe. Before Big Bang there was one point, there wasn't matter and the time was an amorphous infinity. Only with Big bang the time becomes an arrow and the space is being.

SPACE SCIENCE AND ASTROPHYSICS

THE RELATIONSHIP BETWEEN GEOMAGNETIC FIELD COMPONENTS AND AIRCRAFT ACCIDENTS IN CIVIL AVIATION

Goker U.D.
Istanbul Beykent University, Türkiye
denizgoker@beykent.edu.tr

This work is a continuation of a previous study published in Advances in Space Research (Aksen et al., 2024) involving the effect of geomagnetic storms (GSs) on aircraft accidents depending on seasonal changes, solar activity (SA), and geomagnetic activity (GA) between the years 1919 and 2023 in civil aviation. We combined the results of our previous study with the effects of solar wind (SW) parameters on the Earth's atmosphere and the components of the Earth's magnetic field (MF), including D, H, and z observations in detail, along with solar activity cycles (SACs) 18-24. We collected D, H, and z data from various Earth-based telescopes, while P, ß, T, np, Vp, B, and V; and Hp, He, Hn components of the SW and interplanetary magnetic field (IMF); and magnetosphere were obtained from satellite measurements for latitudes between $\pm 10^0 \leq \varphi \leq \pm 90^0$, respectively. The MATLAB R2018a Programming Language was used to determine and draw all data, and these data were reconstructed using the ARIMA Forecasting Model to handle the years with missing data.

The highest number of accidents, depending on the GSs, occurred during the decreasing phases of SACs, and they were also higher at equinox times. In contrast, lower values were observed at the solstices. The total number of accidents increased in the decreasing phases of SACs, except for SAC 24. GSs have a serious impact on these accidents. Still, there were also changes in the Earth's position that affected the components of the Earth's MF, such as, during the decreasing phase of the solar cycle (SC) 19, even fewer aircraft accidents occurred than in the SC 18; there were much more significant fluctuations, and during the decreasing phase of the SC 20, where more accidents occur, there was a more stable change seen. At the same time, there were no major fluctuations for the MF components of Earth related to the SA in the SAC 24. Significant increases and fluctuations in the Earth's MF components have been observed during the decreasing phases of SCs 22 and 23, directly proportional to aircraft accidents.

The velocity of the SW plasma that affects Alfven MA has directly changed in almost all cycles, but in SC19, the number of GSs was high. At the same time,

the lowest Vp was also seen towards the interplanetary medium. Other cycles exhibit similar Vp changes, regardless of their number. The lowest ß was seen in the SCs 21, 22, and 23, while the highest changes were seen in SCs 18 and 19. There has been more change in P for the SACs 21, 22, 23, and 24, while the T is at its lowest values in SCs 20 and 22. The Bz component will have the greatest impact on Earth; only the Bx component is lower in SC 23, while only the By component is lower in SC 22. As for the parameters of the magnetosphere, the most significant change in all graphs was observed for the Hn parameter; the jump was seen for the SC 20, while the quietest variation occurred in SC 21. The real abnormalities began after the SC 21.

DETERMINATION OF FUNDAMENTAL PARAMETERS OF stars: HD2885 (A3IV) AND HD1280 (A2V) BAZED ON PHOTOMETRIC QUANTITIES [c1], Q, β

Samadov Z.A., *Abdulova L.A.
Baku State University. Azerbaijan
lemanabdulova19@gmail.com

In this study, the effective temperature (Teff) and surface gravity (g) of the stars HD2885 (A3IV) and HD1280 (A2V) were determined. The effective temperature (Teff) and surface gravity (g) are key fundamental parameters of stars. Knowing these parameters makes it possible to estimate other essential stellar properties, such as mass, radius, luminosity, and age. Moreover, the effective temperature (Teff) and surface gravity (g) serve as basic input parameters for stellar atmosphere models.

The determination of Teff and log g through modeling is based on a comparison of the observed and theoretical values of several photometric characteristics of stars, as well as the equivalent widths (or profiles) of the hydrogen Balmer lines. The analysis employs parameters from the Johnson UBV photometric system Q=(U-B) -0,72(B-V), and from the Stömgren *ubvy* system *[c1]= c1-0.2 (b-y)* and including β. The β index reflects the absorption in the Hβ line and measures the intensity of this line relative to an adjacent continuum. For the star HD2885 (A3IV), the observed values of [c1], Q, β were; [c1]= 0,8416, Q=-0,0851 and β=2,838; for the star HD1280 (A2V), these parameters were; [c1]= 1,0438, Q=0,0032 and β=2,881.

By comparing the observed and theoretical values of [c1], Q, β, pairs of Teff and logg were determined. These pairs were plotted on a Teff-log g diagram,

and the intersection point of the corresponding curves yielded the star's effective temperature and surface gravity. As a result, for HD2885 (A3IV), Teff=8180K, log g=4.36; for star HD1280 (A2V) Teff=8700K, log g=4.52 were obtained, respectively.

DETERMINATION OF FUNDAMENTAL PARAMETERS (T_{eff} logg) OF THE STARS: HR33, HR64 AND HR140

***Aliyeva Z.F., Jafarli E.B.**
Baku State University, Azerbaijan
zaminaaliyeva@bsu.edu.az

Effective temperature and on the acceleration of gravitational force on their surfaces are the main fundamental parameter of every star. By knowing these parameters, the mass, radius, luminosity and age, which are the evolutionary parameters of stars, can be determined.

In this work, the $[c_1]$, Q quantities were calculated for the stars HR33, HR64 and HR140 using the GCPD - General Catalogue of Photometric Data - photometric database. Then, based on the comparison of the observed and theoretical values of the photometric quantities $[c_1]$, Q and β , the effective temperature and surface gravity of these stars were determined. We calculated the theoretical values of the photometric quantities $[c_1]$, Q and β using the Kuruç models. The obtained results are shown in the table below. Here, E(B-V) is the color excess, A(v) is the amount of absorption in interstellar space, π - the annual parallax of the star, and β measures the intensity of the H_β line of the Balmer series of hydrogen . (b-y) are the color indices in the Strömgren midband photometric system, and (B-V) and (U-B) are the color indices in the Johnson-Morgan broadband photometric system.

star names	b-y	c_1	$[c_1]$	E(B-V)	A(v)	π
HR33	0.328	0.405	0.3394	0.0215	0.06665	0.05295
HR64	0.288	0.615	0.5574	0.0660	0.20460	0.00900
HR140	0.297	0.421	0.3616	0.0114	0.03534	0.03882

star names	V	B-V	U-V	Q	β
HR33	4,895	0.492	-0.014	-0.36824	2,621
HR64	6,761	0.453	0.069	-0.25716	2,665
HR140	5,569	0.466	-0.016	-0.35152	2.660

For these stars, the observed values of [c1], Q, and β were compared with the theoretical values, and the logg, Teff pairs were determined. These pairs were plotted on the logg-Teff diagram, and the corresponding graphs were constructed. The Teff and logg of each star were determined according to the intersection point of the graphs. It was found that for HR33 the effective temperature for the star is 6307 K, log g=3.98; for the star HR64, the effective temperature is 6473 K, log g=2.93; and for the star HR140, the effective temperature is 6425 K, log g=3.92.

THE EFFECT OF SOLAR ACTIVITY ON ACADEMIC PERFORMANCE OF STUDENTS

*__Bashirov M.M., Ahmadova K.N.__
Baku State University, Azerbaijan
mbashirov@bsu.edu.az

Solar activity, which includes magnetic phenomena observed on the Sun's surface and in its atmospheric layers, rarely passes without influencing life on Earth. The Sun consists of ionized plasma whose motion generates a powerful magnetic field. The differential motion of this plasma alters the magnetic field, leading to variations in solar activity and the manifestation of space weather phenomena. Numerous studies have investigated the relationship between fluctuations in solar activity and human physiological, psychological, and behavioral indicators. To determine the influence of solar activity on human health, brain functions, and psycho-emotional state, a study was conducted in the Baku region of Azerbaijan between 2006 and 2008. The results indicated that, for certain latitudes, human physiology and psychology are affected by geomagnetic disturbances caused by the Sun. Another significant finding of the study was that levels of stress, concentration ability, and work productivity may also vary depending on changes in solar activity parameters. In another investigation carried out in the Baku region, researchers explored a potential link between variations in solar activity and the incidence of sudden cardiac death. The findings suggested that disturbances in the Sun's geomagnetic field could influence the frequency of such cases.

In the present work, the dependence of the academic performance of students at the Faculty of Physics of Baku State University on solar activity parameters was analyzed. It was determined that the academic achievements of students aged 18–22 may be directly or indirectly associated with fluctuations in

solar activity parameters. The following linear correlations were obtained from the analysis:

$$K = 100 - 3.5L - 0.3849C + 4.7600M - 15.657X$$
$$M = 100 - 0.095L - 0.1476C - 2.2077M + 8.806X$$
$$D = 0.77866L + 0.23544C - 1.35486M + 8.073X$$

Here, K, M, and D represent the parameters of quality, achievement, and attendance, respectively; L denotes the number of sunspots, while C, M, and X correspond to the number of solar flares of classes C, M, and X occurring on the Sun.

Solar activity appears to stimulate both the physical and mental performance of humans, influencing academic outcomes either directly or indirectly. Throughout human evolution, individuals have adapted to solar variations, and therefore, solar phenomena should not be perceived as a threat. Instead, these events must be studied comprehensively, and the knowledge gained should be applied practically to enhance daily life and scientific understanding.

INFORMATION - LIMITED GRAVITY: BANDWIDTH CONSTRAINTS AS THE ORIGIN OF DARK PHENOMENA

[1*]Allahyarov E., [2]Jonathan Washburn

[1]Case Western Reserve University, Cleveland, Ohio, USA; Heinrich-Heine-Universität Düsseldorf, Germany

[2]Recognition Science Institute, Austin, Texas, USA

elshad.allakhyarov@case.edu

We propose that gravitational anomalies attributed to dark matter and dark energy emerge from finite information-processing bandwidth in maintaining gravitational fields. Building on holographic principles (Susskind 1995; 't Hooft 1993) and entropic gravity (Verlinde 2011; Jacobson 1995), we derive a source-side modification where systems with long dynamical times experience a refresh lag, manifesting as enhanced effective gravity. Our goal was to test whether a strictly global, bandwidth-limited phenomenology with zero per-galaxy parameters can reproduce galactic dynamics. Using four-loop QCD and standard RG methods, we define a weight w(r)=λξn(r)(Tdyn/τ0)α ζ(r) with globally fixed constants (α=0.191). In our Information-Limited Gravity (ILG), the effective acceleration is given as αeff(r)=w(r) αboryon(r). On SPARC galaxies (N=127, quality Q=1), the proposed ILG framework achieves a median χ^2/N=2.75 across 126 galaxies under identical constraints as a fair MOND

baseline (median 2.47, 125 galaxies). The MOND acceleration scale a0≈10-10 m/s^2 emerges naturally without tuning. Cosmological tests show w(k, a) modifies growth and lensing coherently while preserving PPN parameters and Solar System tests. This is unique because: the anchor scale and all parameters are fixed globally from information theory; both galactic and cosmological "dark" effects arise from one mechanism; the predictions include scale-dependent growth f(k,z) and CMB-galaxy cross-correlation sign. The framework suggests dark phenomena reflect computational constraints rather than exotic particles.

MHD INSTABILITIES IN SHEAR FLOWS OF ANISOTROPIC COSMIC PLASMAS: NUMERICAL SOLUTION OF FIRE HOSE MODES USING BOUNDARY VALUE PROBLEM TECHNIQUES

*Samadov J.H., Dzhalilov N.S.

Shamakhy Astrophysical Observatory named after N.Tusi,
Ministry of Science and Education, Azerbaijan
jannat.samadov@gmail.com

The stability of anisotropic collisionless plasma layers in shearing flows is examined within the MHD framework, incorporating heat fluxes along the magnetic field derived from the Vlasov kinetic equation. For a smooth hyperbolic tangent velocity profile, the boundary value problem for small perturbations is formulated as a second-order ordinary differential equation governing the magnetic field perturbation Bx. The derived dispersion relation captures body and surface instabilities, including aperiodic oblique fire-hose modes, in finite-width layers with arbitrary velocity gradients.

This study emphasizes numerical solutions to identify complex growth rates Ω where body fire-hose modes transition to surface Kelvin-Helmholtz modes as the shear layer narrows. Implemented in Python with scipy. integrate.solve_ivp, the code employs high-order integrators (RK45 and DOP853) to solve the initial value problem from the left asymptotic boundary ($\tau \to -\infty$) to the right ($\tau \to +\infty$), scanning a grid in the complex Ω plane (Re[Ω] from -1 to 1, Im[Ω] from 0 to 1) to minimize boundary mismatch. Residual errors and comparisons with analytic asymptotic solutions (exponential forms at large $|\tau|$) validate the approach, revealing enhanced instability growth with increasing shear gradients. Results align with cosmic plasma contexts like solar wind interfaces, suggesting avenues for turbulence initiation. Future work may refine mesh adaptation in low-error regions for improved eigenvalue precision.

A COMPARATIVE INVESTIGATION OF THE GALACTIC DISTRIBUTION OF WOLF–RAYET AND O-TYPE STARS

*__Abdulkarimova A.F., Rustamov J.N.__

Shamakhy Astrophysical Observatory named after N.Tusi, Ministry of Science and Education, Azerbaijan

We present a comparative analysis of the Galactic distributions of Wolf–Rayet (WR) and O-type stars using updated Gaia distances. By cross-matching recent WR and O-star compilations with Gaia astrometry, applying quality cuts, and projecting sources onto a spiral-arm framework, we map arm-by-arm surface densities and subtype demographics. WR stars are found to concentrate predominantly in the Sagittarius and Scutum–Crux arms, consistent with ongoing massive-star formation there. The Perseus arm hosts fewer WR stars and is comparatively enriched in WN subtypes. The WR distribution closely follows that of O-type stars but with sharper concentrations near major star-forming segments, supporting an evolutionary connection while allowing for binary-interaction channels. Using Gaia distances for both WR and O stars – primarily Gaia-based distances for the O-star sample – our updates reduce systematics from earlier studies and produce revised spatial maps and subtype ratios as functions of Galactocentric radius and spiral-arm segment. As new WR candidates are identified and Gaia astrometry is refined, periodic re-assessment remains essential. These results provide an up-to-date baseline for testing population synthesis predictions that couple metallicity, star-formation activity, and WR subtype formation across the Milky Way.

NEUTRINO OSCILLATIONS AND MATTER ENHANCEMENT OF NEUTRINO OSCILLATIONS, THE MSW (MİKHEYEV-SMİRNOV-WOLFENSTEIN) EFFECT

*__Rahimov D.M., Jalilov N.S.__

Shamakhy Astrophysical Observatory named after N.Tusi, Ministry of Science and Education, Azerbaijan
dashdemirraqimov82@gmail.com

Neutrino oscillations represent one of the most striking manifestations of physics beyond the Standard Model. There are three types (leptonic flavors) of neutrinos – electron, muon, and tau – and as they propagate through space, one flavor can transform into another.

This phenomenon occurs because the neutrino mass eigenstates do not

coincide with their flavor eigenstates. The mixing matrix (Pontecorvo–Maki–Nakagawa–Sakata matrix, PMNS) connects these bases and determines the probability of transition from one flavor to another. Experimental observations of solar, atmospheric, reactor, and accelerator neutrinos have confirmed the existence of oscillations.

The behavior of neutrinos propagating through matter is of particular interest.

The most significant mechanism is the resonant enhancement of oscillations, known as the Mikheyev–Smirnov–Wolfenstein (MSW) effect. Its essence lies in the fact that electron neutrinos experience an additional effective potential due to weak interactions with the electrons in the medium. This potential modifies the phase evolution of neutrinos and can lead to a resonant increase in the probability of transition to another flavor state.

The MSW phenomenon plays a key role in solving the solar neutrino problem.

Classical experiments (Homestake, Kamiokande, GALLEX, SAGE) recorded a significant deficit of electron neutrinos compared to the predictions of the solar model. Modern detectors (Super-Kamiokande, SNO, Borexino) have shown that this deficit is not due to the absence of neutrinos, but to their transformation into other flavors. The MSW resonance occurring as neutrinos pass through the inner layers of the Sun provides an efficient conversion of electron neutrinos into muon and tau neutrinos.

Thus, the study of neutrino oscillations and the MSW effect has established not only the nonzero mass of neutrinos but also refined the mixing parameters and confirmed the accuracy of models describing the internal structure of the Sun.

In the future, such studies may shed light on the nature of the neutrino mass (Dirac or Majorana type), the hierarchy of mass eigenstates, and possible manifestations of new physics beyond the Standard Model.

ON THE DIFFERENTIAL ROTATION OF CELESTIAL BODIES: CORIOLIS FORCE AND ROSSBY-LIKE WAVES

Babayev E.F.

Shamakhy Astrophysical Observatory named after N.Tusi,
Ministry of Science and Education, Azerbaijan
eminbabaye0505@gmail.com

Rotation of celestial bodies is a fundamental process that determines the evolution of planetary systems, the dynamics of atmospheres and oceans, as

well as the formation of cosmic objects. According to the law of conservation of angular momentum, the rotation of stars and planets is inherited from the initial motion of gas-dust clouds. Subsequently, collisions, tidal interactions, and internal processes influenced both the speed and direction of rotation.

A vivid example of complex dynamics is the Sun, which exhibits differential rotation: the equatorial zones rotate faster than the polar ones. This affects plasma circulation, the twisting of magnetic field lines, and the formation of sunspots. The interaction between differential rotation and the Coriolis force generates global magnetic fields and determines the 11-year solar activity cycle.

The Coriolis force plays a key role in Earth's atmospheric and climatic processes. It deflects air and ocean currents (to the right in the Northern Hemisphere and to the left in the Southern Hemisphere), forming cyclones, anticyclones, and jet streams. It is also associated with Rossby waves, which regulate the movement of atmospheric systems and determine extreme climatic events such as anomalous winters, summer heatwaves, floods, and droughts. Similar processes are observed on other celestial bodies, in particular on the Sun, where magnetic Rossby waves influence plasma circulation and solar activity.

Thus, differential rotation and the Coriolis force are key factors in the dynamics of atmospheric and magnetic processes on Earth and other planets. Their study is crucial for understanding global climate, forecasting extreme events, and exploring the evolution of planetary systems.

ESTIMATION OF THE EFFICIENCY OF DETECTING NEUTRINOS FROM SUPERNOVAE USING ELECTRON OPTICAL MODULES OF THE BAIKAL GVD

***Rahimov D.M.**

Shamakhy Astrophysical Observatory named after N.Tusi, Ministry of Science and Education, Azerbaijan

dashdemirraqimov82@gmail.com

One of the key tasks of modern astrophysics is the study of astrophysical neutrinos – high-energy neutrinos of galactic and extragalactic origin, including those produced by supernovae. Having an extremely small interaction cross-section, neutrinos travel from their sources without interacting with matter, so their direction remains almost unchanged. This makes neutrinos unique carriers of information among elementary particles, as they deliver nearly undistorted data from distant cosmic sources. However, due to their weak interaction with matter, neutrino detection is challenging and requires large detec-

tor volumes. One of the modern large-volume neutrino detectors is Baikal-GVD, located in Lake Baikal, along with KM3NeT in the Mediterranean Sea and IceCube in Antarctica. The detector consists of clusters of strings (garlands) of optical modules that record Cherenkov radiation from charged particles produced in neutrino interactions with the surrounding medium.

The main purpose of large-volume detectors such as Baikal-GVD is to detect very high-energy neutrinos and reconstruct their tracks. One of the applied research goals of the detector is to assess its potential response to a supernova burst. Supernova neutrinos are low-energy, typically around 10–20 MeV. When such low-energy neutrinos interact within the detector volume, they trigger individual optical modules. Although these events are insufficient to reconstruct tracks, the intensity of localized triggers – when combined with data from other detectors optimized for supernova neutrino detection – can serve as an effective confirmation method for supernova events.

This study focuses on the potential for detecting supernova neutrinos with the Baikal-GVD neutrino telescope. The research involves the analysis of experimental data obtained using a "monopole" trigger on an optical string in the Baikal detector. The data analysis was carried out using the ROOT software framework and C++ programming tools. Based on the results of this analysis, the detection efficiency of supernova neutrinos has been evaluated.

The presented analysis method makes it possible to identify neutrino events from supernovae within the collected data. Since the energies of these neutrinos are on the order of several tens of MeV, they do not produce visible tracks but instead cause a simultaneous illumination of all optical modules. This effect can be observed as a significant deviation in the counting rate from the expected Gaussian distribution.

PREDICTING THE PRESENCE OF CLOUDS A PRIORI IN GAS GIANT EXOPLANETS' ATMOSPHERES

*Siddiqui F.R.
Baku State University, Azerbaijan
shahfouzsiddiqui@gmail.com

This work exhibits the correlational study between Planetary Physical Properties and H2O – J Index, since the characterization helps in building a library of favorable targets for future telescopes and JWST, aiding in increasing telescope efficiency and limited time. defined as H_2O – J Index, which represents

the presence or absence of clouds and hazes in an exoplanet atmosphere, we established the strength of water features probed with HST/WFC3 transmission spectra, we used units of atmospheric scale height for expressing the H_2O – J Index, and then we compared the strength of spectral features with data of 34 exoplanets. We found that H_2O – J Index is weakly correlated with Temperature(eq) ρ=+0.25 (Kelvin), Planetary Gravity (m/s^2) ρ=+0.33, and moderately correlated in (log g) ρ=+0.58. We also found that H_2O – J Index is strongly correlated with Planetary Density as ρ=+0.64. Under the boundary lines classifications of <1500K for temperature, <20 m/s^2, log g 2.8 dex for Surface Gravity, and < 0.5jup for Density, the exoplanets are likely to have clearer skies with stronger water features. These trends have been cross-verified with recent exoplanets' (WASP-39b, K2-18b, GJ 1132b, and WASP-17b) atmosphere detections of water molecules with the James Webb Space Telescope; corroborating their physical parameters aligning with our boundary line conditions, and establishing standards for a recommendation system for future observations of JWST and other time-machines. We also report that the exoplanetary parameters do have a decisive role in the emergence of H_2O features in Exoplanetary Atmospheres.

HOW CAN USING SATELLITE NETWORKS HELP ACHIEVE BIGGER DATA SETS AND RESULTS FOR ASTRONOMICAL OBSERVATIONS

Huseynli M.

The University of Edinburgh, Scotland
misirhuseynli26@gmail.com

Since the beginning of early human society, people have observed the skies for prediction, forecasting, guidance, and curiosity. Although the reasoning has changed, the importance of observations remains the same. Due to technological development, the quality and distance of sky objects we observe have improved dramatically. Ancient Greeks could only see five planets, but as of today, our telescopes can detect celestial objects that are hundreds of millions of light-years away.

Utilizing this type of satellite technology enables us to explore and understand the universe and its origin in a more accurate and accessible manner than older methods, due to factors such as light pollution, atmospheric changes, and clouds having a lesser impact on satellites compared to ground-based telescopes. However, this technology is still mostly limited to big companies and

scientific organizations, limiting the availability of cosmic observations for a substantial chunk of the population.

A possible way to address the limited access to high-quality astronomical data is by combining telescope networks with satellite communication models. This idea is based on systems like Viasat-3, which allows satellites to communicate directly with one another without the need for ground-based relays. Implementing a similar concept within the Skynet Robotic Telescope Network, which links twenty ground-based telescopes worldwide and supports both astronomers and public users capturing images (more than twenty million as of today), could create an integrated system by enabling telescopes and satellites to share observation data while in orbit. This framework would reduce data latency, improve global coverage, and enable both professional and amateur astronomers to participate in observations. Broadening access through either free or paid models could raise interest in the public, creating continually updated datasets, encouraging discoveries, and long-term archiving.

ON SOME SPECTRAL AND PHOTOMETRIC FEATURES OF SYMBIOTIC STARS: AGPeg, AG Dra, CH Cyg, and EG And

[1]Mikailov Kh.M., [2*]Rustamova A.B., [1,2]Rustamov B.N.

[1]Baku State University, Azerbaijan

[2]Shamakhy Astrophysical Observatory named after N.Tusi, Ministry of Science and Education, Azerbaijan

mikailov.kh@gmail.com

The optical spectra of the investigated stars were obtained at the Cassegrain focus of the 2-m telescope of the Shamakhy Astrophysical Observatory named after N.Tusi, using the fiber echelle spectrograph (ShAFES) with a spectral resolution of R = 28000 and partially taken from the ARAS Spectral Database. The reduction of the echelle spectra was carried out according to the standard procedure using the new version of the DECH 30 program. Photometric data are taken from the International Database AAVSO (American Association of Variable Star Observers).

Symbiotic stars represent a special type of close binary systems that typically consist of a cool giant, a hot compact white dwarf, and a surrounding gas–dust nebula. Therefore, to explain the results obtained from observations of these stars, it is necessary to perform a comparative analysis of the charac-

teristic physical parameters of the cool giant and the white dwarf, as well as the features of the accretion disk formed from the material flowing from the cool giant to the white dwarf.

Several periods characteristic of binary star systems are observed in the changes in the spectral and photometric parameters of the stars under study. In the present work, radial velocity curves were constructed for each of the studied stars based on the mean values of the radial velocities of pure (unblended) absorption lines formed in the atmosphere of the cool giant, and the corresponding spectral parameters were determined from these curves. In constructing these curves, we used either refined or previously known values of the photometric periods. For the emission lines formed in the gas stream flowing from the giant near the hot white dwarf and/or in the accretion disk of the white dwarf, radial velocity curves were constructed for the hydrogen Balmer series lines (particularly the Hα line), as well as for selected helium and forbidden lines.

As a result, a comparative analysis of the periodic variations in the radial velocities and intensities of the absorption and emission lines in the spectra of the studied stars is presented.

MORPHOLOGIES OF THE Hα AND Hβ LINES IN YOUNG HERBIG Ae/Be STARS: HD 31648, HD 52721, HD 53367

[1,2]Rustamov B.N., [1]Mikailov Kh.M., [2]Mammadova S.O., [2*]Aliyeva V.I., [2]Rustamova A.B.

[1]Baku State University, Azerbaijan
[2]Shamakhy Astrophysical Observatory, named after N.Tusi, Ministry of Science and Education, Azerbaijan
bayram_rustam@yahoo.com

The Balmer hydrogen lines, particularly the Hα line, are among the most informative emission features in the spectra of young Herbig Ae/Be stars. The shape (morphology) of these lines reflects the structure and dynamics of the circumstellar environment, including accretion flows, stellar winds, and the possible presence of a gaseous envelope. Based on their morphology and radial structure, the Hα emission profiles of these stars can be classified into several types: single-peaked emission profiles, double-peaked profiles, P Cyg-type profiles, inverse P Cyg-type profiles, and emission profiles with central absorption.

In this study, three typical Herbig Ae/Be stars were selected – HD 31648, HD 52721, and HD 53367 – whose spectra exhibit almost all of the aforemen-

tioned forms of Hα emission profiles. For comparative purposes, the behavior of the Hβ lines was also analyzed. The Hα and Hβ line profiles were constructed, and their main profile parameters were measured.

The optical spectra of the investigated stars were obtained at the Cassegrain focus of the 2-m telescope of the Shamakhy Astrophysical Observatory named after N. Tusi, using the fiber echelle spectrograph (ShAFES) with a spectral resolution of R = 28000 and partially taken from the Be Stars Spectra Database, with a spectral resolution of R ≈ 11.000.

SPECTROPHOTOMETRIC STUDY OF PLANETARY NEBULA NGC 7009

*Alili A.H., Mikailov Kh.M., Alisheva K.I.
Baku State University, Azerbaijan
aynuraalili@bsu.edu.az

The electron temperature and electron density of NGC 7009 were calculated from the [OIII] (λ4959+λ5007)/λ4363 intensities ratio, and the ionized mass was calculated from the H_β flux. The flux in the H_β emission line and the intensities in the [OIII] forbidden emission lines were identified from the spectra obtained from the archive of the European Southern Observatory. The observed intensities for O[III] lines and flux for H_β were corrected for interstellar reddening. The electron temperature and electron density were calculated from the formulas

$$T_e = \frac{14320}{lgR[OIII] - 0.89} R[OIII] = \frac{7.9e^{\frac{32900}{T_e}}}{1 + 4.5 \cdot 10^{-4} \frac{n_e}{T_e^{0.5}}},$$

where R[OIII] is [OIII] (λ4959+λ5007)/λ4363 ratio. The ionized mass was calculated from the formula

$$M = 11.06 F(H_\beta) d^2 t^{0.88} n_e^{-1} M_\odot .$$

The intensity ratio of 134,21 and the flux Hb of $5.31 \cdot 10^{-11}$ were found. Respectively, the electron temperature of 11569 K, the electron density of $2.7 \cdot 10^{-3}$ and ionized mass of 0,`18 M0 were found for the NGC 7009. The results obtained were compared with the results of other authors.

DETERMINATION OF FUNDAMENTAL PARAMETERS OF STARS: HD1279 (B7III) and HD1438 (B8V) BASED ON PHOTOMETRIC QUANTITIES [c_1], Q, β

Samadov Z.A., *Hashimova J.A.
Baku State University, Azerbaijan
jalahasimova@icloud.com

The effective temperatures of stars T_{eff} and the surface gravity (g) are their main fundamental parameters. Knowing these parameters, the evolutionary parameters of stars: mass, radius, luminosity, age are determined. Also, T_{eff} and log g are the basic parameters of models of stellar atmospheres.

One of the accurate methods for determining T_{eff} and log g is the model method. This method is based on the comparison of observed and theoretically calculated values of a number of photometric and spectral quantities of stars. In this work, the effective temperature and surface gravity of the stars HD1279 (B7III) and HD (B8V) were determined based on the following criteria:

- Comparison of observed and theoretical values of the photometric quantity [c_1],
- Comparison of observed and theoretical values of the photometric quantity Q,
- Comparison of observed and theoretical values of the photometric quantity β.

The quantity [c_1] is defined as [c_1] =c_1-0.2(b-y) in the ubvy photometric system, and the quantity Q is defined as Q= (U-B)-0.72(B-V) in the UBV photometric system. The quantity β is related to the absorption in the Hβ line of the Balmer series of hydrogen, and determines the intensity of this line relative to the continuous spectrum around Hβ. The quantities [c_1] and Q are free from the influence of absorption in interstellar space.

For the star HD1279 (B7III), the observed values of [c_1], Q and β are [c_1]=0.592, Q=-0.3752 and β=2.675, respectively; for the star HD1438 (B8V), the values are [c_1]=0.6836, Q=-0.3024 and β=2.751,respectively.

Based on the comparison of the observed and theoretical values of [c_1], Q and β, T_{eff} = 13310K, log g = 4.15 for the star HD1279 (B7III); T_{eff} = 12470K, log g = 4.08 for the star HD1438 (B8V).

COMPARATIVE PHOTOMETRIC AND SPECTROSCOPIC EVOLUTION OF NOVA SCO 2023 AND RX PUP

*Alisheva K.I., Mikailov Kh.M., Isagova N.R.
Baku State University, Azerbaijan
kamalaalisheva@bsu.edu.az

This study presents a comparative investigation of the photometric and spectroscopic behavior of the classical nova Nova Sco 2023 (V1716 Sco) and the symbiotic recurrent nova RX Pup, emphasizing the contrasting physical mechanisms governing their eruptions. By incorporating real observational parameters obtained from ARAS, AAVSO, ShAO, and previously published datasets, we examine how thermonuclear runaway (TNR), shock interactions, and circumstellar density shape the dynamical and radiative evolution of these two systems.

Nova Sco 2023 exhibited the hallmarks of a fast classical nova triggered by a TNR in a thin hydrogen envelope accreted onto a relatively massive white dwarf (≈1.1 $M_\odot$ or higher). Its maximum brightness reached V ≈ 7.8–8.1 mag with an outburst amplitude of nearly 9 mag. The decline rates (t_2 ≈ 10–13 days, t_3 ≈ 24–28 days) clearly classify it as a fast nova. The estimated ejecta mass is (1–5) × 10^{-5} $M_\odot$. Early post-outburst spectra were dominated by Fe II emission lines with pronounced P Cygni absorption, corresponding to expansion velocities of 2000–2800 km/s and extended line wings of up to 3500–3800 km/s – indicative of nearly ballistic expansion into a low-density environment. Around days 10–12, the nova transitioned into the He/N spectral class, showing the emergence of He II 4686 Å with EW ≈ 4–7 Å. Forbidden [O III] 5007 Å emission appeared around days 20–25, reflecting rapid rarefaction and increasing ionization of the ejecta. The overall evolution is consistent with a classical nova governed primarily by the impulsive TNR energy release.

In contrast, RX Pup evolves within a fundamentally different physical environment dictated by its symbiotic nature. The white dwarf accretes from the dense slow wind of a red giant (Vwind ≈ 10–20 km/s), creating a circumstellar medium with densities two to three orders of magnitude higher than those around classical novae. As a result, RX Pup's ejecta undergo strong deceleration, with Hα line widths corresponding to only 90–120 km/s. Outbursts are dominated not by a single explosive impulse but by long-lived shock interactions. High-ionization lines – including He II 4686 Å (EW ≈ 10–40 Å), [Fe VII] 6087 Å, and [Ne V] 3426 Å – persist for months or even years. The photometric signature of RX Pup is likewise distinct: instead of a fast decline, the system displays extended plateaus of 200–400 days with amplitudes of 3–5 mag, sustained by

continuous accretion and radiative shocks. Shock-heated plasma reaches temperatures of (2–5) × 10^5 K, forming a long-lasting, highly ionized nebular region incompatible with classical nova behavior.

The contrasting roles of the donor stars are critical in shaping the physical evolution of both systems. In Nova Sco 2023, a low-mass main-sequence donor provides material via Roche-lobe overflow, allowing the accreted layer to ignite explosively under TNR conditions. The ejecta subsequently expand freely with minimal interaction. In RX Pup, however, the dense red-giant wind produces multiple interacting shells and shock fronts that dominate the system's post-outburst dynamics, leading to complex multicomponent spectral profiles, extended ionization phases, and a significantly slower decline.

Overall, the comparison demonstrates that Nova Sco 2023 is an archetypal TNR-driven classical nova characterized by rapid expansion and short-lived high-excitation phases, whereas RX Pup is governed by long-term interaction between ejecta and a dense circumstellar medium, resulting in shock-dominated, slow, and highly ionized evolution. These fundamental differences influence not only their photometric and spectroscopic behavior but also the physical structure and lifetime of their ejecta, highlighting the essential role of environmental density in nova evolution.

THE POSSIBLE ROLE OF COMETS IN ANALYSING THE PROBLEM OF AN UNKNOWN PLANET

[1*]Gadirov E.K., [2]Guliyev A.S.

[1]Baku State University, Azerbaijan
[2]Shamakhy Astrophysical Observatory named after N.Tusi, Ministry of Science and Education, Azerbaijan
quliyevayyub@gmail.com

A ninth planet in the Solar System has been proposed to explain strange behavior in its outermost regions, particularly the persistent clustering of the orbits of extreme trans-Neptunian objects. Simultaneously, because they respond strongly to gravitational forces on the edges of the Solar System, long period and hyperbolic comets are also significant for studying the outer Solar System. Comets' orbital characteristics can provide clues unknown massive bodies because they comprise the largest group of small bodies originating from the Oort cloud and other far-off reservoirs.

The known giant planets are unable to account for a number of dynamic

irregularities in the outer Solar System's current structure. Long period and hyperbolic comets also exhibit a number of odd patterns in addition to the clustering of extreme TNO orbits. These consist of an oddly slanted plane with a high concentration of perihelia, a surprisingly high number of aphelia situated between 250 and 400 AU, distinct peaks in the Tisserand parameter values concerning a potential distant perturber, and an uneven distribution of hyperbolic comets.

The effects of the giant planets, the Galaxy, or stars that pass close by cannot fully explain these features. This means that there may be another big object in the outer parts of the Solar System.

First, there is the Planet Nine hypothesis developed by Batygin and Brown. In this scenario a distant planet with a mass of about five to ten Earth masses moves on a very long and eccentric orbit with a semi major axis of roughly four hundred to eight hundred astronomical units and a moderate inclination. Numerical simulations show that such a body can keep the orbits of the most distant trans Neptunian objects in a common direction and can explain the observed clustering in their perihelion arguments, nodes and inclinations. These studies suggest that the outer Solar System requires a stable additional source of gravity in order to reproduce the present orbital structure of extreme TNOs.

Guliyev and colleagues advanced a different but related perspective, which used long-period and hyperbolic comets as tracers of a hidden massive body. By statistically analyzing more than 1,000 long-period comets, they detected 2 preferred planes of perihelia, an excess of aphelia between about 250 and 400 AU, and characteristic peaks in the Tisserand parameter with respect to a possibly distant perturber. If there is another planet with a mass of order 10 Earth masses on a moderately eccentric and strongly inclined orbit at a semi-major axis of around 300–350 a.u., then one could account for these properties. Under this scheme comets form a dynamical family controlled by the unknown planet, and their orbital distribution can be considered as a means of indirectly locating a large trans-Neptunian object.

This paper uses cometary data from 2017 onward to study, on a dynamical and statistical level, the properties of long-period and hyperbolic comets and to examine whether these recently observed objects provide indirect evidence for a large trans-Neptunian body that may directly influence the outer Solar System. This approach would be aimed at showing if the distribution of perihelia, aphelia, nodes and the Tisserand parameter observed in a large comet sample can be interpreted as evidence of an unknown planet somewhere around 250 to 400 AU. It also proposes a compromise between alternative analysis

techniques such as geometric orbit analysis, the shortest distances between orbits and dynamic evolution indicators like the Tisserand parameter. The goal is finding out where a hypothetical planet might actually be (or where we know it is most likely to be) and then improving our knowledge about that hypothetical planet's orbit - the mass, inclination, eccentricity and semi-major axis.

ARTIFICIAL INTELLIGENCE ENVİRONMENT FOR PRECISE SATELLITE DATA PROCESSING

[1]Guliyev J., [2]Muhammad A.İ., [3]Mustafa K., [1*]Rustamov R.B.

[1]Institute of Physics, Ministry of Science and Education, Azerbaijan
[2]NED University of Engineering and Technology, Pakistan
[3]Wimbledon College, UK
r_rustamov@hotmail.com

Soil salinization is a critical factor of land degradation in arid regions with intensive agriculture, posing challenges to sustainable development. Taking into account of the significant cost and infrequency of conventional field surveys, the use of satellite-based methodologies is imperative for the effective monitoring of ecological systems.

The aim of the current study is the scalable spatial-temporal approach for assessing soil salinity in the Karabakh region (South Caucasus, Azerbaijan) using GeoTIFF satellite data, development of Geographic Information System (GIS), and application of Artificial Intelligence for achievement of the high precise data processing.

The present phase implements the Salinity Index (SI), while subsequent studies will explore the Normalized Difference Vegetation Index (NDVI), the Normalized Difference Salinity Index (NDSI). A final comparative analysis will identify the most accurate and reliable index for monitoring soil salinization as expected to demonstrate advantages and weaknesses of the methods selected for task solutions.

CONTENT

MATERIAL SCIENCE

CONDENSED MATTER

9th INTERNATIONAL CONFERENCE MTP-2025: MODERN TRENDS IN PHYSICS

BOOK OF ABSTRACTS

November 27 – 28, 2025
Baku State University, Baku, Azerbaijan

Printed: 26.11.2025
Volume 16,5 p.s.. Amount 100

Baku State University Publishing House.
33, Acdemician Z. Khalilov street, Baku, Azerbaijan
Tel: (+99412) 538 87 39 / 538 50 16
e-mail: bduneshrevi@bsu.edu.az
com www.bsu.edu.az

BAKU STATE UNIVERSITY
33, Academician Zahid Khalilov Street,
Baku, Azerbaijan
Phone: (+994 12) 430 32 45
E-mail: info@bsu.edu.az